Local crystal structure of Bi-based perovskites solved by RMC modeling

Thesis submitted in accordance with the
requirements of the University of Liverpool
for the degree of Doctor in Philosophy
by Robert Jan Szczecinski

April 2013

Local crystal structure of Bi-based perovskites solved by RMC modeling

The local structure investigation by Reverse Monte Carlo modeling and comparison to average crystallographic structure of Bi-based perovskite materials are presented in this thesis. This novel technique using neutron total scattering is applied in search of possible short-range correlations between atoms to understand complex structure of these materials.

Chapter One gives an introduction into perovskite structure and its properties. Chapter Two describes the difference between periodic and aperiodic crystals, which average crystallographic structure has been adopted by materials presented in this thesis. It also describes the total scattering and Pair Distribution Functions used in Reverse Monte Carlo modeling.

The next chapters describe the local and average structure investigated during this thesis. Chapter Three describes the local and average perovskite structure of $BiTi_{3/8}Fe_{1/4}Mg_{3/8}O_3$ at various temperatures, where local structure analysis revealed particular displacements and correlations of A site and B site cations not captured by average crystallographic structure. Chapter Four compares local structure derived from RMC modeling and average incommensurate and commensurate crystallographic structures of $Bi_2Mn_{4/3}Ni_{2/3}O_6$ at room and high temperatures respectively, demonstrating importance of recognizing the length-scale of the probe used for structural characterization. Chapter Five describes the work on $BiFe_{0.6}Mn_{0.4}O_3$ perovskite which was investigated by traditional crystallography to determine the modulated behavior and distorted structure of this material. The last Chapter 6 contains main conclusions from all experimental chapters.

Acknowledgments

This research project would not have been possible without the support of many people. Firstly I would like to thank my supervisors Prof. Matthew Rosseinsky and Dr. John B. Claridge for all their help and guidance throughout this PhD.

Many thanks to all members of MJR group, in particular Sam and Phil who helped me a lot in preparing and analyzing PDF data. I would like to also thank Natasha, Alicia, and Umut. It was big pleasure to share office with You! Frantisek thanks for the hot chocolate breaks when we chatted most of time about running and cycling.

Thanks to the brilliant beamline scientist Dr. Matthew G. Tucker at ISIS.

Last but not least I would like thank my parents for unwavering support and my wife Malwina for being with me throughout this time.

The work presented in this thesis was carried out by myself, except where stated, at the Chemistry Department, University of Liverpool between May 2009 and April 2013 under the supervision of Prof Matthew J. Rosseinsky and Dr. John B. Claridge. This work has not been submitted for any other degree at this or any other university.

Robert J Szczecinski April 2013

Contents **Page**

Chapter 1. Introduction

1.1 Introduction and Thesis Aim

The interplay between atomic structure and physical properties provide the opportunity to improve the macroscopic properties by first understanding the atomic structure. All crystalline materials possess an atomic structure where locations of atoms are described by traditional crystallography. This approximation defines average positions of atoms within a unit cell, which are perfectly periodic. Thermal displacement parameters applied in describing crystallographic structure define all atoms, vibrating within the crystalline lattice, which are averaged over all the unit cells and time. This approach of describing materials by traditional crystallography does not always fully describe the atomic structure of complex materials. Thus, due to averaged atomic positions and their thermal parameters, the local chemical or displacive deviations are usually lost in the average long-range structure. Information on these deviations is contained underneath the Bragg peaks in a diffraction pattern, within the background as diffuse scattering. The combination of Bragg and diffuse scattering as total scattering [1] allows evaluation of both long- and short-range order in the material. The Reverse Monte Carlo (RMC) [2, 3] modeling uses the total scattering in both reciprocal and real space. Thanks to the simultaneous refinement of Bragg profile and total scattering in reciprocal space, and Pair Distribution Function (PDF) in real space, the RMC modeling, described in a chapter 2, can fully characterize structure of complex materials.

The PDF approach by total scattering analysis has been used to establish the local structures of lead based perovskite materials, which received huge commercial and scientific attention. However, due to environmental concerns leading to lead compounds being defined as hazardous substances, there has been a great boost to search for lead-free materials. Bismuth atoms so far are the best alternative to Pb^{2+} due to the presence of $6s^2$ lone electron pairs where hybridization between the Bi 6s states and oxygen 2p states stabilizes the off-centering displacement of Bi atoms, producing ferroelectricity. The investigation of A site doped Bi-based

perovskite ferroelectric materials revealed significant differences between average and local structures, and played an important role in determining the ferroelectric properties [4-6]. On the other hand, the local structures of pure Bi-based perovskite have not been studied extensively and the possible short-range correlations within these materials have not been previously reported.

In this thesis, the PDF approach by total scattering analysis in the RMC modeling has been used to establish the local structures of $Bi_2Mn_{4/3}Ni_{2/3}O_6$ [7] and $BiTi_{3/8}Fe_{1/4}Mg_{3/8}O_3$ [8]. Local structures derived from these simulations are compared to average crystallographic structures, which is equally important in characterization of the material's structure. Moreover, the $BiFe_{0.6}Mn_{0.4}O_3$ perovskite was also investigated by traditional crystallography to determine the modulated behavior and distorted structure of this material.

1.2 Perovskite structure

The ferroelectric and antiferroelectric materials presented in this thesis adopt the perovskite structure. Perovskite as a mineral was first discovered in the Ural mountains of Russia in 1830's and named after the Russian mineralogist Lev Alekseevich Perovski. However, it took one hundred and ten years until 1940s when investigations of its physical, chemical and structural properties as a ABO_3 perovskite structure were started.

The general chemical formula ABO_3 contains two metal cations occupying A and B site and O anions bonding metals, where non distorted highest symmetry has a cubic structure e.g. $SrTiO_3$ (Figure 1.1) [9]. Metalic cations on the B site occupying the center of the unit cell are coordinated by six oxygen anions creating BO_6 octahedron. The A site cations occupy the eight corners in the unit cell and are usually coordinated by twelve oxygens.

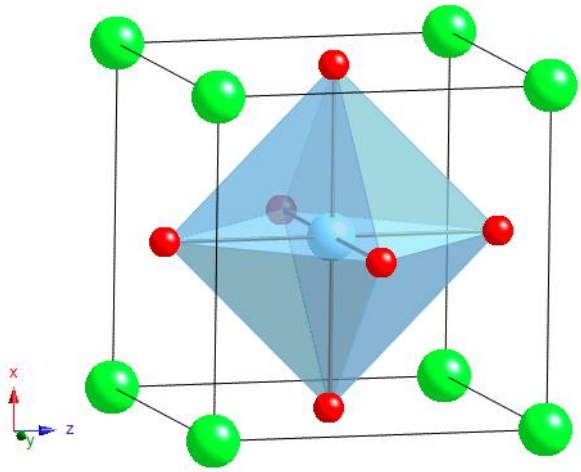

Figure 1.1. *Structure of example perovskite $SrTiO_3$. Green spheres are the A site cations, and blue sphere is B site cation linked with red oxygen anions constitute the octahedron.*

The ideal cubic perovskite $SrTiO_3$ presented above has a simple cubic structure, however a large number of materials with formula ABO_3 possess lower symmetry than cubic, as an effect of deficiency of large cations and is reflected in the distortions of the structure. The distortions of the octahedra, tilting, and displacement of A and B site cations allows to acquire stable bonding in the structure and also support ferroelectricity, which description will be described in section 1.2.1.

To estimate the degree of distortion of perovskite structure, the Goldschmidt's tolerance factor [10, 11] was introduced as a ratio:

$$t = \frac{(r_A + r_O)}{\sqrt{2}(r_B + r_O)} \qquad \text{Equation 1.1}$$

where:

r_A, r_B *and* r_O are ionic radii of A site, B site and oxygen ions.

In the ideal cubic structure when the structure is non distorted, the ratio in the Goldschmidt's tolerance factor is equal to one, while the perovskite structure with a tolerance factor departing from unity increase the distortions in the unit cell. The Perovskite structure is only stable when the Goldschmidt's tolerance factor is in

the range $0.9 < t < 1.1$ according to the rule of thumb, whereas factors outside the range, prevent to form a composition ABO_3. There is a non-general formula where structures with $t > 1$ prefer to be tetragonal with distortions observed along cubic $\langle 100 \rangle_p$ direction ($\langle \rangle_p$ refer to the parent cubic perovskite unit cell) (Table 1.1). On the other hand, a tolerance factor with a smaller value than unity ($t < 1$), gives rhombohedral or orthorhombic structures with directions of distortions along $\langle 111 \rangle_p$ and $\langle 110 \rangle_p$ respectively. Thus, the sizes of ionic radii of A and B site cations play important role in forming different crystal symmetry of perovskite structure [12].

Table 1.1. *Directions of distortions and resulting crystal symmetry [12].*

Crystallographic direction	Resulting unit cell
$\langle 100 \rangle_p$	Tetragonal
$\langle 110 \rangle_p$	Orthorhombic
$\langle 111 \rangle_p$	Rhombohedral
$\langle hk0 \rangle_p$ and $\langle hkl \rangle_p$	Monoclinic and Triclinic

1.2.1 Ferroelectricity and ferroelectric materials

Ferroelectricity as a property of materials investigated in this thesis has the attribute of spontaneous electric polarization direction, which can be switched by applying electric field. The history of this phenomena started in 1920's, where in potassium sodium tartrate called Rochelle salt [13, 14] discovered the piezoelectricity, which triggered the development of a theory about ferroelectric phase transitions [15]. During the second world war and late 1940s, the successful discovery of barium titanate and other perovskite oxides [16] contributed to expanding research on the ferroelectric materials. These primary materials with other materials like lead zirconate titanate [17] helped to establish and understand physics of ferroelectric materials. Since that time, the technology development led to many commercial applications like capacitors due to high dielectric permittivity or actuators, transducers and Ferroelectric Random Access Memory

(FERAMs) due to their piezoelectricity [18]. Thus, ceramic materials possessing ferroelectricity have found applications in very wide range of devices.

Ferroelectric materials produce a permanent dipole moment in the structure due to short-range coulomb repulsion in balance with hybridization between neighbouring orbitals of transition metal atoms and oxygen anions. These materials are sometimes called polar, as they possess an unique polar axis within a lattice, where ions are aligned in one direction. An ionic polarization is expressed by u_i the displacement of the ion *I* and its charge q_i [19]:

$$p = \sum_i q_i u_i \qquad \text{Equation 1.2}$$

Ferroelectric materials show a nonlinear spontaneous nonzero polarization when the applied field *E* is zero (Figure 1.2a) in contrast to paraelectric materials, where ions are randomly oriented in the material. This arrangement of unaligned electric dipoles produces overall lack of polarization upon removing the field E (Figure 1.2b). Another distinctive feature of ferroelectrics over paraelectrics is that the spontaneous polarization can be reversed by an applied electric field.

On the other hand dielectric materials are electrical insulators presenting linear dependence of electrical polarization induced by external electrical field (Figure 1.2c), in contrast to nonlinear polarization dependence on field taking place in ferro- and paraelectrics.

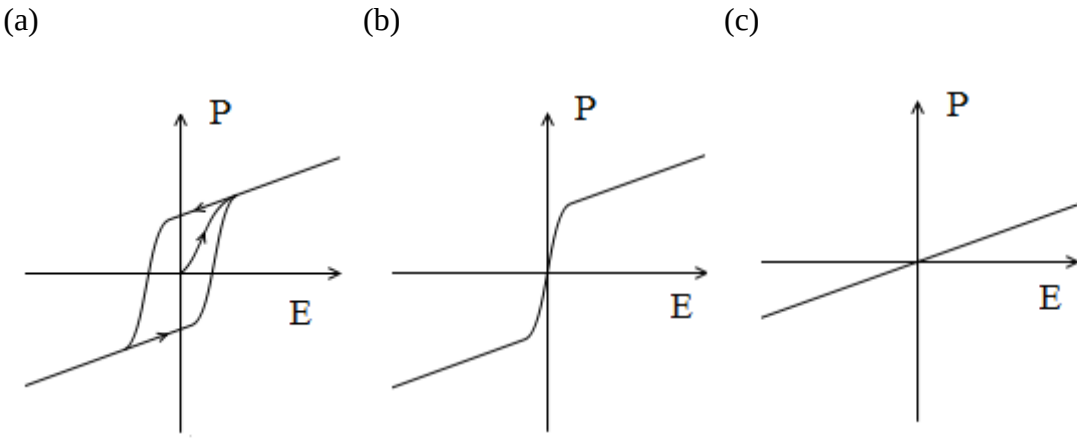

Figure 1.2. *Polarization versus external electric field E for (a) ferroelectrics, (b) paraelectrics and (c) dielectrics.*

The most important ferroelectric materials like $BiFeO_3$ [20], $BaTiO_3$ [21] or $Pb(Zr,Ti)O_3$ [17] adopt the perovskite structure. $BaTiO_3$ for example undergoes the series of ferroelectric phase transitions starting from tetragonal through orthorhombic with final polarization along $\langle 111 \rangle_p$ direction in the rhombohedral phase at low temperatures. Titanium ions of the d^0 state at ferroelectric phases hybridize with O 2p ions generating displacement of Ti^{4+} cations from the center of oxygen centroid and create a dipole moment. Furthermore $BaTiO_3$ at high temperature adopt the cubic phase where ionic charges cancel out producing non-polar material.

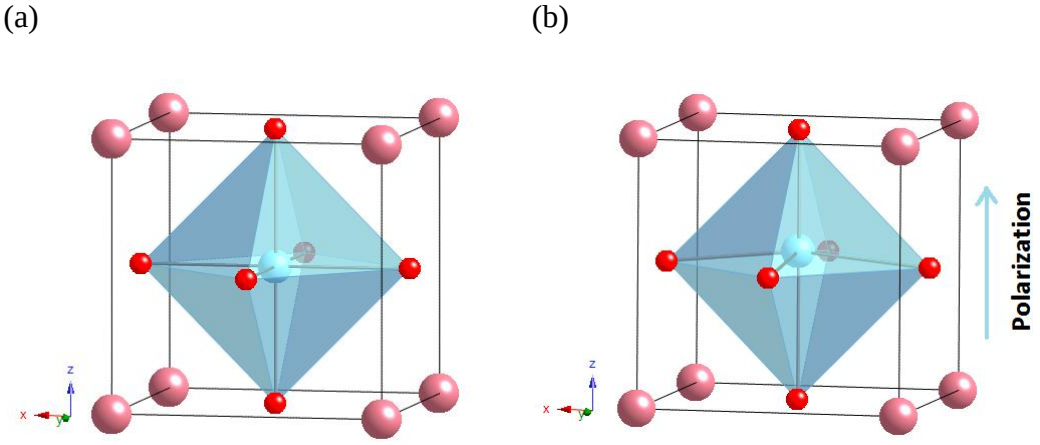

Figure 1.3. *Non-polar high temperature cubic phase and (b) polar tetragonal phase of $BaTiO_3$ with displacement of Ti^{4+} cations along z direction.*

The distortions like in the case of $BaTiO_3$ demonstrate hybridization of metal cation with oxygen 2p state which is essential to produce and stabilize ferroelectricity. Another important example are lead based perovskites with electron configuration [Xe] $4f^{14}$ $5d^{10}$ $6s^2$, where lone pair of two electrons with antiparallel spins in the outermost filled subshell $6s^2$ occupy one side of the ion. This feature helps to strongly hybridize electrons between Pb 6s and O 2p states, and stabilize the ferroelectric distortions of polarized Pb cations. The most well-known lead based perovskite is Pb(Zr,Ti)O3 (PZT), which became interest of extensive study as it has been shown excellent piezoelectric properties at the morphotropic phase boundary (MPB), where phase transition between rhombohedral and tetragonal occured at composition $PbZr_{0.52}Ti_{0.48}O_3$ [17, 22]. The extensive work on the MPB between rhombohedral and tetragonal phases of PZT material revealed the local displacements along one of the directions $\langle 100 \rangle_p$ and $\langle 110 \rangle_p$ for rhombohedral and tetragonal PZT phases respectively, which probably act as a precursor in the transformation from rhombohedral to tetragonal phase in the MPB. The investigation of PZT by Noheda have revealed local disordered shifts of the Pb atoms with magnitude of 0.2 Å perpendicular to the polar axis $\langle 111 \rangle_p$ for tetragonal phase, which were assigned to the presence a new monoclinic phase between the previously established tetragonal and rhombohedral phases [23] (Figure 1.4). These large atomic displacements are only observed in compositions close to MPB, indicated that the piezoelectric strain, which generate such striking electromechanical properties close to MPB, is along directions associated with the monoclinic distortions, instead of polar directions as previously thought [22, 23].

(a)

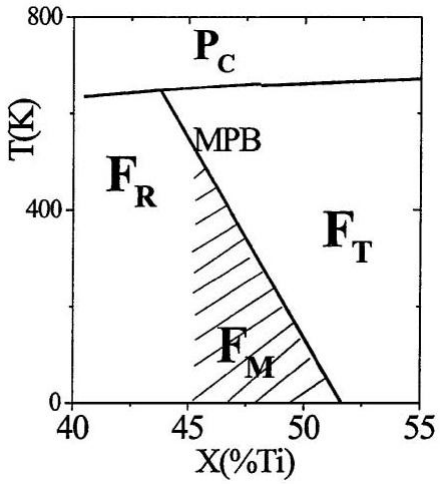

(b)

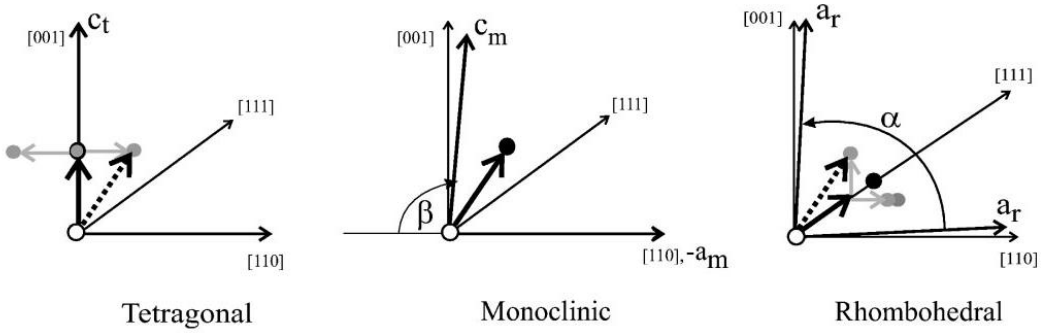

Figure 1.4. *(a) PZT phase diagram demonstrating the monoclinic region F_M close to MPB between rhombohedral F_R and tetragonal F_T phase [22]; (b) Schematic view of distortions: tetragonal (left), monoclinic (center) and rhombohedral (right) on the pseudocubic plane {110}; (solid circles describe the observed shift of Pb cations with respect to the ideal cubic phase, while the grey circles represents the local shifts; the polar axes in the monoclinic phase (center) is contained between tetragonal and rhombohedral polar axes [23].*

Despite the very good piezoelectric properties of PZT, there are also other Pb-based perovskites like $PbMg_{1/3}Nb_{2/3}O_3$ (PMN) [24], $PbSc_{1/2}Nb_{1/2}O_3$ (PSN) [25] or $PbMg_{1/3}Ta_{2/3}O_3$ (PMT) [26] with peculiar structures and properties. They are called relaxor ferroelectrics [27-29], as upon cooling at Burns temperature (transition temperature - T_B) are transformed from non-polar paraelectric phase to

relaxor state, with appearance of polar nanoregions in nanometer scale (NPR). These polar regions with temperatures close to T_B, are very dynamic (ergodic state), while upon further cooling their dynamics gradually decrease and at low temperature T_f become frozen (nonergodic state) in a similar kind like dipole glasses. The very important feature of relaxor is that, the nonergodic state can be irreversibly transformed into ferroelectric state by applying external electric field. This is important characteristic of relaxor which distinguished them from dipole glasses [30]. The effect of condensation of static polar nanoregions (PNR) from dynamic polarization at high temperature was investigated and explained by PDF analysis in Pb(Mg, Ta)O3 [31-34]. The locally off-centered Pb ions in the low temperature cubic phase, in comparison to non-displaced ions within the average crystallographic structure, explained the formation of static PNR which produce the relaxation behaviour.

Bismuth based perovskites were also extensively studied as they possess the same lone pair of electrons on the $6s^2$ subshell (Figure 1.5). This mechanism of ferroelectricity was used in materials investigated in this thesis: $Bi_2Mn_{4/3}Ni_{2/3}O_6$ [35], $BiTi_{3/8}Fe_{2/8}Mg_{3/8}O_3$ [36] and $BiFe_{0.6}Mn_{0.4}O_3$ or one of the most highly studied Bi-based perovskites $BiFeO_3$ [20, 37]. $BiFeO_3$ adopts a rhombohedrally distorted structure in the polar space group *R*3*c*, giving rise to the well-characterized properties of ferroelectricity (T_C = 1103 K) and antiferromagnetism (with a Neel temperature T_N = 643 K) with spiral modulated spin structure (SMSS) [38-41]. The ferroelectric state is realized by a large displacement of the Bi ions along $\langle 111 \rangle_p$ crystallographic direction with respect to the Fe octahedras (Figure 1.5). The tolerance factor of $BiFeO_3$ is far below unity (t=0.88), and requires buckling of oxygen octahedra to fit into the small unit cell [20]. The linear magneoelectric effect is observed in $BiFeO_3$ where both large increase of polarization and weak ferromagnetism exist when magnetic field is applied [42]. Due to both electric and magnetic order, $BiFeO_3$ belong to multiferroic materials which has wide range of applications in information storage, sensors, actuators and spinotronic devices.

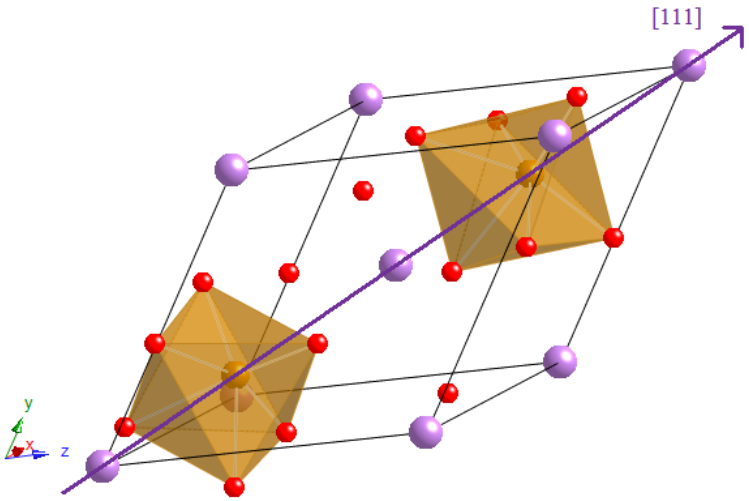

Figure 1.5. *$BiFeO_3$ in rhombohedral R3c structure showing displacements of Bi^{3+} cations along $\langle 111 \rangle_p$ crystallographic direction .*

Most Bi-based perovskites require high pressure (HP) synthesis due to the difficulty of accommodating the small Bi^{3+} cation on the 12 coordinate A site [43-46] *e.g.* $BiMnO_3$ and Bi_2MnNiO_6 which has multiple B site cations, ordered in a rock salt configuration. The latter compound is ferroelectric (T_C = 485 K) and ferromagnetic (T_C = 140 K) due to ferromagnetic coupling between partially filled Ni^{2+} ($t_{2g}^6 e_g^2$) and empty Mn^{4+} (t_{2g}^3) e_g orbitals [47, 48]. It is thus of interest to expand the number of materials with Bi^{3+} on the perovskite A site which are accessible under ambient pressure synthesis conditions. This can be achieved by increasing the number of cations on the B site, like in the case of $BiTi_{3/8}Fe_{2/8}Mg_{3/8}O_3$ [8, 36] or $Bi_2Mn_{4/3}Ni_{2/3}O_6$ [7, 35], the subjects of local structure study in this thesis. The $BiTi_{3/8}Fe_{2/8}Mg_{3/8}O_3$ is ferroelectric material with *R3c* phase and major polar displacement of Bi cations along $\langle 111 \rangle_p$ crystallographic direction (chapter 3), while $Bi_2Mn_{4/3}Ni_{2/3}O_6$ is antiferroelectric with incommensurate structure (chapter 4). There are also few more perovskites characterized by superstructure, which are obtained by chemical substitution in Bi-based perovskites. The solid solution synthesis of (1-x)BiFeO3-$LaFeO_3$ demonstrate ferroelectric *R3c* phase only within region x=0-0.1, while incommensurate modulated phase is formed within x=0.19-0.3. This is an effect of coupling of antipolar displacement of Bi cations with tilting distortions of B site cations octahedra [49]. Incommensurate structure is also formed in

$Bi_{2/3}Sr_{1/3}MnO_3$ where superstructure is based on orthorhombic Imma $\sqrt{2}a_p \times 2a_p \times \sqrt{2}a_p$ subcell, and demonstrates double Mn stripes due to coexistence modulated displacive ordering of O atoms and charge-orbital ordering of Mn^{3+}/Mn^{4+} cations [50]. Thus, in addition to Bi-based perovskites, which possess ferroelectric properties like $BiFeO_3$ or $BiTi_{3/8}Fe_{2/8}Mg_{3/8}O_3$, there are also several Bi-based perovskites synthesized at ambient pressure which adopt incommensurate structure in a similar way to the subject of this study $BiFe_{0.6}Mn_{0.4}O_3$.

1.2.2 Magnetic ordering

Magnetic behavior is not a main focus in this thesis, although due to the presence of magnetic Bragg peaks in the diffraction pattern of $BiFe_{0.6}Mn_{0.4}O_3$ (chapter 5), the introduction about magnetic ordering will be given. Magnetic effects [51, 52] as a results of unpaired spins of electrons creating magnetic dipole moments by coupling spins and orbital angular momentum. There is an analogy between the behavior of creating magnetic and electric dipole moments. Ferromagnets like ferroelectrics have spontaneous magnetization even in the absence of applied field. In the ferromagnets, electrons tend to line up in the same direction and as a consequence the net magnetic moment is obtained (Figure 1.6a). On the other hand, if unpaired electrons have a random orientation, then are called paramagnetics (Figure 1.6b). If the antiparallel ordering of spins of neighbouring atoms occurs, the material is known as antiferromagnetic with overall magnetic moment reduced to zero (Figure 1.6c). Furthermore, ferrimagnetic materials have antiparallel spins like antiferromagnetic materials but some dipole moments are larger than others and in that case material has a net overall magnetic moment (Figure 1.6d).

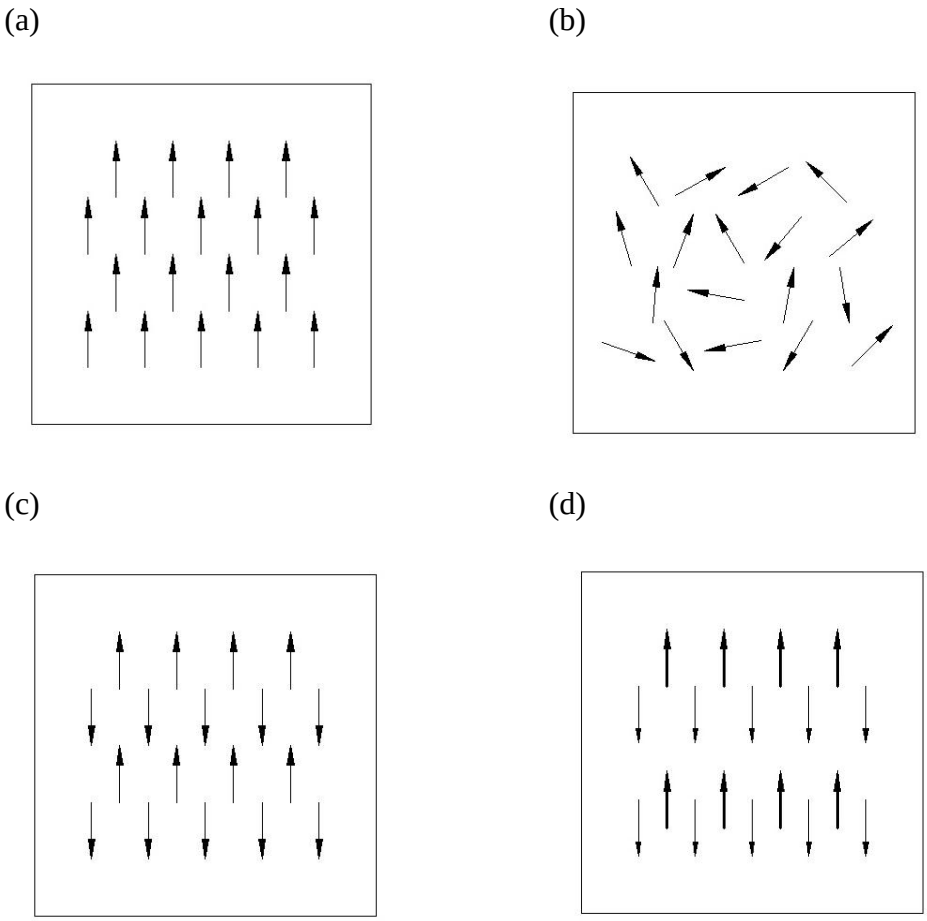

Figure 1.6. *Magnetic dipoles ordering in (a) ferromagnetic; (b) paramagnetic; (c) antiferromagnetic and (d) ferrimagnetic materials.*

There are a few types of driving forces like direct, indirect and superexchange [52], which cause parallel or antiparallel spins alignment. Direct exchange operates between moments, which are close enough to have sufficient overlap of neighbouring atom orbitals. This is a strong but short-range coupling giving rise to antiparallel alignment when the interatomic distance is small, as a consequence of Pauli's exclusion (Figure 1.7). When the distance is bigger, then electron-electron repulsion is minimized and produces positive exchange with parallel alignment. Another driving force is indirect exchange, which works between moments on longer distances than direct exchange. This exchange take place usually in metals where a magnetic ion induces a spin polarization in the conduction electrons in its neighborhood. Magnetic ferromagnetic or antiferromagnetic coupling depends on the separation between a pair of ions.

(a) (b)

Figure 1.7. *Direct exchange with (a) antiparallel spins which allows hopping electrons to the neighbouring site; (b) parallel spin does not allow hopping due to the Pauli principle [53] .*

Superexchange proposed first by Kramers [54] and Anderson [55], and later developed by Kanamori [47] and Goodenough [48] is the most important type of exchange as describing the interaction between moments on ions, coupled over a relatively long distance through a non-magnetic material. This long-range magnetic coupling occurs between the metal cations separated by anions e.g. oxygen, where hopping between d orbitals of transition metal cations occur via intermediate p orbital of oxygen ligand (Figure 1.8). The superexchange is antiferromagnetic when interaction occur between two magnetic ions with half occupied d orbitals and an intermediate non-magnetic anion p orbital, while interaction between metal occupied and unoccupied d orbitals and anion occupied p orbital, gives rise to parallel alignment of electrons and ferromagnetism (e.g. ferromagnetic coupling between partially filled Ni^{2+} ($t_{2g}^{6}e_{g}^{2}$) and empty Mn^{4+} (t_{2g}^{3}) e_g orbitals.).

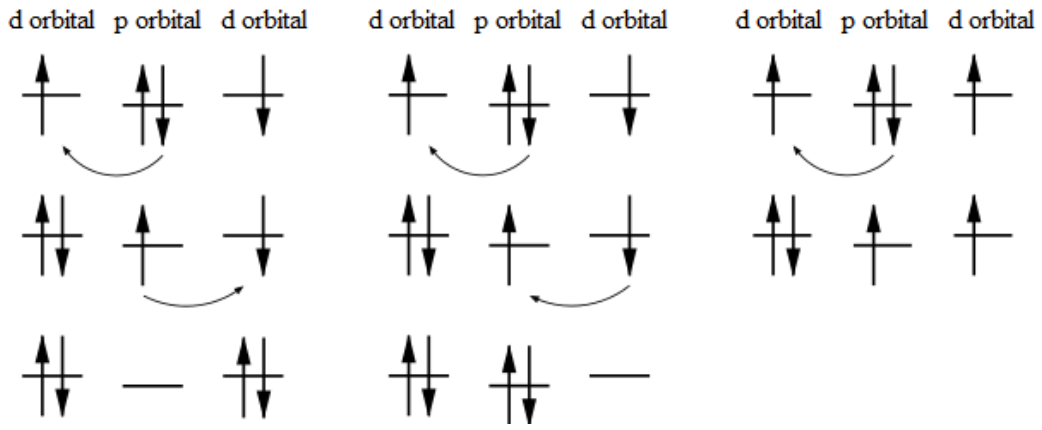

Figure 1.8. *Schematic representation of superexchange interaction occur between two transition metal d orbitals and oxygen p orbital; If spins on the d orbitals are antiparallel (left and centre) then two ways of hopping is allowed, in contrast to parallel spins where only one way of hopping is allowed (right) [53].*

Magnetic structures are described by Eigenfunctions of the magnetic Hamiltonian where the propagation vector ***k*** describes the relation between spins of atoms in unit cells [56, 57]:

$$m_i = \sum_k \sum_v \psi_{ik}^v \exp(-2\pi i \boldsymbol{kT}) \qquad \text{Equation 1.3}$$

where:

m_i – magnetic moment of atom *i*

ψ_i^v – basis function of atom *i* labeled with index *v*.

T – lattice vector in real space.

k – the propagation vector describe the magnetic order of atoms and is defined with respect to nuclear unit cell.

As the propagation vector ***k*** is described in reciprocal space, so the module of this vector is inversely proportional to the size of magnetic and nuclear unit cell as well. When magnetic and nuclear cells are equal and spins align parallel in all directions then a material is ferromagnetic and the propagation of the magnetic vector *k* will be described by values 0, 0, 0 (Figure 1.9a). On the other hand, if antiferromagnetic materials have spins antiparallel along *a* directions, then it

results with magnetic structure of twice size along this direction and vector *k*=1/2,0,0 (Figure 1.9b).

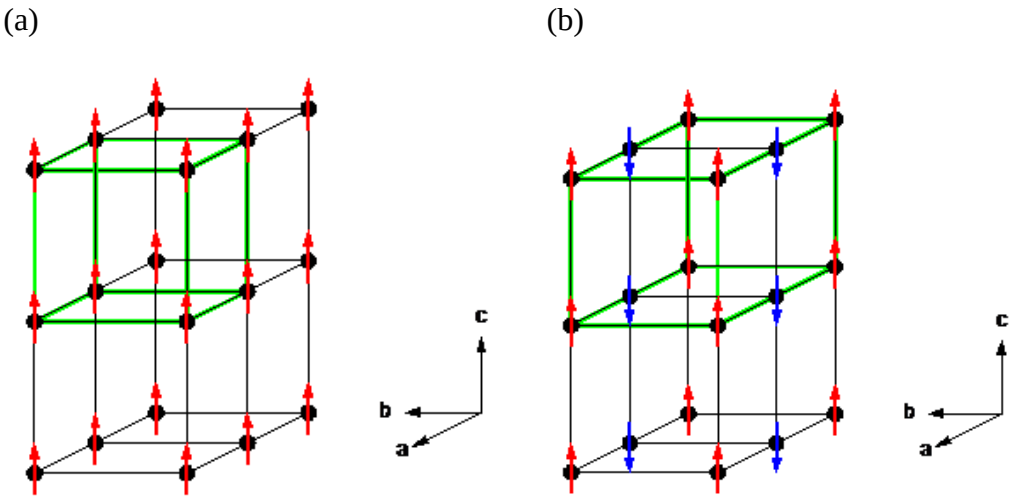

Figure 1.9. *Schematic representation of different propagation of magnetic vector* ***k****: (a) (0, 0, 0) and (b) (1/2, 0, 0). (Fundamental cell is denoted in black, while magnetic cell with magnetic atoms and electron spins up (red) and down (blue) is coloured in green.*

1.3. References

1. Proffen, T., Kim, H., *Advances in total scattering analysis.* Journal of Materials Chemistry, 2009. **19**(29): p. 5078-5088.
2. McGreevy, R.L., *RMC - Progress, problems and prospects.* Nuclear Instruments & Methods in Physics Research Section a-Accelerators Spectrometers Detectors and Associated Equipment, 1995. **354**(1): p. 1-16.
3. McGreevy, R.L., *Reverse Monte Carlo modelling.* Journal of Physics-Condensed Matter, 2001. **13**(46): p. R877-R913.
4. Norberg, S.T., Hull, S., Mathieu, R., Eriksson, S. G., *Local structural properties of* $0.5BiMnO_3$-$0.5ATiO_3$ *(A = Ba or Sr).* Chemical Communications, 2010. **46**(9): p. 1455-1457.
5. Jeong, I., Park, D. J., Kim, C. Y., Kim, S. H., Moon, B. K., Kim, W., Ahn, C. W., *Neutron total scattering studies on A-site disorder in lead-free*

ferroelectric $Bi_{0.5}(Na_{(1-x)}K_{(x)})_{0.5}TiO_3$. Zeitschrift Fur Kristallographie, 2011. **226**(2): p. 150-154.

6. Keeble, S. D., Barney, E.R., Keen, D. A., Tucker, M. G., Kreisel, J., Thomas, P. A., *Bifurcated Polarization Rotation in Bismuth-Based Piezoelectrics.* Advanced Functional Materials, 2012. **23**(2): p. 185-190.
7. Szczecinski, R. J., Chong, S. Y., Chater, P. A., Hughes, H., Tucker, M. G., Claridge, J. B., Rosseinsky, M. J., *Local crystal structure of antiferroelectric $Bi_2Mn_{4/3}Ni_{2/3}O_6$ in commensurate and incommensurate phases described by Pair Distribution Function (PDF) and Reverse Monte Carlo (RMC) modeling.* Chemistry of Materials (in progress), 2013.
8. Chong, S.Y., Szczecinski, R. J., Bridges, C. A., Tucker, M. G., Claridge, J. B., Rosseinsky, M. J., *Local Structure of a Pure Bi A Site Polar Perovskite Revealed by Pair Distribution Function Analysis and Reverse Monte Carlo Modeling: Correlated Off-Axis Displacements in a Rhombohedral Material.* Journal of the American Chemical Society, 2012. **134**(13): p. 5836-5849.
9. Cowley, R.A., *Lattice dynamics + phase transition of Strontium Titanate.* Physical Review a-General Physics, 1964. **134**(4A): p. A981-&.
10. Goldschmidt, V.M., *"Geochemische Verteilungsgesetze der Elemente. VII: Die Gesetze der Krystallochemie".*
    Shrifter utgitt av det Norske Videnskaps Akademi i Oslo, Shrifter Norskevidenskop-Akad. I. . Matem.-Naturvid. Klasse, 1926. **2**: p. 5-116.
11. Bhalla, A.S., Guo, R.Y., and Roy, R., *The perovskite structure - a review of its role in ceramic science and technology.* Materials Research Innovations, 2000. **4**(1): p. 3-26.
12. Rodel, J., Jo, W., Seifert, K. T. P., Anton, E. M., Granzow, T., Damjanovic, D., *Perspective on the development of lead-free piezoceramics.* Journal of the American Ceramic Society, 2009. **92**(6): p. 1153-1177.
13. Pockels, F., Abh. Gott, 1894. **39**(1).
14. Busch, G. and P. Scherrer, Naturwissenschaften, 1935. **23**: p. 737.
15. Slater, J.C., J. Chem. Phys., 1941. **9**: p. 16.

16. Von Hippel, A., Breckenridge, R. G., Chesley, F. G., Tisza, L., Ind. Eng. Chem. Res. , 1946. **38**: p. 1097.
17. Jaffe, H., *Piezoelectric ceramics.* Journal of the American Ceramic Society, 1958. **41**(11): p. 494-498.
18. Haertling, G.H., *Ferroelectric ceramics: History and technology.* Journal of the American Ceramic Society, 1999. **82**(4): p. 797-818.
19. Dove, M.T., *Structure and Dynamics: An atomic view of materials.* 2010: Oxford University Press.
20. Catalan, G. and J.F. Scott, *Physics and applications of Bismuth Ferrite.* Advanced Materials, 2009. **21**(24): p. 2463-2485.
21. Arlt, G., D. Hennings, and G. Dewith, *Dielectric properties of fine grained Barium Titanate ceramics.* Journal of Applied Physics, 1985. **58**(4): p. 1619-1625.
22. Guo, R., Cross, L. E., Park, S. E., Noheda, B., Cox, D. E., Shirane, G., *Origin of the high piezoelectric response in* $PbZr_{1-x}Ti_xO3$. Physical review letters, 2000. **84**(23): p. 5423-5426.
23. Noheda, B., Gonzalo, J. A., Cross, L. E., Guo, R., Park, S. E., Cox, D. E., Shirane, G., *Tetragonal to monoclinic phase transition in a ferroelectric perovskite: The structure of* $PbZr_{0.52}Ti_{0.48}O_3$. Physical Review B, 2000. **61**(13): p. 8687-8695.
24. Bonneau, P., Garnier, P., Calvarin, G., Husson, E., Gavarri, J. R., Hewat, A. W., Morell, A., *X-ray and neutron diffraction studies of the diffuse phase transistion in* $PbMg_{1/3}Nb_{2/3}O_3$ *ceramics.* Journal of Solid State Chemistry, 1991. **91**(2): p. 350-361.
25. Malibert, C., Dkhil, B., Kiat, J. M., Durand, D., Berar, J. F., SpasojevicdeBire, A., *Order and disorder in the relaxor ferroelectric perovskite* $PbSc_{1/2}Nb_{1/2}O_3$ *(PSN): comparison with simple perovskites* $BaTiO_3$ *and* $PbTiO_3$. Journal of Physics-Condensed Matter, 1997. **9**(35): p. 7485-7500.
26. Akbas, M.A. and Davies, P.K.., *Domain growth in Pb(Mg1/3Ta2/3)O-3 perovskite relaxor ferroelectric oxides.* Journal of the American Ceramic Society, 1997. **80**(11): p. 2933-2936.

27. Cross, L.E., *Relaxor ferroelectrics.* Ferroelectrics, 1987. **76**(3-4): p. 241-267.

28. Samara, G.A., *The relaxational properties of compositionally disordered ABO_3 perovskites.* Journal of Physics-Condensed Matter, 2003. **15**(9): p. R367-R411.

29. Ye, Z.G., *Relaxor ferroelectric complex perovskites: Structure, properties and phase transitions.* Oxides, 1998. **155-1**: p. 81-122.

30. Bokov, A.A. and Ye, Z.G., *Recent progress in relaxor ferroelectrics with perovskite structure.* Journal of Materials Science, 2006. **41**(1): p. 31-52.

31. Egami, T., Dmowski, W., Akbas, M., Davies, P. K., *Local structure and polarization in Pb containing ferroelectric oxides*, in *First-Principles Calculations for Ferroelectrics*, R.E. Cohen, Editor 1998, Amer Inst Physics: Melville. p. 1-10.

32. Egami, T., *Local structure of ferroelectric materials*, in *Annual Review of Materials Research*2007, Annual Reviews: Palo Alto. p. 297-315.

33. Teslic, S., Egami, T., and Viehland, D., *Local atomic structure of PZT and PLZT studied by pulsed neutron scattering.* Journal of Physics and Chemistry of Solids, 1996. **57**(10): p. 1537-1543.

34. Jeong, I.K. and Lee, J.K., *Local structure and medium-range ordering in relaxor ferroelectric Pb(Zn1/3Nb2/3)O-3 studied using neutron pair distribution function analysis.* Applied Physics Letters, 2006. **88**(26).

35. Claridge, J.B., Hughes, H., Bridges, C. A., Allix, M., Suchomel, M. R., Niu, H., Kuang, X., Rosseinsky, M. J., Bellido, N., Grebille, D., Perez, O., Simon, C., Pelloquin, D., Blundell, S. J., Lancaster, T., Baker, P. J., Pratt, F. L., Halasyamani, P. S., *Frustration of Magnetic and Ferroelectric Long-Range Order in $Bi_2Mn_{4/3}Ni_{2/3}O_6$.* Journal of the American Chemical Society, 2009. **131**(39): p. 14000-14017.

36. Bridges, C.A., Allix, M., Suchomel, M. R., Kuang, X. J., Sterianou, I., Sinclair, D. C., Rosseinsky, M. J., *A pure bismuth a site polar perovskite synthesized at ambient pressure.* Angewandte Chemie-International Edition, 2007. **46**(46): p. 8785-8789.

37. Lebeugle, D., Colson, D., Forget, A., Viret, M., Bataille, A. M., Gukasov, A., *Electric-field-induced spin flop in $BiFeO_3$ single crystals at room temperature*. Physical review letters, 2008. **100**(22): p. 227602.

38. Fischer, P., Polomska, M., Sosnowska, I., Szymanski, M., *Temperature dependence of the crystal and magnetic structures of $BiFeO_3$.* Journal of Physics C-Solid State Physics, 1980. **13**(10): p. 1931-1940.

39. Sosnowska, I., Loewenhaupt, M., David, W. I. F., Ibberson, R. M., *Investigation of the unusual magnetic spiral arrangement in $BiFeO_3$.* Physica B-Condensed Matter, 1992. **180**: p. 117-118.

40. Sosnowska, I. and A.K. Zvezdin, *Origin of the long-period magnetic ordering in $BiFeO_3$.* Journal of Magnetism and Magnetic Materials, 1995. **140**: p. 167-168.

41. Sosnowska, I.M., *Neutron scattering studies of $BiFeO_3$ multiferroics: a review for microscopists.* Journal of Microscopy, 2009. **236**(2): p. 109-114.

42. Popov, Y.F., Zvezdin, A. K., Vorobev, G. P., Kadomtseva, A. M., Murashev, V. A., Rakov, D. N., *Linear magnetoelectric effect and phase-transitions in Bismuth Ferrite, $BiFeO_3$.* Jetp Letters, 1993. **57**(1): p. 69-73.

43. Ishiwata, S., Azuma, M., Takano, M., Nishibori, E., Takata, M., Sakata, M., Kato, K., *High pressure synthesis, crystal structure and physical properties of a new Ni(II) perovskite $BiNiO_3$.* Journal of Materials Chemistry, 2002. **12**(12): p. 3733-3737.

44. Kimura, T., Kawamoto, S., Yamada, I., Azuma, M., Takano, M., Tokura, Y., *Magnetocapacitance effect in multiferroic $BiMnO_3$.* Physical Review B, 2003. **67**(18).

45. Azuma, M., Takata, K., Saito, T., Ishiwata, S., Shimakawa, Y., Takano, M., *Designed ferromagnetic, ferroelectric Bi_2NiMnO_6.* Journal of the American Chemical Society, 2005. **127**(24): p. 8889-8892.

46. Suchomel, M.R., Thomas, C. I., Allix, M., Rosseinsky, M. J., Fogg, A. M., Thomas, M. F., *High pressure bulk synthesis and characterization of the predicted multiferroic $Bi(Fe_{1/2}Cr_{1/2})O_3$ (vol 90, art no 112909, 2007).* Applied Physics Letters, 2007. **90**(20).

47. Kanamori, J., *Superexchange interaction and symmetry properties of electron orbitals.* Journal of Physics and Chemistry of Solids, 1959. **10**(2-3): p. 87-98.
48. Goodenough, J.B., *Theory of the role of covalence in the perovskite-type manganites La,M(II)MnO_3.* Physical Review, 1955. **100**(2): p. 564-573.
49. Rusakov, D.A., Abakumov, A. M., Yamaura, K., Belik, A. A., Van Tendeloo, G., Takayama-Muromachi, E., *Structural Evolution of the BiFeO3-LaFeO3 System.* Chemistry of Materials, 2011. **23**(2): p. 285-292.
50. Hervieu, M., Malo, S., Perez, O., Beran, P., Martin, C., Baldinozzi, G., Raveau, B., *New type of charge/orbital ordering above room temperature in the perovskite Bi2/3Sr1/3MnO3.* Chemistry of Materials, 2003. **15**(2): p. 523-527.
51. Blundell, S.J., *Magnetism in condensed matter*. 2001, Oxford: Oxford University Press.
52. West, A.R., *Solid State Chemistry and its Applications.* 1984: John Wiley & Sons.
53. Pavarini, E., Koch, E., Anders, F., Jarell, M., *Correlated electrons: From models to materials.* 2012: Forschungszentrum Jülich GmbH, Institute for Advanced Simulation.
54. Kramers, H.A., *The interaction between the magnetogenic atoms in a paramagnetic crystal.* Physica, 1934. **1**: p. 182-192.
55. Anderson, P.W., *New approach to the theory of superexchange interactions.* Physical Review, 1959. **115**(1): p. 2-13.
56. Wills, A.S., *Validation of magnetic structures.* Zeitschrift Fur Kristallographie, 2007: p. 53-58.
57. Wills, A.S., *Indexing magnetic structures and crystallographic distortions from powder diffraction: Brillouin zone indexing.* Zeitschrift Fur Kristallographie, 2009: p. 39-44.

Chapter 2. Methods

2.1 Principles of Diffraction

2.1.1 Bragg's Law

The structural characterization of materials has an important role in understanding the observed physical properties. The crystal structure of a material can be deduced via a diffraction experiment, when beams of radiation are scattered by atoms within a material according to the Bragg's Law (Figure 2.1). To obey the Bragg equation (Equation 2.1) reflected and transmitted photons scattered by the atomic planes must be in phase. The simplest representation of this process is described by two beams of radiation 1 and 2. The second beam 2 must travel an extra distance (FG+GH) in comparison to reflected radiation 1 at point O, and differ in path length by an integer number of wavelength to completely constructive interference. These coherent superposition of the waves, produce reflections at different angles to form a diffraction pattern.

$$\text{Path difference (FG + GH)} = 2d_{hkl}\, sin(\theta) = n\lambda \qquad \text{Equation 2.1}$$

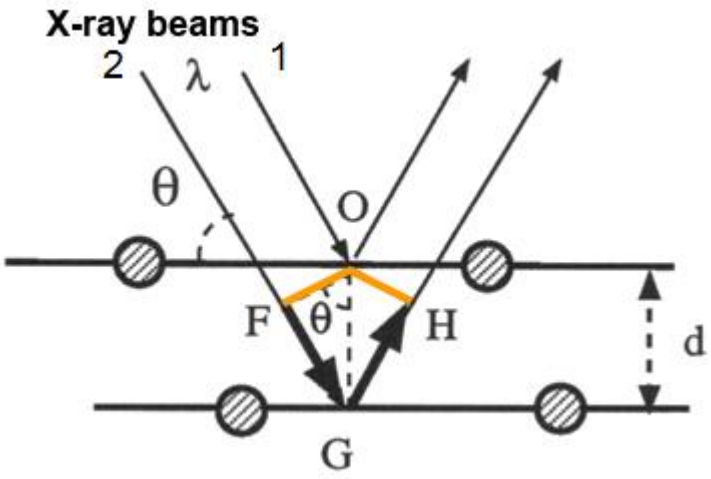

Figure 2.1. *Geometric construction of a Bragg reflection* [1].

2.1.2 Powder diffraction

Powder diffraction used is the more common technique for the structural characterization of solid oxides, in comparison to single crystal diffraction, which have not been used in this thesis. In diffraction from a single crystal we observe reflections from each lattice plane as a point on a reciprocal lattice. However, powder samples contain huge number of crystallites adopting randomly a broad range of possible orientations and produce cones of diffraction for each lattice spacing in the crystal. Every diffraction cone is made up by the large number of crystallites in the sample giving rise to diffracted dots, which overlap forming one continuous cone pattern at each angle (Figure 2.2).

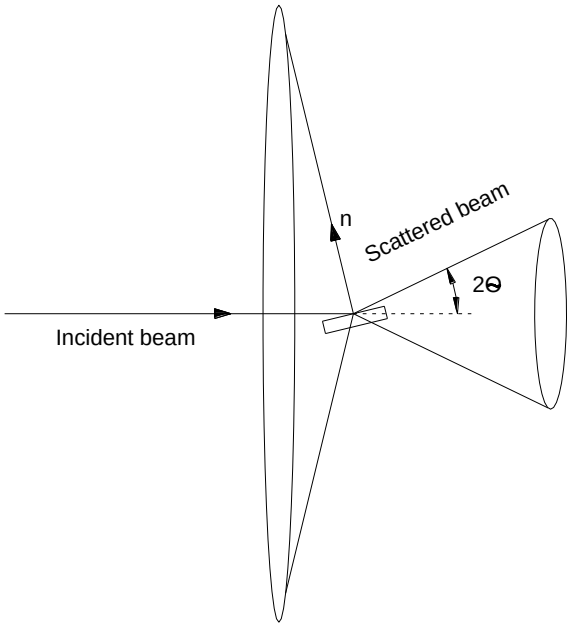

Figure 2.2. *Continuous diffraction cone obtained by scattering of powder crystalline sample* [2].

To determine the structure of materials and their average atomic positions, the unit cell must be defined. The unit cell is the smallest repeating unit with a periodic arrangement of atoms in the structure and it can adopt different sizes, represented by crystal systems. There are seven different crystal systems, where unit cell is defined using three edge lengths *a*, *b* and *c* called lattice parameters, and three internal angles between these edges α, β and γ. These values are

different for every crystal system (Equation 2.2), and thus, every crystal system possesses different interplanar spacings *d*, which are based on the Miller indices *hkl* (Table 2.1).

Table 2.1. *Interplanar spacings for all crystal systems* [3].

Crystal systems	Constraints	$\frac{1}{d_{hkl}^2} =$
Cubic	$a = b = c;$ $\alpha = \beta = \gamma = 90°$	$\frac{h^2 + k^2 + l^2}{a^2}$
Tetragonal	$a = b;$ $\alpha = \beta = \gamma = 90°$	$\frac{h^2 + k^2}{a^2} + \frac{l^2}{c^2}$
Orthorhombic	$\alpha = \beta = \gamma = 90°$	$\frac{h^2}{a^2} + \frac{k^2}{b^2} + \frac{l^2}{c^2}$
Hexagonal	$a = b;$ $\alpha = \beta = 90°,$ $\gamma = 120°$	$\frac{4}{3}\frac{h^2 + hk^2 + k^2}{a^2} + \frac{l^2}{c^2}$
Trigonal/ Rhombohedral	$a = b = c;$ $\alpha = \beta = \gamma = 90°$	$\frac{(h^2 + k^2 + l^2)sin^2\alpha + 2(hk + hl + kl)(cos^2\alpha - cos\alpha\alpha)}{a^2(1 - 3cos^2\alpha + 2cos^3\alpha)}$
Monoclinic	$\alpha = \gamma = 90°$	$\frac{h^2}{a^2 sin^2\beta} + \frac{k^2}{b^2} + \frac{l^2}{c^2 sin^2\beta} - \frac{2hl\, cos\beta}{ac\, sin^2\beta}$

$$\frac{1}{d_{hkl}^2} = \frac{h^2}{a^2} + \frac{k^2}{b^2} + \frac{l^2}{c^2} \qquad \text{Equation 2.2}$$

By rearranging interplanar spacing d_{hkl} and Bragg equation for the orthorhombic system, each Bragg reflection can be assigned to Miller indices and powder diffraction pattern with the unit cell information.

$$sin^2\theta = \frac{\lambda}{4}\left(\frac{h^2}{a^2} + \frac{k^2}{b^2} + \frac{l^2}{c^2}\right) \qquad \text{Equation 2.3}$$

2.1.3 Diffraction intensity

The diffraction pattern is produced by interaction between waves and matter and depends on many factors like distribution of atoms in the unit cell. If the

amplitude of the wave scattered by a material is expressed in terms of fractional coordinates *x*, *y* and *z* in the equation:

$$Ae^{i\phi} = fe^{2\pi i(hx+ky+lz)} \qquad \text{Equation 2.4}$$

Then, the total charge distribution of atoms in the unit cell described by structure factor F_{hkl} is denoted by:

$$F_{hkl} = \sum_i f_i N_i (e^{2\pi i(hx+ky+lz)}) e^{(-M_i)} \qquad \text{Equation 2.5}$$

where:

f_i – atomic scattering factor

N_i – occupancy factor of the atom

x_i, y_i, z_i – fractional coordinates of the i^{th} atom in the unit cell

$$M_i = 8\pi^2 \overline{U_{iso}^2} sin^2 \frac{v}{\lambda^2}$$

U_{iso}- mean thermal parameter

Thus, the structure factor depends on the Miller indices of the reflection under consideration, the positions of the atoms in the unit cell and the atomic scattering factor. The modulus square of structure factor $|F_{hkl}|^2$ is directly proportional to the intensity of diffraction I_{hkl}, so by knowing the structure factors, the unique powder diffraction pattern is obtained in terms of the positions and intensities of the observed reflection.

2.1.4 Symmetry operations and the crystal systems

The symmetry operations describing unchanged positions of all atoms in the unit cell are expressed by the space group. The list of possible symmetry operations is introduced here:

Identity **(1) -** operation where fractional coordinates (x, y, z) are transformed to itself (x, y, z).

Inversion **($\bar{1}$) -** operation where fractional coordinates (x, y, z) are translated to (−x, −y, −z). Inversion operation contains centrosymmetric space groups.

Reflections **(m) -** operation where atoms are reflected through a mirror plane.

Proper Rotations also called rotoreflections **(n) -** describe rotations of the objects (atoms) about a point by angle 2π/n, where n describe order of rotation e.g. for n=2; 360/2=180° and thus we receive two-fold rotation.

Improper Rotation **($\frac{n}{m}$; $\bar{n}$)** – are rotations followed by reflections or rotations called rotoreflections and rotoinversions respectively.

Screw Axis **(N_n) -** helical movement operation, where axis has simultaneously proper rotation of a point by 360°/N and translation vector of order n, where n is natural number $1 \leq n \leq N$. The degree of translation presented as a subscript shows how far objects (atoms) are translated along the axis, as a portion of the parallel lattice vector.

Glide Plane **(a, b, c, n, d)** – operation where mirror reflection is combined with translation by usually ½ parallel to the plane. The notations **a, b** or **c** mean that glide are translated by **a**/2 , **b**/2 and **c**/2 respectively. If the gliding translation happens along diagonal directions with vector 1/2 then is denoted by n and gliding translations can be (**b**+**c**)/2, (**a**+**c**)/2 or (**a**+**b**)/2. The gliding vector can also be equal to 1/4 of diagonal translation which is called diamond plane as it occurs in the crystals of diamond and is denoted by **d**. The following are different **d** planes with translations: (**b**±**c**)/4, (**a**±**c**)/4 or (**a**±**b**)/4. The translations are not arbitrary like in the case of screw axis, therefore operations move objects (atoms) to equivalent original position but in the neighbouring unit cell.

The presence of symmetry operators like screw axes or glide planes cause also occurrence of systematic absences in a diffraction pattern, because of destructive interference between diffracted waves. The cancelled intensities of diffracted waves produce the structure factor of a Bragg reflection equal to zero for some classes of reflections, as they are absent in a systematic way. For the primitive cubic lattice we always observe all reflections as there are atoms only at the

corners of the unit cell. However if we consider a body-centered lattice (I), where the same atoms occupying corners are also in the centre of the unit cell, then the sum of Miller indices must be even to observe reflections:

$$h+k+l = 2n \qquad \text{Equation 2.6}$$

On the other hand, to see reflections in a face-centered cubic lattice (F) where atoms occupy corners and the center of the six sides, the different conditions are preferred where *h*, *k*, *l* must be all odd or all even:

$$h, k, l = 2n$$

$$or \qquad \text{Equation 2.7}$$

$$h, k, l = 2n+1$$

Different symmetry operations can be combined like in the example of screw axis and glide planes. When we consider all combinations of operations in 3 dimensions excluding only translations, we receive 32 possible point groups where symmetry elements are going through one unchanged point (Table 2.2). The crystal systems have different point groups which are denoted by one of the symbols.

The point groups are able to fully describe all the atoms within the unit cell in 3 dimensions. They are contained in the symmetry groups called space group, which divides unit cell into discrete repeatable domains. The International Tables of Crystallography contains all basic 230 space groups starting from the lowest symmetry triclinic *P*1 and finishing with the high symmetry cubic space group e.g. $Pm\bar{3}m$.

Table 2.2. *List of the 32 point groups* [3].

Crystal systems	Points groups		Laue classes	Lattice points groups
	Non-centrosymmetric	Centrosymmetric		
Triclinic	1	$\bar{1}$	$\bar{1}$	$\bar{1}$
Monoclinic	2 *m*	2/*m*	2/*m*	2/*m*
Orthorhombic	222 *mm*2	*mmm*	*mmm*	*mmm*
Tetragonal	4 $\bar{4}$ 422 4*mm*, 4$\bar{2}m$	4/*m* 4/*mmm*	4/*m* 4/*mmm*	4/*mmm*
Trigonal	3 32 3*m*	$\bar{3}$ $\bar{3}m$	$\bar{3}$ $\bar{3}m$	$\bar{3}m$
Hexagonal	6 $\bar{6}$ 622 6*mm*, $\bar{6}$2*m*	6/*m* 6/*mmm*	6/*m* 6/*mmm*	6/*mmm*
Cubic	23 432 $\bar{4}$3*m*	*m* $\bar{3}$ *m* $\bar{3}$ *m*	*m* $\bar{3}$ *m* $\bar{3}$ *m*	*m*$\bar{3}$ *m*

2.1.5 Commensurate and incommensurate structures

The diffraction pattern of a regular crystal is made up of Bragg peaks, where their positions correspond to the separation distances of lattice planes in the unit cell, and their intensities are determined by the atomic positions and thermal vibrations within the unit cell. However, in aperiodic crystals where atomic structure has long-range order but no translation symmetry, the structure description requires a more complex explanation. The symmetry of periodic crystals are described by space groups which are based on 3 dimensional symmetry operations whereas the symmetry of aperiodic crystal, due to lack of translation symmetry, must include additional higher dimensional space (d=1,2,3), which are represented by superspace (3+d)D [4].

The periodically distorted atomic positions within modulated structure result in additional Bragg peaks called satellite reflections, usually surrounding the main reflections. To describe the fundamental structure the smallest possible unit cell

is used, whereas the complete modulated structure contains a number of these fundamental unit cells, depending on the periodicity of modulations.

These additional periodicities describing atomic positions, occupancies or displacement parameters are called atomic modulation functions (AMF) [5]. Depending on the shape of this function, the AMF can be continuous and each parameter of the modulated structure, as $Bi_2Mn_{4/3}Ni_{2/3}O_6$ (described in chapter 4), where two modulation wave vector exist, can be expressed by Fourier series of sine/cosine terms [6]:

$$u_i^{\mu}(\bar{x}_4, \bar{x}_5) = \sum_{n_1=1}^{\infty}\sum_{n_2=1}^{\infty} A_i^{n_1,n_2}(\mu)\sin[2\pi(n_1\bar{x}_4 + n_2\bar{x}_5)] + B_i^{n_1,n_2}(\mu)\cos[2\pi(n_1\bar{x}_4 + n_2\bar{x}_5)]$$

Equation 2.8

where:

u – modulated function of atom μ is a vector function with component $(u_1^{\mu},\ u_2^{\mu}, u_3^{\mu})$ along three basis vectors $\{\boldsymbol{a}_1,\ \boldsymbol{a}_2, \boldsymbol{a}_3\}$.

$$A_i^{n_1,n_2}(\mu) = [A_1^n(\mu), A_2^n(\mu), A_3^n(\mu)] \text{ and } B_i^{n_1,n_2}(\mu) = [B_1^n(\mu), B_2^n(\mu), B_3^n(\mu)]$$

Equation 2.9

are Fourier amplitudes, which define the modulation functions of atom μ, while lower index *i* show number of modulation vectors.

The arguments of wave functions $u_i^{\mu}(\bar{x}_4, \bar{x}_5)$ are described by:

$$\bar{x}_4(\mu) = t + \boldsymbol{q_1}\overline{\boldsymbol{x}} \text{ and } \bar{x}_5(\mu) = u + \boldsymbol{q_2}\overline{\boldsymbol{x}}$$

Equation 2.10

t and *u*- real numbers describing the initial phase of the waves

$\boldsymbol{q_1}\overline{\boldsymbol{x}}$ is the scalar product of vectors $\boldsymbol{q}_{1,}\boldsymbol{q}_2$ **and** $\overline{\boldsymbol{x}}$

$\overline{\boldsymbol{x}}$ – the position of atom μ with respect to the origin of the unit cell

$$\boldsymbol{q_1}, \boldsymbol{q_2} = \sigma_1\boldsymbol{a}_1^* + \sigma_2\boldsymbol{a}_2^* + \sigma_3\boldsymbol{a}_3^*$$

Equation 2.11

are wave vectors define the direction of the wave and its wavelength with respect to reciprocal lattice vectors of basic structure $\{\boldsymbol{a}_1^*,\ \boldsymbol{a}_2^*, \boldsymbol{a}_3^*\}$. The three components $\sigma_1, \sigma_2, \sigma_3$ are irrational numbers in an incommensurate structure, as periodicity is not equal to an integral number of lattice translations of the basic cell.

Thus, when the incommensurate case occurs, the modulation functions are no described by a simple fraction of the fundamental unit cell (Figure 2.3a). On the other hand, when periodicity is equal to the integral number of lattice translations of the basic cell then the structure is called commensurate (Figure 2.3b). The modulation vectors q (Equation 2.11) both in the commensurate and incommensurate structures define substructure of the reciprocal lattice with respect to the basic structure. To restore periodicity additional Miller indices are needed to index both Bragg and satellite reflections e.g. *hklmn* in a case of two satellite reflections m≠0 and n≠0 of order $|m|$ and $|n|$ respectively.

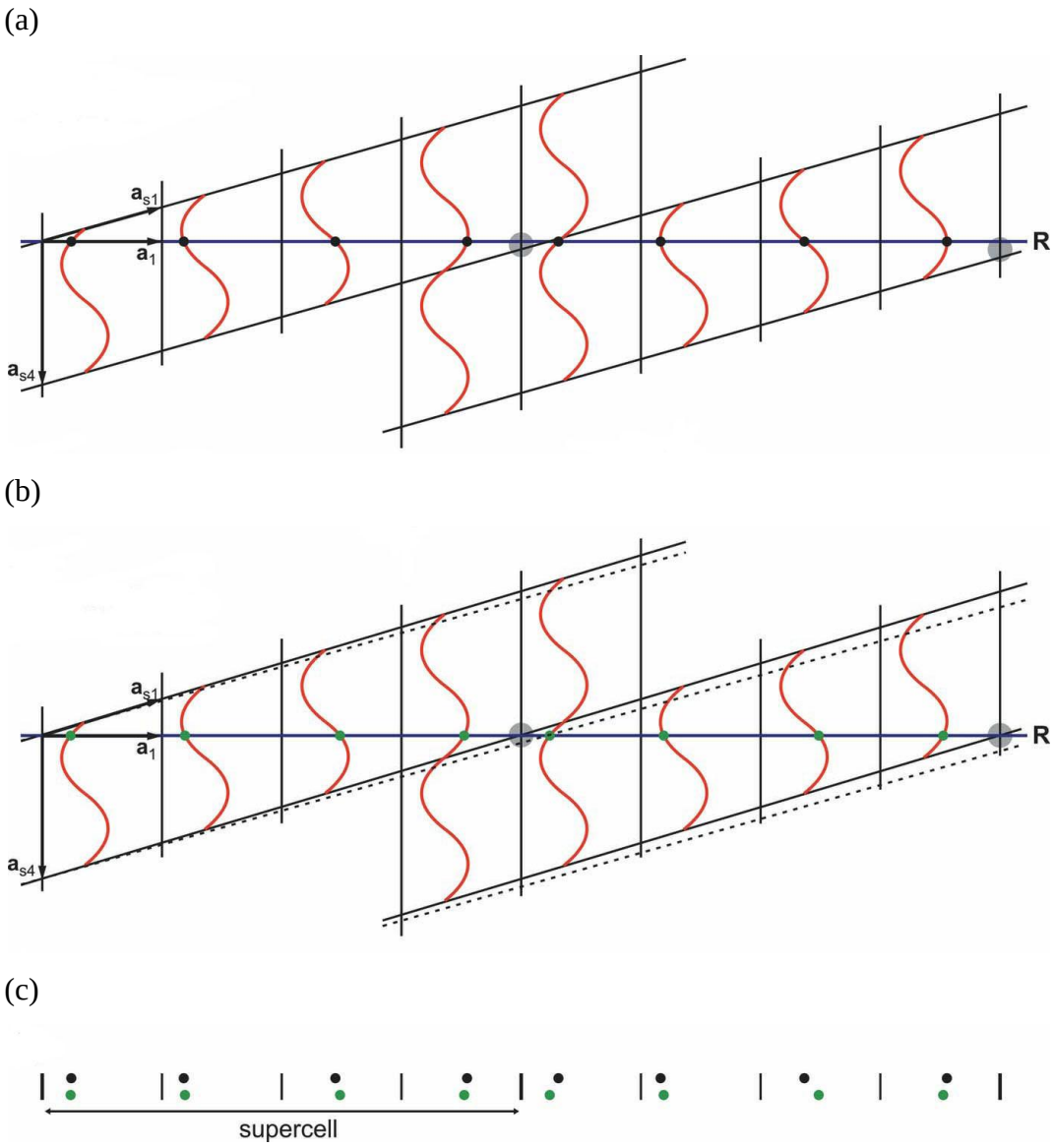

Figure 2.3. *(a) Incommensurate case with non integral* ***q*** *modulation vector 0.238 (b)* ***q*** *modulation vector equal 0.25 represent fourfold superstructure (c) The black and green circles demonstrate different atomic positions for incommensurate and commensurate structures respectively as an effect different modulation functions [5].*

There is requirement in the equation 2.8, to apply the infinite number of parameters to define the shapes of modulation function, although only a finite number of them can be determined in practice. The application of finite number of parameters however, does permit comparing them with possible commensurate non-modulated approach

On the other hand when the AMF is discontinuous, then modulations can be described as block wave for occupational modulation structures [7]. The discontinuous functions are using for strong occupational modulation waves, where average occupational probabilities of atom μ are defined with two values 0 and 1[6]:

$$\sum_{\mu=1}^{N} P^0(\mu) = 1 \text{ and } P^0 \geq 0 \qquad \text{Equation 2.12}$$

Thus, the discontinuous function like block wave is applied in cases when the complete order is achieved and value 1 is obtained, while in a case of two chemical types on the site, the occupational probability always will be larger than 0 and smaller than 1. There also others discontinuous like, crenel or sawtooth functions used to describe the modulated atomic positions (Figure 2.4) [5]. In contrast to continuous modulated function, where molecule is shifted along *c* direction (red function in Figure 2.4a), the second Figure 2.4b demonstrate rotated molecule around an axis parallel to *a* and is described by the sawtooth function (blue) with discontinuity between molecules 1 and 8. The other type of discontinuous modulation is crenel function (Figure 2.4c), where steps of this function (green) was used to describe two different orientations of molecule.

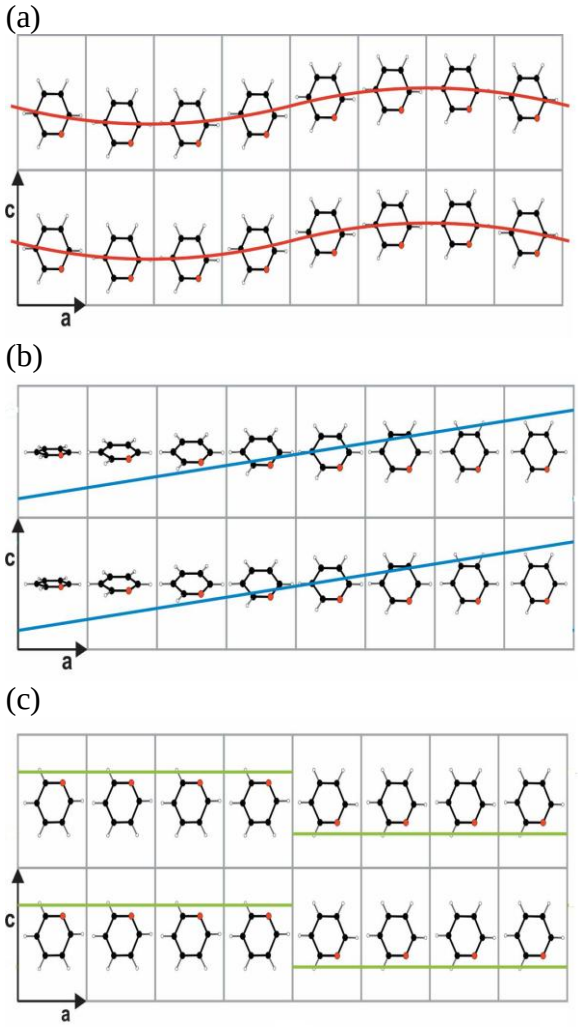

Figure 2.4. *Schematic representation of different modulation functions: (a) continous harmonic; (b) discontinuous sawtooth and (c) discontinuous crenel [5].*

The example of incommensurate structure is Bi-based perovskite $Bi_2Mn_{4/3}Ni_{2/3}O_6$ which was the object of this study [8]. The structure was described in the 5 dimensional *Ibmm(α00,0β0)ss.gm* superspace group, where first three dimensions describe the basic orthorhombic centrosymmetric structure *Ibmm*. The additional two modulation vectors *(α00,0β0)* along the *x* and *y* directions with values 0.491132 and −0.501449 mean that the complete full structure is approximately twice the size the fundamental basic structure along these directions.

2.1.6 X-ray Diffraction

Traditional crystallography is based on the Bragg scattering where atomic positions are averaged over all the unit cells in the sample and over the time. It is usually implemented to analyze the structure of materials by using X-ray and neutron radiation. X-rays are electromagnetic waves with wavelengths range 0.1-100 Å and interact with electrons in the matter. To generate X-rays, a beam of electrons strike a metal target to eject core electrons from atoms of the metal target. This creates vacancies and electrons from higher shells drop down into empty shell, losing energy and emitting X-rays with energies corresponding to the difference between the atomic shells.

$$\Delta E = hv \qquad \text{Equation 2.13}$$

The laboratory sources are usually X-ray vacuum tubes where by heating a tungsten filament, created electrons are accelerated by a high voltage towards a metal target. When the electrons hit the target (e.g. copper or cobalt are the most common in crystallography) X-rays are created by two different atomic processes. The first process generates background radiation called Bremstrahlung or white with continuous spectrum. The electrons scattered by the strong electric field are decelerated as they enter the metal, and lose energy to produce broad distribution of X-rays with minimum wavelength related to energy of incident electrons.

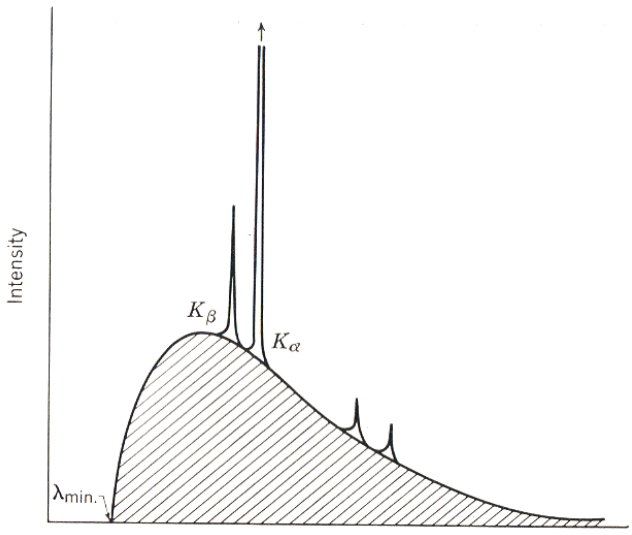

Figure 2.5. *Schematic plot of characteristic X-ray spectrum [9].*

When electrons accelerated towards the metal system have enough energy, then core electrons are knocked out of the metal target and the X-ray photons are emitted producing emission spectrum at several certain frequencies (Figure 2.5). The transitions where electrons falling from the upper L to the lower shell K (e.g. $2 \rightarrow 1$) are called K_{α}. On the other hand, when the two orbitals are not adjacent and are separated by another shell (e.g. $3 \rightarrow 1$), then the spectral line is called K_{β}. The splitting of the energy within each shell causes observation of two transitions close to each other $K_{\alpha 1}$ and $K_{\alpha 2}$ with similar energies. To select single wavelength $K_{\alpha 1}$ which has the greatest intensity a single crystal monochromator is used and the final single wavelength can be used to an X-ray diffraction experiment.

In the powder diffraction technique used in this thesis, we obtain a diffraction cone for each lattice spacing, as described in 2.1.2 section. To analyze the material, the positions of diffracted cones have to be measured by the detector. The modern way to measure it is to use an electronic detector which gives intensity directly and more accurately than photographic film used in the past. In a powder diffractometer with Bragg-Brentano geometry (Figure 2.6), the detector is scanning the sample around semicircle and is able to cut through the diffraction cones at various diffraction maxima. This technique and the applied geometry produce powder X-ray diffraction pattern with intensity as a function of detector angle 2θ.

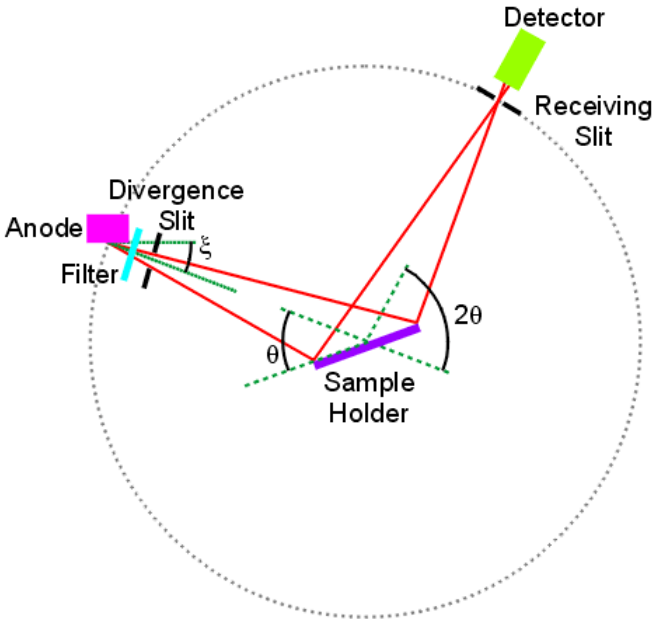

Figure 2.6. *Schematic diagram of the X-ray optics with Bragg-Brentano geometry [10].*

2.1.7 Neutron diffraction

Neutron diffraction is a technique similar to X-ray diffraction, but due to their different scattering properties, neutrons and X-rays give complementary information. Neutrons are usually produced by one of two different mechanisms.

2.1.7.1 Reactor Source

Beams of neutrons are created by nuclear fission reactions in a reactor from fissile materials like uranium. This radioactive decay process, where the nucleus of an atom splits into lighter nuclei, produces high-energy neutrons with variable wavelength. Nuclear reactors also contain lighter elements than uranium like water or graphite in moderator. The role of the moderator is to slow down high-energy neutrons by inelastic collisions with atoms, resulting in the loss of kinetic energy. The ideal energy of neutrons is close to room temperature for most applications, and is achieved by controlling the temperature of the moderator. Beams of neutrons have a broad range of wavelengths but as in X-ray diffraction, the single wavelength must be selected. This is usually achieved by applying a single crystal monochromator, where the single crystal transmits a single

wavelength and the beam leaving the monochromator can be used for diffraction. The wavelength of neutron λ with energy E is obtained by finding relation between equations of momentum $\boldsymbol{p}$ and energy E [11]

$$\boldsymbol{p} = \hbar\boldsymbol{k}; \quad |\boldsymbol{p}| = mv = \frac{h}{\lambda}; \quad k = |\boldsymbol{k}| = \frac{2\pi}{\lambda} \qquad \text{Equation 2.14}$$

$$E^2 = \frac{\boldsymbol{p}^2}{2m} \qquad \text{Equation 2.15}$$

Thus,

$$\lambda = \frac{(2\pi\hbar)^2}{\sqrt{2mE}} \qquad \text{Equation 2.16}$$

2.1.7.2 Spallation Source

The second types of neutron sources are spallation sources, where high-energy intense protons in a synchrotron are focused onto a metal target which is usually made from uranium, mercury or tantalum. The protons strike the nuclei and kick off neutrons, which have very high energies and cannot be used for any applications at an initial stage. To enable these high-energy neutrons to take part in diffraction, they are moderated in a medium like liquid hydrogen or methane to slow down the neutrons by reducing their kinetic energy. A pulsed incident proton source gives rise to a pulsed neutron beam. The pulsed beam of neutrons containing spectrum of wavelengths is usually generated from pulsed beam of protons and depends on the type of moderator being applied. Pulsed neutron sources containing a spectrum of wavelengths are normally utilised in a time-of-flight neutron diffraction experiment.

If we apply the de Broglie equation, then the relationship of distance D and time t, to the wavelength of the neutron beams λ is expressed by:

$$\lambda = \frac{h}{mv} = \frac{ht}{mD} \qquad \text{Equation 2.17}$$

D – total distance of neutrons between the moderator and the sample and between the sample and the detector.

2.1.8 The difference between X-rays and neutrons

The primary difference between X-rays and neutron is their scattering mechanisms. X-rays interact with electron clouds of the scattering material using electrostatic forces over a distance of 10^{-10} m. Thus, the scattering amplitude of X-rays increases with the atomic number of the atoms in a sample, and as a result X-rays are dominated by heavier elements with bigger number of electrons, than lighter elements e.g. oxygen. As the scattering angle is increased, X-ray scattering intensity gradually diminishes and produces tail-off of intensity, as they are scattered at different location within unit cell and produce phase differences. On the other hand, neutrons interact with nucleus by nuclear forces over much shorter distance (10^{-13} m) than electrons, and due to the small size of nucleus, do not show angular dependence of form factor and have comparable intensity among whole range of scattering angles (Figure 2.7).

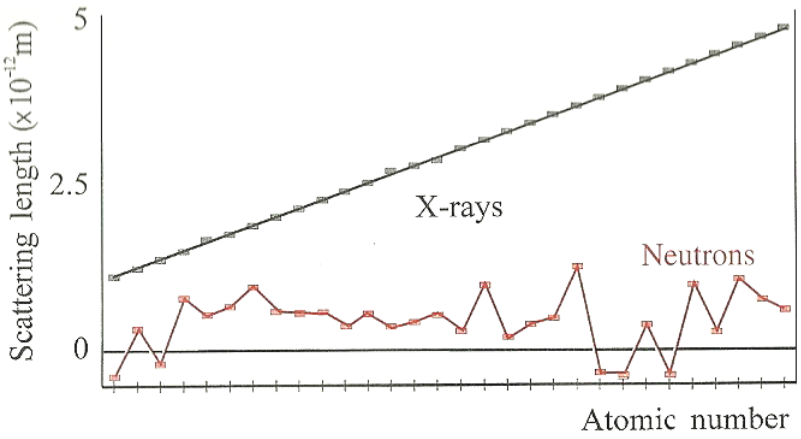

Figure 2.7. *Variation of scattering length for X-rays and neutrons with atomic number [12].*

Due to this feature, elements which possess similar number of electrons may be better identified by neutrons, as the neutron scattering is not dominated by electrons. On the other hand, if atoms possess similar neutron scattering length and different atomic number then the X-rays will be more helpful in identifying the atoms.

2.1.9 X-ray and neutron diffractometers

2.1.9.1 Laboratory X-ray diffractometer - Panalytical X'PERT PRO

Panalytical X'PERT PRO is a high-quality X-ray diffractometer used mostly for polycrystalline materials. The X-ray diffractometer has a cobalt source fitting with a Ge monochromater, supplying $K_{\alpha 1}$ radiation at a wavelength of λ=1.789Å. The Bragg-Brentano geometry described in previous section 2.1.6 is applied here, as the diffractometer operates in reflection geometry. In a Bragg-Brentano geometry, the X-ray source and the detector are always situated on the same circle, which improve the resolution by optimizing the focusing of the source to the sample and to the detector. To minimize effect of preferred orientation on the diffraction pattern, the sample on the holder is rotated perpendicular to the incident radiation.

The X-rays used during the diffraction experiment can generate fluorescence for certain elements. This unwanted phenomenon occurs when incident X-rays radiation knock electrons entirely out of the atom within material and leave an ionized atom with missing electron. Due to an unoccupied electron energy level within this atom, other electrons with a higher energy to fill the vacancy will drop down to this lower energy level, emitting in the same time an X-ray. The emission of fluorescent photons are called secondary radiation as it is much weaker than the primary beam, but has influence on the quality of diffraction pattern. The fluorescence mostly increase the background in the diffraction pattern, whereas absorption cause reduction in intensity. They are emitted by all atoms but its amount depends on the elements in the sample which create characteristic transitions within the electron orbitals of source material like cobalt, in the case of Panalytical X'PERT PRO. In this thesis the effect of both fluorescence and absorption was minimize by using diffractometer with Co source (fluorescence of Mn) which decrease signal-to-noise ratio less than diffractometer with Cu source (Mn and Fe fluorescence) in the $BiFe_{0.6}Mn_{0.4}O_3$.

2.1.9.2 Neutron Powder Diffraction Experiments

Two types of neutron diffractometers were used in this thesis. Both, POLARIS and GEM diffractometers are at the ISIS neutron spallaton source, Rutherford Appleton Laboratories and produce time of flight diffraction data.

2.1.9.2.1 POLARIS Diffractometer at ISIS, Oxford, UK

The Polaris instrument at the ISIS spallation neutron source is a high intensity, medium resolution powder diffractometer. The high counting rate and intense incident neutron flux provide collection of data sets from small amount of materials in short time, helping in a rapid characterization of structures. The materials can be studied under non-ambient conditions, where the whole range of time-of-flight powder diffraction pattern is collected at a single, fixed scattering angle [13].

POLARIS diffractometer has four banks A, B, E and C which contains 434 scintillator detectors of ^{3}He gas and ZnS. These detectors arranged in the 4 banks are presented in detail in table 1.3, covering a full range of interplanar d-spacings for the resulting diffraction pattern and providing a medium resolution (max. $\Delta d/d$ $\sim 7x10^{-3}$) diffraction pattern.

Experiments of $BiFe_{0.6}Mn_{0.4}O_3$ sample were carried out inside a vanadium can and collected at room temperature.

Table 2.3. *Details of the detector banks on the POLARIS.*

	Low Angle (A)	Low Angle (B)	backscattering (C)	90 degrees (E)
Detector type	^{3}He	ZnS	^{3}He	ZnS
No. of detector elements/modules	80/2	80/4	80/2	216/6
2θ range (˚)	28 - 42	13 - 15	130 -160	83 - 97
Δd/d	~1x10^{-2}	~3x10^{-2}	~5x10^{-3}	~7x10^{-3}
d-range (Å)	0.5 - 8.3	0.5 - 21.6	0.2 - 3.2	0.2 – 4.0
Q-range (Å^{-1})	0.75 – 12.6	0.3 – 12.6	2.0 – 31.4	1.5 – 31.4

2.1.9.2.2 GEM Diffractometer at ISIS, Oxford, UK

GEM (GEneral Materials) [14] is a more advanced materials neutron diffractometer than Polaris. The high count rate and very stable detectors covering very wide range of scattering angle from 1.2˚ to 171.4˚ leads to very wide range in scattering vector, ***Q***:

$$\boldsymbol{Q} = 4\pi sin\frac{\theta}{\lambda} \qquad \text{Equation 2.18}$$

The high real-space resolution of GEM is caused by high maximum momentum transfer of scattering vector ***Q*** of approximately 55Å^{-1}.

$$\Delta r \approx \frac{2\pi}{Q_{max}}; \text{so for } Q_{max} = 55\text{Å}^{-1}\ \Delta r \approx 0.13\text{Å} \qquad \text{Equation 2.19}$$

The detectors are arranged in seven banks with details given in table 1.4. They are all ZnS/^{6}Li scintilator detectors, organized in arrays with very large area of 7.270 m^2 and are extremely stable with 0.1% variation over 24 hours period.

Table 2.4. *Parameters of GEM detectors.*

Detector Bank	2θ range	No. of detector elements/modules	Resolution ΔQ/Q (%)	Min. accessible momentum transfer Q_{min} ($Å^{-1}$)
0	1.21 – 3.18	80/4	5 - 10	0.04
1	5.32 – 12.67	330/6	4.7	0.17
2	13.44 – 21.59	320/4	2.4	0.43
3	24.67 – 45.61	900/10	1.7	0.79
4	50.07 – 74.71	1400/14	0.79	1.56
5	79.07 – 106.6	2160/18	0.51	2.35
5X	106.02 – 114.72	720/18	0.5	2.95
6	142.5 – 149.72	560/14	0.34	3.5
7	149.98 – 171.4	800/10	0.35	3.57

Due to the high count rate (obtained by the large number of detectors covering a high proportion of the diffraction cone) and high real-space resolution, GEM has found applications in structural studies of disordered materials. In this thesis the total neutron scattering data obtained from GEM was analyzed by investigating the local structure of perovskites $Bi_2Mn_{4/3}Ni_{2/3}O_6$ [15] and $BiTi_{3/8}Fe_{2/8}Mg_{3/8}O_3$ [16]. The samples were measured inside the vanadium cans and data was collected at various temperatures using a cryostat and a furnace at low and high temperatures, respectively.

2.1.10 Transmission Electron Microscopy (TEM)

Electron microscopy is another method to characterize the structure of materials, which requires very small amounts of sample. Electrons, due to their short wavelength when they are accelerated upon application of high voltage, provide better resolution in contrast to optical microscopes. The beam of electrons passes through the sample are being scattered by atoms to form a diffraction pattern. As the electron wavelength is orders of magnitude smaller than the interplanar spacing in most crystals, the diffraction angles are reduced in comparison to X-ray diffraction and therefore diffraction cones are centered around the electron beam.

The smaller angle between incident and scattered electron radiation form diffraction spots in the reciprocal space which are focused by lenses onto a CCD to generate an image. The reciprocal space defines the direction and distance of the diffracted beam as it is inversely proportional to the size and shape of the unit cell. Thus, obtained diffraction pattern of spots in TEM, can help to identify unit cell parameters by measuring distances between the diffracted spots. Moreover, analysis of the systematic absences of spots in the pattern helps to determine the space group. To establish correct unit cell parameters and finally the space group, at least several diffraction patterns must be studied at different planes.

Furthermore, the chemical analysis can been done in a TEM microscope by X-rays energy dispersive spectrometry (EDS). It helps to establish presence of the correct ratio of elements in the material and identify impurity the phases by studying every crystallite.

Electron microscopy, thanks to the scattering cross section of electrons being 10^3 to 10^4 times larger than X-rays and neutrons, allows studying much smaller objects. Being able to detect small deviations from the average structure, TEM possess great sensitivity to analyze small structure features. Thus, the crystal defects in the form dislocations, stacking faults or phase boundaries can be seen directly by TEM imaging.

Another advantage of the strong scattering of electrons is the ability to detect modulations of the average structure, which result in the form of weak superstructure spots. Electron microscopy work in this thesis, was carried out for the incommensurate structure of perovskite $BiFe_{0.6}Mn_{0.4}O_3$.

2.1.10.1 TEM experiments

A transmission electron microscope JOEL-200FX equipped with EDAX analyzer for energy dispersive spectroscopy (EDS) analysis was used to examine the sample of $BiFe_{0.6}Mn_{0.4}O_3$ at an accelerating voltage of 120 kV. The TEM experiments with EDS analysis were carried out by Dr. Z. Xu.

2.1.11 Structural analysis

The crystallographic average structure describes the unique arrangement of atoms or molecules in a crystalline material where atomic positions repeat periodically infinitely within unit cells in three dimensions. This approximation which characterize majority of crystalline materials is established based on the Rietveld refinement.

The Rietveld refinements in this thesis were carried out first for perovskites $Bi_2Mn_{4/3}Ni_{2/3}O_6$ and $BiTi_{3/8}Fe_{2/8}Mg_{3/8}O_3$ to obtain an average crystallographic structure and then compare to a local structure. The same technique was also applied for $BiFe_{0.6}Mn_{0.4}O_3$ to derive the incommensurate crystallographic structure.

2.1.11.1 Profile matching

The structural analysis usually starts with profile matching which provides information about unit cell parameters, peak shapes and background function, without knowing the structural model. Profile matching is usually done by Le Bail or Pawley fit. In this thesis the Le Bail method [17] was applied for fitting background coefficients, peak shapes and lattice parameters of unit cell of collected diffraction patterns. The program used to Le Bail fit of 3 dimensional non modulated structure was GSAS (General Structure Analysis System) [18], while Jana 2006 [19] was applied to determine profile of incommensurate structure $BiFe_{0.6}Mn_{0.4}O_3$.

2.1.11.2 Rietveld refinement

When a profile matching is determined (Le Bail or Pawley fit), a starting crystallographic model is needed to start a structural Rietveld refinement. The Rietveld refinement uses a least squares minimization approach, where the starting model is refined until the theoretical pattern becomes a good match to the measured profile of the experimental diffraction pattern. The calculated pattern providing crystallographic structure of atoms within unit cell, is based on the simultaneous refinement of atomic and thermal positions, lattice parameters and profile parameters of the experimental diffraction pattern. This minimization

technique must be carried out carefully, by checking the atomic positions or thermal parameters of atoms, to keep a model physically sensible.

The diffraction pattern is a function represented by intensity in terms of scattering angle (*2θ*), energy parameter (*time of flight)* or *wavelength*, depending on which diffractometer is applied (e.g. X-ray or neutron). In every case, the Rietveld technique utilizes the same principle where minimization technique of least-squares refinement is expressed by:

$$LS = \sum_i w_i (I_i^{obs} - I_i^{calc})^2 \qquad \text{Equation 2.20}$$

where:

w_i - statistical weight

$$w_i = \frac{1}{I_i^{obs}} \qquad \text{Equation 2.21}$$

I_i^{obs} – observed, experimental intensity of the i^{th} step

I_i^{calc} - calculated intensity of the i^{th} step

The diffraction pattern is represented by Bragg intensity where each individual intensity corresponds to the reflection from a specific plane, described by Miller indices *hkl*. These Bragg intensities in their position, height and width for every scattered material is proportional to the structure factor as described earlier in the section 2.1.3. Thus, the calculated intensity of reflections is represented by the structure factor and the background:

$$I_i^{calc} = S_j \sum_{k=1}^{Npeaks} L_k |F_{k,j}|^2 \; S_j\left(2\theta_i - 2\theta_{k,j}\right) P_{k,j} A_j + bkg_i \qquad \text{Equation 2.22}$$

where:

S_j – phase scale factor is written as:

$$S_j = S_F \sum_{j=1}^{Nphases} \frac{f_j}{V_j^2} \qquad \text{Equation 2.23}$$

S_F – beam intensity

F_j – phase volume fraction

V_j – phase cell volume

L_k – Lorentz- Polarization factor, depending on the instrument geometry, e.g. for Bragg-Brentano

$$Lk = \frac{1+cos^2 2\theta}{sin^2 2\theta cos\theta} \qquad \text{Equation 2.24}$$

$F_{k,j}$ – the structure factor for k, j reflection

A_j – absorption factor defined as:

$$A_j = \frac{1}{2\mu} \qquad \text{Equation 2.25}$$

μ - linear absorption coefficient

$P_{k,j}$ – The texture (preferred orientation function)

$S_j\left(2\theta_i - 2\theta_{k,j}\right)$ – profile shape function, where different types are available:

G – Gaussian

V, PV – Voigt or Pseudo-Voigt

C – Cauchy

bkg_i – background intensity of the i^{th} step.

In a short simplification, the refined parameters in the calculated intensity pattern are divided into two groups: structural and profile parameters. The profile parameters are calculated during Le Bail profile match and include lattice parameters, peak shape and the background coefficients. The background is usually calculated by linear interpolation of previously selected points. It is often necessary in a case of complex background to increase the number of points in the diffraction pattern in order to improve the intensity of background.

On the other hand, the structural parameters which determine the intensity of reflections are calculated by the structure factor which include atomic positions, fractional occupancies and thermal parameters.

The quality of Rietveld refinement is usually represented by goodness of fit or several R- factors, depending if factors are weighted R_{wp} or not R_p [20, 21]. These functions define the agreement between calculated and observed diffraction pattern, and their updating with every cycle are very useful, to control refinement of crystallographic structure.

1. Profile R-factor

$$R_p = \frac{\sum_i |y_{i(obs)} - y_{i(calc)}|}{\sum_i y_{i(calc)}} \qquad \text{Equation 2.26}$$

2. Weighted profile R-factor

$$R_{wp} = \sqrt{\frac{\sum_i w_i |y_{i(obs)} - y_{i(calc)}|^2}{\sum_i w_i (y_{i(calc)})^2}} \qquad \text{Equation 2.27}$$

where:

w_i – statistical weight defined in equation 1.19

3. Goodness of fit

$$\chi^2 = \left(\frac{R_{wp}}{R_{exp}}\right)^2 \qquad \text{Equation 2.28}$$

where:

R_{exp}^2 - expected R-factor

$$R_{exp}^2 = \frac{N}{\sum_i w_i (y_{i(calc)})^2} \qquad \text{Equation 2.29}$$

The most trustworthy factor is the weighted profile R-factor where the square root of the minimized quantity is scaled by the statistical weight. Another meaningful factor is goodness of fit, which during least-squares refinement should approach to 1, which is the ideal situation when weighted R-factor is equal to the expected R-factor, while the value below 1 indicates over-fitting data.

2.2 Introduction to total scattering and Reverse Monte Carlo modeling

The general description of a crystallographic structure is described in the section 2.1, where a unit cell and its contents represent the long-range average atomic structure by translation in 3 dimensions to infinity. However, in many cases the crystallographic structure, determined by Bragg scattering, does not fully describe the structure. Real structures are frequently disordered and in most cases are more complex than implied by the averaged atomic positions and thermal parameters (represented by ellipsoidal isotropic or anisotropic displacement parameters) used in the unit cell description. As the materials sometimes owe their properties to defects or disorder within their structure, determination of true local atomic positions is essential to derive the complete structure and to understand the properties of materials.

Short-range structural information is contained in the diffraction pattern in the form of diffuse scattering; this manifests as broad oscillations which lie underneath the Bragg peaks. The combination of diffuse scattering information with Bragg scattering is called total scattering, and provides an excellent tool to

study of disordered materials as combines both short- and long-range structural information.

2.3 Total scattering and Reverse Monte Carlo modeling

2.3.1 Diffuse and total scattering – reciprocal space

The diffraction pattern of aperiodic crystals contain diffuse scattering [22], where intensity is much weaker than Bragg intensities by approximately 10^3-10^4 times, and as a consequence is difficult to detect. Due its weak intensity, diffuse scattering information is usually lost within the background of a diffraction pattern, and in traditional crystallography analysis is simply removed by fitting a polynomial to the observed background. Thus, the information contained within diffuse scattering is simply ignored from traditional diffraction analysis. However, owing the advanced high intensity pulsed neutron sources combined with diffractometers capable of measuring to high momentum transfer like GEM [14] at ISIS pulsed spallation neutron source, the measurement of diffuse scattering data is possible. To be able to determine the diffuse scattering component of a total scattering analysis, a procedure with several separate measurements must be applied, which is explained in a section 2.3.2.2.

In this thesis, the total scattering analysis is based on the measurement of the intensity of scattered neutrons. In contrast to X-rays, where the scattering power of an atom or ion is proportional to the number of electrons, the neutron scattering cross section varies randomly between heavy and light elements. For the materials studied in this thesis, neutrons are an ideal probe for both heavy Bi cations and light O anions in $Bi_2Mn_{4/3}Ni_{2/3}O_6$ or $BiTi_{3/8}Fe_{1/4}Mg_{3/8}O_3$ with approximately the same detectable efficiency. To derive the neutron scattering cross section, the incident flux of neutron beams should be defined first [23]:

$$\Psi = \frac{number\ \ of\ neutrons\ \ impinging\ \ on\ a\ surface\ \ per\ second}{surface\ \ area\ \ perpendicular\ \ \ to\ the\ neutron\ \ beam\ \ directio\ n} \qquad \text{Equation 2.30}$$

The neutrons interact within the sample, where they are scattered within the solid angle Ω, and are collected by a detector placed at some distance from the sample.

As the detector counts all scattered neutrons arriving within a solid angle $d\Omega$, the counting rate per solid angle and energy interval can be expressed by differential scattering cross section;

$$\frac{d\sigma}{d\Omega} = \frac{1}{\Psi}\frac{number\ \ of\ neutrons\ \ scattere\ d\ per\ \ second\ \ into\ \ solid\ \ angle\ \ d\Omega}{d\Omega} \qquad \text{Equation 2.31}$$

where the neutron scattering cross section, σ, is given by:

$$\sigma = \frac{1}{\Psi} number\ of\ neutrons\ scattered\ per\ second \qquad \text{Equation 2.32}$$

The simplest form of differential neutron cross section is represented by the sum of self, inelastic and distinct scattering:

$$\frac{d\sigma}{d\Omega} = \frac{d\sigma}{d\Omega_{self}} + \frac{d\sigma}{d\Omega_{inelastic}} + \frac{d\sigma}{d\Omega_{distinct}} \qquad \text{Equation 2.33}$$

The double differential neutron cross section per unit solid angle, Ω, for a multi-component system is expressed by Keen [24] as;

$$\frac{1}{N}\frac{d^2\sigma}{\mathrm{d}\Omega \mathrm{d}\omega} = \frac{\boldsymbol{k}'}{\boldsymbol{k}}\sum_{i=1}^{n}\overline{b_i^2}S_i^s(\boldsymbol{Q},\omega) + \frac{\boldsymbol{k}'}{\boldsymbol{k}}\sum_{i,j=1,i\neq j}^{n}\overline{b_i}\overline{b_j}S_{ij}^d\ (\boldsymbol{Q},\omega) \qquad \text{Equation 2.34}$$

where:

$\boldsymbol{k}$ and $\boldsymbol{k'}$ - the initial and final wave vectors of scattered neutrons,

$\boldsymbol{Q}$=k- k' is the scattering vector,

$$\boldsymbol{Q} = 4\pi sin\theta/\lambda \qquad \text{Equation 2.35}$$

$S_i^s(Q,\omega)$ - the self scattering part of the structure factor,

$S_{ij}^d(Q,\omega)$ - the distinct scattering part of the structure factor,

$\overline{b_i}$ - the coherent bound neutron scattering length of species i,

σ_i - the total scattering cross section.

If coherent and incoherent scattering can be separated, and equation 2.34 integrated, then the cross section in the static approximation (where scattering depends only on the magnitude **Q** wave vector) will be expressed;

$$\frac{1}{N}\frac{d\sigma}{d\Omega} = \sum_{i,j=1}^{n} c_i c_j\ \overline{b_i}\overline{b_j}\left[A_{ij}(\boldsymbol{Q}) - 1\right] + \sum_{i=1}^{n} c_i\overline{b_i^2} \qquad \text{Equation 2.36}$$

where;

$A_{ij}(Q)$ - the Faber-Ziman partial structure factor,

$4\pi\sum_i c_i\overline{b_i^2}$ - the total scattering cross section of the material.

The normalized total scattering structure factor is expressed then by:

$$S(Q) = \left(\sum_{i=1}^{n} c_i \bar{b}_i\right)^{-2} \sum_{i,j=1}^{n} c_i c_j \, \bar{b}_i \bar{b}_j A_{ij}(Q) \qquad \text{Equation 2.37}$$

with limiting values:

$$S(Q \to 0) = \frac{\sum_{i=1}^{n} c_i \bar{b}_i^{\,2}}{\left(\sum_{i=1}^{n} c_i \bar{b}_i\right)^2} \qquad \text{Equation 2.38}$$

$$S(Q \to \infty) = 1 \qquad \text{Equation 2.39}$$

The total scattering function in this thesis is usually expressed as reduced structure function *F(Q)*. As the scattering vector ***Q*** approaches infinity *F(Q)* approaches 0, instead of 1 for *S(Q)*.

$$F(Q) = Q[S(Q) - 1] \qquad \text{Equation 2.40}$$

2.3.2 Pair Distribution function – real space

The two total scattering functions *S(Q)* and *F(Q)* contain scattered intensity information in reciprocal space and provide indirect information about the positions of the atoms. The Fourier transformation of one of the total scattering structure function *S(Q)* and *F(Q)* yields to the Pair Distribution Function (PDF) in real space. The PDF gives the probability of finding two atoms of types *i* and *j*, lying within a spherical shell of radius *r* and weighted by scattering lengths. Thus, this function has significant physical importance as it provides average separation of pair of atoms separated by a distance *r*, and hence structural information as a function of length-scale. The total radial distribution function *G(r)* consists contributions from all atomic partial distribution functions $g_{ij}(r)$:

$$G(r) = \sum_{i,j} c_i c_j \, b_i b_j \left[g_{i,j}(r) - 1\right] \qquad \text{Equation 2.41}$$

where $g_{ij}(r)$ is defined as:

$$g_{ij}(r) = \frac{n_{ij}(r)}{4\pi r^2 dr \, \rho_j} \qquad \text{Equation 2.42}$$

The total radial distribution function *G(r)* in real space and total scattering structure function *F(Q)* in reciprocal space are related to each other by Fourier transformation:

$$G(r) = \frac{1}{(2\pi)^3 \rho_0} \int_0^\infty 4\pi Q^2 F(Q) \frac{sinQr}{Qr} dQ \qquad \text{Equation 2.43}$$

There are several PDF functions in the literature, for example differential correlation function *D(r)*, which is related to *G(r)* by:

$$D(r) = 4\pi\rho_0 G(r) \qquad \text{Equation 2.44}$$

The differential correlation function *D(r)* is negative at low *r* values below the shortest interatomic distance, thus it is more sensible to use the function *T(r)* called total correlation function, which has a value of 0 below the shortest interatomic distance.

$$T(r) = D(r) + T^0(r) \qquad \text{Equation 2.45}$$

where:

$$T^0(r) = 4\pi r \rho_0 \left(\sum_{i=1}^n c_i \bar{b}_i\right)^2 \qquad \text{Equation 2.46}$$

In this thesis both total radial distribution function *G(r)* and total correlation function *T(r)* were implemented, in order to investigate the local structure of Bi-based perovskites, whereas all atomic partial distribution functions $g_{ij}(r)$ were normalised during RMC refinement to make possible comparison between atomic pairs containing positive and negative scattering lengths.

2.3.2.1 Useful information from PDF

The PDF was described in the previous section 2.3.2 using the formulas of total radial distribution function *G(r)*, total correlation function *T(r)* and differential correlation function *D(r)*. All three functions represent the average separation of pairs of atoms, and thus from the peak positions we obtain direct information about distances between the atoms in the structure, while the shape, width and height provides the real atomic probability distribution (Figure 2.8).

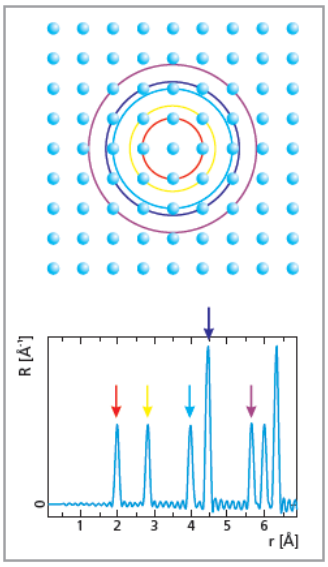

Figure 2.8. *Schematic diagram of structure and its corresponding Pair Distribution Function [25]. Coloured arrows in the PDF (below) correspond to the coloured shells of atoms around the central atom of a structure (above).*

The difference between the local structural information obtained from total scattering and crystallographic structure is that the peaks gradually become broader as a distance is increased in the case of local structure. On the other hand, when we look at the PDF calculated from the crystallographic atomic positions, this provide only sharp peaks as all neighbours are perfectly defined due to long-range order.

Such sharp peaks do not occur in the real materials, where the local structure contains disorder due to the effect of thermal motion of atoms or static displacements from the ideal average positions. This is reflected in the broadening of PDF peaks, where bond distances are usually derived by fitting single or multiple Gaussian functions depending on the PDF peaks' shape.

Another very important piece of information obtained from the PDF peaks is the coordination number. The coordination number of the central atom can be derived by integrating the intensity under the peak of partial pair distribution function. To establish the average number of atoms surrounding a central atom (e.g. B site cation ordering), the nearest neighbour calculations *n(r) [26]* are implemented.

$$n(r) = \int_{r_1}^{r_2} 4\pi r^2 c_j \rho_0 g_{ij}(r) dr \qquad \text{Equation 2.47}$$

where;

$$\rho_0 = \frac{N}{V} \qquad \text{Equation 2.48}$$

ρ_0 - the average density number of material,

g_{ij} - represents the partial distribution function between type of atoms *i* and *j*.

In this thesis, *n(r)* were directly calculated from partial pair distribution function $g_{B\text{-}B}(r)$, where the average numbers of neighbours for each pair of B site cations between distances r_1 and r_2 have been extracted. These average numbers of neighbours for every B site shell are derived from the plateaus observed in the *n(r)*. The presence of plateau is crucial when calculating B site ordering, as it provides the constant number of neighbours sorrounded the atom and ensure that atoms from outern shells are not involved in the calculations of nearest neighbours. An example from our study of the material $Bi_2Mn_{4/3}Ni_{2/3}O_6$ is shown in Figure 2.9 [15].

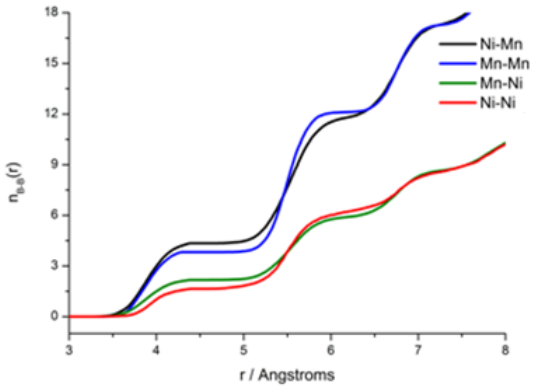

Figure 2.9. *Nearest neighbour functions $n_{B\text{-}B}(r)$ for $Bi_2Mn_{4/3}Ni_{2/3}O_6$.*

2.3.2.2 Data collection and analysis

Alongside the total scattering data from the sample of interest, the measured scattering data contains additional incoherent scattering and scattering from the sample holder. These components of scattering, which are irrelevant to the structure determination, must be removed from collected data in order to be able

to investigate the coherent scattering properly. Thus, to exclude the true background not coming from the sample, the scattering intensity must be measured without the sample in place to account for instrumental backgrounds. Several separated measurements must be carried out in order to obtain the total scattering contribution from the sample only:

- Sample data in a sample holder
- Empty sample holder (sample environment)
- Empty instrument, without the sample or sample holder at the sample position (instrument environment)
- Vanadium rod of equal volume to the sample holder. Vanadium is an almost complete incoherent scattering material, and is used to determine the source spectrum.

To obtain the differential cross scattering function and then reduced total scattering *F(Q)*, a computer program Gudrun for analysis of neutron diffraction data was implemented [27]. The total scattering of the time of flight TOF diffraction data collected on a diffractometer (e.g. GEM at the ISIS pulsed spallation neutron source) are extracted using Gudrun. The data files corresponding to the sample, empty sample holder, instrument environment and vanadium rod, allow subtract unwanted background. However to obtain a good differential cross section and total scattering, the scattering intensity must be normalized by taking into account sample absorption, multiple scattering or inelasticity corrections. These sample effects are calculated and included during data processing (Figure 2.10).

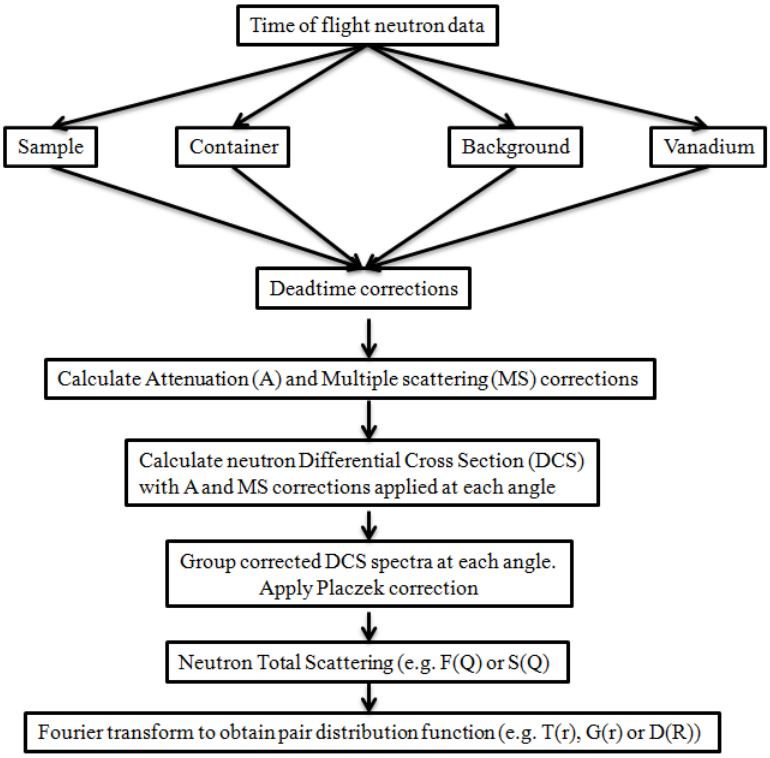

Figure 2.10. *Flowchart of data processing of neutron time of flight data in the program Gudrun [28].*

The first correction which should be taken into account before any normalization, is deadtime correction. Even highly efficient detectors are described as "dead" for short periods of time after every detection event while they are reset, and during this time the next neutron cannot be detected. To account for this inability to count every neutron entering the detector, deadtime corrections are applied in the Gudrun by including a deadtime constant file.

After deadtime correction, the spectrum source normalization is applied as there are some small variations in the beam intensity, caused by slight variations in proton beam steering which changes the energy dependence of the spectrum. The observed data is divided by the incident flux, which is measured by detector in the incident beam monitor; this means that the dependence on the incident spectrum is removed for each data collection, providing a consistent data collection which has a minimal contribution from the neutron source and the detectors.

Some neutrons during measurement are scattered twice or more, before they reach the detector, thus multiple scattering must be also included in the process of

correction. In addition, the scattered intensity must be corrected for sample absorption as some of the scattering coming from the unwanted background is also modified by sample absorption. In this thesis, Gudrun was used to correct both corrections based on the sample composition and number density. The scattering intensity is normalized with respect to the number of atoms in the sample, so it is divided by a number of atoms in the sample. The number density of a sample as a number of atoms per unit volume with units of g/cm^3 is usually taken from Rietveld refinement performed in GSAS [18].

During inelastic scattering neutrons exchange energy with atoms within the sample, so after scattering their energies can significantly differ. This generates a problem as scattered neutrons with different energies can be wrongly attributed to coherent scattering at a different scattering vector ***Q***. To avoid this, the Placzek corrections $P(Q_e,\theta)$ have been implemented, which define the difference between the static approximation of total scattering and thermal differential cross section. The Placzek corrections $P(Q_e,\theta)$ are obtained by providing the temperature of sample and vanadium rod, to finally derive reduced total scattering *F(Q)* from differential cross section.

$$P(Q,\theta) = F(Q) - \sum(Q,\theta) \qquad \text{Equation 2.49}$$

When all corrections and normalization are processed, the total scattering function in reciprocal space, *F(Q)*, is produced. The *F(Q)* can be transformed to give the pair distribution function in real space. It is important to determine total scattering to a high value of ***Q*** (typically 55 Å^{-1}) in order to achieve the best possible real space resolution in *G(r) or T(r).* The resolution is given as;

$$\Delta r \approx \frac{2\pi}{Q_{max}} \qquad \text{Equation 2.50}$$

where;

Q_{max} - the maximum value of scattering vector ***Q***.

This produces good real space resolution $\Delta r \approx 0.13$ Å for $Q_{max}=55$Å^{-1}.

However, the finite range of ***Q*** and the presence of noise in the data at high ***Q*** (which has less statistics than the data at lower ***Q***) introduce ripple peaks into the computed *T(r)* or *G(r)* function during the Fourier transform.

This termination ripple problem can be reduced by introducing a modification function *M*(*Q*) to the *F(Q)* which decreases smoothly to zero at Q_{max} prior to the

Fourier transform. The modification function used in this thesis is called the Lorch function [9] after its discoverer. The application of the Lorch function generates another problem, as peaks of a modified total correlation function will be artificially broadened after the Fourier transform. However, the reduction in termination ripples, which could otherwise be misinterpreted as a real feature of the *G(r)* data, was deemed more beneficial than the slight reduction in data quality due to broadening of the data, and so the Lorch function was applied using the *stog* utility. The best compromise for such a difficult problem is to apply the Fourier transform up to a maximum $\boldsymbol{Q}$ value where the statistics are still good enough to minimise the contribution from noise (i.e. not necessarily the highest $\boldsymbol{Q}$ value collected) and to use a maximum $\boldsymbol{Q}$ value where the intensity of *F(Q)* reaches a value of zero.

In this thesis the correction of total scattering data for both BMN and BTFM were normalized and corrected using Gudrun software [27]. The obtained experimental *F(Q)* functions in Gudrun were transformed to the total correlation function *G(r)* using the *stog* utility in RMCProfile [29, 30]. The application of Q_{max} = 30 $Å^{-1}$ helped to maximize resolution while simultaneously minimizing termination ripples. The reciprocal space of total scattering data were also convoluted with a box function to account for the broadening in the calculated data due to the finite RMC configuration size. Fits to *S(Q)* data were carried out for $\boldsymbol{Q}$ < 30 $Å^{-1}$. Furthermore, the real space data of the total correlation function were fit over the range of the RMC configuration with *r* corresponding to the shortest lattice vector.

2.3.3 Reverse Monte Carlo modeling

The reverse Monte Carlo (RMC) [31-33]method is a technique of modeling which uses statistical principles. RMC modeling is a method used to generate a three-dimensional atomistic model starting from a supercell of the average structure which simultaneously matches the Bragg profiles, the total scattering in reciprocal space and the pair distribution function data in real space. RMC modeling was originally developed for application to the structures of liquids and glasses [34]

but now, due to recent developments and the improvement in *Q* range resolution of diffractometers, have increasingly been applied to crystalline and magnetic structures [35-38].

The aim of the RMC modeling is to achieve agreement between experimental and calculated functions using the Monte Carlo algorithm which is presented here as a flowchart:

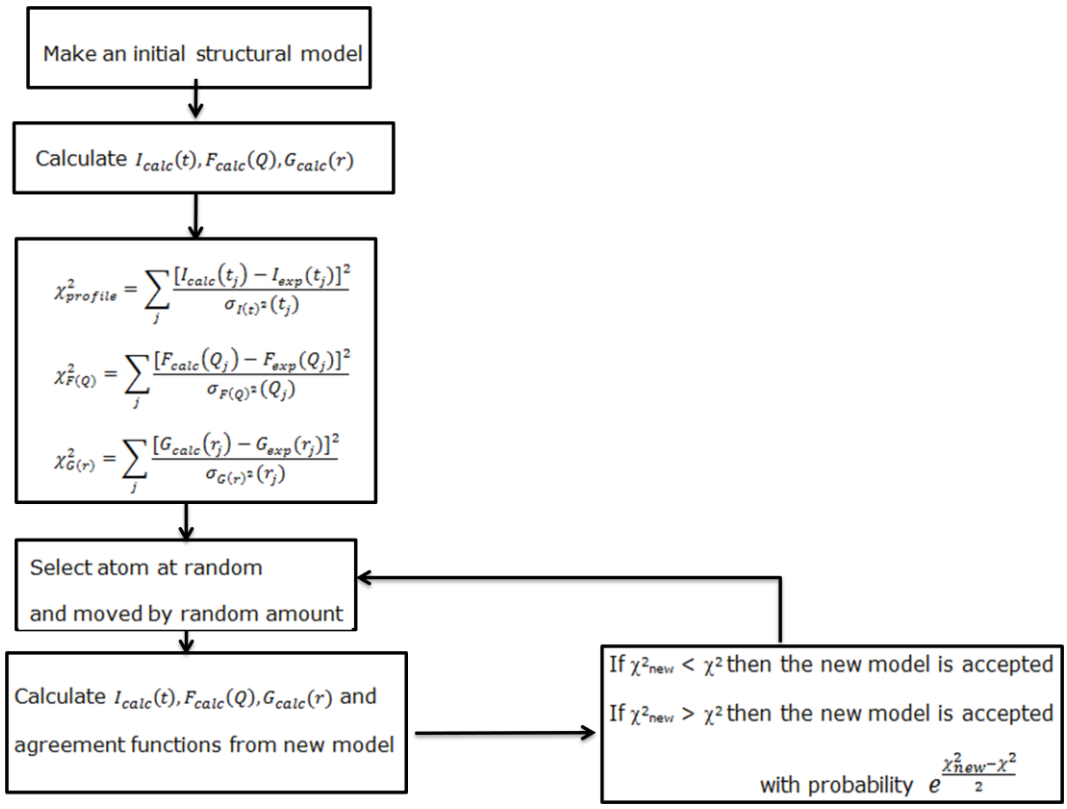

Figure 2.11. *Flowchart of the algorithm used during RMC modeling.*

The steps will now be described in more detail in turn.

1. The initial model is based on the average crystallographic structure, obtained by Rietveld refinement in GSAS [18]. The starting configuration is generated by multiplicity of lattice parameters of a crystallographic structure along the x, y and z directions. The obtained initial model, called a supercell, contains N atoms with periodic boundary conditions as an effect of translation of $n_1 \times n_2 \times n_3$ crystalline unit cells (subcells of the supercell) where n_1, n_2 and n_3 are

chosen to maximize the minimum lattice vector, normally resulting in as close to cubic supercells as possible (Figure 2.12).

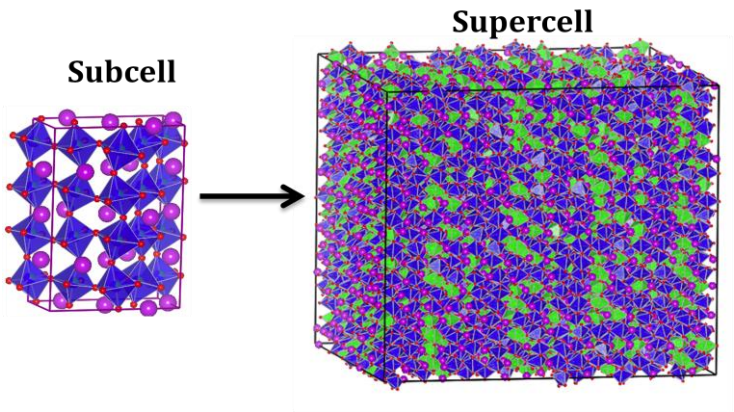

Figure 2.12. *Example of a subcell of an average crystallographic structure and an RMC supercell obtained by multiplicity of the subcells.*

2. The simulation starts by calculating the Bragg profile, total scattering function *F(Q)* and pair distribution function *G(r)*. However, due to limited size of the RMC supercell and *r* range, the calculated *F(Q)* obtained from *G(r)* is artificially broadened. To be able to compare calculated and experimental *F(Q)*, the latter one must be degraded by convolution function with a box defined by the dimension of the supercell;

$$F_{box}(Q) = \frac{1}{\pi}\int_{-\infty}^{+\infty} F_{exp}(Q')\frac{sin\ L(Q-Q')/2}{(Q-Q')}dQ' \qquad \text{Equation 2.51}$$

where:

L is the smallest dimension of the RMC configuration (supercell) and defines the upper limit of the calculated pair distribution function *G(r)*.

3. In the next step, the difference (agreement function) between the experimental Bragg profile, *F(Q)* and *G(r)*, and calculated Bragg profile, *F(Q)* and *G(r)* from the previous step is calculated.
4. An atom from the configuration is randomly selected and a random move (or swap) is generated.

5. The new value of the agreement function for the Bragg profile, *F(Q)* and *G(r)* data is calculated for the configuration with the atom in its new location.
6. In this step program decides whether to accept/reject the calculated move. When the agreement function is smaller than that obtained in the previous step $\chi^2_{new} < \chi^2_{old}$, then move is accepted, but if $\chi^2_{new} > \chi^2_{old}$ the move is accepted with the probability $e^{\frac{\chi^2_{new} - \chi^2_{old}}{2}}$.
7. The process repeats from point 4.

The RMC modeling is repeated until there is no further improvement in the quality of the fit with goodness of fit oscillating about the same number and the final 3-dimensional configuration is consistent with the experimental data. The simultaneous refinement of these three functions provides a real advantage since 1) the fit to the Bragg scattering ensures that average structure is correct and 2) the total scattering and PDF incorporates the diffuse scattering information about the short-range order. Thus, this results in an atomic configuration which is consistent with the long- and short-range order observed by total scattering.

Typically the supercells are large with approximately 20,000 atoms for the starting configuration. The reason for these large configurations is that the RMC method is based in statistical mechanics, so its the algorithm will tend to maximize the degree of disorder in the configurations. Thus, the RMC modeling will provide the most disordered atomic configuration which is consistent with the experimental data. There can be an infinite number of different disordered configurations showing the same agreement between experimental and calculated data. Thus, in practice it should be run at least several RMC simulations for the same material.

The RMC modeling based on the RMCProfile software [29] was applied in this thesis to investigate the local structure of $Bi_2Mn_{4/3}Ni_{2/3}O_6$ or $BiTi_{3/8}Fe_{1/4}Mg_{3/8}O_3$. At least 18 RMC simulations were run for single temperature data of both materials in order to obtain a statistically relevant sample of data. The simultaneous fit of intensity of Bragg peaks, total scattering function *F(Q)* and pair distribution function *G(r)* yielded a good match to the experimental data for both perovskite structures, and the results are presented in chapters 3 and 4.

2.3.3.1 Constraints

The RMC method is stochastic and because of that, it tends towards a maximum of disorder in the configuration. This can lead to broken chemical bonds or unreasonably displaced cations, which usually happens towards the beginning of simulation. It can also occur during whole minimization process, when the applied data weightings are too low. Thus, to keep a model physically sensible we use restraints and constraints, so that the atomic coordinates are no longer completely free variables.

There are several types of restraints and constraints which can be applied in RMC modeling, however here only types used in this thesis will be described.

2.3.3.1.1 Distance windows constraints

Distance window constraints (DW) [29] define the closest minimum distance that two atom types can come together and a maximum distance where two atoms types are allowed to move apart. This provides a window within which atom pairs are allowed to move. To apply DW constraints the file with extension .dw must be present in the RMC simulation folder (others RMC file will be explained in the section 2.3.3.2). The .dw file has a simple structure, containing only two lines of instructions. The first line defines the minimum approach distance whereas the second line provides the maximum distance within which two atoms are allowed to move. The presented example of a .dw file is for $Bi_2Mn_{4/3}Ni_{2/3}O_6$ where four types of atoms create 10 possible atom pairs.

Table 2.5. *Distance windows constraints.*

	Bi-Bi	Bi-Mn	Bi-Ni	Bi-O	MnMn	Mn-Ni	Mn-O	Ni-Ni	Ni-O	O-O
Min	3.5	2.7	2.7	2.0	3.1	3.1	1.6	3.1	1.6	2.4
Max	4.5	4.3	4.3	3.5	4.5	4.5	2.5	4.5	2.5	3.7

The list of atomic pairs is generated during first run of RMCprofile. The defined distance window of the atomic pairs with closest and furthest distances of atom pairs are usually based on the results of Rietveld refinement of average crystallographic structure.

2.3.3.1.2 Bond Valence Sum (BVS) constraints

This soft chemical constraint based on bond valence calculations provide extra chemical information during RMC modeling but also enforce sensible bonding distances. The fitting of bond valence distances between the cations and oxygen atoms to their empirical values [39] were applied to RMC modeling of $Bi_2Mn_{4/3}Ni_{2/3}O_6$ and $BiTi_{3/8}Fe_{1/4}Mg_{3/8}O_3$ according to equation 2. 52:

$$s_{ij} = exp\left[\left(R_0 - r_{ij}\right)/b\right] \qquad \text{Equation 2.52}$$

where:

s_{ij} - the individual bond valences between atoms *i* and *j*

R_0 and *b* - empirical parameters [40].

The new agreement factor based on BVS calculation is added to RMC modeling:

$$\chi^2_{BVS} = \sum_{j=1}^{N}\left(V_j - V_i\right)^2/\sigma_i \qquad \text{Equation 2.53}$$

where:

$V_{j,}$ - the sum of the bond valence for atom *j*,

V_i - the expected bond valence for atom of type *i*,

σ_i - the weighting factor for atom of type *i* [41].

This extra BVS agreement factor introduced during the RMC minimization process help to avoid damage such as breaking of chemical bonds, especially at the initial stage, where the biggest changes usually occur and unphysical distances are generated. The BVS constraints monitor the changes in the atomic configuration and accept them if are consistent with empirical bond valence rules.

The example of .bvs file is presented in Table 2.6, where first four rows show type of atom and the next row define their weightings. The A site and B site cations bonded to oxygen in the configuration are fitted to the empirical parameters of the atomic pairs Bi-O, Mn-O and Ni-O presented in the rows 8, 10 and 11. The last two rows in the file define how frequently the BVS parameters for every atom in the configuration are saved, so that the progress of the RMC modeling can be monitored.

Table 2.6. *Contents of a bond valence sum constraints file for RMCProfile.*

```
Bi  3                 // atom #1
Mn  4                 // atom #2
Ni  2                 // atom #3
O  -2                 // atom #4

0.0340 0.0340 0.0340 0.1400    // chi^2 weights (for each type)

0 0 0                 // Bi-Mn (Rij, B, cut-off distance)
0 0 0                 // Bi-Ni (Rij, B, cut-off distance)
2.094 0.37 3.8          // Bi-O  (Rij, B, cut-off distance)
0 0 0                 // Mn-Ni (Rij, B, cut-off distance)
1.753 0.37 2.6        // Mn-O (Rij, B, cut-off distance)
1.654 0.37 2.6        // Ni-O (Rij, B, cut-off distance)

100000                // "intermediate save"
100000                // "neighbour list update"
```

2.3.3.1.3 Interatomic potentials

In addition to BVS the use of interatomic potentials [30] help to prevent, unphysical bond distances in the configuration by improving the simulation with the introduction of interatomic contacts. There are two potentials included into the restraints:

- Bond-stretching potential described by Morse equation;

$$E_M = D\alpha^2(r - r_0)^2 \qquad \text{Equation 2.54}$$

where:

D - the energy required to break a bond

r_0 - the average bond length

α - a constant with a value of 2.55 $Å^{-1}$ for all atom pairs.

- Bond-angle potentials, where energy of bending bonds is defined by using harmonic cosine potential:

$$E = \frac{1}{2}K(cos\theta - cos\theta_0)^2 \qquad \text{Equation 2.55}$$

where:

θ - the instantaneous bond angle

θ_0 - the defined average angle

The example of interatomic potential presented in Table 2.7 is a part of a main control file which will be explained in the section 2.3.3.2. Bond-stretching and bond-angle potentials were applied to Ni-O atom pair with energies of 0.3 eV and 3 eV respectively:

Table 2.7. *Interatomic potentials block in the main control file for RMCProfile.*

```
POTENTIALS ::
  > STRETCH :: Ni O 0.3 eV 2.1 Ang
  > STRETCH_SEARCH :: 20%
  > ANGLE :: Ni O O 3 eV 90.0 deg 2.1 2.1 Ang
  > ANGLE_SEARCH :: 12 deg
  > TEMPERATURE :: 300 K
```

The Ni-O interatomic potential constraints combined with BVS constraints for all cation-O pairs were applied to material $Bi_2Mn_{4/3}Ni_{2/3}O_6$ and helped to separate the Mn/Ni cation species that share the same crystallographic B site and possess a similar neutron scattering length.

2.3.3.2 RMC files

The RMC modeling requires several input files to start a simulation. The .dw and.bvs files containing distance windows and bond valence sum constraints and, part of the main control file relating to interatomic potentials are responsible for constraints in the configuration and have already been discussed in the previous section. Other files are responsible for different aspects of the RMC modeling. The most important and valuable is the main control file with extension .dat where all information about the material are collected in the several blocks (Table 2.8). The example a .dat file for RMC Profile version 6 for $Bi_2Mn_{4/3}Ni_{2/3}O_6$ shows the basic information like title, material, phase, density together with constraint information on the minimum closest approach for each atom pair and the maximum distance for any move for every atom type. It also contains time limits for simulation, 900 minutes in this example, and the type of input and output configuration file, .rmc6f. This example is using PDF *G(r)* data in NEUTRON_REAL_SPACE_DATA block and total scattering *S(Q)* data NEUTRON_RECIPROCAL_SPACE_DATA to fit the calculated data. To be able to distinguish atom pairs, and then analyze distribution of bond distances, the *G(r)* and *S(Q)* blocks contain NEUTRON COEFFICIENTS (neutron scattering length) for each atom pair. The block ATOMS simply defines every chemical element in the material, while BRAGG block contains a Bragg profile fitted with the gsas2 profile shape. The RMC configuration is specified by the supercell, to be of a

multiplicity of 10 × 5 × 4 unit cells. The last block POTENTIAL was explained earlier.

Table 2.8. *Main control file for RMCProfile.*

```
TITLE :: BiMnNiO
MATERIAL :: BiMnNiO
PHASE :: P1
TEMPERATURE :: 293K
INVESTIGATOR :: Robert
COMMENT ::

NUMBER_DENSITY :: 0.08383244
MINIMUM_DISTANCES :: 3.0 2.4 2.4 1.9 3.4 3.3 1.72 3.3 1.8 2.1
MAXIMUM_MOVES ::   0.05 0.05 0.05 0.1
R_SPACING ::  0.0200
PRINT_PERIOD :: 1000
TIME_LIMIT ::     900
SAVE_PERIOD ::    60

INPUT_CONFIGURATION_FORMAT ::  rmc6f
SAVE_CONFIGURATION_FORMAT  ::  rmc6f

NEUTRON_REAL_SPACE_DATA :: 1
  > FILENAME :: bmn_rt_gr_rmc.dat
  > DATA_TYPE :: G(r)
  > FIT_TYPE :: G(r)
  > START_POINT :: 1
  > END_POINT :: 1501
  > CONSTANT_OFFSET ::   0.000
  > NEUTRON_COEFFICIENTS :: 0.029118007  -0.017057857  0.023200216  0.1188269
0.0024982004  -0.0067955535  -0.034805469  0.0046212813  0.047338560  0.1212293
  > WEIGHT ::   0.001
  > NO_FITTED_OFFSET

 NEUTRON_RECIPROCAL_SPACE_DATA :: 1
  > FILENAME :: sq_conv_27p5506.dat
  > DATA_TYPE :: F(Q)
  > FIT_TYPE ::  F(Q)
  > START_POINT :: 1
  > END_POINT :: 1445
  > CONSTANT_OFFSET ::   0.0000
  > NEUTRON_COEFFICIENTS :: 0.029118007  -0.017057857  0.023200216  0.1188269
0.0024982004  -0.0067955535  -0.034805469  0.0046212813  0.047338560  0.1212293
  > WEIGHT ::   0.003
  > NO_FITTED_OFFSET
  > NO_FITTED_SCALE

ATOMS :: Bi Mn Ni O
FLAGS ::
  > NO_MOVEOUT
  > NO_SAVE_CONFIGURATIONS
  > NO_RESOLUTION_CONVOLUTION
  > CSSR

CML :: ccViz
```

```
BRAGG ::
 > BRAGG_SHAPE :: gsas2              ! Which peakprofile to use
 > SUPERCELL ::  10 5 4
 > RECALCULATE
 > WEIGHT ::   0.0005

POTENTIALS ::
 > STRETCH :: Ni O 0.25 eV 2.1 Ang
 > STRETCH_SEARCH :: 20%
 > ANGLE :: Ni O O 3 eV 90.0 deg 2.1 2.1 Ang
 > ANGLE_SEARCH :: 12 deg
 > TEMPERATURE :: 300 K
```

The starting RMC model is based on the average crystallographic structure, as the Bragg scattering enables RMC to reproduce the distribution of atomic position in the configuration. Thus to start the simulation, the information about the average structure must be provided. This is achieved by generating four files from Rietveld refinement performed with GSAS.

- .bragg file presented in Table 2.9 contains the Bragg scattering, where intensity is presented as a function of time-of-flight. It also contains the number of data points, 1077, the detector bank (backscattering bank in GEM), a scale factor, 0.81626, and the volume of the unit cell, 954.192Å^3.

Table 2.9. *File with .bragg extension for RMCProfile.*

```
                1077         6  0.8162600       954.1920
Time I(obs)
   6.765675      2.4522200E-02
   6.771085      2.4583900E-02
   6.776500      2.4810500E-02
     …
  15.99350       3.6956199E-02
```

- .back file contains the parameters for a Chebychev polynomial used to model the background function in GSAS.
- .inst file provides the correct instrumental profile parameter for each detector bank.
- .hkl file presented in Table 2.10 defines minimum and maximum values for Miller indices to be calculated, which refers to the fundamental unit cell in a supercell, and the minimum value of *d* spacing to be considered is given in the first line.

Table 2.10. *File with .hkl extension for RMCProfile.*

```
 0.7500000
-30.00000      30.00000      1.000000
-30.00000      30.00000      1.000000
-30.00000      30.00000      1.000000
```

These four files generated from GSAS reproduce the Bragg scattering in a format compatible with the RMC modeling algorithm, where initial atomic positions are contained in the configuration file with the extension .rmc6f or .cfg, depending on the version of RMCProfile. Both configuration files contain fractional coordinates, the number of atoms and the density and dimensions of the supercell. An example .rmc6f file of $Bi_2Mn_{4/3}Ni_{2/3}O_6$ is given in Table 2.11.

Table 2.11. *Configuration file with .rmc6f extension.*

```
(Version 6f format configuration file)
Metadata owner:     Rob
Metadata date:      09-10-2010
Metadata material:  BMN
Number of moves generated:          0
Number of moves tried:              0
Number of moves accepted:           0
Number of prior configuration saves: 0
Number of atoms:                 16000
Number density (Ang^-3):             0.083837
Cell (Ang/deg):    55.107002   55.739498   62.132000   90.000000   90.000000   90.000000
Lattice vectors (Ang):
   55.107002    0.000000    0.000000
    0.000000   55.739498    0.000000
    0.000000    0.000000   62.132000
Atoms:
    1   Bi    0.099045    0.151616    0.125000    1   0   0   0
    2   Bi    0.099045    0.151616    0.375000    2   0   0   0
    3   Bi    0.099045    0.151616    0.625000    3   0   0   0
        …
 16000   O     0.900818    0.808201    0.875000 16000   0   0   0
```

Once all of the files required by RMCProfile are collated into one folder (main control .dat, configuration .rmc6f, constraints and the files reproducing Bragg scattering), RMC modeling with simultaneous fit of Bragg profile, *F(Q)* and *G(r)* during minimization process can be started. The RMC modeling is repeated until there is no further improvement in the quality of fit of the Bragg profile data, the total scattering structure factor *F(Q)* and the pair correlation function *T(r)*. The goodnesses of fits χ^2 in all RMC models in chapters 3 and 4 were oscillating about the same number and the final 3-dimensional configuration was consistent

with the experimental (Table 2.12). When the consistency between calculated and experimental data was achieved, the analysis the local structures information contained within the atomic configurations of the perovskite materials were performed.

Table 2.12. *Example of goodness of fit during RMC modeling for* $BiTi_{3/8}Fe_{1/4}Mg_{3/8}O_3$ *at low temperature (goodnesses of fits differ between Bragg profile, T(r) and F(Q), due to different weightings applied during RMC modeling).*

	$\chi^2_{Initial}$	χ^2_{Final}
Bragg profile	4256.8	152.8
T(r)	$7.055*10^5$	128.1
F(Q)	263.4	21.6

2.4. References

1. Perutz, M. *Crystallography. Chapter 5. Scattering and diffraction.* 1996; Available from: http://www.xtal.iqfr.csic.es/Cristalografia/parte_05_5-en.html.
2. Radaelli, P.G. *Crystal Structure and Dynamics*. Part 2: Scattering theory and experiments 2012; Available from: http://www2.physics.ox.ac.uk/students/course-materials/c3-condensed-matter-major-option.
3. Giacovazzo, C., *Fundamentals of Crystallography* Second edition ed2002: Oxford University Press.
4. Van Smaalen, S., *An elementary introduction to superspace crystallography.* Zeitschrift Fur Kristallographie, 2004. **219**(11): p. 681-691.
5. Wagner, T. and Schonleber, A. *A non-mathematical introduction to the superspace description of modulated structures.* Acta Crystallographica Section B-Structural Science, 2009. **65**: p. 249-268.
6. Van Smaalen, S., *Incommensurate Crystallography.*2007: Oxford University Press.

7. Petricek, V., Vanderlee, A., and Evain, M., *On the use of crenel functions for occupationally modulated structures.* Acta Crystallographica Section A, 1995. **51**: p. 529-535.
8. Claridge, J.B., Hughes, H., Bridges, C. A., Allix, M., Suchomel, M. R., Niu, H., Kuang, X., Rosseinsky, M. J., Bellido, N., Grebille, D., Perez, O., Simon, C., Pelloquin, D., Blundell, S. J., Lancaster, T., Baker, P. J., Pratt, F. L., Halasyamani, P. S., *Frustration of Magnetic and Ferroelectric Long-Range Order in $Bi_2Mn_{4/3}Ni_{2/3}O_6$.* Journal of the American Chemical Society, 2009. **131**(39): p. 14000-14017.
9. Dinnebier, R.E., *Modern XRD methods in mineralogy*2000, Max-Planck-Institute for Solid State Research.
10. Cockcroft, J.K. *Powder Diffraction on the Web. Instrument X-ray Optics. .* 1999; Available from: http://pd.chem.ucl.ac.uk/pdnn/inst1/optics1.htm.
11. Dove, M.T., *Structure and Dynamics: An atomic view of materials*2010: Oxford University Press.
12. Dann, S.E., *Reactions and Characterization of Solids*2000: Royal Society of Chemistry.
13. Hull, S., Smith, R. I., David, W. I. F., Hannon, A. C., Mayers, J., Cywinski, R., *The Polaris powder diffractometer at ISIS.* Physica B, 1992. **180**: p. 1000-1002.
14. Hannon, A.C., *Results on disordered materials from the GEneral Materials diffractometer, GEM, at ISIS.* Nuclear Instruments & Methods in Physics Research Section a-Accelerators Spectrometers Detectors and Associated Equipment, 2005. **551**(1): p. 88-107.
15. Szczecinski, R.J., Chong, S. Y., Chater, P. A., Hughes, H., Tucker, M. G., Claridge, J. B., Rosseinsky, M. J., *Local crystal structure of antiferroelectric $Bi_2Mn_{4/3}Ni_{2/3}O_6$ in commensurate and incommensurate phases described by Pair Distribution Function (PDF) and Reverse Monte Carlo (RMC) modeling.* Chemistry of Materials (in progress), 2013.
16. Chong, S.Y., Szczecinski, R. J., Bridges, C. A., Tucker, M. G., Claridge, J. B., Rosseinsky, M. J., *Local Structure of a Pure Bi A Site Polar Perovskite Revealed by Pair Distribution Function Analysis and Reverse Monte*

Carlo Modeling: Correlated Off-Axis Displacements in a Rhombohedral Material. Journal of the American Chemical Society, 2012. **134**(13): p. 5836-5849.

17. Le Bail, A., H. Duroy, and J.L. Fourquet, *Ab Initio Structure Determination of $LiSbWO_6$ by X-ray Powder Diffraction.* Materials Research Bulletin, 1988(23(3)): p. 447-52.
18. Larson, A.C. and R.B. Von Dreele, *General Structure Analysis System (GSAS).* Los Alamos National Laboratory Report LAUR 86-748, 2004.
19. Petrícek V, D.M.a.P.L. *Jana2006 - the crystallographic computing system.* 2006; Available from: www-xray.fzu.cz/jana.
20. Toby, B.H., *R factors in Rietveld analysis: How good is good enough?* Powder Diffraction, 2006. **21**(1): p. 67-70.
21. Young, R.A., *Introduction to the Rietveld method* 1993: Oxford University Press, Oxford.
22. Welberry, T.R., *Diffuse x-ray scattering and models of disorder* 2004: Oxford University Press.
23. Lefmann, K., *Neutron scattering: theory, instrumentation and simulation*2007.
24. Keen, D.A., *A comparison of various commonly used correlation functions for describing total scattering.* Journal of Applied Crystallography, 2001. **34**: p. 172-177.
25. Gateshki, M. *X'Pert PRO MPD - atomic scale structural characterization of nanomaterials*. X'Press magazine 2009; Available from: http://www.panalytical.com/index.cfm?pid=1196.
26. Hui, Q., Dove, M. T., Tucker, M. G., Redfern, S. A. T., Keen, D. A., *Neutron total scattering and reverse Monte Carlo study of cation ordering in $Ca_xSr_{(1-x)}TiO_3$*. Journal of Physics-Condensed Matter, 2007. **19**(33).
27. McLain, S.E., Bowron, D. T., Hannon, A. C., Soper, A. K., *Gudrun. A computer program developed fro analysis of neutron diffraction data.*2006, ISIS Facility, Rutherford Appleton Laboratory, Chilton, Didcot, OXON, UK, OX11 0QX.

28. Benmore, C. *Pair Distribution Function analysis*. 2009; Available from: http://neutrons.ornl.gov/conf/nxs2009/pdf/Benmore_NXschool09.pdf.

29. Tucker, M.G., Keen, D. A., Dove, M. T., Goodwin, A. L., Hui, Q., *RMCProfile: reverse Monte Carlo for polycrystalline materials.* Journal of Physics-Condensed Matter, 2007. **19**(33).

30. Tucker, M.G., Goodwin, A.L., and Dove, M.T., *RMCProfile User Manual: Code version 6.4.7*2010.

31. McGreevy, R.L. and Pusztai, L., *Reverse Monte Carlo simulation: a new technique for the determination of disordered structures.* Molecular Simulation, 1988. **1**(6): p. 359-367.

32. McGreevy, R.L., *Reverse Monte Carlo modelling.* Journal of Physics-Condensed Matter, 2001. **13**(46): p. R877-R913.

33. Mellergard, A. and McGreevy, R.L., *Reverse Monte Carlo modelling of neutron powder diffraction data.* Acta Crystallographica Section A, 1999. **55**: p. 783-789.

34. Keen, D.A. and McGreevy, R.L., *Structural modeling of glasses using reverse Monte Carlo simulation.* Nature, 1990. **344**(6265): p. 423-425.

35. Dove, M.T., Tucker, M.G., and Keen, D.A., *Neutron total scattering method: simultaneous determination of long-range and short-range order in disordered materials.* European Journal of Mineralogy, 2002. **14**(2): p. 331-348.

36. Keen, D.A. and McGreevy, R.L., *Determination of disordered magnetic structures by RMC modeling of neutron diffraction data.* Journal of Physics-Condensed Matter, 1991. **3**(38): p. 7383-7394.

37. Keen, D.A., Tucker, M.G., and Dove, M.T., *Reverse Monte Carlo modelling of crystalline disorder*. Journal of Physics-Condensed Matter, 2005. **17**(5): p. S15-S22.

38. Tucker, M.G., Dove, M.T., and Keen, D.A., *Total scattering and reverse Monte Carlo modelling of disordered crystalline materials*. From Semiconductors to Proteins: Beyond the Average Structure, ed. S.J.L. Billinge and M.F. Thorpe2002, New York: Kluwer Academic/Plenum Publ. 85-103.

39. Brese, N.E., O'keeffe, M., *Bond-valence parameters for solids.* Acta Crystallographica Section B-Structural Science, 1991. **47**: p. 192-197.

40. Brown, I.D. and Altermatt, D., *Bond valence parameters obtained from a systematic analysis of the inorganic crystal structure database.* Acta Crystallographica Section B-Structural Science, 1985. **41**(AUG): p. 244-247.

41. Norberg, S.T., Tucker, M.G., and Hull, S., *Bond valence sum: a new soft chemical constraint for RMCProfile.* Journal of Applied Crystallography, 2009. **42**: p. 179-184.

Chapter 3. Local and crystallographic average structure of $BiTi_{3/8}Fe_{1/4}Mg_{3/8}O_3$ (BTFM) in various temperatures

3.1 Crystallographic average structure of BTFM at room temperature

The perovskite material $BiTi_{3/8}Fe_{1/4}Mg_{3/8}O_3$ (BTFM) was synthesized at ambient pressure and the average structure was determined through Rietveld refinement on X-ray and neutron powder diffraction data by Dr. Craig A. Bridges [1]. BTFM is a solid solution of antiferroelectric (AFE) material $BiMg_{1/2}Ti_{1/2}O_3$ which adopts the structure of well-known $PbZrO_3$ [2], and ferroelectric (FE) material $BiFeO_3$ [3].

The average crystallographic structure of BTFM and its crystallographic symmetry is complex, as it contains multiple B site cations disordered onto one side. The Rietveld refinements of high-resolution neutron powder diffraction data showed anisotropic line-broadening, revealing that the structure of BTFM is a polar perovskite with line-broadening consistent with *R*3*c* symmetry. BTFM is a ferroelectric with the structural distortions of Bi cations displacements along $\langle 111 \rangle_p$ ($\langle \rangle_p$ refer to the parent cubic perovskite unit cell), and thus adopting the bismuth ferrite F_R (ferroelectric rhombohedral) *R*3*c* structure. The B site cations are also displaced along $\langle 111 \rangle_p$ towards a triangular face of the octahedron, which maximize their distances from the Bi atoms, displaced towards the opposite face (Figure 3.1).

However, by lowering the structural symmetry to the monoclinic space group *Cc* with 2/*m* symmetry-strain broadening, we obtain an improved fit to the diffraction data. Nevertheless, the atom positions have strong *R*3*c* pseudosymmetry and there are also no extra reflections characteristic of the lower symmetry in the diffraction pattern. The cation displacements away from the rhombohedral axis $\langle 111 \rangle_p$ and low-symmetry microstrain both indicate that the simple rhombohedral model of $BiFeO_3$ and monoclinic *Cc* model with refinement in the space group *Cc*, do not fully describe BTFM structure.

Thus, the average crystallographic structure cannot be fully understood from Rietveld refinements and an investigation of local structure is necessary. The main

focus of this study were on correlations of Bi^{3+} displacements away from the $\langle 111 \rangle_p$ direction, which help to differentiate between rhombohedral and monoclinic symmetry, and also to clarify the role of the three distinct B site cations (Ti^{4+}, Fe^{3+} and Mg^{2+}) in stabilizing BTFM at ambient pressure.

(a)

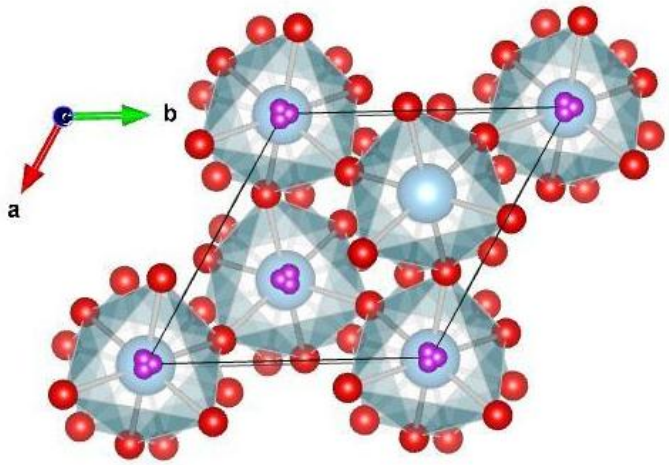

(c)

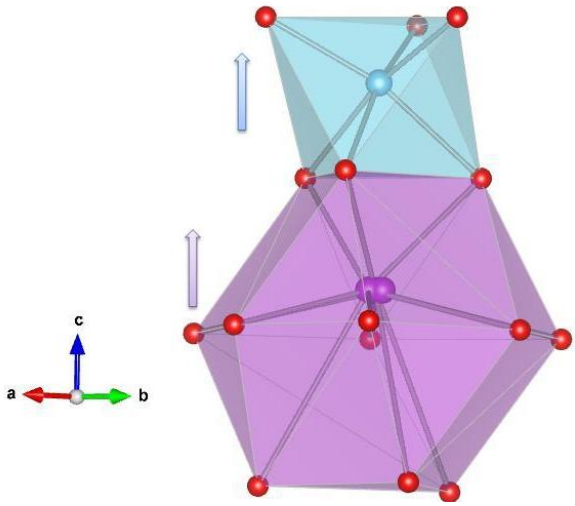

Figure 3.1. *(a) The crystallographic representation of BTFM in R3c (hexagonal settings) with view along c axis which correspond to* $\langle 111 \rangle_p$ *direction, whereas a and b axes correspond to* $\langle 110 \rangle_p$ *and* $\langle 1\bar{1}0 \rangle_p$ *directions respectively; (b) A and B site cation environment demonstrating displacement along* $\langle 111 \rangle_p$ *(c axis); Bi atoms shown in purple color, O atoms as red spheres and B site cations (Ti, Fe amd Mg) residing inside blue octahedras.*

3.2 Local structure of BTFM at room temperature (RT)

The PDF data correction and the study of local structure at room temperature by partial PDF analysis and A site displacements and correlations were performed by Dr. Samantha Chong. In this section the work of Dr. Chong is described alongside my further work investigating the B site displacements, B site and A site - B site correlations.

3.2.1 Generation of RMC model

Neutron powder diffraction data were collected on the GEM instrument at the ISIS pulsed spallation neutron source as described in the section 2.3.2. Data were collected on approximately 5 g of the sample contained in an 8 mm diameter vanadium can for 940 μAh over the range $0.3 \leq Q \leq 50$ Å^{-1}. The total scattering data were normalized and corrected using the GUDRUN software [4]. The experimental *F(Q)* was extracted using the ATLAS suite of programs [5] and subsequently transformed to the total correlation function *T(r)* using the *stog* utility in RMCProfile [6, 7] with Q_{max} = 30 Å^{-1}, which maximized the resolution of the *T(r)* while minimizing the appearance of termination ripples. The total scattering data were also convoluted with a box function to account for the broadening in the calculated data due to the finite RMC configuration size and fits were carried out for Q < 30 Å^{-1}. To build the initial RMC model, the Rietveld refinement of the neutron diffraction data from the backscatter bank of the GEM diffractometer was carried out in GSAS using a monoclinic *Cc* model with cell parameters related to the rhombohedral *R*3*c* structure (Figure 3.2) as shown the equation 3.1:

$$\begin{bmatrix} a_m \\ b_m \\ c_m \end{bmatrix} = \begin{bmatrix} \frac{2}{3} & \frac{1}{3} & \frac{\overline{2}}{3} \\ 0 & 1 & 0 \\ \frac{2}{3} & \frac{1}{3} & \frac{1}{3} \end{bmatrix} \begin{bmatrix} a_h \\ b_h \\ c_h \end{bmatrix} \qquad \text{Equation 3.1}$$

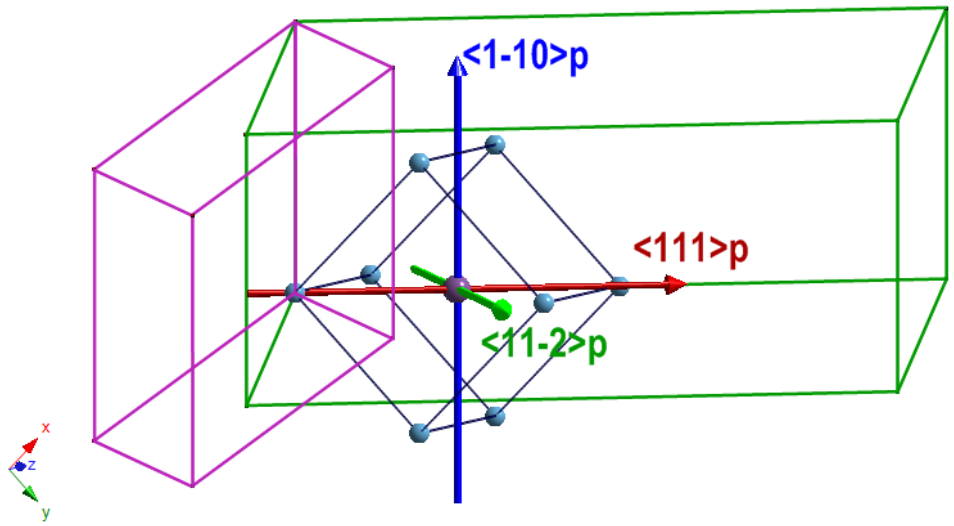

Figure 3.2. *The representation of pseudocubic (dark-blue), rhombohedral R3c in hexagonal settings (green), and monoclinic Cc (purple) unit cells with orthogonal model directions (arrows) and the corresponding pseudocubic directions indicated.*

RMC refinements were performed with RMCProfile, where starting configurations were obtained by using the multiplicity of lattice parameters 6*a* × 11*b* × 11*c*. This produce a RMC supercell with dimension of approximately 59 × 62 × 62 Å along each direction and consists of 14, 520 atoms. The real-space data total correlation function *T(r)* were fit over the range of the RMC configuration with r < 23.5 Å, which corresponds to the shortest lattice vector. In the first instance a reasonable fit was obtained using only distance window (DW) constraints, but sharp cut-off features caused by the DW minimum and maximum separation boundary were observed for the shortest distances in the partial pair distribution functions. The application of BVS constraints for each cation-oxygen pair improved the cut-off features of partial PDF's as well as, the BVS values (Table 3.1), and helped to distinguish the Ti^{4+}, Fe^{3+} and Mg^{2+} cations which occupy the same crystallographic B site. RMC refinements were run using maximum translation limits of 0.05 Å for all of the A site and B site cations and using 0.1 Å for the oxygen atoms. Both the RMC refinements with allowed swap

moves and static randomized B site cation distributions of the three octahedral cations, were repeated until there was no further improvement in χ^2 of Bragg profile data, the total scattering structure factor *F(Q)* and the pair correlation function *T(r)* and the final 3-dimensional configuration was consistent with the experimental data (Figure 3.3). The refinements were repeated for 18 RMC models to improve the statistical accuracy of the results.

Table 3.1. *Bond valence sum (BVS) values for RMC configurations refined using DW and BVS constraints.*

Cation	BVS / v.u.	
	RMC-distance window constraints	RMC-bond valence sum constraints
Bi^{3+}	3.06(44)	2.97(19)
Ti^{4+}	3.82(36)	3.97(12)
Fe^{3+}	2.74(26)	2.97(13)
Mg^{2+}	2.46(25)	2.18(13)

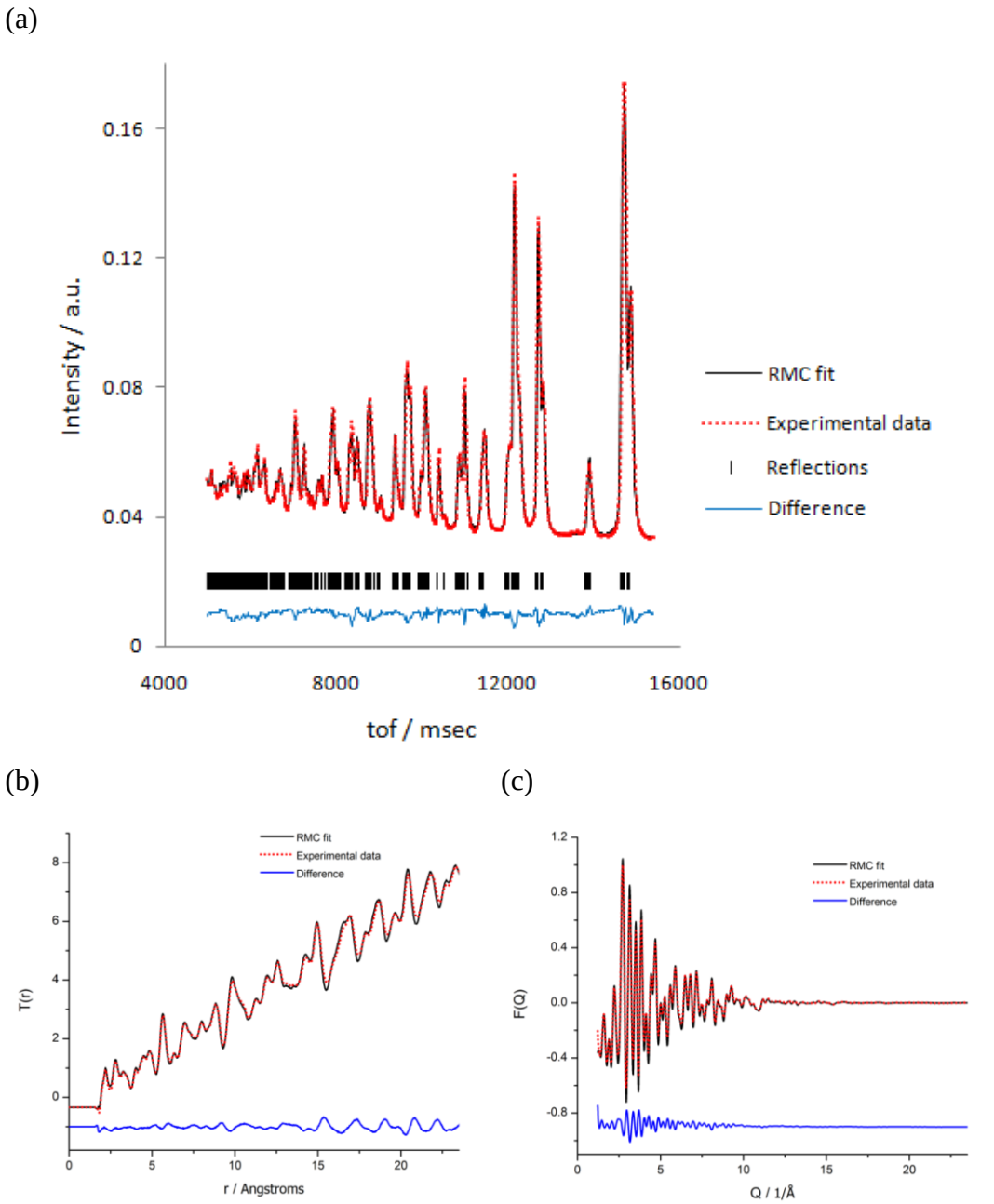

Figure 3.3. *Comparison between measured and modeled functions of one of the RMC model for the local structure of $BiTi_{3/8}Fe_{1/4}Mg_{3/8}O_3$ at RT: (a) Bragg profile data; (b) total correlation function T(r); (c) total scattering structure factor F(Q).*

Refined RMC models were orthogonalized to a Cartesian frame with the *x* axis parallel to $\langle 111 \rangle_p$, *y* along $\langle 1\bar{1}0 \rangle_p$, and *z* along $\langle 11\bar{2} \rangle_p$ (Figure 3.2), and further analysis of the local structure was subsequently based on the orthogonal models.

3.2.2 Analysis of the pair distribution function

Analysis of the pair distribution function, bond angle distribution and the collapsed unit cells of local structure at RT were based on the combined 18 RMC models, to improve the statistical accuracy. Initial analysis of the A site environment partial pair correlation functions showed good agreement with the long-range average structure derived from diffraction data (Table 3.2 and Figure 3.4). The A site bond lengths of the average structure along $\langle 111 \rangle_p$ results in three long bonds (orange), three short (green) bonds to oxygen, and the small disordered off-axis displacement of Bi^{3+} forms a fourth short Bi−O bond (cyan). The five remaining Bi–O bonds fall into two groups (purple, dark blue) of intermediate distance. The local structure in the RMC model as fitted by 3 Gaussian functions, provide the three main group of bonds distances 2.237(1) Å, 2.543(8) Å, and 3.303(3) Å with ratio 3.2:4.2:4.6, which correspond to average short (green and cyan), intermediate (purple and dark blue) and long bond distances (orange) respectively. Thus, the partial pair correlation function $g_{Bi-O}(r)$ showed a distribution of Bi−O distances similar to that observed in the averaged crystal structure.

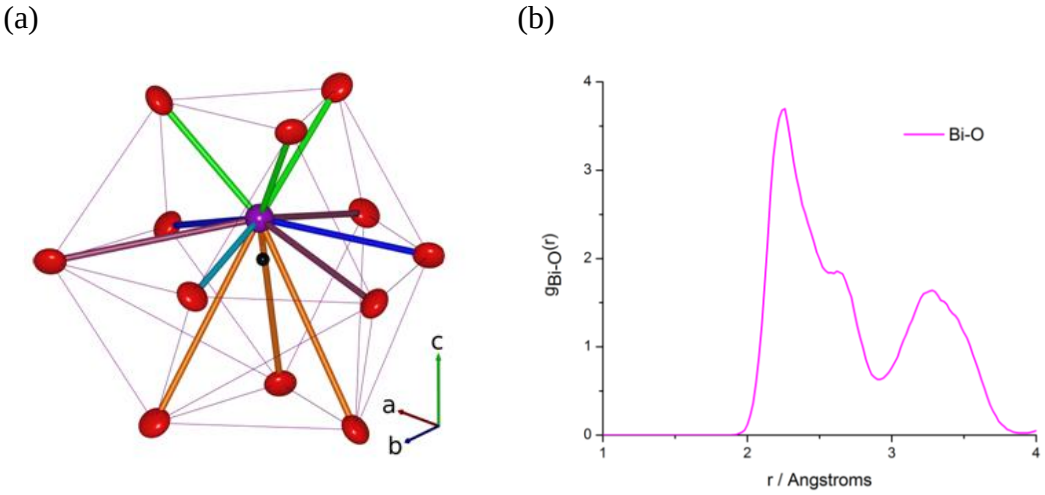

Figure 3.4. *(a) 12-fold coordinated Bi^{3+} cation environment (purple sphere , centroid indicated as a black sphere and O coloured as red spheres) from the crystallographic R3c structure with dominant cation displacements parallel to the pseudocubic $\langle 111 \rangle_p$ polar axis (c direction), whereas a and b axes correspond*

to $\langle 110 \rangle_p$ *and* $\langle 1\bar{1}0 \rangle_p$ *directions respectively; The A site displacement results in three long bonds (orange), three short (green) and the small disordered off-axis displacement of* Bi^{3+} *forms a fourth short Bi−O bond (cyan). The five remaining Bi–O bonds fall into two groups (purple, dark blue) of intermediate distance; (b) partial pair distribution function* $g_{Bi\text{-}O}(r)$ *in the RMC representing three group of Bi-O bond distances.*

Table 3.2. *Comparison of Bi-O bond distances obtained from the long-range average rhombohedral R3c structure (bond distances split over the 3 sites, which results in the 12 unique bond lengths) and partial pair distribution function* $g_{Bi\text{-}O}(r)$ *in the RMC model. Distances for RMC configuration were obtained by fitting Gaussian functions to the observed partial pair distributions function (Figure 3.4b).*

	Average structure / Å	Local structure (RMC model) / Å
Bi-O	2.242(3) 2.282(2) 2.369(4) 2.440(5) 2.598(3) 2.604(3) 3.156(3) 3.161(2) 3.319(5) 3.401(3) 3.432(2) 3.495(3)	2.237(1) 2.543(8) 3.303(3) (3.2:4.2:4.6)*

*Approximate ratio of separations (summed to 12 oxygen coordinate system) obtained from the integrated areas of peaks in $g_{Bi-O}(r)$.

The local bonding at the three B sites is also revealed by the partial pair distribution $g_{B\text{-}O}(r)$ and the instantaneous bond angle distributions $g_{O\text{-}B\text{-}O}(\theta)$, $g_{B\text{-}O\text{-}B}(\theta)$, derived from Gaussian function fits to the observed distributions. Comparison of the $g_{B\text{-}O}(r)$ distributions reveals differences between B site cations (Figure 3.5b). The $g_{Ti-O}(r)$ has a sharp peak centered at 1.818(2) Å, with a broader feature at a higher r value of ~2.11 Å. The shorter distance of the sharp peak is more comparable to the shortest Ti−O distance in tetragonal $BaTiO_3$ [8] (1.83 Å) than Ti−O bond length in $SrTiO_3$ [9], which is shorter by about 0.1 Å.

Furthermore $g_{Ti-O}(r)$ has a breadth and shape of distribution similar to those observed for F_R-PZT [10]. The longer distance indicated by the broad feature is also comparable to the longer Ti−O distances in $BaTiO_3$ (2.13 Å) and a number of monoclinic phases of PZT (2.11−2.15 Å) [11, 12]. Thus, the modeled Ti−O distances agree well with expectations based on a range of polar perovskites containing titanium atoms. On the other hand, the partial $g_{Fe-O}(r)$ and $g_{Mg-O}(r)$ show single peaks centered at 2.021(2) and 2.060(1) Å respectively, consistent with more regular environments, where the displacement is almost exclusively along $\langle 111 \rangle_p$ to form three long and three short Fe/Mg−O bonds as observed in average structure (2.111(3) and 1.960(2) Å) (Table 3.3 and Figure 3.5a).

Table 3.3. *Comparison of B site-O bond distances from the long-range average rhombohedral R3c structure and partial pair distribution function $g_{Bi-O}(r)$ in the RMC model.*

	Average structure / Å	Local structure (RMC model) / Å		
B site – O	3x1.960(2) 3x2.111(3)	Ti - O	Fe – O	Mg-O
		1.818(2) 2.105(10)	2.021(2)	2.060(1)

(a) (b)

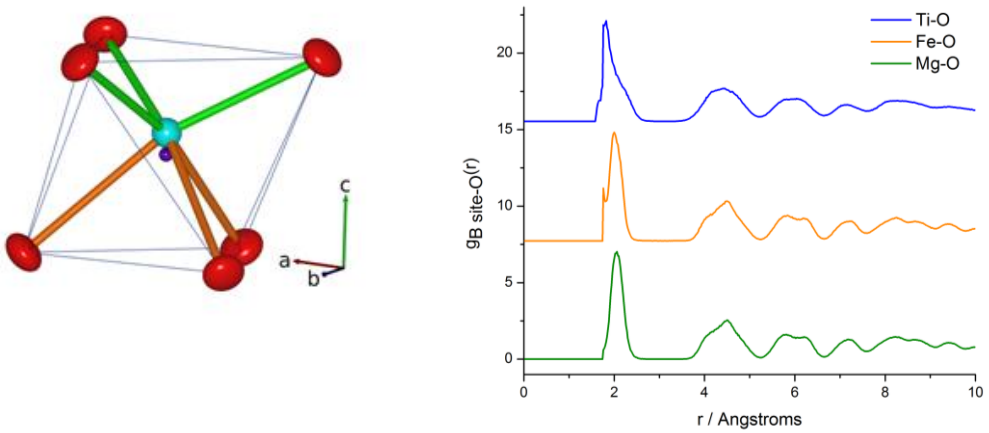

Figure 3.5. *(a) Octahedral B site cation environment (blue sphere , centroid indicated as a violet sphere and O coloured as red spheres) obtained from the*

crystallographic R3c structure with dominant cation displacements parallel to the pseudocubic $\langle 111\rangle_p$ *polar axis (c direction), whereas a and b axes correspond to* $\langle 110\rangle_p$ *and* $\langle 1\bar{1}0\rangle_p$ *directions respectively; (b) partial pair distribution function* $g_{B\text{-}O}(r)$ *in the RMC model.*

The analysis of external bond angles B-O-B show comparable results for all Ti^{4+}, Fe^{3+} and Mg^{2+} cations, whereas internal octahedral angles O-B-O (Table 3.4 and Figure 3.6a, b) reveals different tilting of Ti octahedra with broader distribution indicating more distorted behaviour, in comparison to Fe and Mg atoms. The average distribution of Fe and Mg bond angles are in the agreement with those derived from the average structure but not with the distribution of Ti angles, which is significantly broader.

Table 3.4*. Comparison of bond angle distributions of B-O-B and O-B-O between local and average structures at RT.*

	Average structure angle / ° (RT)	Local structure (RT)	
		Angle / °	FWHM/ °
Ti-O-Ti	156.1(1)	163.9(2)	30.0(3)
Fe-O-Fe		157.14(5)	18.6(1)
Mg-O-Mg		155.04(5)	20.3(1)
Ti-O-Fe		160.29(7)	24.4(2)
Ti-O-Mg		159.69(5)	25.1(1)
Fe-O-Mg		156.26(3)	19.9(1)
O-Ti-O	3x80.5(1)	88.87(9), 180.5(5)	24.4(3), 34.7(9)
O-Fe-O	3x99.9(1), 89.6(1) 88.3(1), 166.1(1)	88.7(1), 177.6(7)	21.8(4), 31.0(1)
O-Mg-O		88.4(2), 178(1)	22.4(5), 31.0(1)

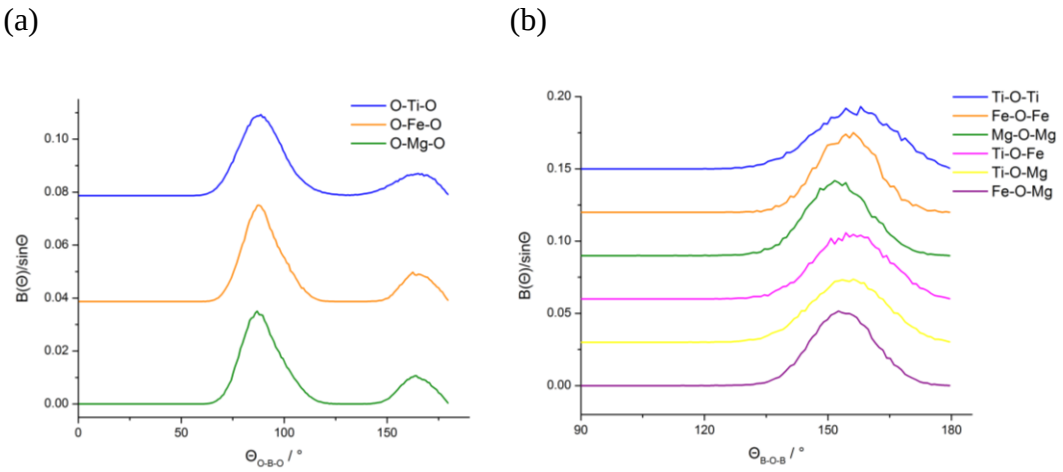

Figure 3.6. *Bond angle distributions of (a) O-B-O; (b) B-O-B for the local structure at RT.*

The B site – B site cation pair correlation functions (Figure 3.7a) are consistent with $g_{B\text{-}O}(r)$ and bond angle distribution, where differences between Ti^{4+} and (Fe^{3+}, Mg^{2+}) cations are noticeable. The $g_{Ti\text{-}Ti}(r)$ shows a much broader distribution of bond distances, demonstrating a wider variation in the separation of homopairs $g_{Ti\text{-}Ti}(r)$ and heteropairs $g_{Ti\text{-}Fe}(r)$, $g_{Ti\text{-}Mg}(r)$ than between combinations of homopairs $g_{Fe\text{-}Fe}(r)$, $g_{Mg\text{-}Mg}(r)$.

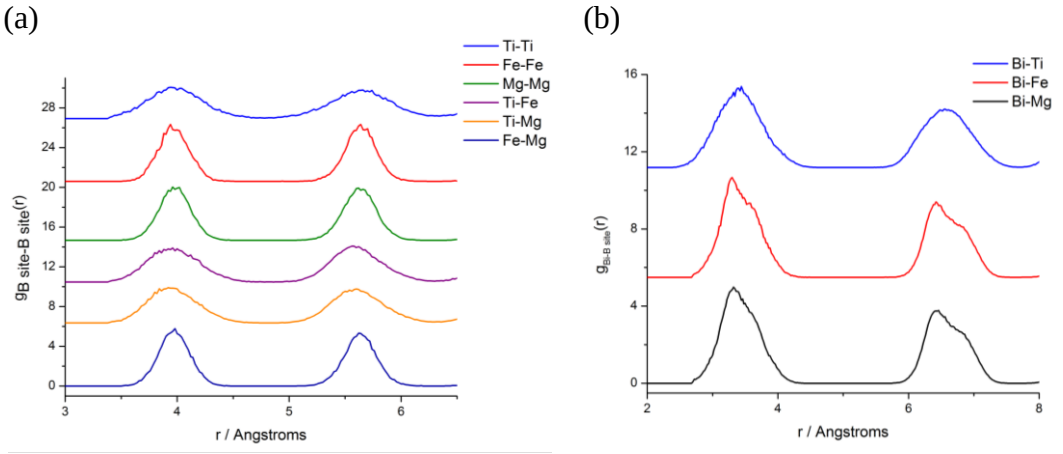

Figure 3.7. *The partial pair distribution function of (a) $g_{B\ site\text{-}B\ site}(r)$ and (b) $g_{Bi\text{-}B\ site}(r)$ in the RMC model.*

The analysis of partial pair correlation functions $g_{Bi-B}(r)$ (Figure 3.7b) show comparable bond distance distribution for Fe^{3+} and Mg^{2+} cations, with defined high-r shoulders for peaks in the $g_{Bi-Fe}(r)$ and $g_{Bi-Mg}(r)$, in contrast to the single broad peaks observed for $g_{Bi-Ti}(r)$. The $g_{Bi-Ti}(r)$ does not have these features, and instead appear as broadened single peaks, which is consistent with its varied displacements. This behaviour of Ti is similar to those observed in the local structure of experimental and computational studies of PZT [13-15], where Ti^{4+} cations were found to be more active in off-center displacement than non-displaced zirconium B site cations.

3.2.3 Analysis of A and B site cation displacements

The condensation of the unit cells from the RMC supercell back into the original monoclinic unit cell, produces a collapsed unit cell with "atom clouds", which correspond to projections of the derived atom positions back into the parent positions in the original cell (Figure 3.8a). The atomic positions are localized close to the original crystallographic coordinates, which can be further transformed to the rhombohedral model for direct comparison (Figure 3.8b). This confirms that the RMC model maintains the long-range crystallographic structure when averaged over the whole RMC configuration, and allows visualization of the atomic displacements from the local structure study. The general shapes of these atom clouds are consistent with those obtained from Rietveld refinement, with the oxygen atom displacement elongated in directions orthogonal to the B site. However, the A site cation clouds display a complex structured shape, which does not have the threefold rotational symmetry expected for a rhombohedral-derived model. This is consistent with the average structure refinement in the lower symmetry monoclinic structure, where the Bi^{3+} position differs from the simple rhombohedral model through displacement away from the threefold axis.

(a)

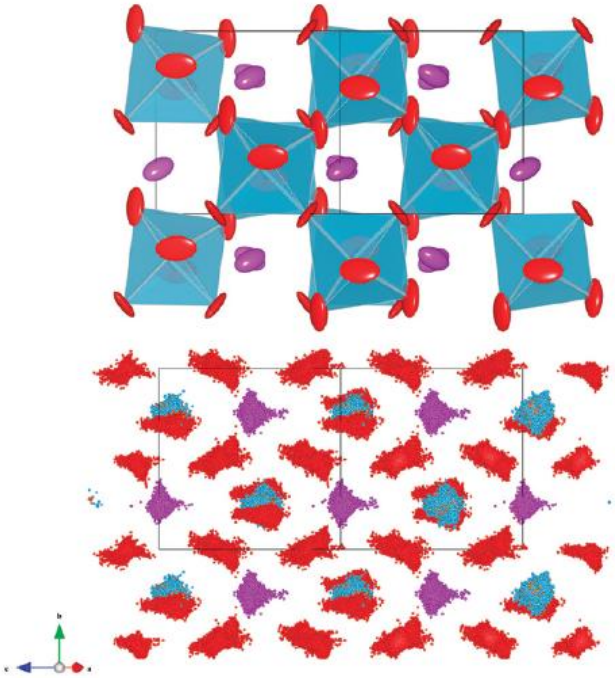

(b)

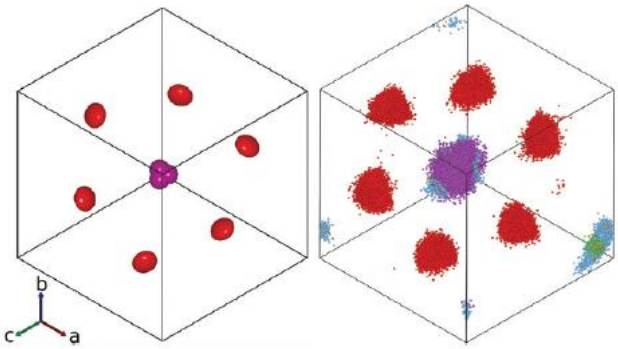

Figure 3.8. *(a) Monoclinic Cc Rietveld model viewed along* [101] *with Bi and O atomic displacement parameter (ADP) ellipsoids (top) and collapsed 18 RMC models into the Rietveld monoclinic unit cell (bottom); (b) (left) Rhombohedral R3c Rietveld model viewed along* $\langle 111 \rangle_p$ *showing the uniform threefold positions of Bi displaced orthogonal to* $\langle 111 \rangle_p$ *and (right) collapsed 18 RMC models into the Rietveld rhombohedral unit cell showing an off-axis cloud of Bi atoms without the expected threefold-symmetric distribution.*

The collapsed supercell also provides an apparent difference in the distributions of the three chemically distinct B site cations (Ti^{4+}, Fe^{3+} and Mg^{2+}) (Figure 3.9). The Ti^{4+} cations appear as diffuse clouds, while Fe^{3+} and Mg^{2+} cations form more densely clustered isotropic cores at each octahedral site. This different behavior of B site cations could not be distinguished from the average crystallographic structure as the average structure only includes one B site.

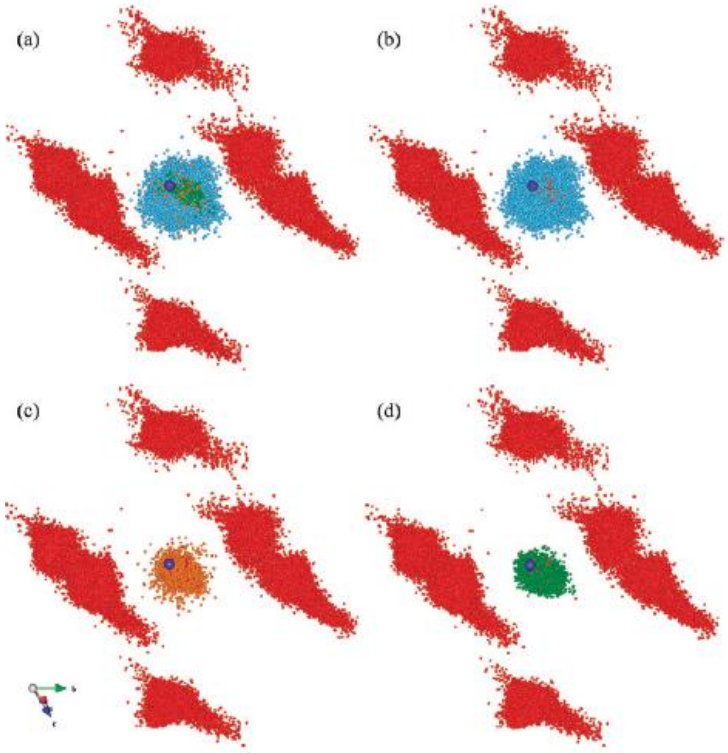

Figure 3.9. *The collapsed RMC models onto the original monoclinic cell, centered on the B site and viewed close to* $[1\bar{0}1]$*, showing distribution clouds for (a) all B site cations, (b)* Ti^{4+}*, (c)* Fe^{3+}*, and (d)* Mg^{2+} *cations (centroid indicated as a violet sphere and oxygens are shown as red spheres).*

The A and B site cations environments in the local structure are studied by calculations of Bi and B site cations displacements from the oxygen centroids within RMC models orthogonalized to a Cartesian frame with axes parallel to directions: $\langle 111\rangle_p$, $\langle 1\bar{1}0\rangle_p$, and $\langle 11\bar{2}\rangle_p$. The results are based on the calculations in the Perl language software, where the source code search of the nearest twelve/six oxygen anions of Bi/B site cations respectively within a distance *r*, and calculate bond distances of Bi-O and Ti/Fe/Mg-O. These bond distances are then subtracted

from the already calculated average position providing the real displacements along $\langle 111\rangle_p$, $\langle 1\bar{1}0\rangle_p$ and $\langle 11\bar{2}\rangle_p$, as opposed to displacements from the average position. The mean displacement calculations of the A site cations in the RMC model, 0.623(1) Å, are comparable to the results obtained for the average structure 0.66 Å. Analysis of the A site cations displacements along each of the crystallographic axes reveals, that the main component of the displacement is parallel to the $\langle 111\rangle_p$ polar direction of the average structure (Figure 3.10a), where all the Bi cations moving in the same sense, confirming that the RMC model retains the ferroelectricity throughout the length scale of the RMC models. The Bi displacement distributions orthogonal to $\langle 111\rangle_p$ are broader than the polar displacement and approximately averaged to zero. This is because of Bi displacements of both polarities along $\langle 1\bar{1}0\rangle_p$ and $\langle 11\bar{2}\rangle_p$, which correspond to a bimodal distribution of displacements. The observed approximately equal mean displacements 0.11(9) Å and 0.10(8) Å in the RMC model along the two directions $\langle 1\bar{1}0\rangle_p$ and $\langle 11\bar{2}\rangle_p$, respectively is represented by two dominant peaks of density (Figure 3.10b) rather than the threefold pattern associated with a purely rhombohedral symmetry.

(a)

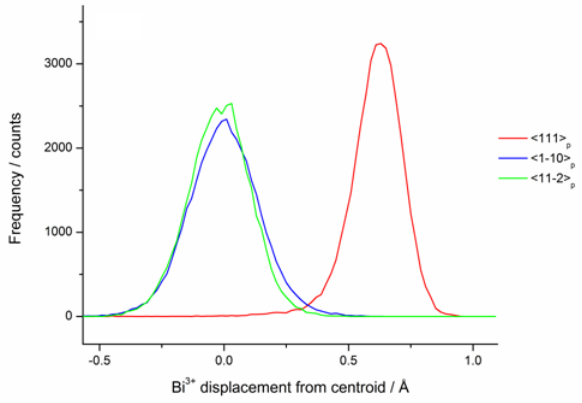

(b)

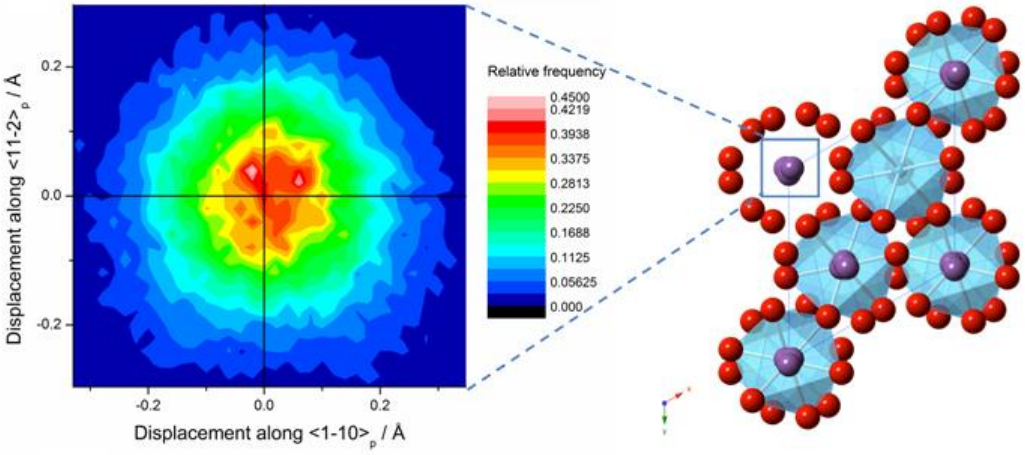

Figure 3.10. *(a) Distribution of Bi displacement along Cartesian model directions (*$\langle 111\rangle_p$, $\langle 1\bar{1}0\rangle_p$, *and* $\langle 11\bar{2}\rangle_p$, *(b) density plot of off-axis components corresponding to a view along* $\langle 111\rangle_p$ *centred on the Bi site showing two peaks (white) away from the origin.*

The B site environment is also analyzed by the displacement of B site cations from the oxygen centroid (Table 3.5 and Figure 3.11). The distribution of the total absolute displacements (Figure 3.11a) shows that Ti^{4+} has a broader range of displacements, demonstrated by the asymmetric peak centered at 0.312(2) Å with a full width at half-maximum (FWHM) of 0.355(6) Å. This is significantly different than Fe^{3+} and Mg^{2+} cations displacements (0.259(2) Å and 0.267(1) Å, respectively) and also greater than the average displacement for the single B site in the *R*3*c* Rietveld model (0.24 Å). The larger mean displacement for Ti atoms is consistent with results obtained for collapsed supercell into the original monoclinic unit cell, where Ti^{4+} cations represented by a diffuse cloud are

significantly more widely spread through the unit cell than less diffuse and isotropic Fe^{3+} and Mg^{2+} cations. The distinctive behavior of the Ti^{4+} cations compared to Fe^{3+} and Mg^{2+} is investigated more closely by examining displacement of these cations along the orthogonal Cartesian directions $\langle 111\rangle_p$, $\langle 1\bar{1}0\rangle_p$ and $<11\bar{2}>_p$. The dominant displacement direction for all three octahedral cations is along the bulk polar axis $\langle 111\rangle_p$ (Figure 3.11b), but the distribution of Ti displacements is less significant (0.131(3) Å) in comparison to Fe and Mg (0.239(5)Å and 0.242(7) Å respectively). Furthermore, the displacement distribution of Ti atoms is more symmetrical and significantly broader (FWHM 0.456(9) Å), than observed for Fe and Mg (0.317(3) Å and 0.315(3) Å respectively). It is also noticed, that the distribution of $\langle 111\rangle_p$ displacements for Ti contains negative displacements, absent for the other B site cations. This shows that the majority of the mean displacement of Ti^{4+} cations is not along polar $\langle 111\rangle_p$, but along other directions. The analysis of B site displacement along $\langle 11\bar{2}\rangle_p$ provide the comparable displacements (~ −0.03 Å) for observed Fe^{3+} and Mg^{2+}cations, and similar results for Ti^{4+} cations −0.007(1) Å with insignificantly broader distribution. On the other hand, the stronger contrast between the B site cations is most noticeable in the displacement along $\langle 1\bar{1}0\rangle_p$. The mean displacement of all three B cations along this direction is small, but the very broad Ti peak (FWHM 0.62(1) Å) demonstrates a broad distribution of Ti^{4+} positions, which are approximately averaged to zero over the scale of the RMC configuration. The distribution of the B site displacements orthogonal to $\langle 111\rangle_p$ (Figure 3.11e) highlights the fact that the most frequent displacements are close to zero, but for Ti^{4+} cations this incorporates a wide range of values. This demonstrates, that there are extensive positive and negative displacements along the $\langle 1\bar{1}0\rangle_p$ direction, which is the Ti displacement direction found in the orthorhombic phase of $BaTiO_3$ [8].

Table 3.5. *Octahedral B site displacements, d, from the centroid of coordinated oxygen atoms obtained from distributions (Figure 3.11a-d) with full width at half maximum (FWHM) of the fitted peak.*

	Ti^{4+}		Fe^{3+}		Mg^{2+}	
	d / Å	FWHM / Å	d / Å	FWHM / Å	d / Å	FWHM / Å
Total absolute displacement	0.312(2)	0.355(6)	0.259(2)	0.274(8)	0.267(1)	0.264(4)
$<111>_p$	0.131(3)	0.456(9)	0.239(5)	0.317(3)	0.242(7)	0.315(3)
$<1\bar{1}0>_p$	−0.003(3)	0.62(1)	−0.004(1)	0.209(3)	0.0009(6)	0.219(2)
$<11\bar{2}>_p$	−0.007(1)	0.279(4)	−0.033(1)	0.203(3)	−0.033(1)	0.239(4)

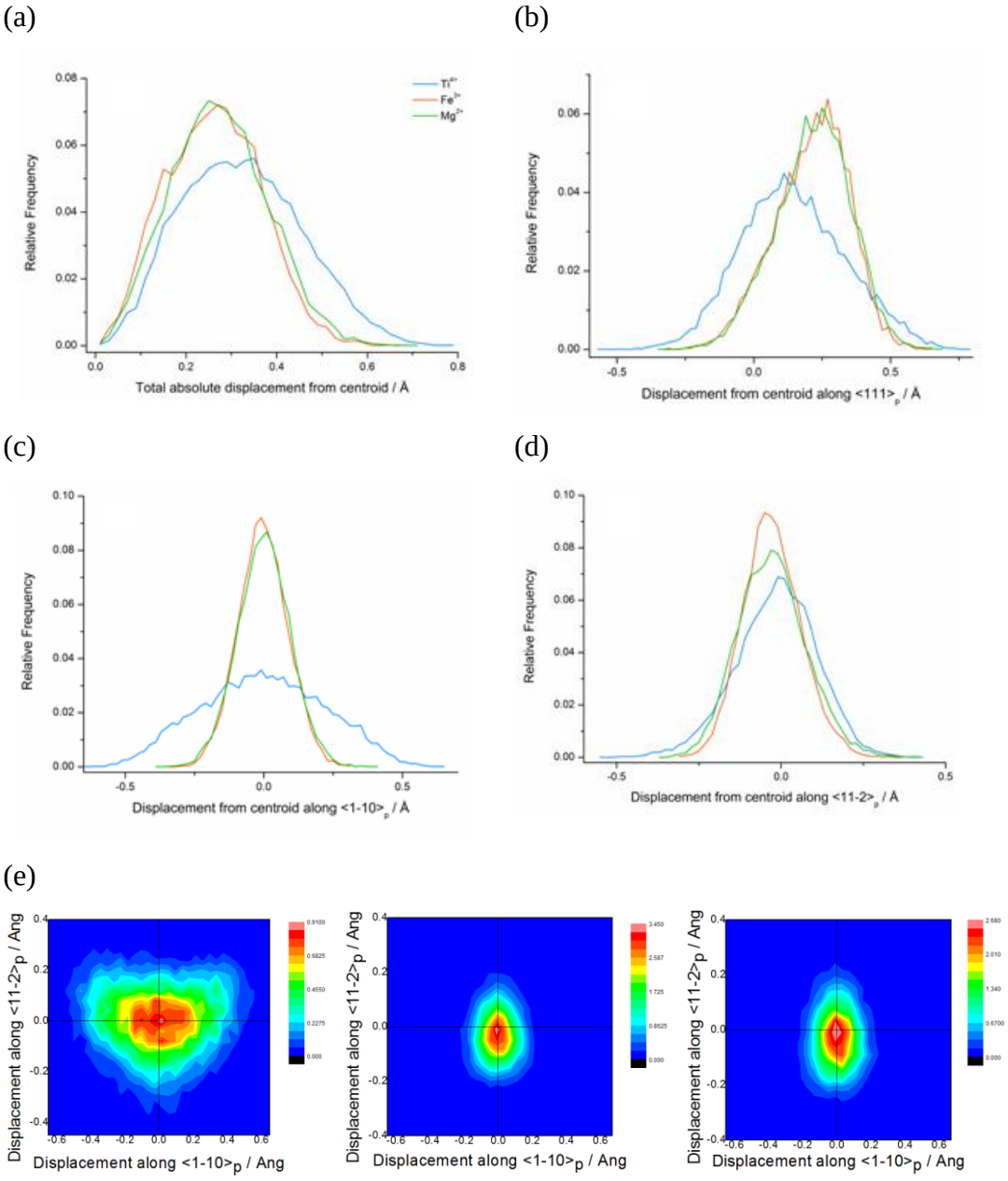

Figure 3.11. *Distribution of (a) total B site cation displacement; and displacements from the oxygen centroid along (b)* $\langle 111 \rangle_p$, *(c)* $\langle 1\bar{1}0 \rangle_p$, *and (d)* $\langle 11\bar{2} \rangle_p$. *(e) Density plots of Ti (left), Fe(center) and Mg(right) corresponding to a view down* $\langle 111 \rangle_p$ *of the off-axis B site cation displacements along* $\langle 11\bar{2} \rangle_p$ *and* $\langle 1\bar{1}0 \rangle_p$.

The local structure representations can be derived by using the most frequently occurring Bi displacement and B site cation displacements within the

crystallographically averaged oxygen coordinates. The A site representation of the structure (Figure 3.12 a-c) emphasizes the displacement of the two Bi positions corresponding to densely populated areas indicated in Figure 3.10ab. On the other hand, the distinct behavior of the B site cations (Figure 3.12 d), shows the similarity of the Fe and Mg displacements, mainly along $\langle 111 \rangle_p$, while the mode Ti position lies close to the centroid despite its broad distribution of displacements as presented on Figure 3.11.

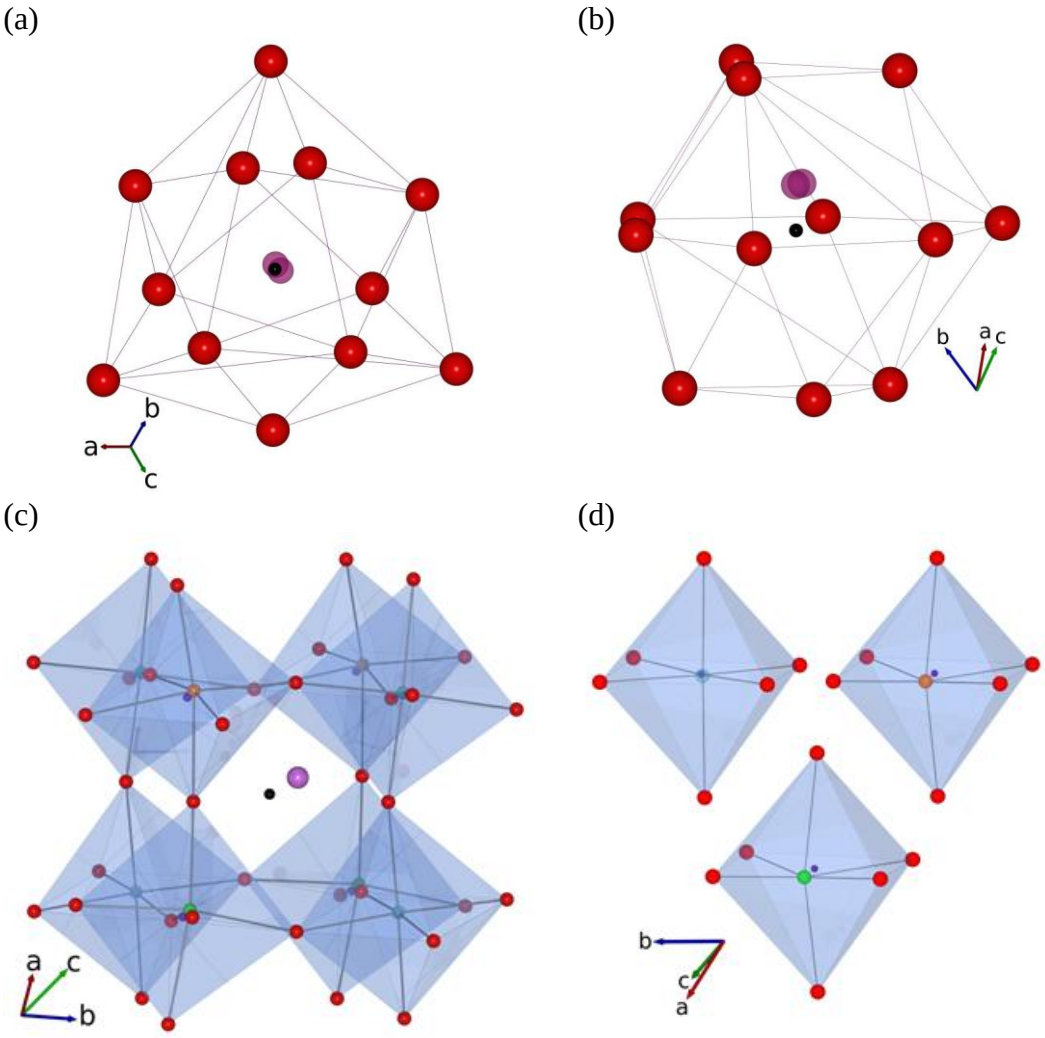

Figure 3.12. *(a) Local coordination environment of Bi viewed along* $[111]_p$ *and (b)* $[\bar{1}01]_p$*; (c) Representation of the local unit cell structure with the Bi (purple) position determined from mode value of displacements in the RMC configurations with a positive component along* $\langle 1\bar{1}0 \rangle_p$*, corresponding to dense regions on*

Figure 3.10b; (d) B site cation positions (Ti-blue, Fe- orange, Mg-green) calculated from their overall mode displacements from the coordinated oxygen centroid (shown in black for Bi and dark blue for B site).

3.2.4 Analysis of A and B site correlations

Correlations between the A and B site cation displacements are identified through evaluation of the displacement correlation function (DCF). The DCF was first applied by Andrew Goodwin to find ferroelectric nanodomains in cubic $SrSnO_3$, where correlations based on the displacements were derived from the average positions without taking into account oxygen atoms [16]. As the displacement of A and B site cations is better described by neighbouring oxygen atoms, thus it was essential to derive correlations based on the previous displacement results in the section 3.2.3. The DCF was calculated by Dr. Samantha Y. Chong to compute correlations between two species, according to equation:

$$\eta(r) = \frac{1}{Nr^2}\sum \boldsymbol{u_i} \cdot \boldsymbol{u_j} \qquad \text{Equation 3.2}$$

where the $\boldsymbol{u_i}$ and $\boldsymbol{u_j}$ vectors define displacement of atoms *i* and *j* respectively (Figure 3.13a).

(a)

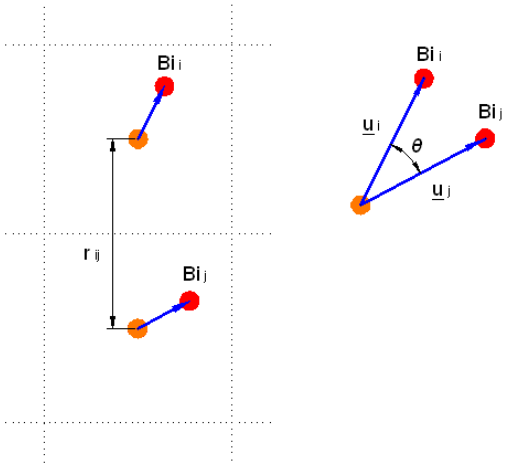

(b)

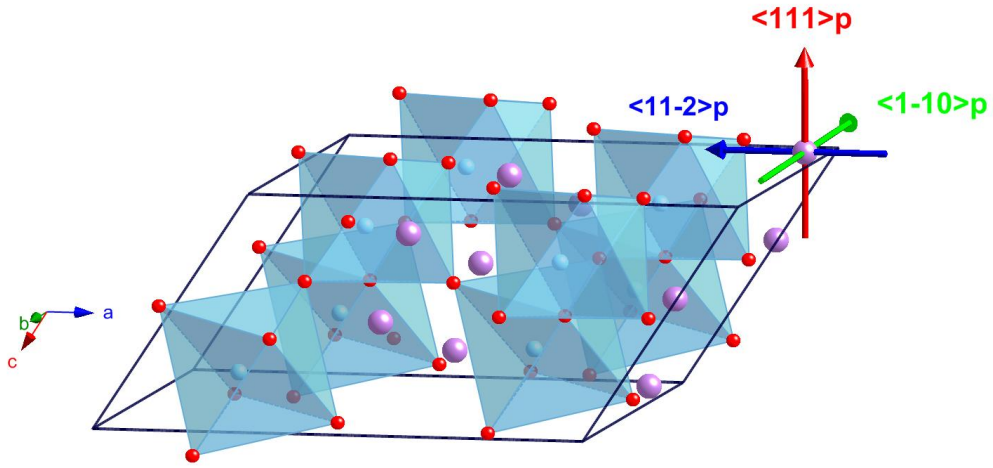

Figure 3.13. *(a) Schematic of displacement correlation function between two Bi cations; (b) The representation of monoclinic unit cell and orthogonalized directions: polar* $\langle 111 \rangle_p$ *and off-polar (summed components along* $\langle 1\bar{1}0 \rangle_p$ *and* $\langle 11\bar{2} \rangle_p$*) used to DCF calculations. The DCF's are also resolved to the 3 separate planes* $\{111\}$, $\{1\bar{1}0\}$ *and* $\{11\bar{2}\}$ *orthogonal to polar and off-polar directions.*

The DCF program written in Fortran computer language [17], compares the displacements between Bi atoms within the RMC supercell, and if atoms are displaced in the same direction it generates the positive dot product and gives their contribution to the function. To eliminate the inherent contribution coming

from the symmetry of the crystallographic average structure, the arrangement of atomic displacements is randomized. Randomized RMC configurations are created by statistically swapping displacements between the atoms. Thus, the difference between the initial RMC configuration and the final randomized configuration called differential DCF provide the real correlations beyond those arising from the average structure in the material. A positive value means that the displacements of Bi atoms separated by distance r are ferroelectrically correlated, while negative peaks indicate antiferroelectric correlations.

The DCFs of A and B sites were calculated and averaged for all 18 RMC models. The total displacement of the A and B site cations is dominated by the component along the polar direction $\langle 111 \rangle_p$, it is thus necessary to separate the DCF into the components along the Cartesian axes related to the perovskite subcell to investigate the correlation of more subtle features along $\langle 1\bar{1}0 \rangle_p$ and $\langle 11\bar{2} \rangle_p$ directions named here as off-polar axes displacements (Figure 3.13b). The DCF of Bi-Bi (Figure 3.14) are also resolved into three separate planes within the structure orthogonal to the directions $\langle 111 \rangle_p$ $\langle 1\bar{1}0 \rangle_p$ and $\langle 11\bar{2} \rangle_p$, to visualise the correlations between Bi atoms within these planes, while the calculations of Bi-B site and B site- B site are resolved by spherical DCF within a volume, with correlations derived only along Cartesian model directions. The DCF of Bi-Bi in both the RMC and disordered configuration show strong correlation of Bi^{3+} displacements along the polar axis (Figure 3.14a). Positive peaks are maintained in the differential $\eta_{Bi-Bi}(r)$ indicating that the correlation between Bi^{3+} displacements along the polar direction is stronger than would be predicted for the long-range averaged structure. This indicates that the ferroelectric Bi displacements are correlated to the extent that the magnitude of polar displacements influences those of surrounding Bi cations, i.e. similarly sized Bi displacements along $\langle 111 \rangle_p$ tend to cluster together. Peaks persist to at least r = 10–15 Å, indicating the large size of ferroelectric correlations.

The DCF calculated for components along $\langle 1\bar{1}0 \rangle_p$ and $\langle 11\bar{2} \rangle_p$ directions, defined here as an off-polar axes displacements (Figure 3.14b), show that the displacements normal to $\langle 111 \rangle_p$ are also correlated. The off-polar axes peaks are

one order of magnitude smaller than those along polar $\langle 111 \rangle_p$, due to the reduced displacement in these directions. Despite the smaller magnitude of Bi^{3+} correlations, the correlation size remains the same, extending to r = 10–15 Å, and suggesting that the correlation of the small off-polar axes displacements persist over a similar range to those of the larger polar displacements. This confirms that displacements orthogonal to the polar axis are correlated monoclinically on a local scale, i.e. the distribution of non-zero off-polar axes displacements is not statistically disordered over the sample, but correlated into local domains where monoclinic off-polar axes displacements. This is similar to those proposed (~0.2 Å) for the monoclinic phase (x = 0.48) of $PbZr_{1-x}Ti_xO3$ material [18, 19].

The domain size calculated from DCF analysis is consistent with the presence of two or more monoclinic domains within the RMC model of dimensions ~59 × 62 × 62 Å. The presence of multiple domains corresponds to the two peaks observed in the off-polar axes Bi density (Figure 3.10b). This locally monoclinic structure would not be apparent over the longer-range of a crystallographic refinement, as the observed nanodomain size would produce symmetry averaging to the rhombohedral phase. This also explains the origin of the observed anomalous microstrain broadening due to the locally monoclinic symmetry. The local symmetry at Bi does not have the threefold axis characteristic of rhombohedral symmetry.

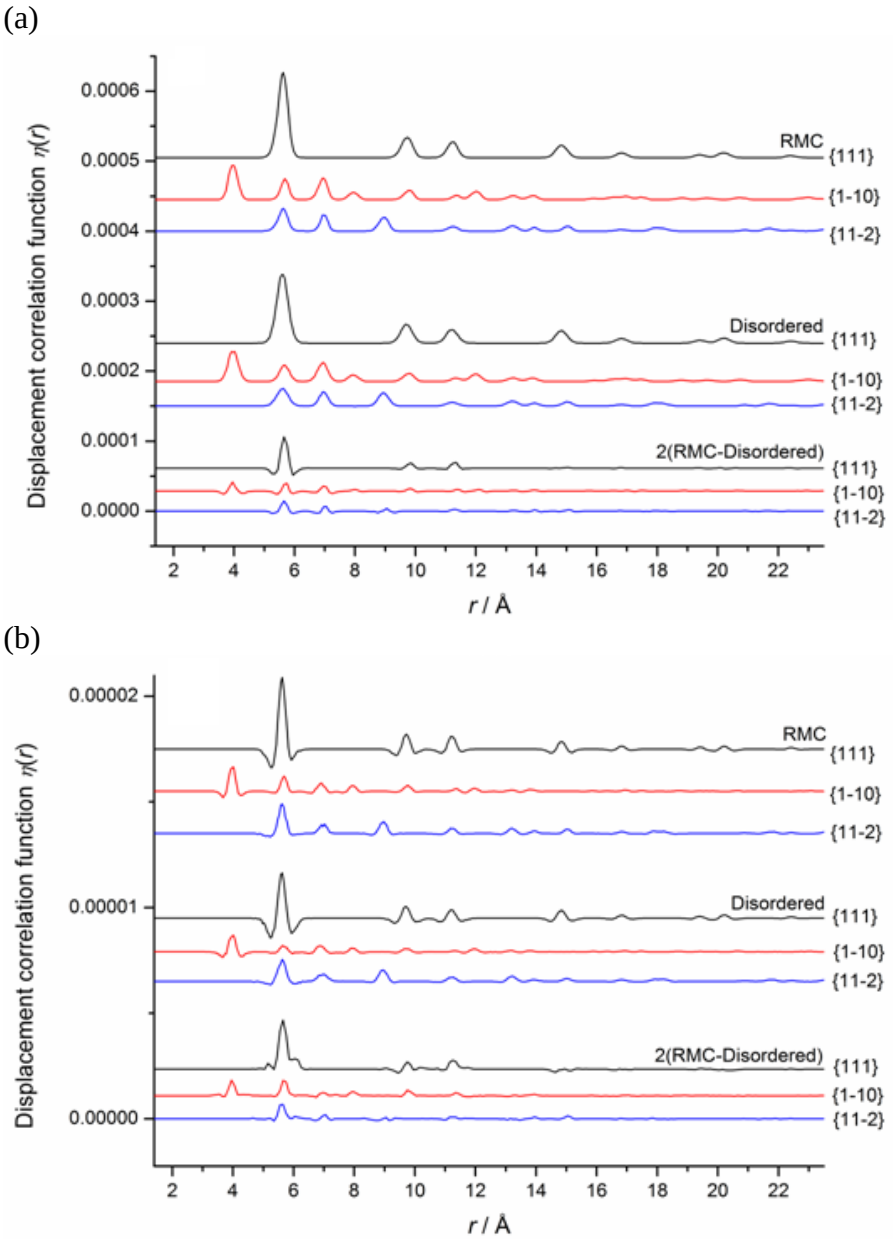

Figure 3.14. *Bi–Bi displacement correlation functions (DCFs) calculated for (a) displacements along the polar axis* $\langle 111 \rangle_p$ *and (b) off-polar axes displacements with summed components along* $\langle 1\bar{1}0 \rangle_p$ *and* $\langle 11\bar{2} \rangle_p$ *and visualized as correlations within the planes normal to those directions.*

The DCF within spherical volume were also calculated between Bi^{3+} and *B* site cations to examine whether the distinctive Ti^{4+} behaviour or Fe^{3+} and Mg^{2+} cations extends to correlation of its displacement with those of A site cations. DCFs were calculated for displacements both along polar $\langle 111 \rangle_p$ and off-polar

axes, and differential spherical DCF are presented here as a difference between the RMC configuration and the randomized configuration. Positive peaks for all Bi - B site correlations along $\langle 111 \rangle_p$ (Figure 3.15a) indicate that the displacements of all three Ti^{4+}, Fe^{3+} and Mg^{2+} cations are correlated with that of A site cations, but the correlations of $\eta_{Bi-Fe/Mg}(r)$ are noticed to have a longer length scale (~20 Å), than observed for $\eta_{Bi-Ti}(r)$ (10–15 Å). This is consistent with previous results, where Ti^{4+} have been displaced significantly along other directions, which reflects its ability to adopt a range of distorted structures in ferroelectric oxides. Furthermore, the distinctive feature of $\eta_{Bi-Ti}(r)$ in comparison to $\eta_{Bi-Fe}(r)$ and $\eta_{Bi-Mg}(r)$, is the shape of the first peak at $r \approx 3.3$ Å, which suggests that the displacement of Bi^{3+} and Ti^{4+} separated by shorter distances are anti-correlated, while those at the longer extreme of the peak are positively correlated. Considering the pattern of both positive and negative Ti displacements along $\langle 111 \rangle_p$ (Figure 3.11b), there is a significant frequency of antipolar displacements in the opposite sense to the majority along this direction within the RMC cell, and this suggests that those displacements occur when short Bi–Ti are in contact. On the other hand, the $\eta_{Bi-Ti}(r)$ along off-polar axes show no significant coupling of the Bi and B cation displacements (Figure 3.15b).

(a) (b)

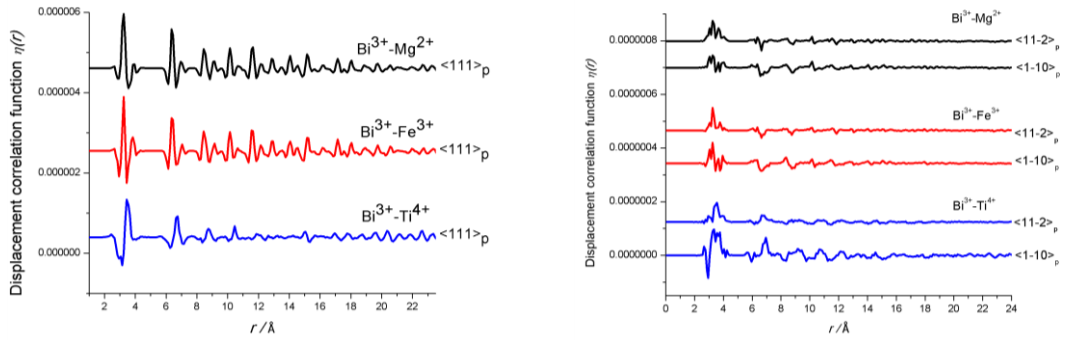

Figure 3.15. *Bi–B site differential spherical DCFs calculated for (a) displacements along the polar axis* $\langle 111 \rangle_p$ *and (b) off-polar axes displacements along* $\langle 1\bar{1}0 \rangle_p$ *and* $\langle 11\bar{2} \rangle_p$.

The different behavior of Ti^{4+} displacements are also observed in the DCFs of B site- B site homopairs (Figure 3.16a, b). While the DCF results show the displacements correlated along $\langle 111 \rangle_p$ for all B site cations, the peaks in $\eta_{Ti-Ti}(r)$

are broader and extend over a shorter distance ~10 Å (Figure 3.16a). The DCFs of heteropairs (Ti−Fe, Ti−Mg, Fe−Mg) along $\langle 111 \rangle_p$, show the correlations in the $\eta_{Fe-Mg}(r)$ along the polar axis (Figure 4.16a), with a similar strength to the observed homopairs $\eta_{Fe-Fe}(r)$ and $\eta_{Mg-Mg}(r)$, as both Fe^{3+} and Mg^{2+} cations have almost identical displacements (Figure 3.11). In contrast, the $\eta_{Ti-Fe/Mg}(r)$ along $\langle 111 \rangle_p$ and off-polar axes (Figure 3.17a, b) are not correlated, which is consistent with frequent off-polar axes Ti^{4+} displacements. The Ti^{4+} cations prefer to be correlated only to other titanium atoms, for example along $\langle 1\bar{1}0 \rangle_p$ direction (Figure 3.16b). On the other hand, the $\eta_{Ti-Fe/Mg}(r)$ shows small negative peaks demonstrating anticorrelation between these atoms with the influence also extending to r = 10−15 Å (Figure 3.17b). In contrast, the $\eta_{Fe/Mg-Fe/Mg}(r)$ along off-polar axes show no correlation between those cation displacements. The different Ti^{4+} cation behavior in comparison to Fe^{3+} and Mg^{2+} cations, can be attributed to the availability of low-energy d states of the d^0 cation and its small size, enabling second-order Jahn−Teller distortion [20]. The highly charged Ti^{4+} cations due to their small size have enough low energy of the d orbital to be able to mix with filled p orbitasals of the oxygen ligands and allowing this type of distortions.

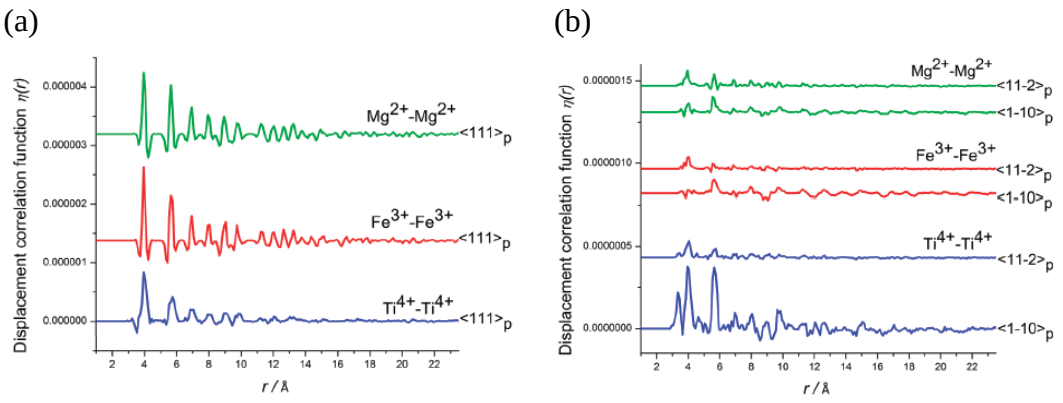

Figure 3.16. *B site–B site (homopairs) differential spherical displacement correlation functions (DCFs) calculated for (a) displacements along the polar axis* $\langle 111 \rangle_p$ *and (b) off-polar axes displacements along* $\langle 1\bar{1}0 \rangle_p$ *and* $\langle 11\bar{2} \rangle_p$.

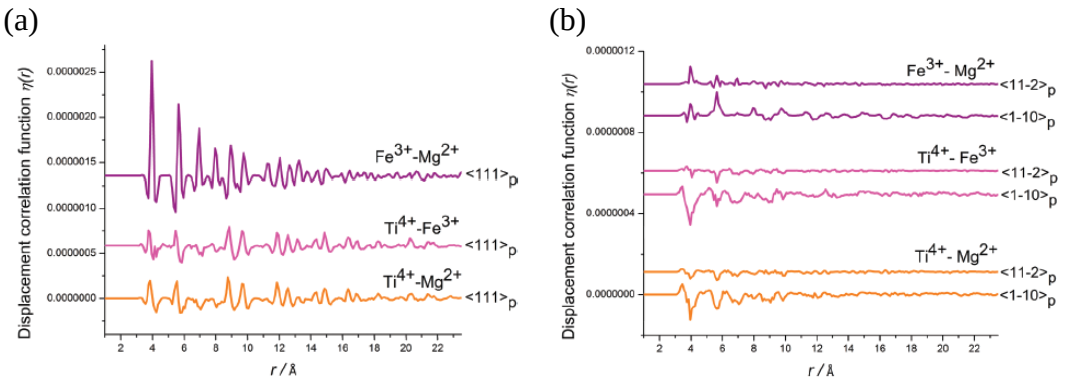

Figure 3.17. *B site–B site (heteropairs) differential spherical displacement correlation functions (DCFs) calculated for (a) displacements along the polar axis* $\langle 111 \rangle_p$ *and (b) off-polar axes displacements along* $\langle 1\bar{1}0 \rangle_p$ *and* $\langle 11\bar{2} \rangle_p$.

3.2.5 B site cation ordering

The B site ordering was calculated directly from partial pair distribution function $g_{B\text{-}B}(r)$ (Figure 3.7), where the average numbers of neighbours $n(r)$ for Ti^{4+}, Fe^{3+} and Mg^{2+} cations have been extracted as described in the section 2.3.1. RMC models with the simulated distribution were compared with the completely disordered distribution, which was obtained by swapping B site cations during RMC modeling in absence of the data. The derived nearest neighbour functions $n_{B\text{-}B}(r)$ show no significant difference in neighbour frequencies to those expected for a completely disordered distribution, indicating that B site ordering is not observed (Table 3.6). Furthermore, the RMC refinements which allowed exchange of the B site cations, showed no significant improvement in the fits to the Bragg profile, pair correlation function $T(r)$ and total scattering structure factor $F(Q)$, which confirm random distribution of the B site cations within the sensitivity of the fitted data. The disordered distribution is also consistent with the disordered B site occupancy of the average structure Rietveld model.

Table 3.6. *B site nearest neighbours for the local structure at RT of* $BiTi_{3/8}Fe_{1/4}Mg_{3/8}O_3$ *. Comparison is given between the refined RMC model with standard errors and a fully disordered B site distribution.*

	n(r) of 1st shell - 6 neighbours		*n(r)* of 2nd shell - 12 neighbours	
	Local structure	Disordered	Local structure	Disordered
Ti-Ti	2.24(1)	2.25	4.49(2)	4.50
Ti-Fe	1.51(1)	1.5	3.04(2)	3.0
Ti-Mg	2.27(1)	2.25	4.49(2)	4.50
Fe-Fe	1.47(1)	1.5	3.00(0)	3.0
Mg-Fe	1.52(0)	1.5	2.98(1)	3.0
Mg-Mg	2.22(0)	2.25	4.57(0)	4.50

3.2.6 Conclusions

The application of time-of-flight neutron total scattering data and RMC modeling at RT revealed local deviations from the crystal average structure, which have been extracted to account for the discrepancies in the refined crystal structure. The analysis of pair distribution function in real space showed similarities between the local and average structures, where mean bond distances, bond angles and displacements are generally in close agreement with those derived from the crystal structure. However, the analysis of the A site cation displacements orthogonal to the bulk polar $\langle 111 \rangle_p$ axis revealed local monoclinic fluctuations within the RMC model, requiring correlation between the cation displacements distinct from the simple correlation of ferroelectric displacements along the $\langle 111 \rangle_p$ direction. These displacement correlations along off-polar axes with positive peaks in the $\eta_{Bi\text{-}Bi}(r)$ occur in a locally coupled way that locally breaks the threefold axis and lowers the symmetry to monoclinic, as the *Cc* cell gives an equivalent fit to the disordered rhombohedral cell in the original structure analysis. The length scale of these correlations indicates a monoclinic domain size of up to 15 Å, and the presence of these monoclinic clusters accounts for the anomalous microstrain broadening required for Rietveld refinement of the rhombohedral model. The $\eta_{Bi-Bi}(r)$ also suggests that Bi displacements along the

$\langle 111 \rangle_p$ polar axis are correlated in both direction and magnitude up to a distance of 15 Å, resulting in a tendency of similarly sized displacements to cluster.

The B site analysis of the RMC model produces a local environment surrounding Ti that contrasts with those around Fe and Mg, resulting in more chemically sensible environments for each cation than in the average structure. While Fe and Mg atoms show little variation from the octahedral coordination described by the Rietveld model, Ti demonstrates extensive flexibility in its coordination geometry, consistently resulting in broader pair distribution functions and displacements. The Ti disorder may be overestimated as a result of Ti as a negative scatterer and interference between negative Ti−B site and positive B site−B site correlations in pair distribution functions, however the good BVS and Rietveld agreement gives confidence in the deduced distributions. In particular, the Ti BVS in the RMC model corresponds more closely to crystal chemical expectations than in the average structure, where the assumption that all three B site cations occupy the same site gives bond lengths that do not suit any of them. The correlations of Ti^{4+} cations displacements were found to differ from those of the other B site cations, with the coupling of polar displacements to Bi^{3+} cations extending over a shorter-range and the correlation of off-polar axes displacements to those of other B cations, with particularly pronounced ferroelectric Ti−Ti correlations along $\langle 1\bar{1}0 \rangle_p$. Both Ti and Bi atoms are displaced from $\langle 111 \rangle_p$ in a locally individually correlated manner, but the off-polar axes Ti and Bi displacements do not appear to be significantly correlated to each other. The Fe^{3+} and Mg^{2+} cation displacements along $\langle 111 \rangle_p$ are similarly correlated to those of Bi, whereas B site Ti behaves differently.

3.3 Crystallographic average structure of BTFM at low temperature (10K)

The perovskite material BTFM does not undergo a structural transition between 10-300K. Thus, the average crystallographic structure of BTFM at low temperature (LT) has the same crystallographic symmetry as at RT. The Rietveld refinement of BTFM at LT was performed in GSAS based on the monoclinic *Cc*

space group, where obtained very good fit of the highest resolution backscattering bank at GEM diffractometer to the neutron diffraction data confirmed the correct choice of the low symmetry monoclinic space group (Figure 3.18). The comparison of monoclinic unit cells between LT and RT revealed significant differences in terms of ADPs (anisotropic displacement parameters) (Table 3.7). The atomic displacements at LT show low atomic vibrations within the crystal lattice of the all atoms in the unit cell (Figure 3.19a), demonstrating almost spherical shape of atoms, which indicate about the low degree of disorder in the structure. In contrast, the atom displacement at RT demonstrate more diffused elongated shape with a higher degree of disorder, where oxygens atoms displacement are elongated in directions orthogonal to the B−O bonds (Figure 3.19b). The less displaced atoms observed at LT in comparison to RT is expected, as there is a significant reduction in thermal motion at 10K compared to 300K (RT).

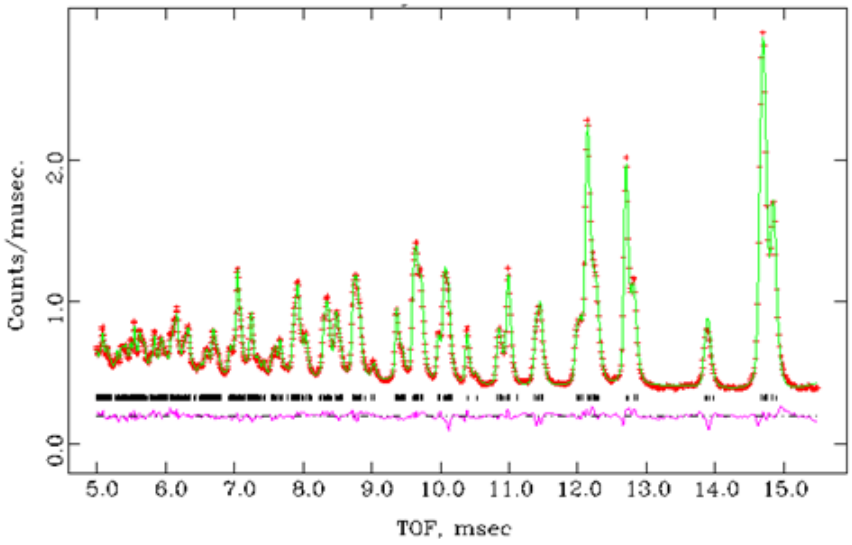

Figure 3.18. *Rietveld refinement of BTFM (backscattering bank) at 10K with space group Cc, lattice parameters a = 9.8100(4) Å b = 5.6057(3) Å, c = 5.6645(3) Å, α=90, β=125.9805, γ=90, and weighted agreement factor R_{wp}=2.58%. The red crosses are observed data, the solid green line is the calculated pattern, whereas the pink line represent the difference between observed and calculated patterns.*

Table 3.7. *Comparison of ADPs values in the LT and RT data.*

ADPs		Bi	(Ti, Fe, Mg)	O1	O2	O3
U_{11}	LT	0.0047(15)	-0.0069(22)	0.0039(18)	0.0016(18)	0.0111(20)
	RT	0.0131(45)	0.0033(14)	0.0116(67)	0.0045(21)	0.0200(72)
U_{22}	LT	-0.0037(17)	0.001(4)	0.0075(4)	-0.0047(34)	0.0040(4)
	RT	0.0120(39)	0.0030(17)	0.0324(82)	0.0135(51)	0.0141(39)
U_{33}	LT	0.0043(20)	-0.0059(4)	-0.0055(21)	0.0052(34)	0.0169(30)
	RT	0.0234(85)	-0.0032(16)	0.0046(11)	0.0180(41)	0.0198(39)
U_{23}	LT	0.0074(26)	0.006(7)	0.010(25)	0.0130(34)	0.008(4)
	RT	-0.0069(16)	0.0030(12)	-0.0003(2)	-0.0018(6)	0.0135(37)
U_{13}	LT	-0.0040(13)	0.001(21)	0.0012(17)	-0.0042(24)	0.005(22)
	RT	0.0125(38)	-0.0002(1)	0.0065(12)	-0.0030(8)	0.0188(41)
U_{12}	LT	0.0101(19)	-0.006(4)	-0.0015(26)	0.0125(26)	0.0260(31)
	RT	-0.0040(9)	0.0059(11)	-0.0058(23)	-0.0039(16)	0.0101(35)

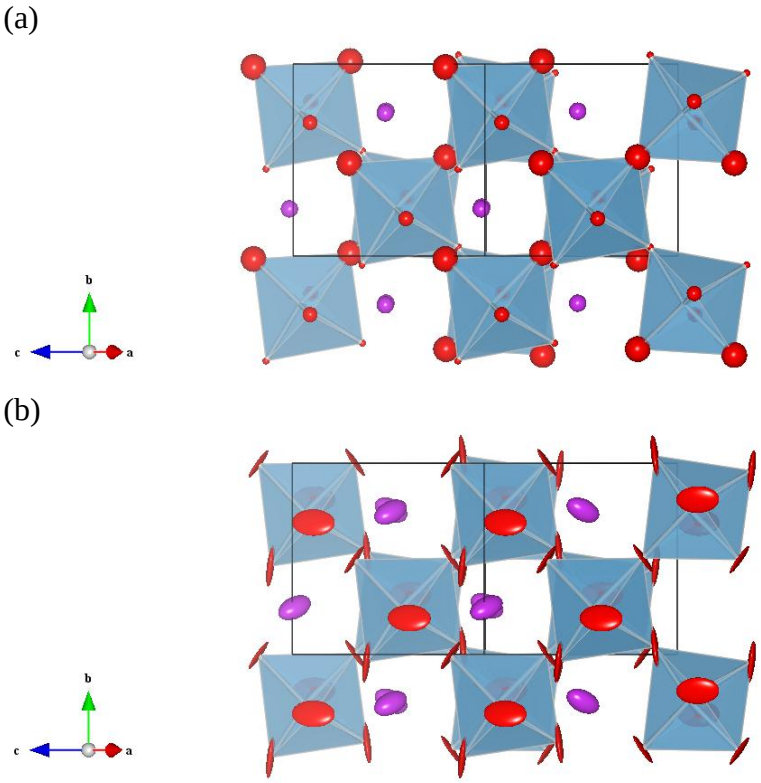

Figure 3.19. *Monoclinic Cc Rietveld model viewed along* [101] *with Bi and O atomic displacement parameter (ADP) ellipsoids for: (a) LT and (b) RT showing differences between the shapes of the ADPs.*

3.4 Local structure at LT

3.4.1 Generation of RMC model

Neutron total scattering data at LT were collected at GEM diffractometer for 1320 μAh over the same data range as the RT $0.3 \leq Q \leq 50$ Å^{-1}. The same procedure using GUDRUN software was applied to correction and normalization of the data, and then the experimental *F(Q)* was extracted and transformed to the total correlation function *T(r)* using the *stog* utility in RMCProfile within the same Q_{max} = 30 Å^{-1}. The total scattering data were also convoluted with a box function to account for the broadening in the calculated data due to the finite RMC configuration size and fits were carried out for $Q < 30$ Å^{-1}. The Rietveld refinement within the monoclinic *Cc* model (Figure 3.18) described in the section 3.3 was applied to build an initial RMC model.

The starting configuration were obtained by using the multiplicity of lattice parameters of the monoclinic subcell *Cc* 6*a* × 11*b* × 11*c*, producing a RMC supercell with dimension of approximately 59 × 62 × 62 Å along each direction and consisting of 14,520 atoms (Figure 3.20).

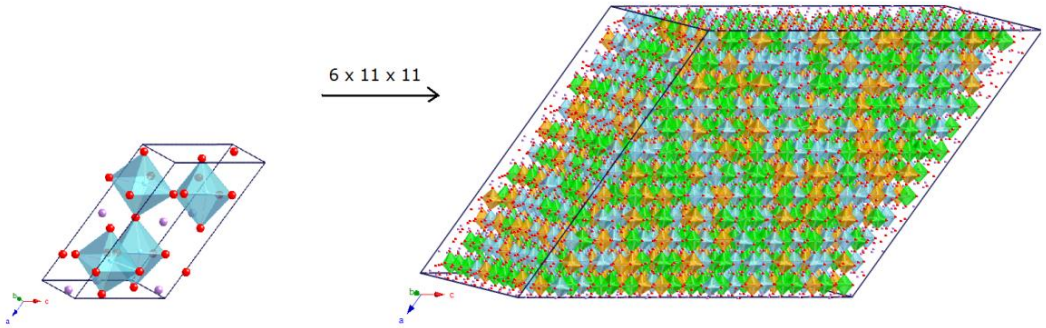

Figure 3.20. *Subcell of monoclinic structure Cc and their supercell obtained by using a multiplicity of their 6 × 11 × 11 subcells. The atom spheres are denoted by colours: Bi (purple), Ti (blue), Fe (orange), Mg (green) and O (red).*

18 RMC refinements were performed with RMCProfile (the same number as performed for the RT data), where the real-space data total correlation function *T(r)* were fit over the range of the RMC configuration with r < 23.5 Å, which represent the shortest lattice vector. The BVS constraints were applied in the RMC refinements for each cation-oxygen pair, which improved the cut-off features of partial PDF's and helped to distinguish between the Ti^{4+}, Fe^{3+} and Mg^{2+} cations which occupy the same crystallographic B site. Furthermore, the identical maximum translation limits have been applied for RMC models at LT as for RT, with 0.05 Å for all of the A site and B site cations and 0.1 Å for the oxygen atoms.

The RMC refinement with BVS constraints applied, allowed swapping of B site cations. The refinement was continued until no further improvement in χ^2 of Bragg profile data, the total scattering structure factor *F(Q)* and the pair correlation function *T(r)* was observed and the final 3-dimensional configuration was consistent with the experimental data (Figure 3.21).

Then the RMC models were orthogonalized to a Cartesian frame with the *x* axis parallel to $\langle 111 \rangle_p$, *y* along $\langle 1\bar{1}0 \rangle_p$, and *z* along $\langle 11\bar{2} \rangle_p$, and all further analysis of

the local structure displacements and correlations was based on these orthogonal models to be able to compare the local structures at LT and RT.

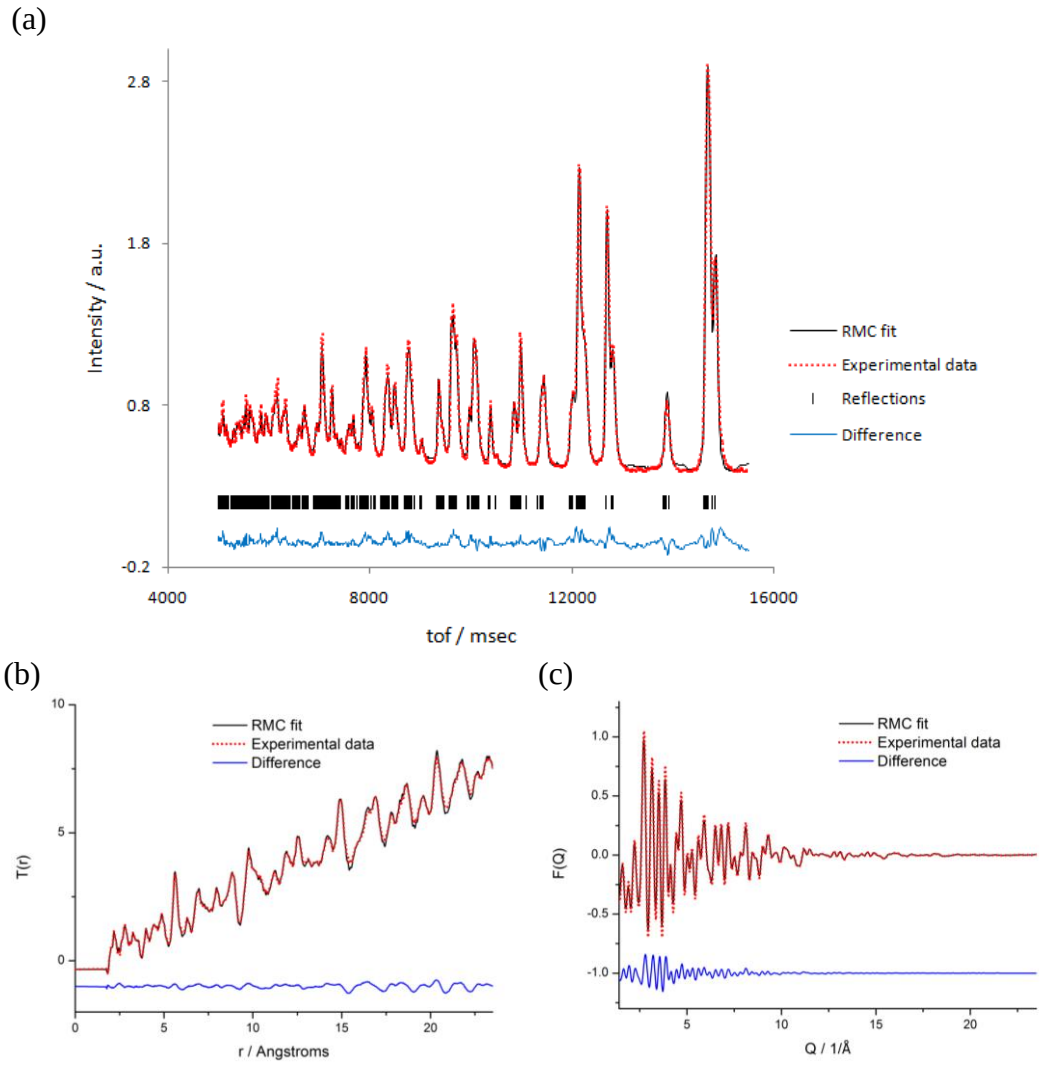

Figure 3.21. *Comparison between measured and modeled functions of one of the RMC model for the local structure of* $BiTi_{3/8}Fe_{1/4}Mg_{3/8}O_3$ *at LT: (a) Bragg profile data; (b) total correlation function T(r); (c) total scattering structure factor F(Q).*

3.4.2 Analysis and comparison of pair distribution function between LT and RT data

The comparison of pair distribution function of local structures at LT and RT are performed on the averaged results from 18 RMC models, to improve the statistical

accuracy, and bond distances are obtained by fitting Gaussian functions to the observed partial pair distributions functions. The initial comparison of the pair distribution functions *G(r)* containing all atomic pairs, revealed a difference between the two temperature data sets, with sharper peaks observed for LT data along the whole range of distance *r* (Figure 3.22a). The comparison of A site environment confirmed this trend of sharper peaks for LT data especially for first oxygen neighbours in $g_{Bi\text{-}O}(r)$ (Figure 3.22b), where four groups of Bi-O bond distances exist, instead of three observed at RT (Table 3.8). The range of Bi-O at both LT and RT remain the same, but the shape of the peaks and calculated area under the peaks indicate that the peaks are getting split into two groups (2.371(29) Å and 2.621(20) Å) in contrast to single peak (2.543(8) Å) at RT data. Furthermore, the wider separation Bi^{3+} cations are observable in the $g_{Bi\text{-}Bi}(r)$ resulting in sharper peaks in the LT data (Figure 3.22c), where atomic thermal motion is reduced to a minimum.

Table 3.8. *Comparison of Bi-O bond distances derived from the RMC model at LT and RT data. Distances for RMC configuration were obtained by fitting Gaussian functions to the observed partial pair distributions functions (Figure 3.22b).*

	Local structure LT / Å	Local structure RT / Å
Bi-O	2.214(9) 2.371(29) 2.621(20) 3.307(3) (2.5:3:2.3:4.2)*	2.237(1) 2.543(8) 3.303(3) (3.2:4.4.6)*

*Approximate ratio of separations (summed to 12 oxygen coordinate system) obtained from the integrated areas of peaks in $g_{Bi-O}(r)$.

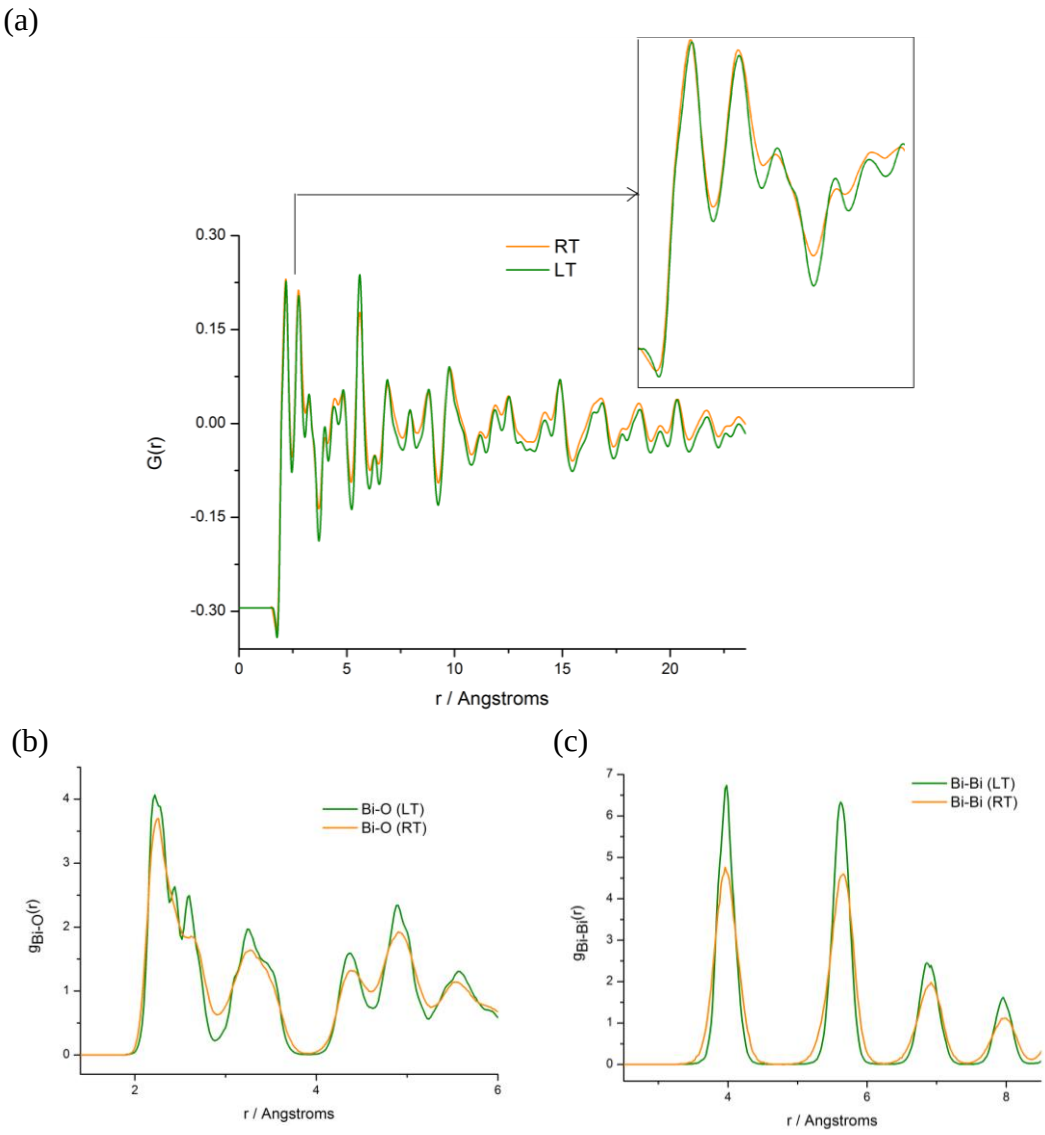

Figure 3.22. *Comparison between RT and LT data for: (a) pair distribution function G(r); (b) $g_{Bi-O}(r)$ and (c) $g_{Bi-Bi}(r)$.*

Comparison of the $g_{B-O}(r)$ distributions also reveals differences between B site cations (Table 3.9 and Figure 3.23). The $g_{Ti-O}(r)$ for both LT and RT data demonstrate comparable shape of peaks, with sharp peaks centered at 1.818(2) Å at RT and 1.838(1) Å at LT. (Figure 3.23a). Despite these similarities, the $g_{Ti-O}(r)$ at LT demonstrate a narrower distribution and a feature observed at a lower 2.010 Å in contrast to 2.105(10) Å at RT. This suggests that the flexibility of adopting wide range of bond distances by Ti^{4+} cations at RT is partially caused by temperature differences. On the other hand, the partial $g_{Fe-O}(r)$ and $g_{Mg-O}(r)$ are

very consistent with more regular environments at RT, and show single peaks centered at 2.023(1) Å and 2.061(1) Å, respectively.

Table 3.9. *Comparison of B site-O bond distances derived from the RMC model at LT and RT data. Distances for RMC configuration were obtained by fitting Gaussian functions to the observed partial pair distributions functions (Figure 3.23).*

	Local structure LT / Å			Local structure RT / Å		
B site – O	Ti - O	Fe – O	Mg-O	Ti - O	Fe – O	Mg-O
	1.838(1) 2.010(5)	2.023(1)	2.061(1)	1.818(2) 2.105(10)	2.021(2)	2.060(1)

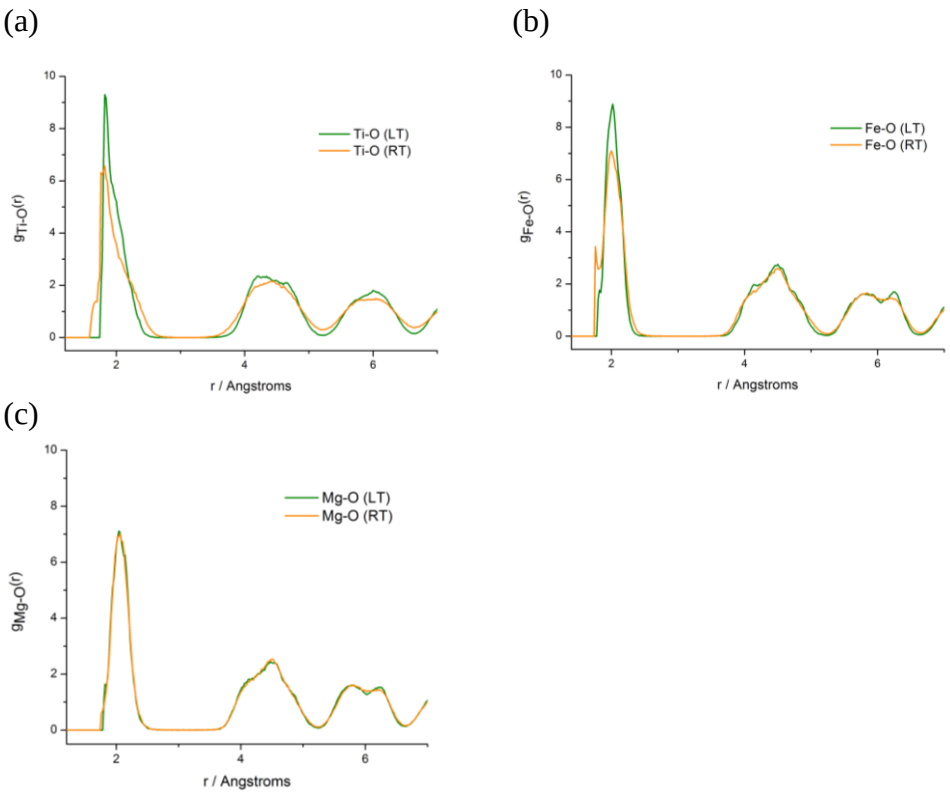

Figure 3.23. *Comparison of B site-O partial pair distribution functions between RT and LT data for: (a) $g_{Ti\text{-}O}(r)$; (b) $g_{Fe\text{-}O}(r)$ and (c) $g_{Mg\text{-}O}(r)$.*

The comparison of the external angles of B-O-B between homopairs (e.g. Ti-O-Ti) and heteropairs (e.g. Ti-O-Fe) show comparable results for all B site cations at

LT and RT, except the bond angles containing Ti^{4+} cations, which demonstrate a broader distribution (Figure 3.24a). The internal octahedral O-B-O angles reveal comparable tilting of Fe^{3+} and Mg^{2+} octahedra for both LT and RT data sets, indicating their temperature independence (Figure 3.24b). On the other hand, the broader distribution of Ti^{4+} demonstrate that the more distorted behavior at RT is slightly reduced at LT as temperature is decreased.

(a) (b)

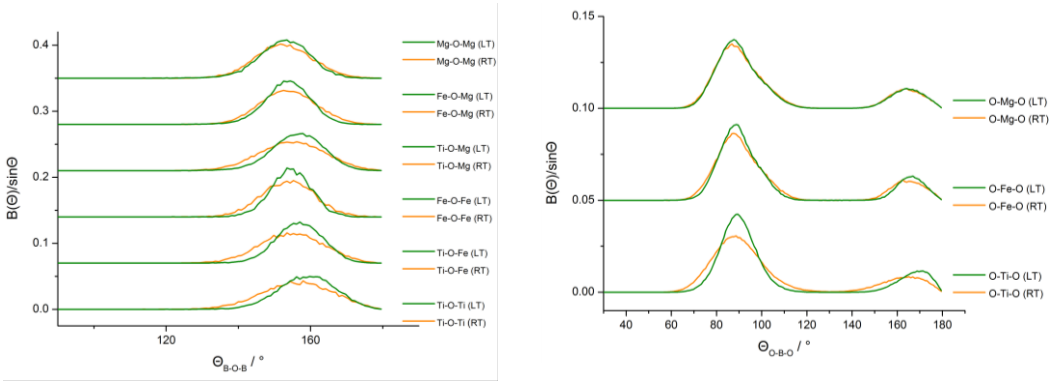

Figure 3.24. *Comparison of bond angle distributions between RT and LT data for: (a) B-O-B and (b) O-B-O.*

The analysis of B site – B site cation pair correlation functions at LT (Figure 3.25a, b) show the same trend with those derived for RT, where homopairs $g_{Ti\text{-}Ti}(r)$ and heteropairs $g_{Ti\text{-}Fe}(r)$, $g_{Ti\text{-}Mg}(r)$ demonstrate broader variation in the separation, than between combinations of homopairs $g_{Fe\text{-}Fe}(r)$, $g_{Mg\text{-}Mg}(r)$. In addition to that, the peaks of $g_{Ti\text{-}Ti}(r)$ and $g_{Fe\text{-}Fe}(r)$ at LT have a narrower distribution of bond distances than those at RT, due to the effect of reduced atomic thermal motion.

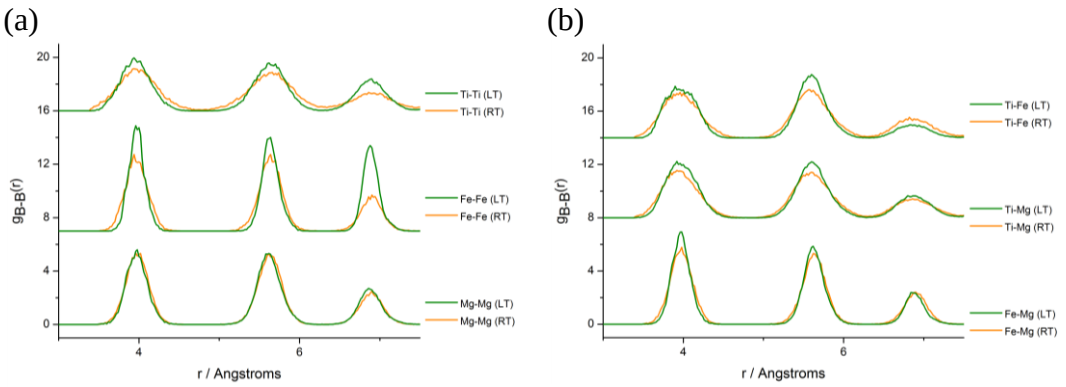

Figure 3.25. *Comparison of B site-B site partial pair distribution functions between LT and RT data for: (a) homopairs and (b) heteropairs.*

The partial pair correlation functions $g_{Bi-B}(r)$ (Figure 3.26) again show a comparable trend of bond distance distributions for all B site cations between LT and RT data sets, with $g_{Bi-Ti}(r)$ being more spread out than $g_{Bi-Fe}(r)$ and $g_{Bi-Mg}(r)$. The various displacements of all peaks at RT are demonstrated by single peaks of symmetric $g_{Bi-Ti}(r)$ (Figure 3.26a) and asymmetric $g_{Bi-Fe}(r)$ and $g_{Bi-Mg}(r)$ (Figure 3.26b, c), while the noticeable peak splitting features are observed at LT, demonstrating more regular separation in the $g_{Bi-Fe}(r)$ and $g_{Bi-Mg}(r)$. The $g_{Bi-Ti}(r)$ display only minor splitting of peaks, confirming that Ti^{4+} cations are more active, demonstrating larger displacements than Fe^{3+} and Mg^{2+} cations on the B site.

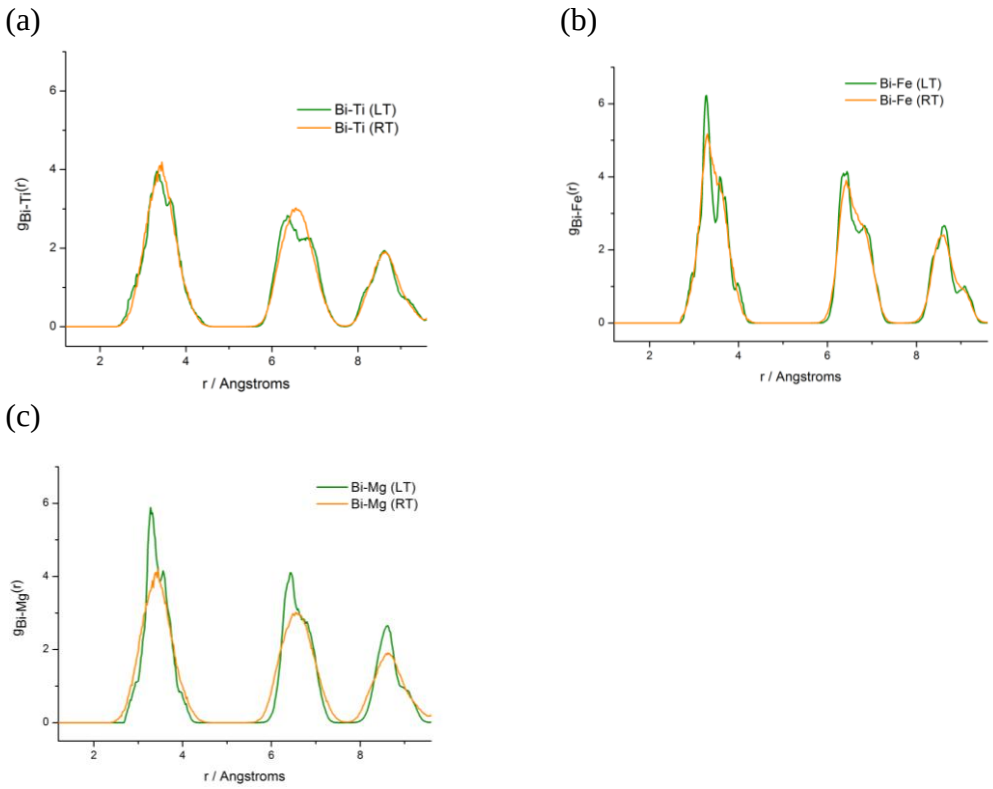

Figure 3.26. *Comparison of partial pair distribution functions between RT and LT data for: (a) $g_{Bi\text{-}Ti}(r)$, (b) $g_{Bi\text{-}Fe}(r)$ and (c) $g_{Bi\text{-}Mg}(r)$.*

3.4.3 Analysis and comparison of A and B site displacements between LT and RT data

Calculations of the displacements of Bi cations and B site cations are performed on the all 18 RMC models and calculated from the centroids of their twelve and six coordinating oxides respectively, along Cartesian model directions $\langle 111 \rangle_p$, $\langle 1\bar{1}0 \rangle_p$, and $\langle 11\bar{2} \rangle_p$. The displacement results of the A site cations at LT and RT data along polar $\langle 111 \rangle_p$ are demonstrate displacement in the same direction with the magnitude of displacements of 0.643(1) Å and 0.623(1) Å respectively, confirming that both RMC models at LT and RT preserve the ferroelectricity (Figure 3.27a). However, the comparison of Bi^{3+} displacements between RT and LT data revealed that that the distribution was slightly narrower for the latter model along the polar direction, whereas the displacements differences are more pronounced along directions orthogonal to it, confirming the reduced thermal

motion of Bi^{3+} cations at LT (Figure 3.27b, c). Furthermore, the Bi^{3+} displacements along $\langle 1\bar{1}0\rangle_p$ and $\langle 11\bar{2}\rangle_p$ at LT still possess broader distribution than along $\langle 111\rangle_p$ and averaged approximately to zero, which is consistent with observed bimodal Bi^{3+} displacements along $\langle 1\bar{1}0\rangle_p$ and $\langle 11\bar{2}\rangle_p$ at RT data.

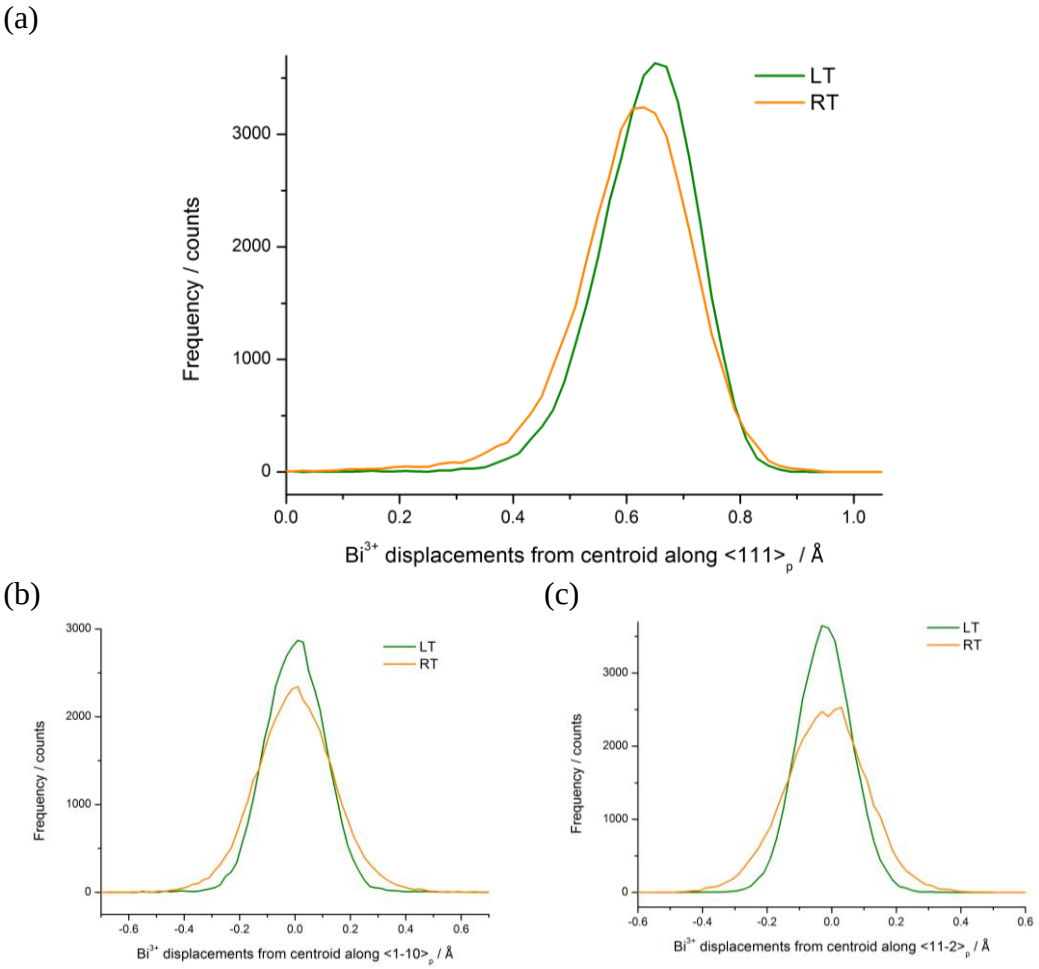

Figure 3.27. *Distribution of Bi displacement along Cartesian model directions (a)* $\langle 111\rangle_p$*; (b)* $\langle 1\bar{1}0\rangle_p$*; and (c)* $\langle 11\bar{2}\rangle_p$.

Calculations of the displacement of B site cations along the three Cartesian model directions show a comparable distribution of Fe^{3+} and Mg^{2+} cations along $\langle 111\rangle_p$, $\langle 1\bar{1}0\rangle_p$ and $\langle 11\bar{2}\rangle_p$ directions (Table 3.10 and Figure 3.28), demonstrating Fe^{3+} and Mg^{2+} temperature independence. Both cations show the majority of the mean displacements along polar $\langle 111\rangle_p$ with values 0.204(1) Å and 0.231(2) Å at LT and 0.239(5) Å and 0.242(7) Å at RT, whereas displacements along $\langle 1\bar{1}0\rangle_p$ and

$\langle 11\bar{2}\rangle_p$ are averaged approximately to zero (e.g. 0.001(1) Å for Fe^{3+} along $\langle 1\bar{1}0\rangle_p$). Thus, the displacements of Fe^{3+} and Mg^{2+} cations at both temperatures are consistent with those results of partial pair distribution function, where distribution of $g_{Fe\text{-}O}(r)$and $g_{Mg\text{-}O}(r)$, did not show broad variation of bond distances at two different temperatures. The broad range of displacements of Ti^{4+} cations is more significant at RT, which is also in agreement with the difference observed in $g_{Ti\text{-}O}(r)$. However, the broad symmetrical distribution of Ti^{4+} along $\langle 1\bar{1}0\rangle_p$, with both positive and negative displacements is still observed at LT (FWHM=0.380(3) Å), and is significantly broader than that of Fe^{3+} and Mg^{2+} cations (0.136(1) Å and 0.215(1) Å respectively). This distribution incorporating a wide range of displacements is consistent with the results obtained at RT and for $BaTiO_3$ [8].

Table 3.10. *The comparison of the octahedral B site displacements d from the centroid of coordinated oxygen atoms obtained from distributions (Figure 3.28) with full width at half maximum (FWHM) of the fitted peak.*

		$<111>_p$		$<1\bar{1}0>_p$		$<11\bar{2}>_p$	
		d / Å	FWHM / Å	d / Å	FWHM / Å	d / Å	FWHM / Å
LT	Ti^{4+}	0.072(1)	0.412(4)	-0.004(1)	0.380(3)	-0.007(1)	0.244(2)
	Fe^{3+}	0.204(1)	0.264(3)	0.001(1)	0.136(1)	-0.044(1)	0.148(1)
	Mg^{2+}	0.231(2)	0.368(5)	-0.002(1)	0.215(1)	-0.056(1)	0.189(2)
RT	Ti^{4+}	0.131(3)	0.456(9)	-0.003(3)	0.62(1)	-0.007(1)	0.279(4)
	Fe^{3+}	0.239(5)	0.317(3)	-0.004(1)	0.209(3)	-0.033(1)	0.203(3)
	Mg^{2+}	0.242(7)	0.315(3)	0.0009(6)	0.219(2)	-0.033(1)	0.239(4)

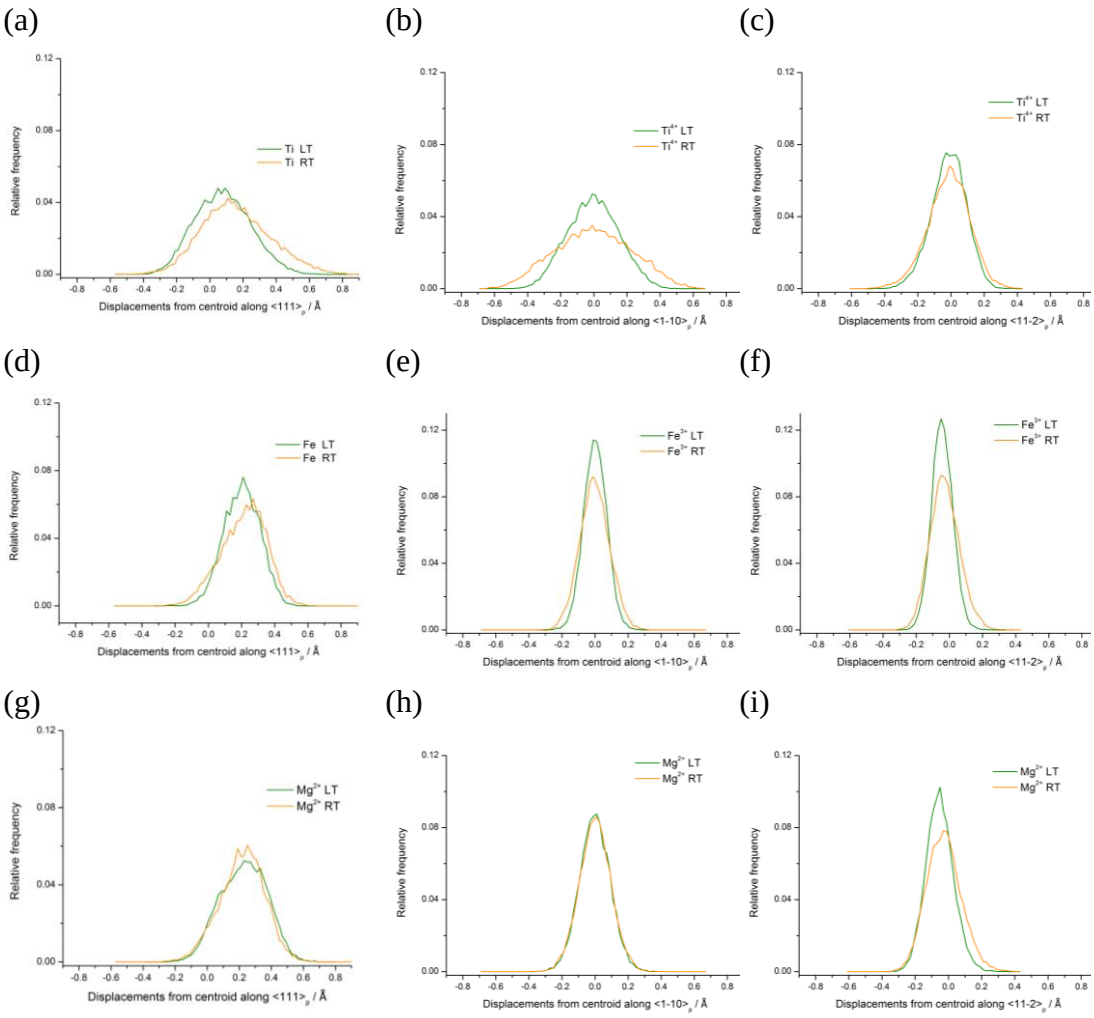

Figure 3.28. *Distribution of B site cation displacements along* $\langle 111 \rangle_p$, $\langle 1\bar{1}0 \rangle_p$ *and* $\langle 11\bar{2} \rangle_p$ *for: (a-c)* Ti^{4+}, *(d-f)* Fe^{3+} *and (g-i)* Mg^{2+} *respectively.*

3.4.4 Analysis and comparison of A and B site displacement correlations between LT and RT data

Correlations between the A and B site cation displacements are identified through evaluation of DCF, as described in the section 3.2.3. The DCFs of A and B site were calculated for all 18 RMC and disordered models, and then subtracted from each other to present differential DCF, which provide the real correlations beyond those arising from the average structure. The differential $\eta_{Bi\text{-}Bi}(r)$ shows correlation of Bi^{3+} displacements along the polar direction (Figure 3.29a),

confirming the ferroelectric correlations of Bi^{3+} cations. The results of differential $\eta_{Bi\text{-}Bi}(r)$ along off-polar axes also show positive peaks, indicating that displacements normal to $\langle 111 \rangle_p$ are correlated as well (Figure 3.29b). The magnitude of these DCFs are significantly smaller compared to those in the polar direction, as the displacements along non-polar directions are much weaker. Despite this, the peaks persist up to r = 10–15 Å which indicate that correlations along both the off-polar and polar axes are correlated over the same range.

Furthermore, the comparison of differential DCFs of Bi-Bi at LT and RT indicate that ferroelectric correlations of Bi atoms along the polar direction are stronger at LT. In addition to that, the comparison of $\eta_{Bi\text{-}Bi}(r)$ in directions orthogonal to the polar axes also demonstrate stronger local ferroelectric correlations of Bi atoms at LT. The peaks in the $\eta_{Bi\text{-}Bi}(r)$ along $\langle 111 \rangle_p$ and off-polar axes directions are twice as strong at LT than at RT, demonstrating static ferroelectric correlations between Bi atoms, whereas the smaller magnitude of ferroelectric correlations existing at RT can be an effect of increased atomic thermal motion. This can suggest that higher temperature correspond to the creation of additional anisotropy of the Bi displacements, as observed from the broadening peaks in the distribution of displacements and in consequence provide the weaker ferroelectric correlation of A site cations at higher temperature.

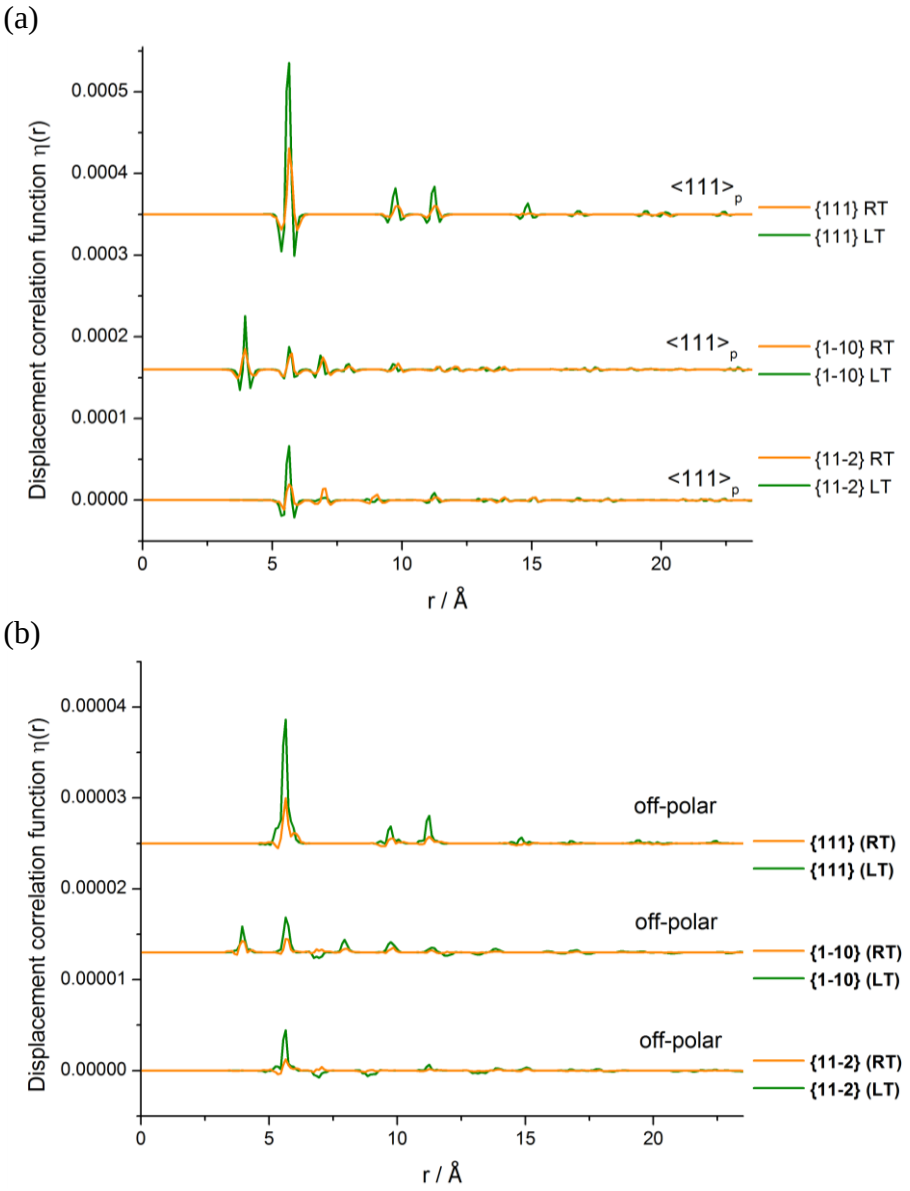

Figure 3.29. *Bi–Bi differential displacement correlation functions (DCFs) calculated for (a) displacements along the polar axis* $\langle 111\rangle_p$ *and (b) off-polar axes displacements with summed components along* $\langle 1\bar{1}0\rangle_p$ *and* $\langle 11\bar{2}\rangle_p$ *and visualized correlations within planes normal to those directions.*

The correlations of the B site cations were calculated by DCFs within spherical volume and compared to results at RT along polar $\langle 111\rangle_p$, and the two non-polar $\langle 1\bar{1}0\rangle_p$ and $\langle 11\bar{2}\rangle_p$ directions. The differential DCFs of homopairs show displacement correlations along $\langle 111\rangle_p$ for all B site cations, but with broader

peaks in the $\eta_{Ti-Ti}(r)$ and extending over a shorter distance (~10 Å) in comparison to $\eta_{Fe-Fe}(r)$ and $\eta_{Mg-Mg}(r)$ (Figure 3.30a). On the other hand, the DCFs of heteropairs only show correlations for $\eta_{Fe-Mg}(r)$ along the polar axis, in contrast to the absence of positive peaks in the $\eta_{Ti-Fe/Mg}(r)$ (Figure 3.30b). Strong ferroelectric correlations in the $\eta_{Ti-Ti}(r)$ in comparison to weak positive peaks in the $\eta_{Fe-Fe}(r)$ and $\eta_{Mg-Mg}(r)$ are observed along $\langle 1\bar{1}0\rangle_p$ (Figure 3.30c), whereas along $\langle 11\bar{2}\rangle_p$ comparable positive peaks for all B site cations were seen (Figure 3.30e). On the other hand, the heteropairs $\eta_{Ti-Fe/Mg}(r)$ along both off-polar axes directions, shows small negative peaks demonstrating anticorrelation between these atoms, while the $\eta_{Fe/Mg-Fe/Mg}(r)$ show no correlation between Fe^{3+} and Mg^{2+} cations (Figure 3.30d, f).

Thus, DCFs results at LT and their comparison to the RT results indicate identical behavior of B site cations with comparable magnitude of correlations. These similar DCF results of B site cations and much stronger ferroelectric correlations of Bi atoms at LT than at RT, suggest that the A site cations displacements do not depend on the B site cations displacements. DCFs calculated between Bi^{3+} and B site cations confirmed it, as the $\eta_{Bi-Ti}(r)$ along off-polar axes show no coupling between Bi^{3+} and Ti^{4+} cations, and only small correlations were observed for only the first neighbours in the $\eta_{Bi-Fe}(r)$ and $\eta_{Bi-Mg}(r)$ (Figure 3.31b). On the other hand, comparable correlations exist along polar direction in both LT and RT data with a longer length scale (~20 Å) and stronger magnitude for $\eta_{Bi-Fe/Mg}(r)$ than $\eta_{Bi-Ti}(r)$ (10–15 Å) (Figure 3.31a). These comparable correlations between Bi and B site cations at LT and RT, in contrast to much stronger ferroelectric correlations of Bi cations at LT than at RT, suggest again that B site cations did not have an influence on the Bi displacements.

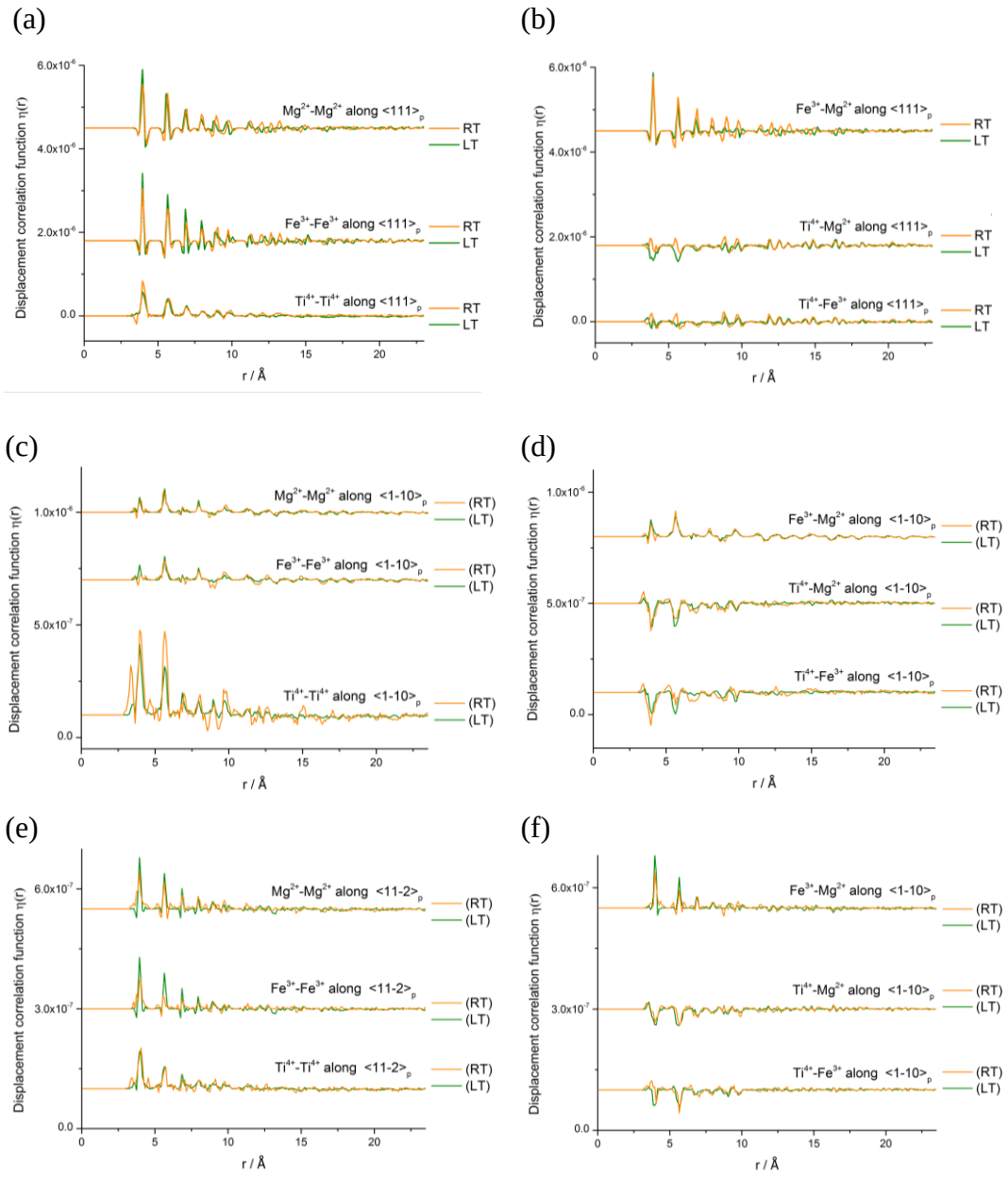

Figure 3.30. *B site–B site spherical differential DCFs calculated for homopairs along (a) polar axis* $\langle 111 \rangle_p$, *(c)* $\langle 1\bar{1}0 \rangle_p$, *(e)* $\langle 11\bar{2} \rangle_p$*; and heteropairs along (b) polar axis* $\langle 111 \rangle_p$, *and two off-polar axes (d)* $\langle 1\bar{1}0 \rangle_p$ *and (f)* $\langle 11\bar{2} \rangle_p$.

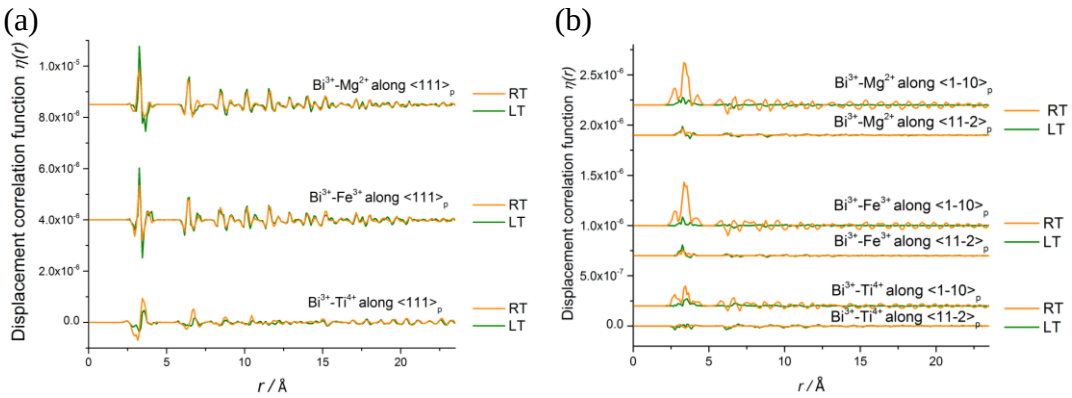

Figure 3.31. *Bi–B site spherical differential DCFs calculated for (a) displacements along the polar axis* $\langle 111 \rangle_p$ *and (b) off-polar axes displacements along* $\langle 1\bar{1}0 \rangle_p$ *and* $\langle 11\bar{2} \rangle_p$.

3.4.5 Comparison of nearest neighbours between LT and RT - B site cation ordering

The B site ordering was calculated directly from partial pair distribution function $g_{B\text{-}B}(r)$ (Figure 3.25). The 18 RMC models were compared with models possessing a completely disordered distribution. The derived nearest neighbour functions $n_{B\text{-}B}(r)$ showed no significant difference in neighbour frequencies to those expected for a completely disordered distribution (Table 3.11). These comparable $n(r)$ results are generally consistent with random distribution at RT data, indicating that there is no B site ordering between Ti^{4+}, Fe^{3+} and Mg^{2+} cations.

Table 3.11. *Comparison of the B site nearest neighbours for the local structure at LT and RT. Comparison is given between the refined RMC model with standard errors and a fully disordered B site distribution.*

	n(r) of 1st shell - 6 neighbours			*n(r)* of 2nd shell - 12 neighbours		
	Local structure LT	Local structure RT	Disordered	Local structure LT	Local structure RT	Disordered
Ti-Ti	2.09(3)	2.24(1)	2.25	4.17(3)	4.49(2)	4.50
Ti-Fe	1.49(2)	1.51(1)	1.5	3.22(4)	3.04(2)	3.0
Ti-Mg	2.41(2)	2.27(1)	2.25	4.62(4)	4.49(2)	4.50
Fe-Fe	1.49(1)	1.47(0)	1.5	2.84(9)	3.00(0)	3.0
Mg-Fe	1.51(2)	1.52(0)	1.5	2.89(3)	2.98(1)	3.0
Mg-Mg	2.08(3)	2.22(0)	2.25	4.50(3)	4.57(0)	4.50

3.4.6 Summary

The application of time-of-flight neutron total scattering data and RMC modeling at LT revealed comparable local deviations to those observed at RT. The initial analysis of pair distribution function in real space showed similar bond distances between local structures at LT and RT, with general trend towards peaks becoming more separated and sharper at LT as the atomic thermal motion is reduced; this is particularly noticeable for the A site environment. Despite the reduced atomic thermal motion at LT, the local B site environment analysis demonstrate more comparable results to the local structure at RT, with an almost identical distribution of bond distances Fe^{3+} and Mg^{2+} cations. On the other hand, Ti^{4+} cations demonstrate the less extensive flexibility in its coordination geometry than at RT, but still possess broader *g(r)*'s and displacements in contrast to other Fe and Mg cations.

The DCFs calculations at LT confirmed the A site local behavior at RT, where displacements of Bi^{3+}cations along off-polar axes are ferroelectric correlated on a local scale. Furthermore, the comparison of the $\eta_{Bi\text{-}Bi}(r)$ shows stronger ferroelectric correlations of Bi atoms both along the polar direction and orthogonal to it in the LT data, indicating that ferroelectric correlations between

Bi atoms are static and that the magnitude of ferroelectric correlations are reduced at RT when the atomic thermal motion is increased.

The DCFs results of B site cations at LT demonstrate almost identical behavior as at RT, with Ti^{4+} cations independently undergo local displacements like Bi^{3+} cations, whereas Fe^{3+} and Mg^{2+} are driven by A site cations. Thus, the identical DCFs of B site results at LT and RT in comparison to stronger ferroelectric correlations of Bi cations observed at LT, indicate that the B site cations do not play important role in the formation of local ferroelectric correlations of Bi^{3+} cations. Further analysis of B site cations ordering are consistent with results at RT and do not show any evidence for ordering of the octahedral cations.

3.5 Crystallographic average structure of BTFM at high temperature (1023K)

The perovskite material BTFM has a phase transition at 1023K from a disordered average rhombohedral structure which is locally monoclinic at LT and RT, into non-disordered cubic phase with space group $Pm\bar{3}m$. The Rietveld refinement of BTFM was performed in GSAS [21] and yielded a very good fit to observed neutron diffraction data (Figure 3.32).

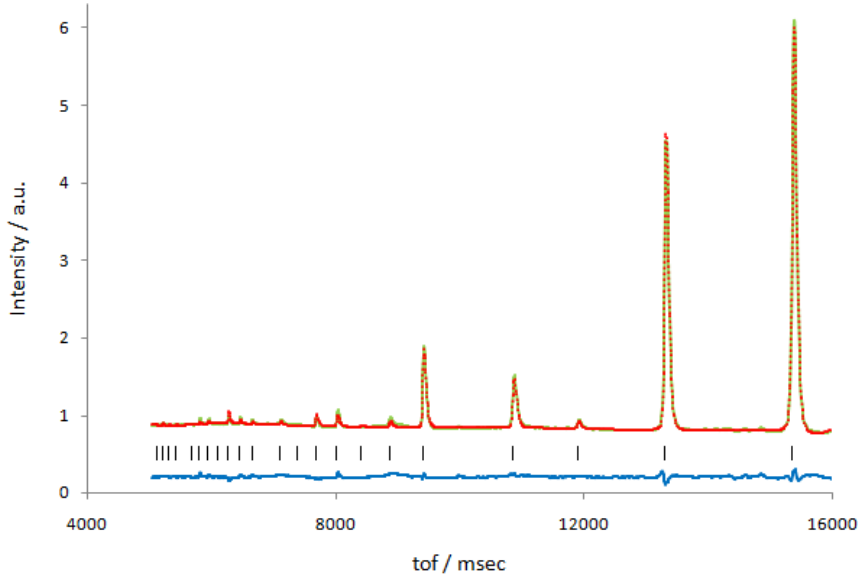

Figure 3.32. *Rietveld refinement of BTFM (90 degrees bank) at 1023K with space group $Pm\bar{3}m$, lattice parameters a = 4.000(2) Å and weighted agreement*

factor R_{wp}=2.18%. The red crosses are observed data, solid green and blue lines are the calculated pattern and difference, whereas the black marks correspond to reflections.

3.6 Local structure at HT

3.6.1 Generation of RMC model

Neutron total scattering data at HT were collected at GEM diffractometer for 1320 μAh over the range $0.3 \leq Q \leq 50$ Å^{-1}. The same procedure applied previously to the correction and normalization data was used for all data sets at various temperatures. The total correlation function *T(r)* was generated from experimental *F(Q)* using the *stog* utility in RMCProfile within the same Q_{max} = 30 Å^{-1} as applied in LT and RT data.

To build the initial RMC model, the structure from the neutron refinement was used and transformed to the monoclinic *Cc* space group in order to be able to compare directly with the local structures at LT and RT (Figure 3.33a, b). The starting RMC configuration were obtained by multiplicity of lattice parameters of the transformed monoclinic subcell *Cc* 6*a* × 11*b* × 11*c*, which produce a supercell of size 59 × 62 × 62 Å and consists 14,520 atoms (Figure 3.33c). The total scattering data was convoluted with a box function to account for the broadening in the calculated data due to the finite RMC configuration size and fits were carried out for $Q < 30$ Å^{-1}. The total correlation function *T(r)* were also fitted over the range of the RMC configuration with length of the shortest lattice vector of 24 Å.

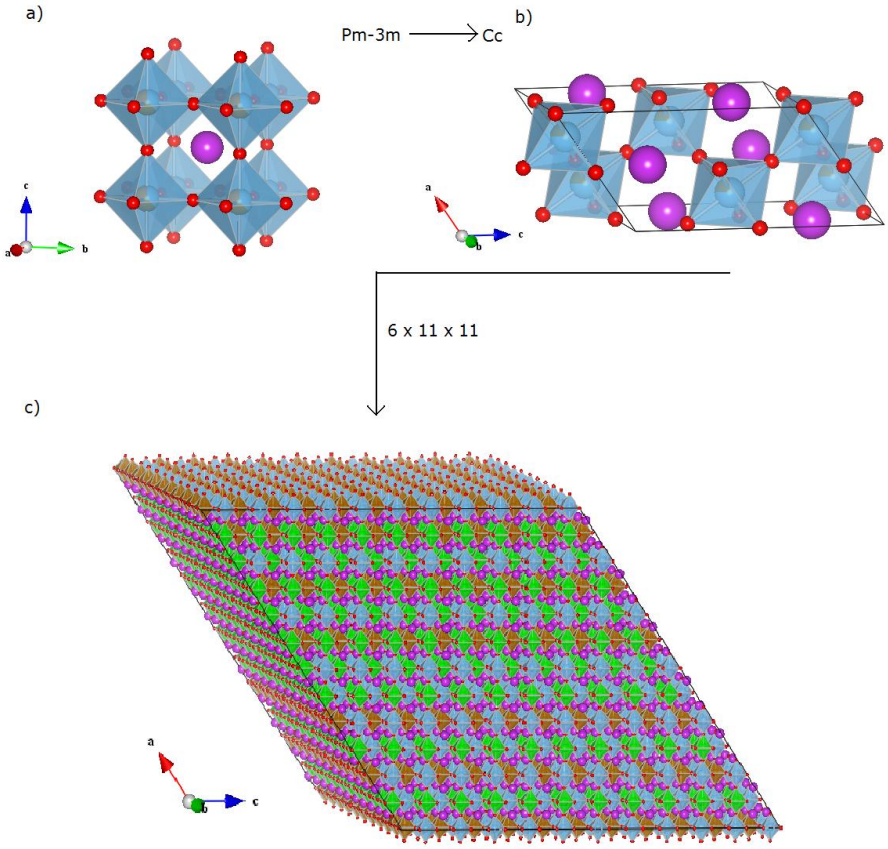

Figure 3.33. *(a) Crystallographic structure of cubic phase $Pm\bar{3}m$ and its transformation to subcell of monoclinic phase Cc; (c) supercell obtained by using a multiplicity 6 × 11 × 11 of monoclinic subcells. The atom spheres are denoted by colours: Bi (purple), Ti (blue), Fe (orange), Mg (green) and O (red).*

The same number of 18 RMC refinements as used for the LT and RT analyses, were performed with RMCProfile. The BVS constraints were applied in the RMC refinements for each cation-oxygen pair, which improved the cut-off features of partial PDF's and helped to distinguish between the Ti^{4+}, Fe^{3+} and Mg^{2+} cations which occupy the same crystallographic B site. The identical maximum translation limits have been applied for all RMC models of HT with 0.05 Å for all of the A site and B site cations and 0.1 Å for the oxygen atoms.

The RMC refinement with applied BVS constraints and swapping of B site cations was continued until no further improvement in χ^2 of Bragg profile data, the total scattering structure factor *F(Q)* and the pair correlation function *T(r)* was observed (Figure 3.34).

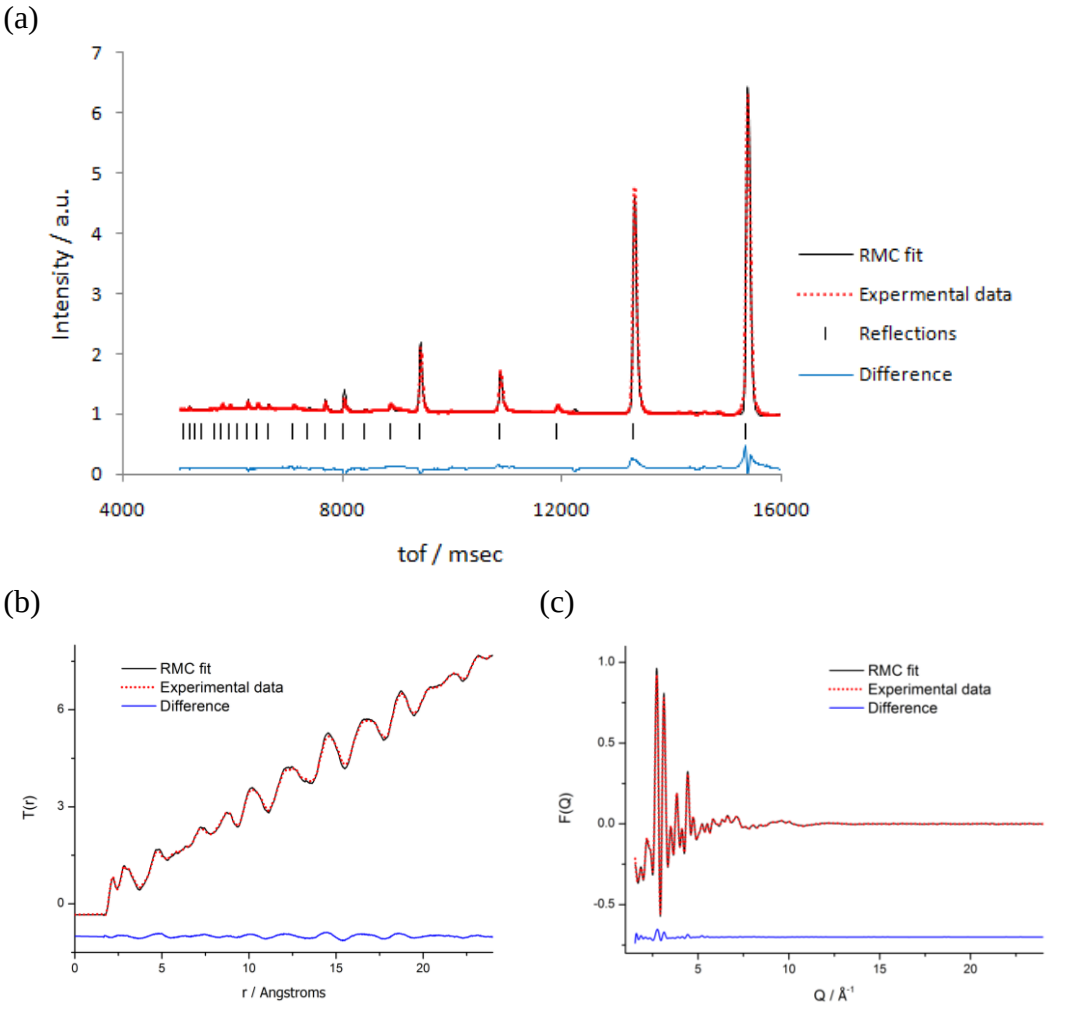

Figure 3.34. *Comparison between measured and calculated functions of one of the RMC models for the local structure of $BiTi_{3/8}Fe_{1/4}Mg_{3/8}O_3$ at HT: (a) Bragg profile data; (b) total correlation function T(r); (c) total scattering structure factor F(Q).*

3.6.2 Analysis and comparison of pair distribution function between HT, RT and LT data

The pair distribution function of local structures at HT were averaged from all 18 RMC models, and compared to average structure and local structures at LT and RT. The bond distances were obtained by fitting Gaussian functions to the observed partial pair distributions functions. The initial comparison of the pair distribution functions $g_{Bi\text{-}O}(r)$, revealed a significant difference between the local and average structures and various temperatures investigated earlier. There are

only two groups of Bi-O bond distances 2.146(3) Å and 2.872(4) Å observed in the local structure at HT, instead of three in the $g_{Bi\text{-}O}(r)$ of LT and RT data (Table 3.12). The initial analysis of bond distance of 2.872(4) Å (Figure 3.35a) indicate agreement with average cubic structure, where nearest 12 oxygen anions form with Bi^{3+} cation identical bond distances at 2.828(4)Å (Figure 3.35b). However, this peak is significantly asymmetric indicating that there is a non-Gaussian distribution of the longer bond distances. The shorter bond distance of 2.146(3) Å indicates that Bi^{3+} cations are off-center from the 12 coordinating oxygen anions. The integrated area under these two peaks provide the ratio of approximately 2.5:9.5 for the 12 nearest oxygen anions between the short and long Bi-O bond distances. These ratios are more consistent with Bi^{3+} cations creating the short bond distances by displacement towards a triangular face (consisting of 3 oxygens) of the cuboctahedron oxygen environment, as opposed to a square face (consisting of 4 oxygens) which has been observed previously for Bi compounds [22]. A displacement towards a triangular face generating the short Bi-O bonds would necessarily produce an asymmetric distribution of longer bond lengths, which is observed in the $g_{Bi\text{-}O}(r)$, as not all of the resulting longer Bi-O distances will be affected to the same degree by the displacement. This explains the asymmetric shoulder at high *r* in the long bond distribution in the $g_{Bi\text{-}O}(r)$. In order to confirm the direction of the Bi displacement from the centre of the cuboctahedron, the magnitude of Bi displacements along different directions were calculated and are discussed in section 3.6.3. The same asymmetric displacement feature was observed earlier, where the PDF approach has been used to establish the local structures of Pb-based perovskite materials in relaxor ferroelectrics [23-26]. The observation of locally off-centered Pb ions in the low temperature cubic phase, in comparison to non-displaced Pb in the average crystallographic structure, explained the formation of static PNR which produce the relaxation behavior. Both Pb^{2+} and Bi^{3+} cations contain lone pair of electrons on the atomic shell $6s^2$, and this suggest that their presence generate the off-center displacement from the centre of the oxygen centroid.

Table 3.12. *Comparison of Bi-O bond distances derived from the RMC model at RT, LT and HT data. Distances for RMC configuration were obtained by fitting Gaussian functions to the observed partial pair distributions functions (Figure 3.35a).*

	Local structure LT / Å	Local structure RT / Å	Local structure HT / Å
Bi-O	2.214(9) 2.371(29) 2.621(20) 3.307(3) (2.5:3:2.3:4.2)*	2.237(1) 2.543(8) 3.303(3) (3.2:4.4:4.6)*	2.146(3) 2.872(4) (2.5:9.5)*

*Approximate ratio of separations (summed to 12 oxygen coordinate system) obtained from the integrated areas of peaks in $g_{Bi-O}(r)$.

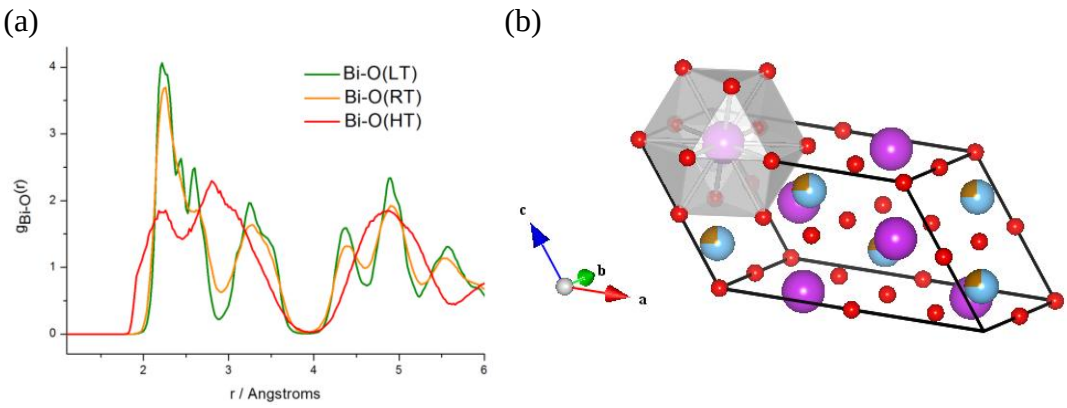

Figure 3.35. *(a) Comparison of pair distribution function $g_{Bi-O}(r)$ between LT, RT and HT data; (b) Representation of Bi^{3+} cation (blue) average crystallographic structure environment within its nearest oxygens (red) creating cuboctahedron with identical bond distance ~2.8Å.*

The B site environment analysis also demonstrate significant differences in bond distances between non-distorted single bonds in cubic average structures 2.0 Å, and distorted bond distances distributions $g_{B-O}(r)$ in local structure. On the other hand, the comparison of the $g_{B-O}(r)$ distributions between HT, RT and LT data sets did not reveal significant differences between B site cations (Figure 3.36). The $g_{Ti-O}(r)$ in HT data demonstrate comparable shape of peaks to RT than LT

data, with sharp peaks centered at 1.807(4) Å and a broad asymmetric feature observed at 2.065(46), indicating the flexibility of Ti^{4+} cations to adopt wide range of bond distances. The partial $g_{Fe\text{-}O}(r)$ and $g_{Mg\text{-}O}(r)$ have still regular environments at HT as demonstrated by single peaks, but with slightly broader distribution and longer bond distances 2.057(3) Å and 2.074(2) Å, respectively in comparison to LT and RT data (Table 3.13).

Table 3.13. *Comparison of B site-O bond distances derived from the RMC model at LT, RT and HT data. Distances for RMC configuration were obtained by fitting Gaussian functions to the observed partial pair distributions functions (Figure 3.36).*

	Local structure LT / Å			Local structure RT / Å			Local structure HT / Å		
B site – O	Ti - O	Fe– O	Mg-O	Ti - O	Fe–O	Mg-O	Ti - O	Fe–O	Mg-O
	1.838(1) 2.010(5)	2.023 (1)	2.061 (1)	1.818(2) 2.105(10)	2.021 (2)	2.060 (1)	1.807(4) 2.065(46)	2.057 (3)	2.074 (2)

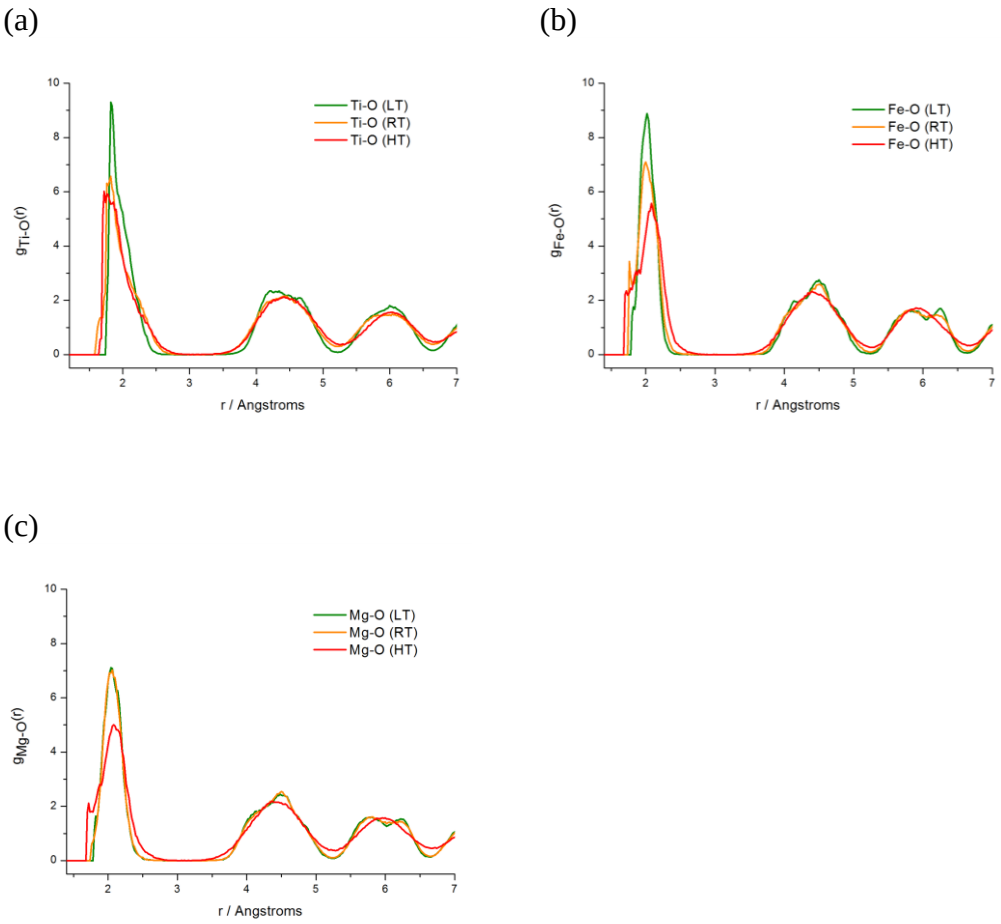

Figure 3.36. *Comparison of pair distribution function between LT, RT and HT for: (a) $g_{Ti\text{-}O}(r)$, (b) $g_{Fe\text{-}O}(r)$ and $g_{Mg\text{-}O}(r)$.*

The comparison of the internal octahedral angles of O-B-O show comparable mean bond angles ~89°, but with broader distribution of Ti^{4+}, Fe^{3+} and Mg^{2+} octahedra 35.1(2) °, 33.5(2) ° and 35.9(2) ° respectively, in comparison to much narrower FWHM of Fe^{3+} and Mg^{2+} (18-24°) in LT and RT data (Table 3.14 and Figure 3.37a). The same FWHM trend is observed for axial angles where the mean angle of ~165° at LT and RT are shifted toward the lower angle of ~160° at HT, indicating stronger distortions of B site octahedra. These results are consistent with $g_{Fe\text{-}O}(r)$ and $g_{Mg\text{-}O}(r)$, where broader distribution in the HT data is observed. Furthermore, the external bond angles $\theta_{B\text{-}O\text{-}B}$ of both homopairs and heteropairs (Table 3.15 and Figure 3.37b) demonstrate similar behavior, where broader distribution are perceived for all B site cations in the HT data. The differences are observed for Fe^{3+} and Mg^{2+} cations, where FWHM of $\theta_{Fe/Mg\text{-}O\text{-}Fe/Mg}$

(~27°) are larger than in the LT and RT data (~17°). There is also a difference for Ti^{4+} cations, but it is less pronounced as Ti octahedral are strongly distorted at all temperatures studied.

***Table 3.14**. Comparison of bond angle distributions of O-B-O for local structures at LT, RT and HT.*

	Local structure					
	LT		RT		HT	
	Angle / °	FWHM / °	Angle / °	FWHM / °	Angle / °	FWHM / °
O-Ti-O	89.35(3) 168.5(1)	17.88(8) 17.0(3)	88.57(5) 163.6(2)	24.7(1) 23.4(5)	88.54(9) 159.4(2)	35.1(2) 30.7(6)
O-Fe-O	88.92(5) 166.2(1)	19.1(1) 14.6(4)	88.68(8) 164.8(2)	21.7(2) 17.9(6)	88.96(7) 161.2(2)	33.5(2) 27.1(5)
O-Mg-O	88.32(8) 164.7(2)	20.9(2) 17.8(7)	88.35(9) 164.3(2)	22.4(2) 18.3(6)	88.2(1) 158.1(3)	35.9(2) 33.1(9)

***Table 3.15**. Comparison of bond angle distributions of B-O-B for local structures at LT, RT and HT.*

	Local structure					
	LT		RT		HT	
	Angle / °	FWHM / °	Angle / °	FWHM / °	Angle / °	FWHM / °
Ti-O-Ti	159.21(3)	18.62(8)	156.54(5)	23.4(1)	156.5(1)	28.3(2)
Fe-O-Fe	154.64(2)	13.04(6)	153.82(4)	17.40(9)	154.63(8)	26.01(2)
Mg-O-Mg	153.03(2)	16.20(6)	152.45(3)	18.58(7)	152.53(7)	28.8(1)
Ti-O-Fe	156.98(1)	15.32(4)	154.87(4)	21.1(1)	155.93(5)	26.3(1)
Ti-O-Mg	156.68(2)	16.54(5)	154.99(2)	21.70(6)	155.28(6)	28.3(1)
Fe-O-Mg	153.85(2)	14.24(4)	153.62(2)	18.30(5)	153.28(5)	27.4(1)

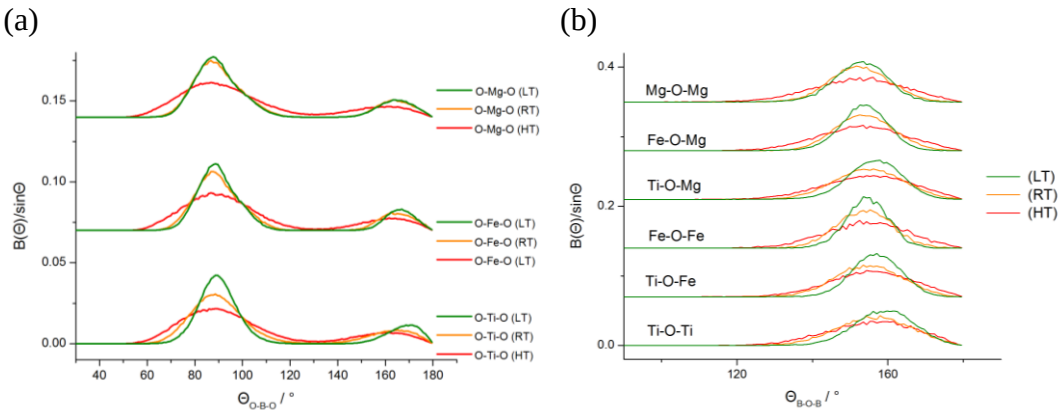

Figure 3.37. *Comparison of bond angle distributions between LT, RT and HT of: (a) O-B-O; (b) B-O-B.*

The comparison of B site – B site cation pair correlation functions at HT show a more significant discrepancies between homopairs than heteropairs. All of the B site homopairs are more widely separated at HT than at lower temperatures, as an effect of increased thermal motion. The broad variation of separation in $g_{Fe\text{-}Fe}(r)$ and $g_{Mg\text{-}Mg}(r)$ is similar to that observed $g_{Ti\text{-}Ti}(r)$ in the HT (Figure 3.38a), which is unusual, as Ti^{4+} cations were more separated than Fe^{3+} and Mg^{2+} at lower temperatures. The heteropairs of $g_{Fe\text{-}Mg}(r)$ are also more separated than their equivalent heteropairs in the LT and RT data (Figure 3.38b). This trend is maintained for $g_{Ti\text{-}Mg}(r)$ and $g_{Ti\text{-}Fe}(r)$, except the nearest neighbours where FWHM values are very comparable.

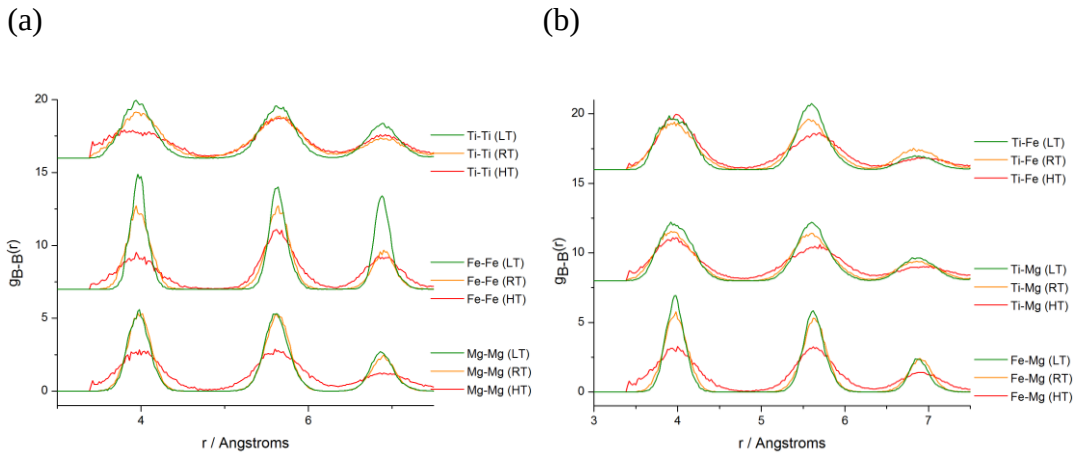

Figure 3.38. *Comparison of partial pair distributions $g_{B\text{-}B}(r)$ between LT, RT and HT data for: (a) homopairs, and (b) heteropairs.*

The partial pair correlation functions $g_{Bi-B}(r)$ (Figure 3.39) show single peaks for all B site cations. The similar results in $g_{Bi-Ti}(r)$, $g_{Bi-Fe}(r)$ and $g_{Bi-Mg}(r)$ are very comparable to the $g_{Bi-B}(r)$ obtained at RT, suggesting that the increase in atomic thermal motion at HT did not affect the separations between A and B site cations.

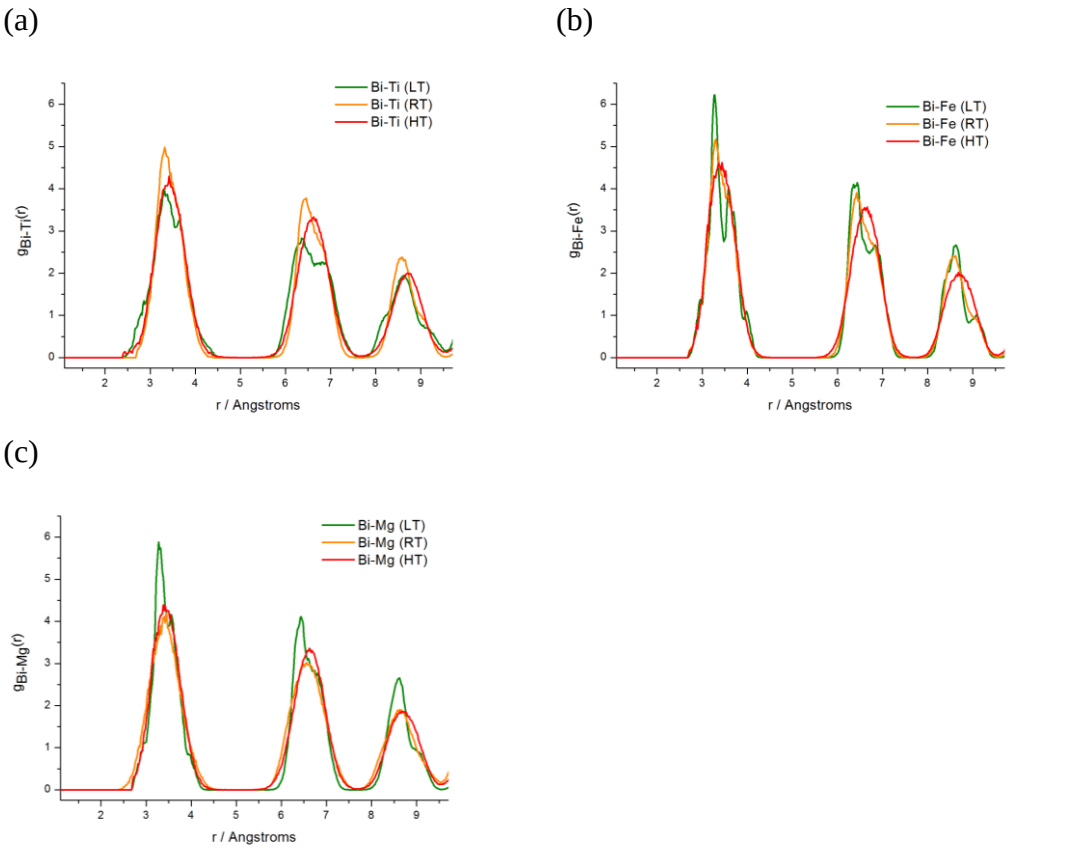

Figure 3.39. *Comparison of pair distribution function $g_{Bi\text{-}B}(r)$ between LT, RT and HT for: (a) $g_{Bi\text{-}Ti}(r)$, (b) $g_{Bi\text{-}Fe}(r)$ and $g_{Bi\text{-}Mg}(r)$.*

3.6.3 Analysis and comparison of A and B site displacements between LT, RT and HT data

The initial calculations of Bi^{3+} displacements from the centroid of their twelve coordinate oxygen environment at HT were carried out along original cubic directions $\langle 100 \rangle_p$, $\langle 010 \rangle_p$ and $\langle 001 \rangle_p$, and demonstrated single broad peaks with comparable range of Bi^{3+} displacements for all directions (Figure 3.40a). This indicated that the strongest displacement of Bi^{3+} cations was not along any of the original cubic directions. The RMC models were collapsed onto the original cubic cell in order to show the general ellipsoid shape (Figure 3.40b). Bi^{3+} cations are displaced from the center of their 12 coordinated environment, which is in agreement with $g_{Bi\text{-}O}(r)$ where two peaks with a ratio of 2.5:9.5 showed the off-center displacement consistent with a movement towards a triangular face of the cuboctahedron oxygen environment. Furthermore, the calculated density plot with

a view along $\langle 001 \rangle_p$ (Figure 3.40c) confirmed the anisotropic behavior of Bi^{3+} cations, and suggest that the particular direction of Bi^{3+} cations displacement may be along one of the diagonal directions (e.g. $\langle 110 \rangle_p$ or $\langle 111 \rangle_p$). Comparison of the possible directions for Bi^{3+} cations displacement revealed that the most significant displacement was along $\langle 111 \rangle_p$, as it demonstrated the two most distinct Bi^{3+} positions (Figure 3.40d). This displacement along $\langle 111 \rangle_p$ direction is then in agreement with the ratio of the bond distances observed in the $g_{Bi\text{-}O}(r)$. Thus the further calculations of A and B site cation displacements and correlations will be performed along Cartesian model directions $\langle 111 \rangle_p$, $\langle 1\bar{1}0 \rangle_p$ and $\langle 11\bar{2} \rangle_p$.

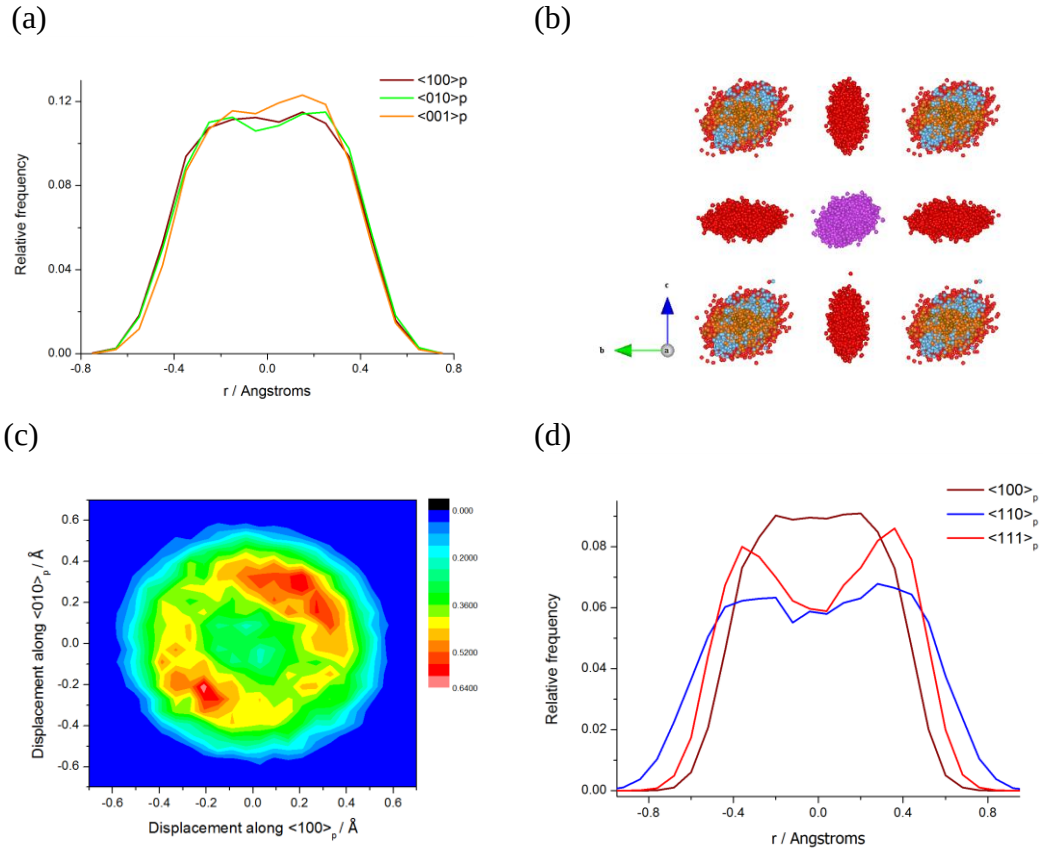

Figure 3.40. *(a) Comparison of Bi displacement distributions along original cubic directions* $\langle 100 \rangle_p$, $\langle 010 \rangle_p$ *and* $\langle 001 \rangle_p$*; (b) The collapsed RMC models onto the original cubic cell, viewed along* [100]*; (c) Density plots corresponding to a view along* $\langle 001 \rangle_p$*; (d) Comparison of Bi displacement distributions along directions* $\langle 100 \rangle_p$, $\langle 110 \rangle_p$ *and* $\langle 111 \rangle_p$.

The calculated displacements of Bi^{3+} cations along these Cartesian model directions at HT, show significantly broad distribution of displacements of bismuth atoms, represented by two peaks along $\langle 111 \rangle_p$ (Figure 3.41a). The Gaussian fit of this distribution provide two symmetrical peaks with negative −0.289(10) Å and positive value 0.302(9) Å and comparable FWHM values (0.467(25) Å and 0.448(22) Å respectively, demonstrating two maxima of Bi^{3+} displacements in the opposite directions (Table 3.16). Thus, the distribution of Bi^{3+} cation displacements in the HT data are significantly different to non-displaced Bi^{3+} cations at average cubic structure and those observed in the LT and RT data, where distributions along $\langle 111 \rangle_p$ contain single peak with Gaussian shape. The presence of two symmetrical peaks at HT indicate two populations of Bi^{3+} cations displaced along $\langle 111 \rangle_p$, while single peak at LT and RT show displaced Bi^{3+} cations within the same manner along this direction. These two peaks is in agreement with $g_{Bi\text{-}O}(r)$ and confirm off-center displacement of Bi^{3+} cations towards a triangular face of the cuboctahedron oxygen environment (Figure 3.42). Furthermore, the peaks in the HT data are much broader (FWHM of 0.467(25) Å and 0.448(22) Å) than obtained single peaks for LT and RT (0.196(1) Å and 0.219(1) Å respectively). The displacements along $\langle 1\text{-}10 \rangle_p$ and $\langle 11\text{-}2 \rangle_p$ also demonstrate a broader distribution (FWHM of 0.746(24 Å and 0.450(3) Å respectively) in comparison to LT (0.250(1)Å and 0.17(1)Å) and RT (0.318(1)Å and 0.289(1)Å) (Figure 3.41b, c). On the other hand, the mean displacements along $\langle 1{-}10 \rangle_p$ and $\langle 11{-}2 \rangle_p$ directions are close to zero for all temperatures.

Table 3.16. *The comparison of the Bi^{3+} cations displacements d from the centre of centroid of coordinating oxygen atoms obtained from distributions (Figure 3.41) of full width at half maximum (FWHM) of the fitted peak.*

	$\langle 111 \rangle_p$		$\langle 1\bar{1}0 \rangle_p$		$\langle 11\bar{2} \rangle_p$	
	d / Å	FWHM / Å	d / Å	FWHM / Å	d / Å	FWHM / Å
LT	0.643(1)	0.196(1)	0.001(1)	0.250(1)	-0.021(1)	0.197(1)
RT	0.623(1)	0.219(1)	-0.001(1)	0.318(1)	-0.015(1)	0.289(1)
HT	-0.289(10) 0.302(9)	0.467(25) 0.448(22)	-0.006(10)	0.746(24)	-0.007(1)	0.450(3)

(a)

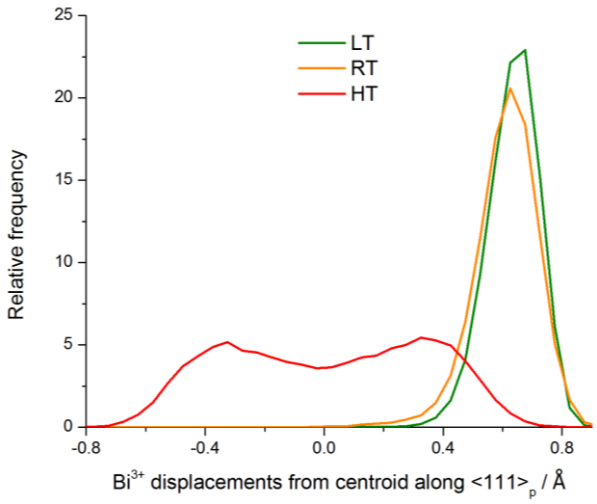

(b)

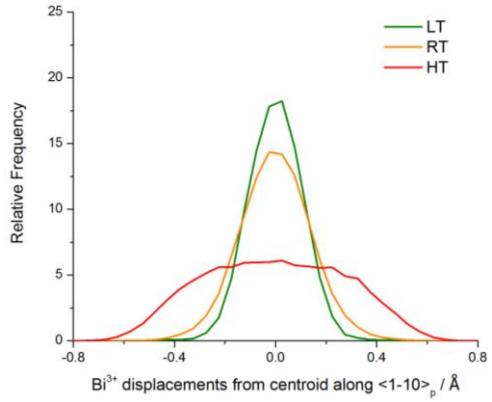

(c)

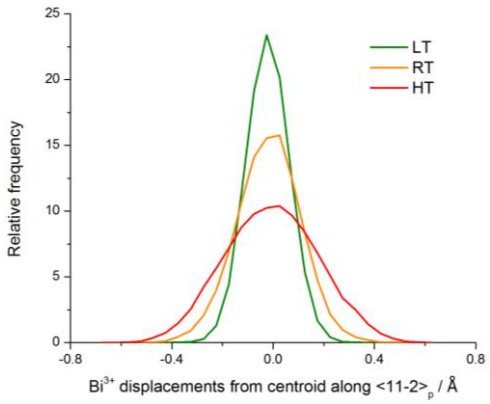

Figure 3.41. *Distribution of Bi displacements along Cartesian model directions (a)* $\langle 111 \rangle_p$*; (b)* $\langle 1\bar{1}0 \rangle_p$*; and (c)* $\langle 11\bar{2} \rangle_p$.

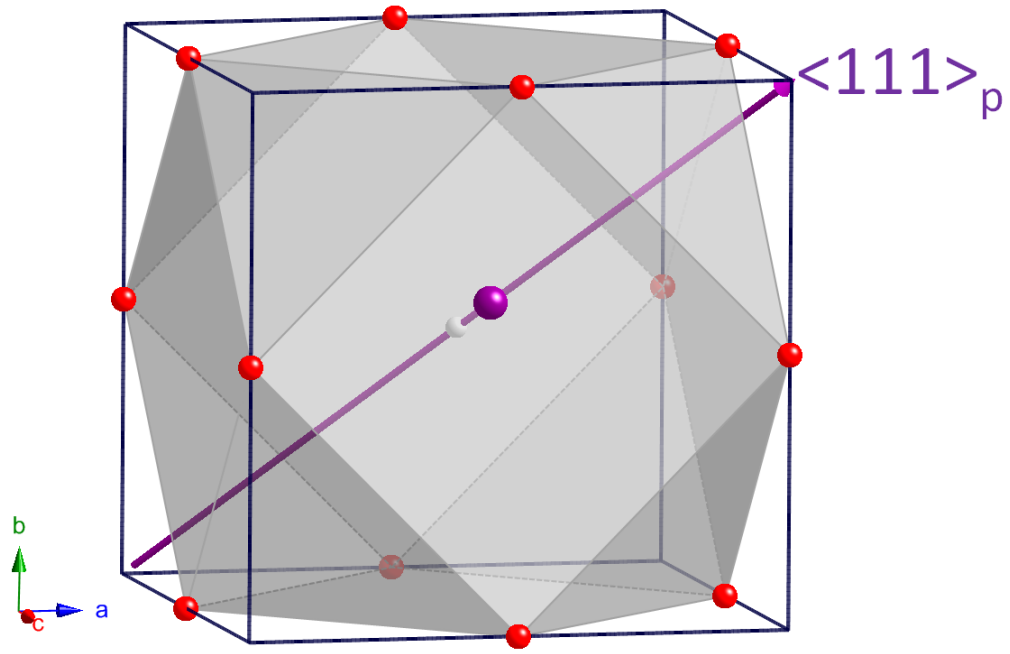

Figure 3.42. *Bi^{3+} cation of the most frequent displacement (0.359 Å) along $\langle 111\rangle_p$ towards a triangular face (consisting of 3 oxygens) within the cuboctahedron of oxygen anions.*

The calculations of displacement of B site cations from the oxygen centroid were performed along the same Cartesian model directions $\langle 111\rangle_p$, $\langle 1\bar{1}0\rangle_p$ and $\langle 11\bar{2}\rangle_p$ (Table 3.17 and Figure 3.43). The initial analysis show mean displacement close to zero for all B site cations at HT, which is consistent with LT and RT data, except those of Fe^{3+} and Mg^{2+} cations demonstrating majority of the mean displacements along $\langle 111\rangle_p$ direction at LT and RT (Figure 3.43d, g). The second pronounced difference between HT and lower temperature data sets is the peak widths. The peaks of Fe^{3+} and Mg^{2+} cations at HT are significantly broader than those in the LT and RT data (Figure 3.43d-i), which indicate about stronger octahedral distortions at HT and also demonstrate significant difference in comparison to non-distorted average cubic structure. The differences in distribution of Ti^{4+} cations are less pronounced as titanium atoms demonstrate broad symmetrical distribution with either positive and negative displacements for both LT, RT and HT data sets. This indicates that distribution of Ti^{4+} cations did

not change significantly between 10-1023K, demonstrating a wide range of displacements.

Table 3.17. *The comparison of the octahedral B site displacements d from the centroid of coordinated oxygen atoms obtained from distributions (Figure 3.43) with full width at half maximum (FWHM) of the fitted peak.*

		$<111>_p$		$<1\bar{1}0>_p$		$<11\bar{2}>_p$	
		d / Å	FWHM / Å	d / Å	FWHM / Å	d / Å	FWHM / Å
LT	Ti^{4+}	0.072(1)	0.412(4)	-0.004(1)	0.380(3)	-0.007(1)	0.244(2)
	Fe^{3+}	0.204(1)	0.264(3)	0.001(1)	0.136(1)	-0.044(1)	0.148(1)
	Mg^{2+}	0.231(2)	0.368(5)	-0.002(1)	0.215(1)	-0.056(1)	0.189(2)
RT	Ti^{4+}	0.131(3)	0.456(9)	-0.003(3)	0.62(1)	-0.007(1)	0.279(4)
	Fe^{3+}	0.239(5)	0.317(3)	-0.004(1)	0.209(3)	-0.033(1)	0.203(3)
	Mg^{2+}	0.242(7)	0.315(3)	0.0009(6)	0.219(2)	-0.033(1)	0.239(4)
HT	Ti^{4+}	0.020(2)	0.634(6)	-0.011(2)	0.481(5)	-0.009(1)	0.403(3)
	Fe^{3+}	-0.008(1)	0.456(4)	0.008(1)	0.167(1)	0.005(1)	0.380(3)
	Mg^{2+}	0.007(1)	0.463(3)	0.009(2)	0.616(5)	0.007(1)	0.463(3)

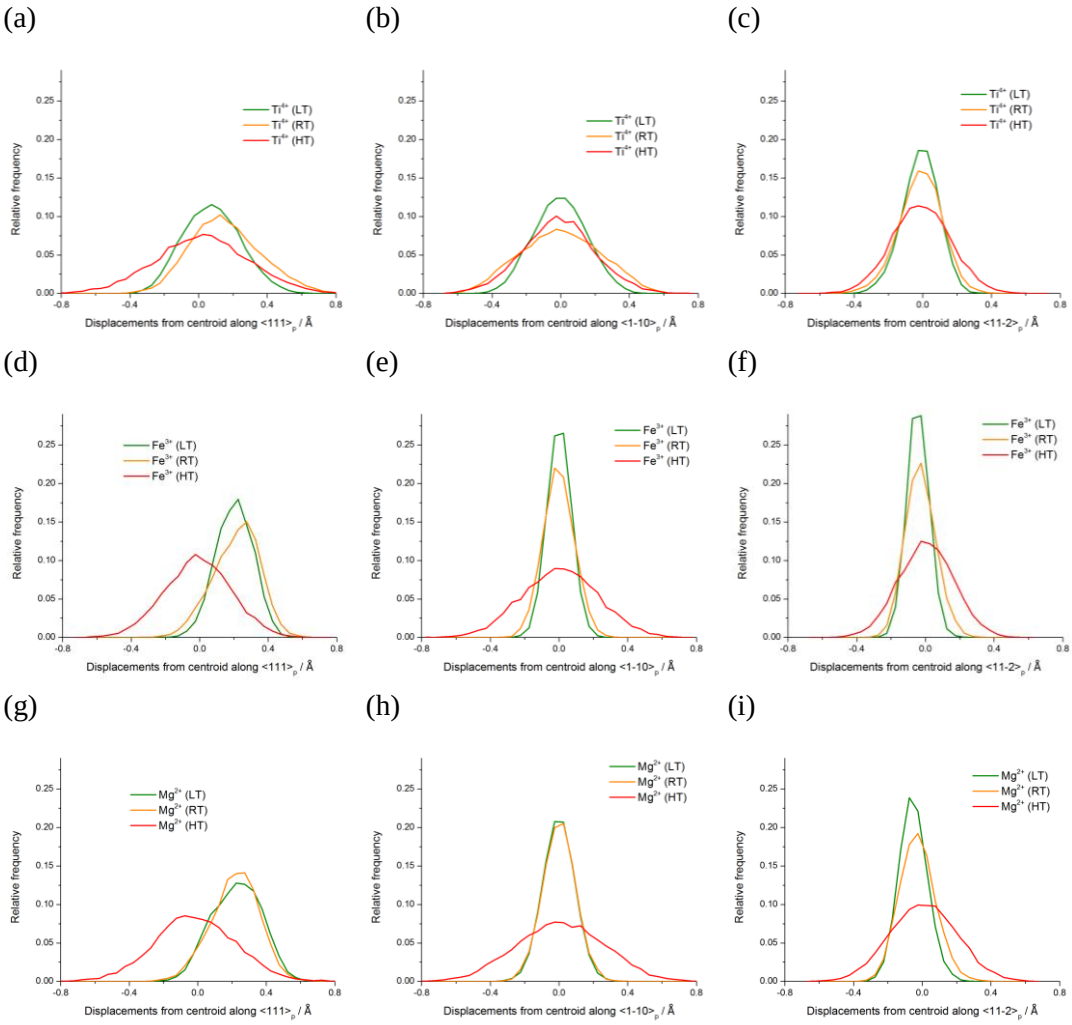

Figure 3.43. *Distribution of B site cations displacement along* $\langle 111\rangle_p$, $\langle 1\bar{1}0\rangle_p$ *and* $\langle 11\bar{2}\rangle_p$ *for: (a-c)* Ti^{4+}, *(d-f)* Fe^{3+} *and (g-i)* Mg^{2+} *respectively.*

3.6.4 Analysis and comparison of A and B site displacement correlations between LT, RT and HT data

DCFs are calculated and averaged for all 18 RMC models in the HT data, where all RMC and disordered models are subtracted from each other, to provide the differential DCF. Thus, the real correlations are obtained and exist beyond those arising from the average structure in the material. DCFs of Bi-Bi are resolved into three separate planes within the structure orthogonal to the directions $\langle 111\rangle_p$, $\langle 1\bar{1}0\rangle_p$ and $\langle 11\bar{2}\rangle_p$, whereas the calculations Bi-B site and B site itself are resolved by spherical DCF within a volume, where correlations are derived only along Cartesian model directions. The results of differential DCF shows that local

correlations of the Bi atoms also exist in the HT cubic phase. The positive peaks of $\eta_{Bi-Bi}(r)$ indicate about local ferroelectric correlations along $\langle 111\rangle_p$ (Figure 3.44a), however they are two times weaker than RT correlations and 4 times weaker than at LT. Furthermore, the comparable magnitude of displacement correlations between temperatures also exist along off-polar axes (Figure 3.44b). These suggest that the off-center displacement group of Bi atoms, as observed in the $g_{Bi-O}(r)$ and displacement results, are also weakly correlated along $\langle 111\rangle_p$, $\langle 1\bar{1}0\rangle_p$ and $\langle 11\bar{2}\rangle_p$ directions. Thus, the investigation of local structure at HT indicate that displacements of bismuth atoms are ferroelectrically correlated in the short-range order (~ 15 Å), whereas the average crystallographic structure in the long-range order demonstrate the cubic phase with non-distorted A site cations.

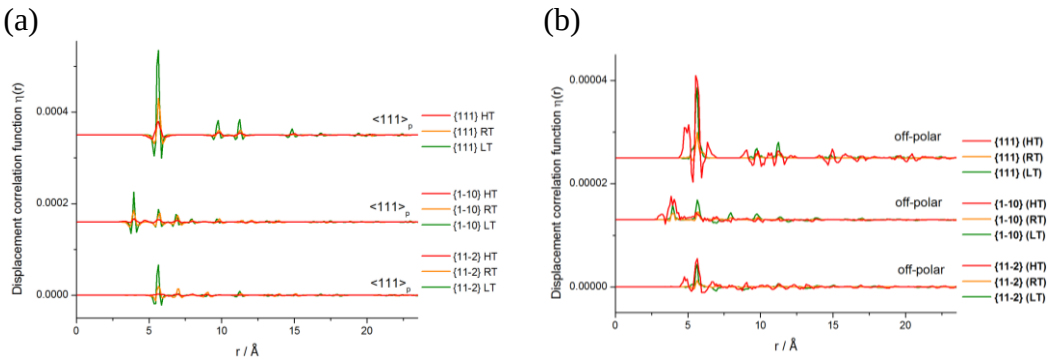

Figure 3.44. *Bi–Bi differential DCFs calculated for (a) displacements along the polar axis* $\langle 111\rangle_p$ *and (b) off-polar axes displacements with summed components along* $\langle 1\bar{1}0\rangle_p$ *and* $\langle 11\bar{2}\rangle_p$ *and visualized as correlations within planes normal to those directions.*

The differential spherical DCFs of B site- B site shows only ferroelectric correlations along $\langle 111\rangle_p$ in the HT cubic phase. The homopairs of $\eta_{Fe-Fe}(r)$, $\eta_{Mg-Mg}(r)$ and heteropair $\eta_{Fe-Mg}(r)$ in the HT show positive peaks within a distance 10-15Å, but the magnitude of displacement correlations are much weaker than in the LT and RT data (Figure 3.45a, b). This is in agreement with B site mean displacements for Fe^{3+} and Mg^{2+} cations which is close to zero, in contrast to significant displacement in the LT and RT data along the polar direction. Ti^{4+} cations show the same behavior for all temperatures, where they do not show any correlations to Fe^{3+} and Mg^{2+} cations along $\langle 111\rangle_p$, and there are only correlated

between each other in $\eta_{Ti-Ti}(r)$, where peaks are broader and extend over a shorter distance (~10 Å) in comparison to $\eta_{Fe-Fe}(r)$ and $\eta_{Mg-Mg}(r)$ (Figure 3.45a). On the other hand, the $\eta_{Ti-Ti}(r)$ and others DCFs of homopairs and heteropairs along off-polar axes show no correlations in the HT data, in contrast to the presence of positive peaks in the $\eta_{Ti-Ti}(r)$ along $\langle 1\bar{1}0\rangle_p$ in LT and RT data (Figure 3.45c). Despite the lack of correlations in the HT data along off-polar axes, the DCFs peaks have stronger intensity (Figure 3.45c, d, e and f), indicating the more distorted B site environment in the HT data, than at lower temperatures. This is consistent with observed B site displacements (Figure 3.43).

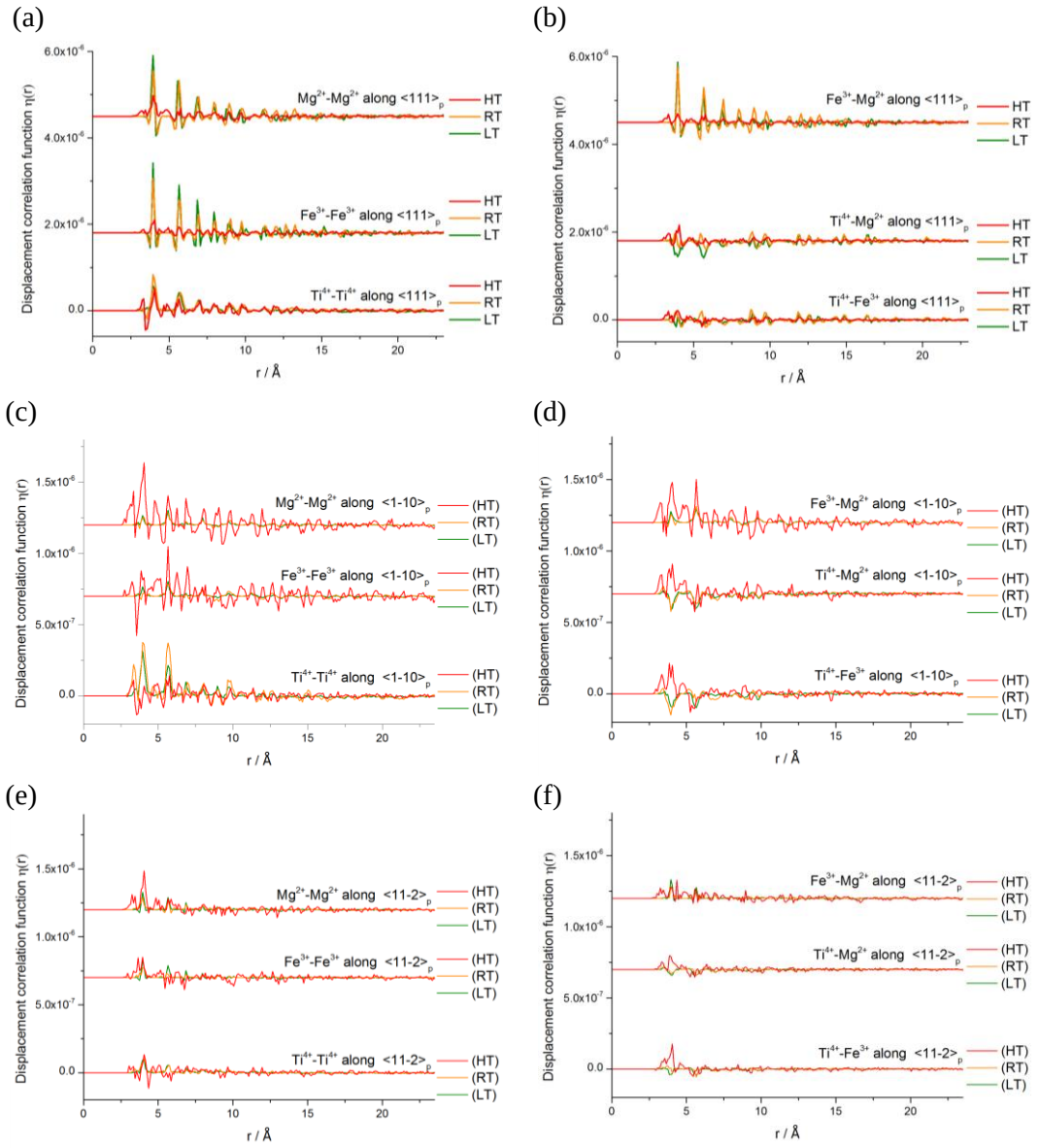

Figure 3.45. *Comparison of B site–B site spherical differential DCFs between LT, RT and HT data, calculated for: homopairs along (a) polar axis* $\langle 111\rangle_p$*, and two off-polar axes (c)* $\langle 1\bar{1}0\rangle_p$*, and (e)* $\langle 11\bar{2}\rangle_p$*; heteropairs along (b) polar axis* $\langle 111\rangle_p$*, and two off-polar axes (d)* $\langle 1\bar{1}0\rangle_p$ *and (f)* $\langle 11\bar{2}\rangle_p$.

The differential spherical DCFs calculated between Bi^{3+} and B site cations along $\langle 111\rangle_p$ at HT show very weak displacement correlations to those of first 2-3 nearest neighbours (~7 Å) for all $\eta_{Bi-Fe}(r)$, $\eta_{Bi-Mg}(r)$ and $\eta_{Bi-Ti}(r)$ functions (Figure 3.46a). This trend is preserved in the $\eta_{Bi-Fe}(r)$ and $\eta_{Bi-Mg}(r)$ along $\langle 1\bar{1}0\rangle_p$, where small positive peaks indicating correlations are probably an effect of increased

thermal motion, as they disappear in the LT data. Furthermore, there is no coupling in the $\eta_{Bi-Fe}(r)$ and $\eta_{Bi-Mg}(r)$ along $\langle 11\bar{2}\rangle_p$ and $\eta_{Bi-Ti}(r)$ along both off-polar axes directions (Figure 3.46b). Thus, the very weak correlations between Bi and B site cations exist in the HT data, however it is unlikely that B site cations have a strong influence on the formation ferroelectric correlations of the A site cations.

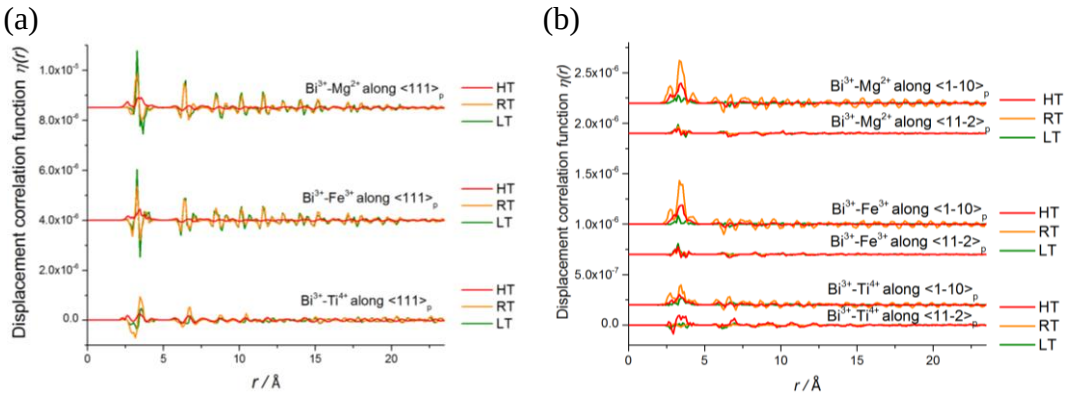

Figure 3.46. *Bi–B site spherical differential displacement correlation functions (DCFs) calculated for (a) displacements along the polar axis* $\langle 111\rangle_p$ *and (b) off-polar axes displacements along* $\langle 1\bar{1}0\rangle_p$ *and* $\langle 11\bar{2}\rangle_p$.

3.6.5 Comparison of nearest neighbours between LT and RT - B site cation ordering

The nearest neighbours for 18 RMC models in the HT data was calculated and averaged. The *n(r)* results differ with disordered B site distribution and results obtained in the LT and RT data (Table 3.18). Such observed differences are an effect of higher temperature, which increases thermal motion of B site cations and provides a very broad distribution of partials $g_{B-B}(r)$ (Figure 3.25). As the nearest B site shells overlap, the accurate estimation of average nearest neighbours results becomes very difficult, and thus *n(r)* results cannot be reliably taken into account when analyzing B site order.

Table 3.18. *Comparison of the B site nearest neighbours in the HT data with the LT and RT data. Comparison is given between the refined RMC model with standard errors and a fully disordered B site distribution.*

	n(r) of 1st shell - 6 neighbours				*n(r)* of 2nd shell - 12 neighbours			
B site – B site	Local structure HT	Disord.	Local structure LT	Local structure RT	Local structure HT	Disord.	Local structure LT	Local structure RT
Ti-Ti	1.90(3)	2.25	2.09(3)	2.24(1)	-	4.50	4.17(3)	4.49(2)
Ti-Fe	1.78(4)	1.5	1.49(2)	1.51(1)	-	3.0	3.22(4)	3.04(2)
Ti-Mg	2.33(3)	2.25	2.41(2)	2.27(1)	-	4.50	4.62(4)	4.49(2)
Fe-Fe	1.09(7)	1.5	1.49(1)	1.47(0)	-	3.0	2.84(9)	3.00(0)
Mg-Fe	1.55(2)	1.5	1.51(2)	1.52(0)	-	3.0	2.89(3)	2.98(1)
Mg-Mg	2.12(2)	2.25	2.08(3)	2.22(0)	-	4.50	4.50(3)	4.57(0)

3.6.6 Summary

The application of time-of-flight neutron total scattering data and RMC modeling at HT revealed significant differences between locally distorted and average non-distorted structure. Furthermore the comparison and analysis of local structures at HT and lower temperatures demonstrated generally more distorted A and B site environment at high temperature.

The analysis of the A site cations environment in the HT cubic phase revealed the presence of locally off-centered Bi^{3+} cations in comparison to non-displaced Bi atoms observed in the average crystallographic cubic structure. The distribution of Bi^{3+} cations displacement confirmed the results of $g_{Bi\text{-}O}(r)$, and demonstrate the off-center displacement of Bi^{3+} cations towards a triangular face of the cuboctahedron oxygen environment, whereas DCF shows locally weak ferroelectric correlations of the Bi^{3+} cations both along this direction $\langle 111 \rangle_p$ and off-polar axes.

The difference observed between B site cations at LT and RT, where Ti demonstrates extensive flexibility in its coordination geometry in contrast to regular coordination of Fe and Mg cations, disappear at HT. All of the B site cations at HT demonstrate broader pair distribution functions and displacements

than their equivalent cations at lower temperatures, indicating stronger octahedral distortions. There are no significant correlations in the HT data between B site and A site - B site cations, although intense DCF peaks confirm the strong character of distorted B site environment in the HT data.

3.7 Conclusions

The application of time-of-flight neutron total scattering data and RMC modeling at various temperatures revealed local deviations from the average crystal structure which have been investigated to extract details of the local structure. The local structures were obtained by the RMC refinement of the Bragg and total scattering in reciprocal space and the pair distribution function in real space.

The analysis of pair distribution function in real space showed comparable bond distances of A site environment between local and average structures at LT and RT data, with more separated and sharper peaks at LT as expected, due to a decrease in atomic thermal motion. On the other hand, the analysis of the A site cations environment in the HT cubic phase revealed the presence of locally off-centered Bi^{3+} cations in comparison to non-displaced Bi atoms observed in the average crystallographic cubic structure.

The DCFs calculations confirmed the presence of ferroelectricity at LT and RT, where local ferroelectric correlations of Bi^{3+} cations exist within 10-15 Å and also demonstrate local monoclinic correlations of Bi^{3+}cations displacements along off-polar axes within the same correlation distance. The comparison of the $\eta_{Bi\text{-}Bi}(r)$ shows stronger ferroelectric correlations of Bi atoms in the LT data, indicating that ferroelectric correlations between Bi atoms are static and increased atomic thermal motion reduce the magnitude of ferroelectric correlations at RT. Calculations of the DCFs at HT also revealed locally weak ferroelectric correlations of the Bi^{3+} cations both along $\langle 111 \rangle_p$ and off-polar axes, which are related to the off-center displaced Bi atoms; these displacements are caused by lone pair of electrons $6s^2$, which also stabilize the off-center displacements of the A site cations in the well-known Pb-based perovskites [23, 24].

The local B site environment analysis demonstrate comparable results at LT and RT, where Ti^{4+} cations demonstrate the more extensive flexibility in its

coordination geometry than Fe^{3+} and Mg^{2+} cations. This behavior of Ti^{4+} cations is similar to those observed in $BaTiO_3$ [8], and also displacements onto lower-symmetry is an effect of lack of the valence electrons in the shell d^0 of Ti^{4+}cations, which permit a broad range of distorted octahedral environments. This ability of Ti to be strongly locally displaced along different directions within the octahedra may play a key role in stabilizing this pure Bi A site perovskite. On the other hand, the Fe displacements along $\langle 111 \rangle_p$ following Bi (shown by the DCF) are expected on the basis of the structure of $BiFeO_3$[3, 27] and the ability of d^5 Fe^{3+}cations to adopt a range of coordination environments, due to its absence of strong ligand-field preferences for specific environments. However, the observation of significant noncentric displacements by Mg is surprising, as s-block cations are usually associated with more symmetrical environments, suggesting that displacements along $\langle 111 \rangle_p$ driven by Bi^{3+} cations produce electrostatic effects that in turn drive coupled Mg displacements. Thus, the displacement correlations of Ti^{4+} cations like Bi^{3+} determine their own local polar displacements whereas those of Fe^{3+} and Mg^{2+} are driven by Bi^{3+} cations. The different behavior of B site cations at LT and RT disappear at HT where all B site cations demonstrate broader pair distribution functions and displacements than at lower temperatures, indicating stronger octahedral distortions. The DCFs results of B site cations do not show any significant correlations with A site cations, except Fe^{3+} and Mg^{2+} cations at RT, indicating that the B site cations do not play important role in the formation of local correlations of Bi^{3+} cations.

3.8 References

1. Bridges, C.A., Allix, M., Suchomel, M. R., Kuang, X. J., Sterianou, I., Sinclair, D. C., Rosseinsky, M. J., *A pure bismuth a site polar perovskite synthesized at ambient pressure.* Angewandte Chemie-International Edition, 2007. **46**(46): p. 8785-8789.
2. Khalyavin, D.D., Salak, A. N., Vyshatko, N. P., Lopes, A. B., Olekhnovich, N. M., Pushkarev, A. V., Maroz,, II, Radyush, Y. V., *Crystal structure of metastable perovskite $Bi(Mg_{1/2}Ti_{1/2})O_3$: Bi-based structural*

analogue of antiferroelectric $PbZrO_3$. Chemistry of Materials, 2006. **18**(21): p. 5104-5110.

3. Kubel, F., and Schmid, H., *Structure of a ferroelectric and ferroelastic monodomain crystal pf the perovskite $BiFeO_3$.* Acta Crystallographica Section B-Structural Science, 1990. **46**: p. 698-702.
4. McLain, S.E., Bowron, D. T., Hannon, A. C., Soper, A. K., *Gudrun. A computer program developed fro analysis of neutron diffraction data.*, 2006: ISIS Facility, Rutherford Appleton Laboratory, Chilton, Didcot, OXON, UK, OX11 0QX.
5. Soper, A.K., Howells, W.S., and Hannon, A.C., *ATLAS: Analysis of time of flight diffraction data from liquid and amorphus samples.* 1989, ISIS Facility, Report RAL-89-046; Rutherford Appleton Laboratory, Chilton, Didcot, Oxon OX1 1 OQX. .
6. Tucker, M.G., Goodwin, A.L., and Dove, M.T., *RMCProfile User Manual: Code version 6.4.7*2010.
7. Tucker, M.G., Keen, D. A., Dove, M. T., Goodwin, A. L., Hui, Q., *RMCProfile: reverse Monte Carlo for polycrystalline materials.* Journal of Physics-Condensed Matter, 2007. **19**(33): p. 335218.
8. Kwei, G.H., Lawson, A. C., Billinge, S. J. L., Cheong, S. W., *Structures of the ferroelectric phases of Barium Titanate.* Journal of Physical Chemistry, 1993. **97**(10): p. 2368-2377.
9. Abramov, Y.A., Tsirelson, V. G., Zavodnik, V. E., Ivanov, S. A., Brown, I. D., *The chemical bond and atomic displacements in $SrTiO_3$ from x-ray diffraction analysis.* Acta Crystallographica Section B-Structural Science, 1995. **51**: p. 942-951.
10. Tucker, M.G., *Unpublished data.* 2010.
11. Frantti, J., Lappalainen, J., Eriksson, S., Lantto, V., Nishio, S., Kakihana, M., Ivanov, S., Rundlof, H., *Neutron diffraction studies of $PbZr_xTi_{1-x}O_3$ ceramics.* Japanese Journal of Applied Physics Part 1-Regular Papers Short Notes & Review Papers, 2000. **39**(9B): p. 5697-5703.

12. Ragini, R., R., Mishra, S. K., Pandey, D., *Room temperature structure of $PbZr_xTi_{1-x}O_3$ around the morphotropic phase boundary region: A Rietveld study*. Journal of Applied Physics, 2002. **92**(6): p. 3266-3274.

13. Dmowski, W., Egami, T., Farber, L., Davies, P. K., *Structure of $Pb(Zr,Ti)O_3$ near the morphotropic phase boundary*, in *Fundamental Physics of Ferroelectrics 2001*, H. Krakauer, Editor 2001, Amer Inst Physics: Melville. p. 33-44.

14. Cooper, V.R., Grinberg, I., Martin, N. R., Rappe, A. M., *Local structure of PZT*, in *Fundamental Physics of Ferroelectrics 2002*, R.E. Cohen, Editor 2002, Amer Inst Physics: Melville. p. 26-35.

15. Grinberg, I., Cooper, V.R., and Rappe, A.M., *Relationship between local structure and phase transitions of a disordered solid solution.* Nature, 2002. **419**(6910): p. 909-911.

16. Goodwin, A.L., Redfern, S. A. T., Dove, M. T., Keen, D. A., Tucker, M. G., *Ferroelectric nanoscale domains and the 905 K phase transition in $SrSnO_3$: A neutron total-scattering study*. Physical Review B, 2007. **76**(17): p. 174114-11.

17. Rajaraman, V., *Computer programming in Fortran 77*. 1997: PHI Learning Pvt. Ltd.

18. Noheda, B., Cox, D. E., Shirane, G., Gonzalo, J. A., Cross, L. E., Park, S. E., *A monoclinic ferroelectric phase in the $PbZr_{1-x}Ti_xO_3$ solid solution.* Applied Physics Letters, 1999. **74**(14): p. 2059-2061.

19. Noheda, B., Gonzalo, J. A., Cross, L. E., Guo, R., Park, S. E., Cox, D. E., Shirane, G., *Tetragonal-to-monoclinic phase transition in a ferroelectric perovskite: The structure of $PbZr_{0.52}Ti_{0.48}O_3$*. Physical Review B, 2000. **61**(13): p. 8687-8695.

20. Kunz, M. and Brown, I.D., *Out of center distortions around octahedrally coordinated d^0 transition metals.* Journal of Solid State Chemistry, 1995. **115**(2): p. 395-406.

21. Larson, A.C. and Von Dreele, R.B., *General Structure Analysis System (GSAS).* Los Alamos National Laboratory Report LAUR 86-748, 2004.

22. Norberg, S.T., Hull, S., Mathieu, R., Eriksson, S. G., *Local structural properties of $0.5BiMnO_3$-$0.5ATiO_3$ (A = Ba or Sr).* Chemical Communications, 2010. **46**(9): p. 1455-1457.

23. Egami, T., Dmowski, W., Akbas, M., Davies, P. K., *Local structure and polarization in Pb containing ferroelectric oxides*, in *First principles calculations for ferroelectrics*, R.E. Cohen, Editor 1998, Amer Inst Physics: Melville. p. 1-10.

24. Egami, T., *Local structure of ferroelectric materials*, in *Annual Review of Materials Research*2007, Annual Reviews: Palo Alto. p. 297-315.

25. Teslic, S., Egami, T., and Viehland, D., *Local atomic structure of PZT and PLZT studied by pulsed neutron scattering.* Journal of Physics and Chemistry of Solids, 1996. **57**(10): p. 1537-1543.

26. Jeong, I.K. and Lee, J.K., *Local structure and medium-range ordering in relaxor ferroelectric $PbZn_{1/3}Nb_{2/3}O_3$ studied using neutron pair distribution function analysis.* Applied Physics Letters, 2006. **88**(26).

27. Catalan, G. and Scott, J.F., *Physics and applications of Bismuth Ferrite.* Advanced Materials, 2009. **21**(24): p. 2463-2485.

Chapter 4. Local and crystallographic average structure of $Bi_2Mn_{4/3}Ni_{2/3}O_6$

4.1 Crystallographic average structure at room temperature

4.1.1 Synthesis

The perovskite material $Bi_2Mn_{4/3}Ni_{2/3}O_6$ (BMN) [1, 2] was synthesized by Dr. Helen Hughes. BMN was prepared by standard ceramic method with a several heating steps within the temperature range 800-875°C; it is one of the few Bi perovskite structures which is stable under ambient pressure. Most Bi-based perovskites require high pressure (HP) synthesis due to the difficulty of accommodating the small Bi^{3+} cation on the 12 coordinate A site [3-9] *e.g.* $BiMnO_3$ and Bi_2MnNiO_6 which has multiple B site cations, ordered in a rock salt configuration. The latter compound is ferroelectric (T_C = 485 K) and ferromagnetic (T_C = 140 K) due to ferromagnetic coupling between partially filled Ni^{2+} ($t_{2g}^6e_g^2$) and empty Mn^{4+} (t_{2g}^3) e_g orbitals [10, 11]. In the BMN perovskite the A site is occupied solely by Bi cations, and there are two different B site cations with three oxidation states (Mn^{4+}, Mn^{3+} and Ni^{2+}) onto one site in the average structure. These multiple B site cations allow stabilization of the small asymmetric Bi^{3+} cations by permitting local structural adjustment to match the bonding requirements of Bi^{3+}.

4.1.2 Incommensurate structure at room temperature (RT)

The crystallographic average structure of BMN [1, 2, 12] at RT was investigated by Dr. Helen Hughes and Dr. John B. Claridge. The BMN structure was first treated as a periodic 3-dimensional structure with the orthorhombic polar space group $P2_1mn$ and cell dimension $2\sqrt{2}a_p \times 4a_p \times \sqrt{2}a_p$ (a_p is cubic perovskite subcell lattice parameter), however, the existence of both weak and intense reflections on electron diffraction (ED) and synchrotron XRD data gives evidence of different periodicities within the material. Careful reconstruction of reciprocal space from ED data and Le Bail refinement of synchrotron and then neutron powder diffraction data helped to establish the incommensurate structure, similar to studies of $Bi_{1-x}Sr_xMnO_3$ [13, 14] and $Bi_{1-x}Ca_xMnO_3$ [15], with a subcell of

dimension $\sqrt{2}a_p \times 2a_p \times \sqrt{2}a_p$, and orthorhombic superspace group *Ibmm(α00, 0β0)mm.ss*. The subcell is modulated by positional and occupational modulations of the atoms in higher dimensional space along the ⟨100⟩ and ⟨010⟩ directions, which correspond to ideal cubic perovskite directions $\langle 1\bar{1}0\rangle_p$ and $\langle 001\rangle_p$ respectively. For consistency, throughout this work we will relate all crystallographic directions back to those of the ideal cubic perovksite unit cell and denote these as $\langle hkl\rangle_p$. The modulation in the BMN structure is described by two modulation vectors $q_1=\alpha a^*$ (α=0.4930(3)) and $q_2= \beta b^*$ (β= –0.4210(7)), which define 4th and a 5th dimension and occur along $\langle 1\text{-}10\rangle_p$ and $\langle 001\rangle_p$ directions respectively.

To demonstrate the behavior of the incommensurate structure the large approximant cell $71\sqrt{2}a_p \times 38a_p \times \sqrt{2}a_p$ was generated based on the subcell $\sqrt{2}a_p \times 2a_p \times \sqrt{2}a_p$ of superspace group *Ibmm(α00, 0β0)mm.ss* (Figure 4.1a, b). The Bi displacements calculated for this large approximant cell along the $\langle 1\bar{1}0\rangle_p$ direction cancel to give an almost non-polar structure with a polarization of 2 μC/cm^2. In contrast the polarization obtained for a small commensurate polar orthorhombic cell *P*2$_1$*mn* ($2\sqrt{2}a_p \times 4a_p \times \sqrt{2}a_p$) (Figure 4.1c), previously identified as the best commensurate approximation to the incommensurate structure is 56 μC/cm^2. This significant difference observed between these two approximant cells indicate that the modulations over a long-range in the large approximant incommensurate supercell $71\sqrt{2}a_p \times 38a_p \times \sqrt{2}a_p$ induce locally polar regions, which cancel over longer length scales to produce long-range antiferroelectricity. The size of polar nanoregions (PNR) cannot be directly determined from the incommensurate or the commensurate structure and it can be only estimate with a good approximation. The reasonably good fit of commensurate subcell *P*2$_1$*mn* to the long-range Bragg data indicate that, the minimum size of the polar regions for the long-range crystallographic structure at RT is at least the size of approximant commensurate subcell $2\sqrt{2}a_p \times 4a_p \times \sqrt{2}a_p$ (a = 11.1496 Å b = 15.5302 Å and c = 5.5092 Å). On the other hand, the absence of polarity in an approximate incommensurate supercell ($71\sqrt{2}a_p \times 38a_p \times \sqrt{2}a_p$) demonstrate that polar regions are at most half this size. What is clear is that the

size of the polar regions are hard to define based on long-range crystallographic models.

(a)

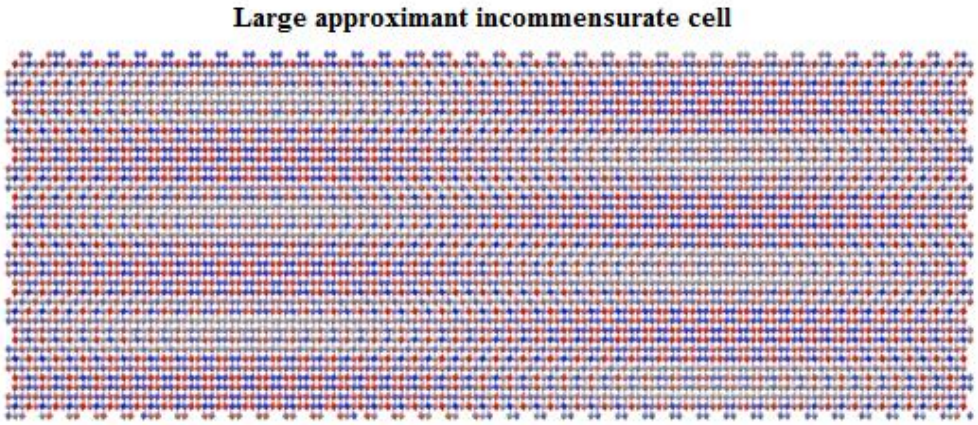

(b) (c)

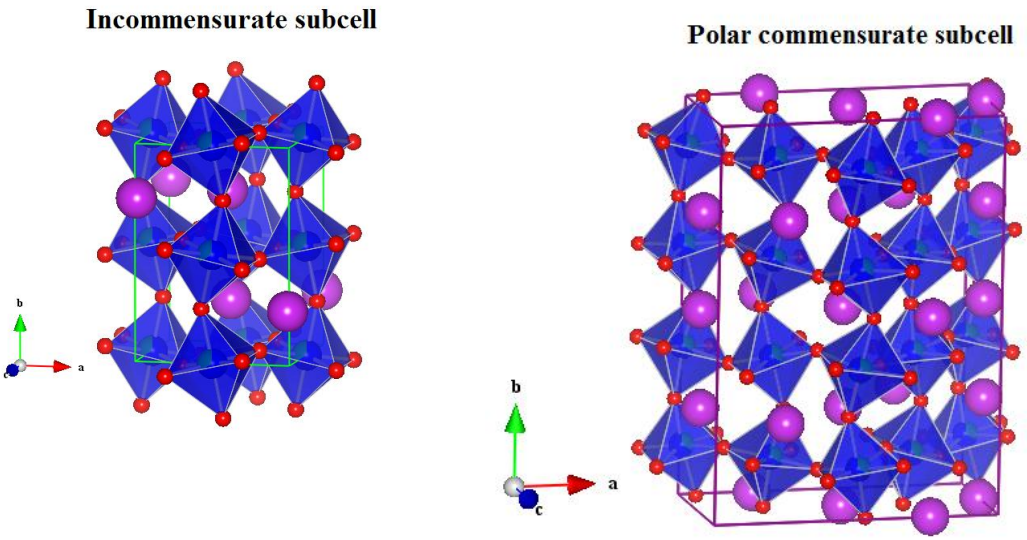

Figure 4.1. *(a) Large approximant cell of dimension* $71\sqrt{2}a_p \times 38a_p \times \sqrt{2}a_p$ *generated from (b) the incommensurate subcell of dimension* $\sqrt{2}a_p \times 2a_p \times \sqrt{2}a_p$*;(c) The best commensurate (periodic 3-dimensional structure) subcell approximation with polar orthorhombic space group* $P2_1mn$ *and cell dimension* $2\sqrt{2}a_p \times 4a_p \times \sqrt{2}a_p$*. The atom spheres are denoted by colours: Bi(purple), Ti, Fe and Mg (blue octahedra) and O(red).*

The BMN structure and the A site environment is distorted due to the long period antiferroelectric displacement modulation giving rise to a wide range of Bi environments.

Table 4.1. *Summary of the A site interatomic distances of $Bi_2Mn_{4/3}Ni_{2/3}O_6$ [12].*

	Average / Å	Min / Å	Max / Å
Bi-O1(i)	2.789(15)	2.217(18)	3.366(12)
Bi-O1	2.822(15)	2.217(18)	3.366(12)
Bi-O1(iv)	3.14(4)	2.85(5)	3.49(5)
Bi-O1(v)	2.47(4)	2.03(5)	2.78(5)
Bi-O2	3.05(3)	2.56(3)	3.62(3)
Bi-O2(vi)	2.52(3)	2.00(4)	3.12(3)
Bi-O2(vii)	2.53(3)	2.01(4)	3.12(3)
Bi-O2(v)	3.03(3)	2.56(3)	3.62(3)
Bi-O2(iii)	2.53(3)	2.00(4)	3.12(3)
Bi-O2(viii)	3.05(3)	2.56(3)	3.62(3)
Bi-O2(ix)	3.05(3)	2.56(3)	3.62(3)
Bi-O2(x)	2.55(3)	2.01(4)	3.12(3)

(a)

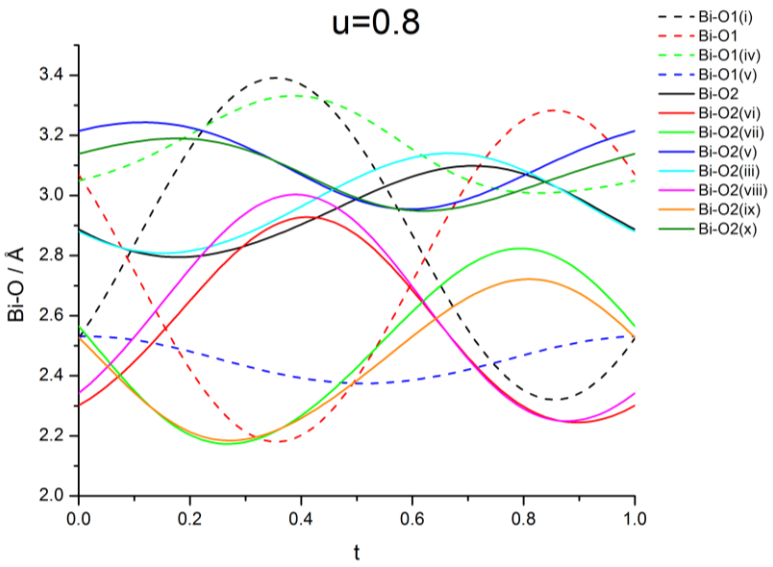

(b)

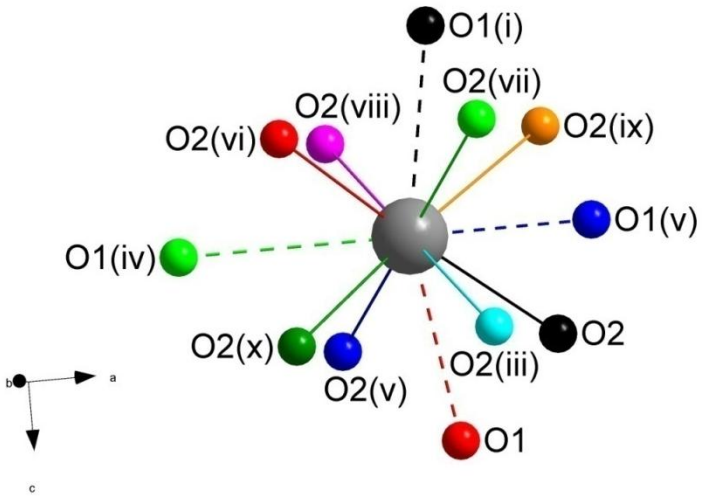

Figure 4.2. *Variation of the Bi-O distances as a function of two origins in 4th (t = 0-1) and 5th (u = 0.8) dimension, where (t, u) are numbers describing the initial phase of the waves; (b) The A site environment within 12 coordinate system in the incommensurate subcell with Bi atom (grey) and the O anions coloured to match the plot in (a) [12].*

The same feature is observed for B site cations, where Mn and Ni octahedras are distorted by the modulation (Table 4.2 and Figure 4.2), however the modulation range is significantly smaller than for A site cations.

Table 4.2. *Summary of the B site interatomic distances of $Bi_2Mn_{4/3}Ni_{2/3}O_6$ [12].*

	Average / Å	Min / Å	Max / Å
Mn-O1	1.99(3)	1.88(3)	2.16(2)
Mn-O1(xi)	1.99(3)	1.88(3)	2.16(2)
Mn-O2	2.00(3)	1.80(3)	2.13(3)
Mn-O2(xi)	2.00(3)	1.80(3)	2.13(3)
Mn-O2(xii)	2.00(3)	1.80(3)	2.13(3)
Mn-O2(x)	2.00(3)	1.80(3)	2.13(3)

(a)

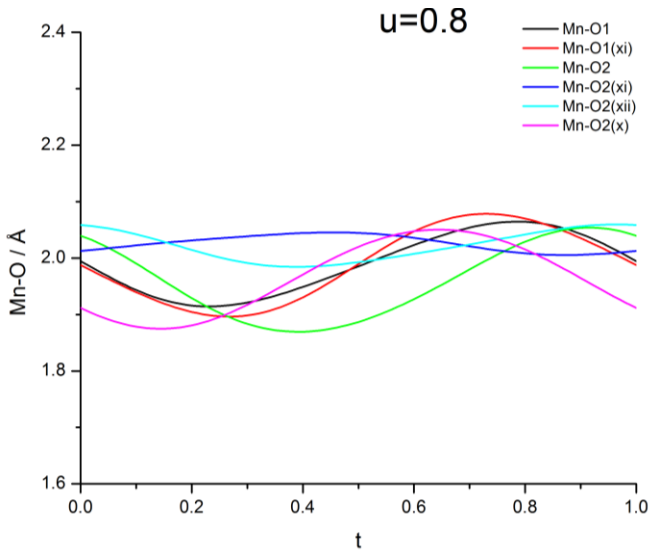

(b)

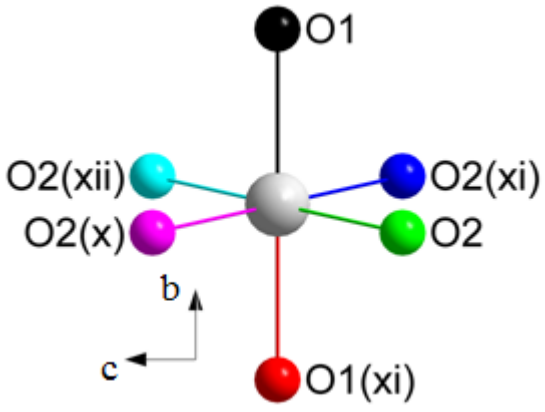

Figure 4.3. *Variation of the Mn/Ni-O distances as a function of two origins in 4^{th} (t = 0-1) and 5^{th} (u = 0.8) dimension; (b) Mn/Ni octahedra in the incommensurate subcell with B site cation atom (grey) and the O anions coloured to match the plot in (a) [12].*

There is B site ordering due to occupational modulations in the incommensurate structure with general pattern of B site ordering observed in the long-range approximant supercell $71\sqrt{2}a_p \times 38a_p \times \sqrt{2}a_p$ (Figure 4.4). The average modulated occupancies of the B site cations with low and high probability of finding Mn are denoted as red and blue atoms respectively, whereas grey atoms correspond to $Mn_{0.667}$, which represents the equal probability of finding Mn and Ni cations on the B site in accordance to 2:1ratio in $Bi_2Mn_{4/3}Ni_{2/3}O_6$. The distinguished Mn and Ni cations based on their fractional modulated occupancies clearly demonstrate the clustering of Mn/Ni cations.

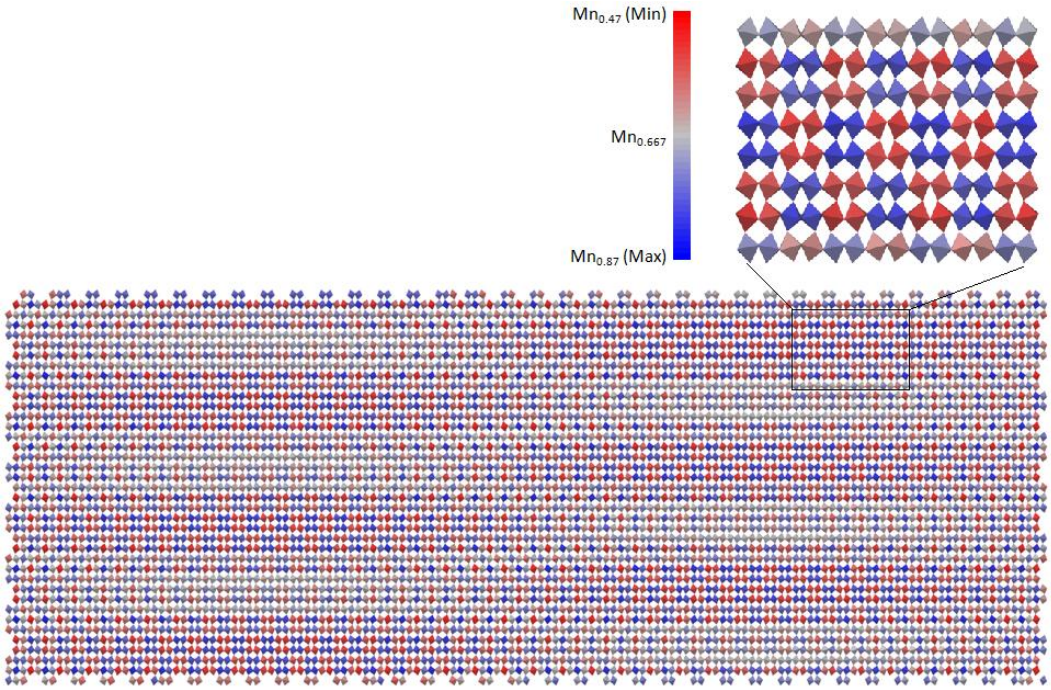

Figure 4.4. *Approximant cell of incommensurate structure ($71\sqrt{2}a_p \times 38ap \times \sqrt{2}a_p$), viewed down along the non-modulated $\langle 110 \rangle_p$ axis. The cell has sufficient size to provide a view of the range of environments and demonstrate the clustering of Mn/Ni cations due to occupational modulations; B site cations are coloured according to fractional occupancy, with blue and red atoms corresponding to high and low occupancy probability of Mn cations whereas grey atoms represent the $Mn_{0.667}$ in accordance to Mn:Ni ratio 2:1.*

The incommensurate structural descriptions are still derived from the long-range phenomena of diffraction, and so represent a long-range average structure which may not faithfully represent the local structure of a complex A site and multiple B

site cations. In order to determine the true local structure of a material one has to reduce reliance on Bragg diffraction make use of diffuse scattering which lies in the background of a diffraction pattern. Thus, an accurate view of the structure requires going beyond the average structure derived from Bragg diffraction and include the local structure information from total scattering.

4.1.3 Supercell of incommensurate structure

To be able to compare the average modulated structure with local structure generated from RMC modeling, the supercell of incommensurate structure was generated. The approximant supercell was obtained from the subcell of *(Ibmm(α00, 0β0)mm.ss)* with dimension $\sqrt{2}a_p \times 2a_p \times \sqrt{2}a_p$ generated using *Jana* [16]. A multiplicity 10*a* 7*b* 10*c* of lattice parameters *a* = 5.5729 Å *b* = 7.7686 Å and *c* = 5.5091 Å give an incommensurate supercell with approximate dimensions of 55 × 55 × 55 Å³ (Figure 4.5). Ten supercells were generated with different origins of the incommensurate modulation (*e.g.* *t*=1/10, *u*=1/10; *t*=1/10, *u*=2/10) where *t* and *u* describe the initial phase of the double modulation wave vectors $q_1=\alpha a^*$ (α=0.4930(3)) and $q_2=\beta b^*$ (β= –0.4210(7)). The results (e.g. bond distances, A and B site displacements) from ten incommensurate supercells were then averaged to produce a result free from any bias from the starting point of the modulation, and thus represent "complete" incommensurate model. The incommensurate cell is aligned with ⟨100⟩ and ⟨010⟩ oriented along $\langle 1\bar{1}0\rangle_p$ and $\langle 001\rangle_p$ respectively in the primitive cubic perovskite cell and ⟨001⟩ oriented along $\langle 110\rangle_p$.

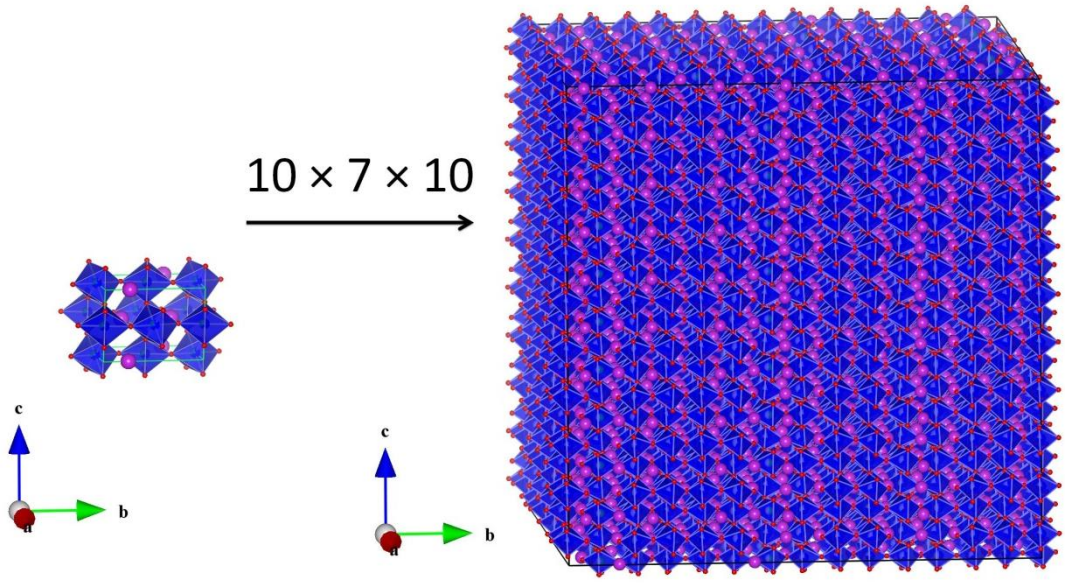

Figure 4.5. *Subcell of incommensurate structure (Ibmm(α00, 0β0)mm.ss with dimension* $\sqrt{2}a_p \times 2a_p \times \sqrt{2}a_p$ *and one of ten supercells obtained by multiplicity of their 10 × 7 × 10 subcells. The atom spheres are denoted by colours: Bi (purple), B site (blue) and oxygen (red).*

4.2 Local structure at RT

4.2.1 Generation of RMC model

Neutron total scattering data at RT were collected at the General Materials diffractometer (GEM) [17] at the ISIS pulsed spallation neutron source as described in the section 2.3.2. The sample of approximate weight 5 g, contained in an 8 mm vanadium can, was collected for 920 μAh over the scattering vector range $0.3 \leq Q \leq 50$ Å^{-1}. The correction of total scattering data were normalized and corrected using GUDRUN software [18] and the *stog* utility in RMCProfile [19, 20] as described in the section 2.3.2. The application of Q_{max} = 30 Å^{-1} simultaneously maximized the real space resolution and minimized termination ripples in the pair distribution function data.

The starting configuration of the RMC model is based on the Bragg intensity of the Rietveld refinement in GSAS, and generated from a commensurate $2\sqrt{2}a_p \times 4a_p \times \sqrt{2}a_p$ subcell (a = 11.1496 Å b = 15.5302 Å and c = 5.5092 Å) in the polar orthorhombic space group $P2_1mn$, previously identified as the best commensurate

approximation to the incommensurate structure (Figure 4.6). 5 × 4 × 10 expansion of this subcell produced a supercell of dimensions 55 × 62 × 55 Å^3 and containing 16,000 atoms (Figure 4.7). The total scattering data, *F(Q)*, were also convoluted with a box function to account for the broadening in the calculated data due to the finite RMC configuration size. Fits to the *F(Q)* data were carried out in the range $Q \leq 30$ Å^{-1}. The real space data total correlation function, *T(r)*, were fit over the range of the RMC configuration with r ≤ 27.5 Å, which corresponds to the shortest lattice vector. The crystallographic directions of the RMC model remain the same as in the applied commensurate subcell. The RMC supercell is aligned then with ⟨100⟩ oriented along $\langle 1\bar{1}0\rangle_p$, the direction of the Bi displacement giving rise to polarity in the commensurate subcell, whereas ⟨010⟩ and ⟨001⟩ are oriented along the non-polar directions $\langle 001\rangle_p$ and $\langle 110\rangle_p$ respectively. Thus both RMC and incommensurate models representing the local and average structure respectively, have the same settings in relation to the crystallographic directions presented on Figure 4.8.

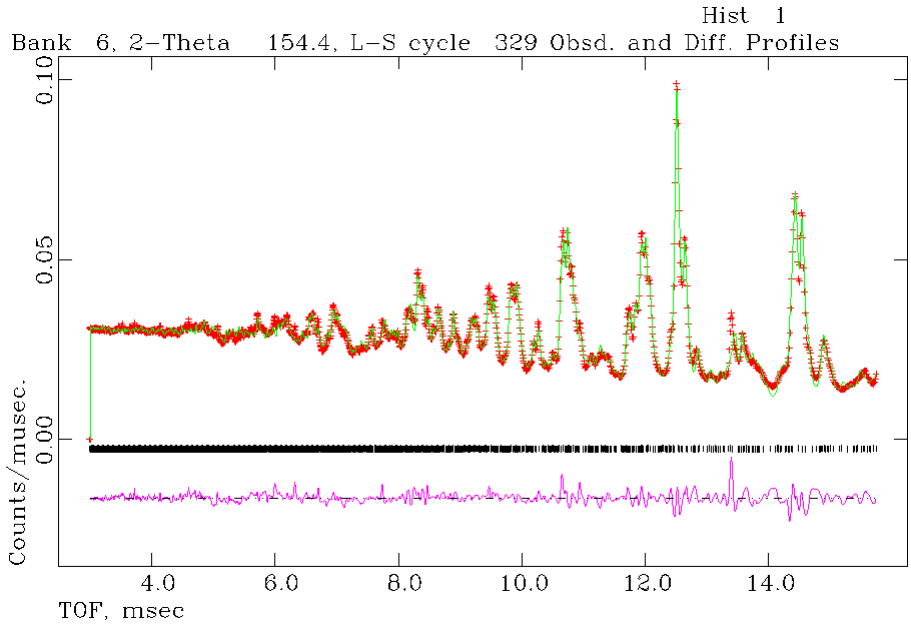

Figure 4.6. *Rietveld refinement (backscattering bank) of* $Bi_2Mn_{4/3}Ni_{2/3}O_6$ *with polar commensurate subcell* $P2_1mn$ *at room temperature, lattice parameters a = 11.1496 Å b = 15.5302 Å and c = 5.5092 Å and weighted agreement factor* R_{wp}*=4.03%. The red crosses are observed data, the solid green line is the*

calculated pattern, whereas the pink line represent the difference between observed and calculated patterns.

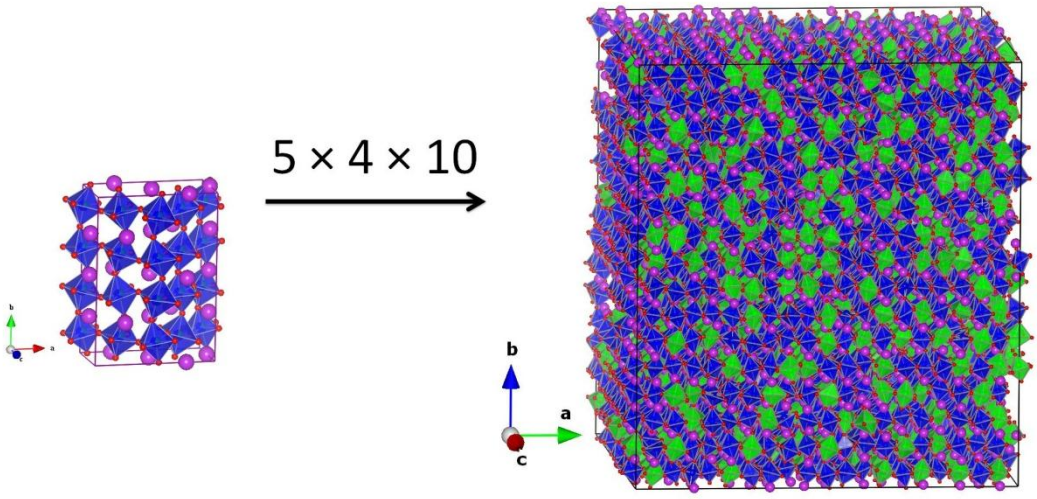

Figure 4.7. *Polar commensurate subcell $P2_1mn$ with dimension $\sqrt{2}a_p \times 2a_p \times \sqrt{2}a_p$ and one of the 20 RMC supercells obtained by multiplicity of their 5 × 4 × 10 subcells. The atom spheres and octahedra are denoted by colours: Bi (purple), Mn (blue), Ni (green) and oxygen (red).*

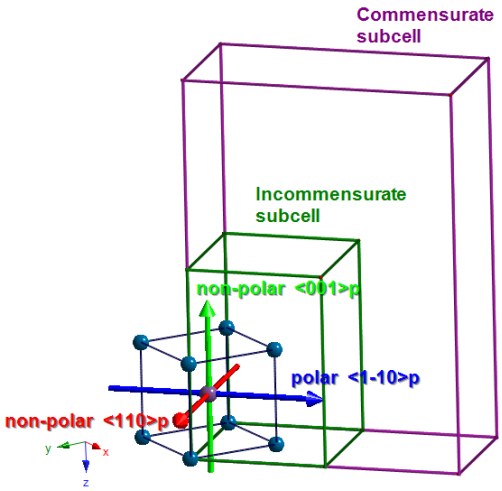

Figure 4.8. *Representation of $Bi_2(Mn_{4/3}Ni_{2/3})O_6$ (Bi shown as pink-purple spheres, B cation site as light blue spheres) within pseudocubic (dark blue), commensurate average $P2_1mn$ (purple) and incommensurate orthorhombic Ibmm (green) unit cells with corresponding pseudocubic polar direction $\langle 1\bar{1}0\rangle_p$, and two non-polar directions $\langle 110\rangle_p$ and $\langle 001\rangle_p$.*

The models during RMC refinement are not constrained by the space group symmetry as they are in the Rietveld refinement. Thus, to keep a model physically feasible during RMC refinement constraints and restraints such as distance windows (DW), bond valence sums (BVS) and interatomic potentials have been applied as described in the section 2.4.1. In the first instance a reasonable fit for the RT structure was obtained using only DW constraints, but sharp cut-off features caused by the DW minimum and maximum separation boundary were observed for the shortest and furthest distances in the partial pair distribution functions (Figure 4.9).

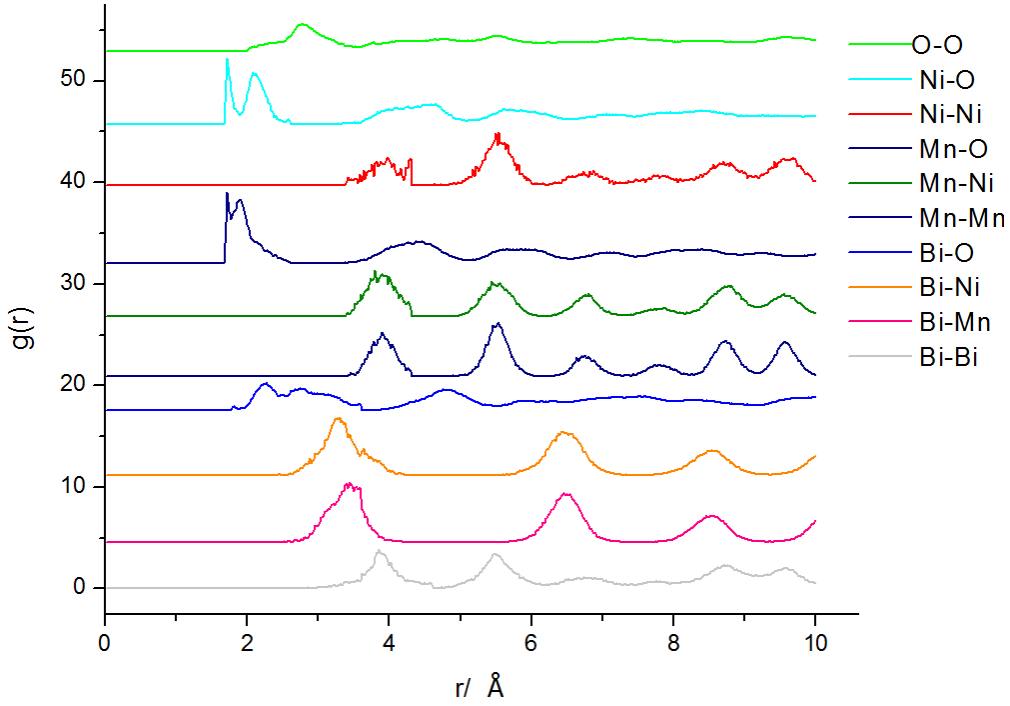

Figure 4.9. *Partial pair distribution functions showing sharp cut-offs in the Ni-O and Mn-O partials at 1.8 Å as a result of DW constraints.*

The application of BVS constraints for each cation-oxygen pair improved these cut-off features, and in combination with interatomic potential constraints (as explained in the section 2.4.1) helped to distinguish the Mn and Ni atoms, which occupy the same crystallographic B site. The interatomic potential restraints allowed the preservation of regular bond Ni-O environments during the refinement while also adequately fitting the observed data (Figure 4.10).

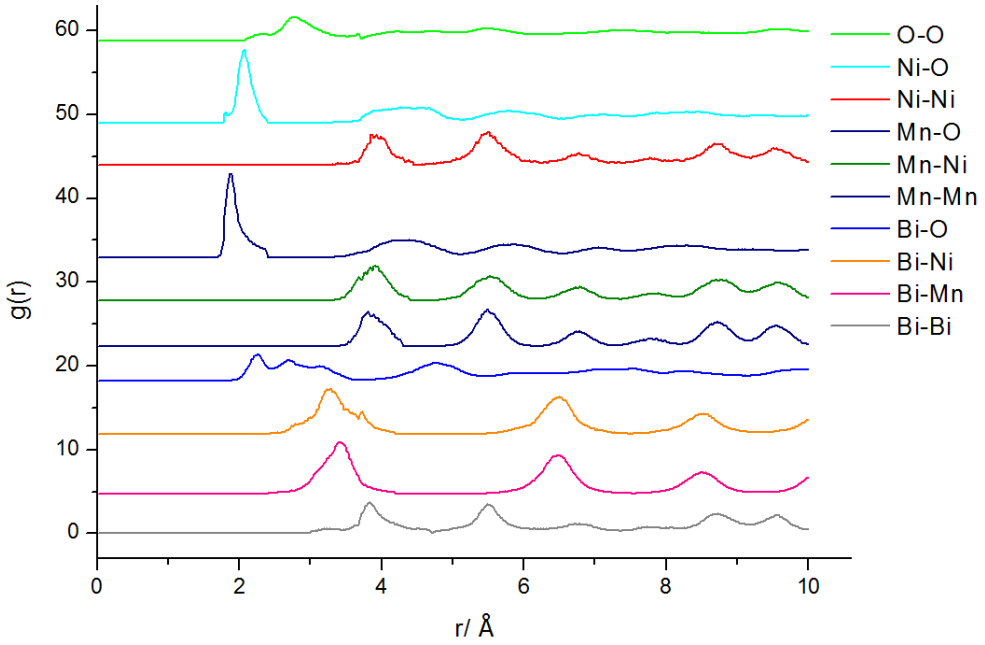

Figure 4.10. *Partial pair distribution function without sharp cut-offs after applying DW, BVS constraints and interatomic potential restraints.*

Reverse Monte Carlo refinements were carried out using *RMCProfile* [20] described in section 2.4. Several RMC refinement stages were applied to obtain good fits to the observed Bragg profile, total scattering structure factor *F(Q)* and the pair distribution function *G(r)*. At the initial stage, the B site cations in the starting configurations were randomly swapped in absence of data, to obtain a completely random distribution. In the next step the RMC fit to the data was initiated in which only swapping of atoms was allowed, with no permitted translation steps. The refinement was continued until no further improvement in χ^2 was observed. In the last stage of RMC refinement the B site atom swapping was replaced by atomic translation moves. B site swapping was not possible while interatomic potential restraints, necessary to maintain chemically sensible Ni-O bond environments, were applied. Thus, the application of DW, BVS constraints and interatomic potential restraints during RMC refinement, provide sensible physical bond distances of atom pairs, and very good fits to the observed Bragg profile, total scattering structure factor *F(Q)* and the pair distribution function *G(r)* (Figure 4.11). The refinements were repeated for 20 RMC models to improve the statistical accuracy of the results.

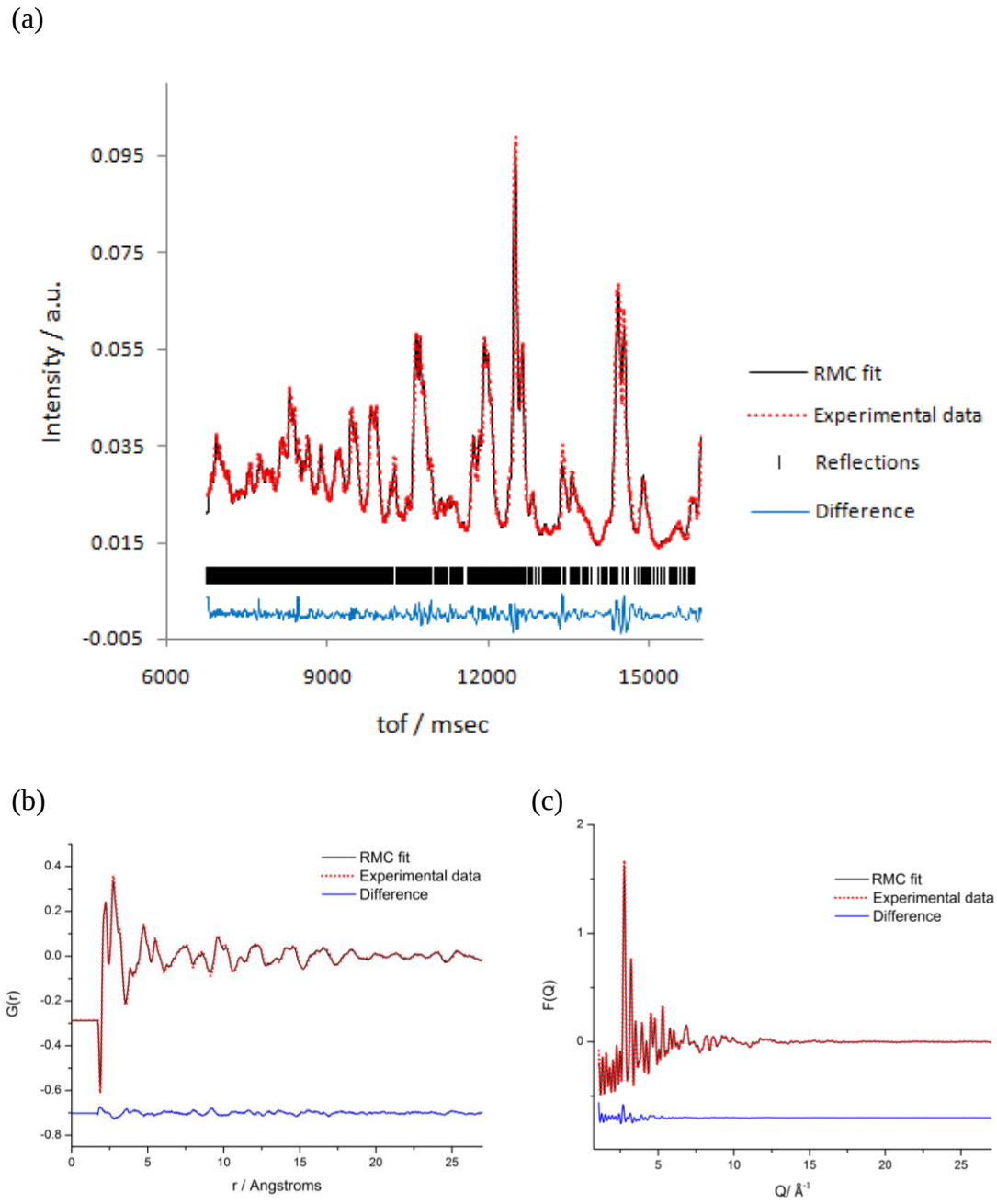

Figure 4.11. *Comparison between measured and calculated functions of one of the RMC model for the local structure of $Bi_2Mn_{4/3}Ni_{2/3}O_6$ at RT showing very good fit for: (a) Bragg profile data; (b) total correlation function G(r); (c) total scattering structure factor F(Q).*

The application of BVS constraints provided sensible oxidation state for every chemical element. There are four distinct chemical elements in the BMN material with calculated oxidation state and averaged for 20 RMC models: Bi=3.04(4),

Mn=3.43(9), Ni=1.88(2) and O=1.99(2) (Figure 4.12). The oxidation state of Mn cations is close to 3.5, as the Mn site is occupied by both Mn^{3+} and Mn^{4+} with an ratio 1:1.

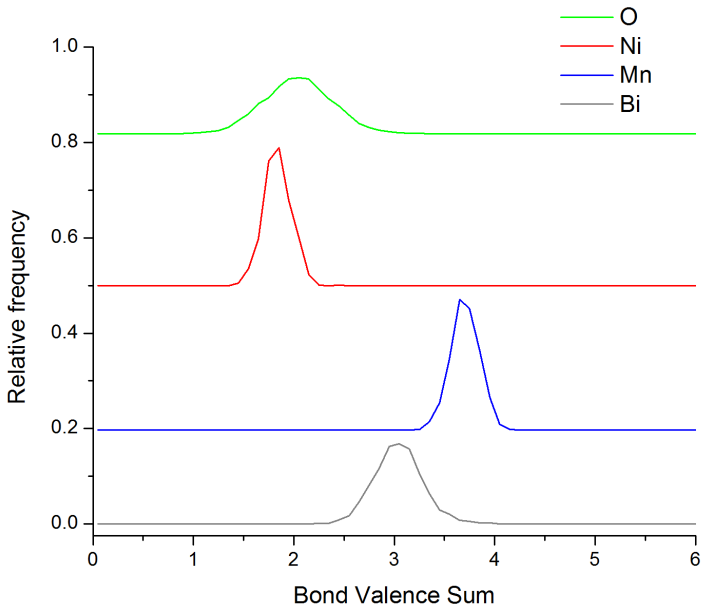

Figure 4.12. *The distribution of Bond Valence Sum values determined for RMC models of BMN at RT.*

4.2.2 Analysis of the pair distribution function

Initial comparison of the partial $g_{Bi\text{-}O}(r)$ between the average incommensurate model and the RMC local structure showed similar Bi-O distances for both models (Table 4.3). The Bi^{3+}-O^{2-} distances at RT produced three main groups of bond distances in the RMC local structure. The first strong peak in the RMC $g_{Bi\text{-}O}(r)$ at the a shortest Bi-O distances of 2.252(5) Å data has a relative area equivalent to 3.84 oxygens, indicating that Bi atoms move towards approximately four nearest oxide neighbours (Figure 4.13). This is identical to the $BiTi_{3/8}Fe_{2/8}Mg_{3/8}O_3$ (BTFM) Bi-O bond distance of 2.25 Å [21] at room temperature, described in chapter 3. The other two Bi-O groups in both RMC and the average incommensurate models (2.685(2) Å, 3.151(9) Å and 2.428(32) Å, 2.989(34) Å respectively) are less comparable to BTFM, as they have shorter bond distances in comparison to the equivalent BTFM peaks 2.79 Å and 3.32 Å.

Table 4.3. *Comparison of Bi-O bond distances from the partial $g_{Bi\text{-}O}(r)$ analysis of BMN calculated for the RMC and average incommensurate models. The mean bond distances were obtained by fitting Gaussian functions to the observed partial $g_{Bi\text{-}O}(r)$ (Figure 4.13).*

	Local structure (RMC model) / Å	Average structure (Incommensurate model) / Å
Bi-O	2.252(5) 2.685(2) 3.151(9) (3.84:4.8:3.36)*	2.241(13) 2.428(32) 2.989(34) (1.29:4.26:6.45)*

* Approximate ratio of bond distances (summed to 12 oxygen coordinate system) obtained from the integrated areas of peaks in $g_{Bi\text{-}O}(r)$ at RT structure.

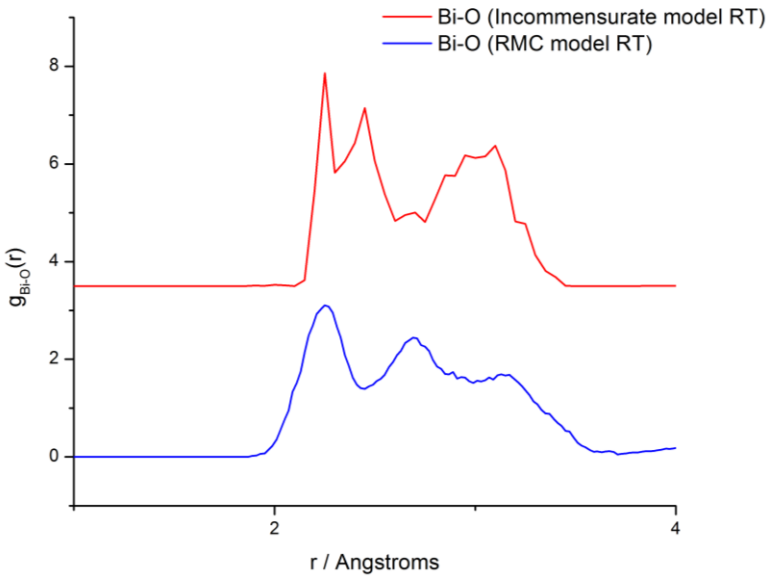

Figure 4.13. *The partial pair correlation functions of $g_{Bi\text{-}O}(r)$ derived from the RMC and average incommensurate model at RT.*

The average incommensurate $g_{Bi\text{-}O}(r)$ also indicates three groups of bond distances, however, closer inspection of the individual distributions for the 10 incommensurate models studied shows two different shapes of distribution (Figure 4.14); half of the models show sharp first peaks and half show distribution of two groups of bond distances, and thus has been fitted to two Gaussian peaks. The presence of two types of $g_{Bi\text{-}O}(r)$ distribution is a result of the modulations used in the incommensurate structure. The distribution with two groups of bonds

defined as incommensurate models part 1 (Figure 4.14) gives Bi-O bond distances of 2.386(4) Å and 3.007(3) Å with a ratio of 5.82:6.18 (Table 4.4). This is consistent with the antiparallel displacement of Bi cations along $\langle 110 \rangle_p$ which would ideally give rise to 5 short, 2 medium and 5 long Bi-O bonds; we do not observe the two medium bonds as they will lie beneath the two main observed peaks in the $g_{Bi\text{-}O}(r)$. The antiparallel displacement of Bi cations along $\langle 110 \rangle_p$ is discussed further in section 4.2.3. On the other hand, the sharp peak in distribution defined as incommensurate models part 2 (Figure 4.14) is likely due to a maxima in the modulations which add up to produce a narrow distribution of short Bi-O bonds which is not representative of the local structure observed by RMC. The application of incommensurate modulations to atomic positions produces a discontinuous distribution of Bi-O distances due to local minima and maxima in the modulated displacements. The average incommensurate model distribution (Figure 4.13) contains features from both types of distribution and as such makes determining average bond lengths and ratios from this data is misleading. Furthermore, the comparison of the groups of Bi-O bond distances between the RMC and the average incommensurate models indicates broader range of Bi-O bond distances. The relatively broad Bi-O distributions in the RMC model are attributed to thermal motion, whereas the average incommensurate model includes thermal motion as time averaged thermal ellipsoids around an average atomic position.

Table 4.4. *Comparison of Bi-O bond distances from the partial $g_{Bi\text{-}O}(r)$ analysis of BMN calculated for the average incommensurate models part 1 and 2. The mean bond distances were obtained by fitting Gaussian functions to the observed partial $g_{Bi\text{-}O}(r)$ (Figure 4.14).*

	Average structure (Incommensurate models part1) / Å	Average structure (Incommensurate models part2) / Å
Bi-O	2.386(14) 3.007(11) (5.82:6.18)*	2.230(12) 2.437(9) 2.965(11) (2.36:3.24:6.40)*

* Approximate ratio of bond distances (summed to 12 oxygen coordinate system) obtained from the integrated areas of peaks in $g_{Bi\text{-}O}(r)$ at RT structure.

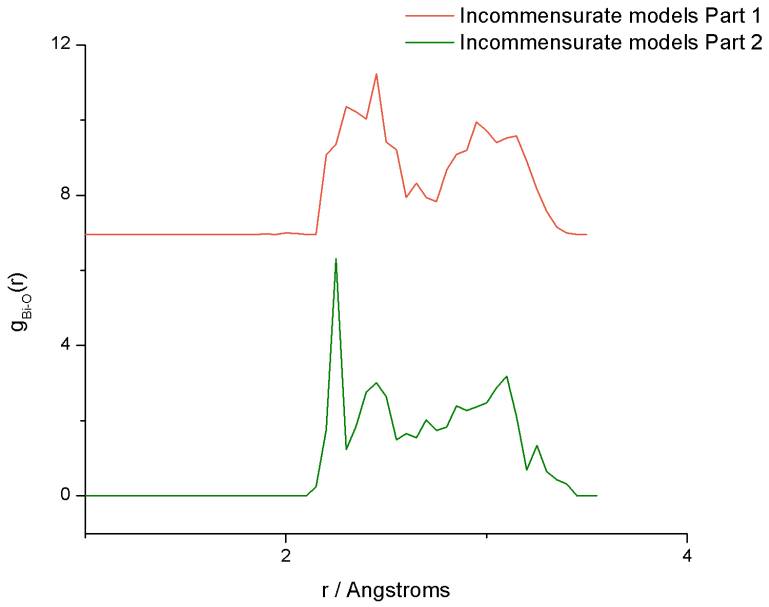

Figure 4.14. *The partial pair correlation functions of $g_{Bi-O}(r)$ derived from the average incommensurate model at RT.*

The Bi^{3+} cations are particularly sensitive to the local B site occupancy. Inspection of the distribution of bond distances between Bi and B site cations (Table 4.5 and Figure 4.15) shows that Bi^{3+} cations prefer to move toward Ni^{2+} neighbours and away from manganese cations (Mn^{3+}, Mn^{4+}) which is in agreement with expectations based on electrostatics. The lower charge of nickel cations causes weaker repulsive forces between Bi-Ni than Bi-Mn, and in consequence this causes more favorable movement of the A site cations towards nickel atoms. These differences are shown by the respective distances: Bi-Mn 3.412(1) Å and Bi-Ni 3.273(1) Å in the RT structure, where we also observe a small splitting of peaks which is possibly an effect of the applied potential restraints.

Table 4.5. *Comparison of Bi-B site bond distances between the incommensurate model and local structure at RT.*

	Average structure (Incommensurate model) / Å	Local structure (RMC model) / Å	
Bi – B site	3.32(4) 3.435(14)	Bi - Mn	Bi – Ni
		3.412(1)	3.273(1)

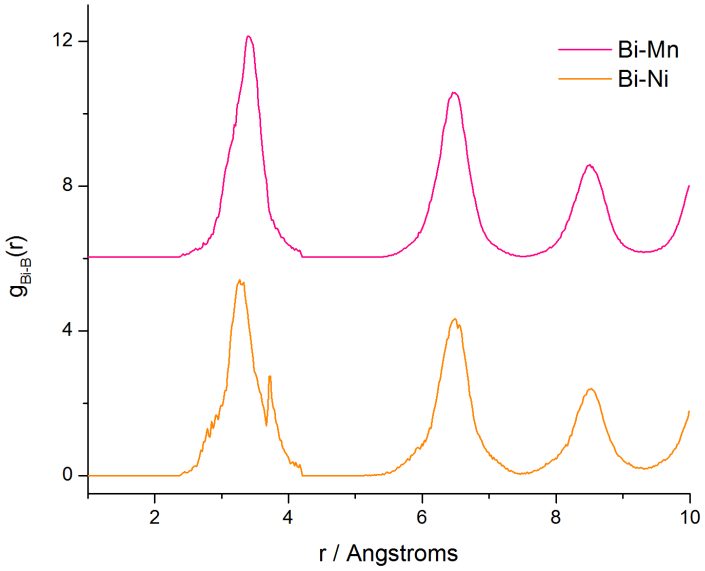

Figure 4.15. *The partial pair correlation functions of $g_{Bi\text{-}B}(r)$ derived from the RMC model at RT.*

The local bonding of the B site environment is also revealed by the partial pair distribution $g_{B\text{-}O}(r)$ and the instantaneous bond angle distributions $g_{O\text{-}B\text{-}O}(\theta)$, $g_{B\text{-}O\text{-}B}(\theta)$. Comparison of the partial $g_{B\text{-}O}(r)$, where two B cations are occupied onto one site, reveals a broader range of bond distances in the RMC local structure. The interatomic potential applied to Ni-O pairs in the RMC refinement yields a distribution of $g_{Ni\text{-}O}(r)$ (Figure 4.16) with very regular bond distances of 2.075(1) Å, which are in agreement with those reported for $Bi^{3+}_{0.5}Bi^{5+}_{0.5}Ni^{2+}O_3$ [3, 9]. The $g_{Mn\text{-}O}(r)$ in contrast presents a more complex asymmetric distribution due to the presence of both undistorted Mn^{4+} and Jahn-Teller (J-T) distorted Mn^{3+}. Both Mn^{3+} and Mn^{4+} have been extensively studied in the past; Mn^{4+} has six bond distances of approximately 1.9 Å, while Mn^{3+} with J-T distortions adopts a broad variety of bond distances. Mn^{3+} owes its distortions to a high spin d^4 electron configuration, where three electrons are in the lower threefold t_{2g} orbitals and one electron occupies the upper twofold degenerate e_g orbital. This doubly degenerate e_g level splits when the local symmetry is lower than octahedral, resulting in a lowering of the energy of the occupied state. Thus, degeneracy of the e_g level is removed by the crystal field of the distorted unit cell and Mn^{3+} induces a J-T distortion in the crystal. On the other hand, Mn^{4+} with the spin configuration d^3

does not generate J-T distortions, as the e_g orbital is unoccupied [22, 23]. The most common J-T phenomena produce lattice distortions giving four short (~1.92-1.96 Å) and two long bond distances (~2.11-2.16 Å) herein referred to as 4:2 J-T, as observed in manganites like $LaMnO_3$ [24] or A site doped $La_{1-x}Ca_xMnO_3$ [25] and $La_{1-x}Sr_xMnO_3$ [26]. However, in a bismuth based perovskite $Bi_{1-x}Ca_xMnO_3$ there is a different pattern of bond distances observed within octahedral symmetry, with two short (~1.9 Å) and two long (~2.1 Å) equatorial bonds, and two apical medium (~1.95 Å) bond distances [15] herein referred to as 2:2:2 J-T. The same J-T feature is also observable in $BiMnO_3$, where ratio 2:2:2 have broader range of bond distance (~1.8 Å, ~2.0 Å and ~2.2 Å) [27], than observed in the $Bi_{1-x}Ca_xMnO_3$. In order to determine which type of J-T distortion is most consistent with our data, the $g_{Mn\text{-}O}(r)$ was fitted with two and three Gaussian peaks. We expect to observe a single Gaussian contribution from undistorted Mn^{4+}, and a range of bond distances from Mn^{3+} (which may be overlapping with Mn^{4+}-O) corresponding to one of the J-T distortion types (4:2 J-T or 2:2:2 J-T). The results of fitting three Gaussian functions to the Mn-O distribution gives a much better fit than the application of two Gaussian functions, and provide average bond lengths of 1.859(9) Å, 1.946(11) Å and 2.146(57) Å (Table 4.6). The ratio of integrated area for these different bond lengths is approximately 6:3:3. The identical ratio for two medium and long bond lengths and better fit of three Gaussian function instead two, indicate Mn-O bond distances in the RMC model are more close with 2:2:2 J-T distortions observed for both $BiMnO_3$ and $Bi_{1-x}Ca_xMnO_3$. The presence of twice the number of short bond lengths than medium or long bonds (ratio of 6:3:3 respectively), is due to the very comparable bond distances for both regular Mn^{4+} and the shortest bond distance in J-T distorted Mn^{3+} cations. However, the integrated area for the different bond lengths is approximately 6:3:3, as opposed to 8:2:2 expected for a purely Mn^{4+} and 2:2:2 J-T Mn^{3+} system, indicating that the observed Mn-O coordination environment is different to an ideal J-T distortion model. The BVS distribution shows a Gaussian distribution around an average oxidation state of 3.43+, indicating that on the local scale Mn adopts an oxygen coordination environment intermediate between that expected Mn^{4+} and Mn^{3+}. The intermediate charge state between that of the J-

T distorted and non-distorted states may explain why the observed $g_{Mn\text{-}O}(r)$ does not completely match that expected for a simple J-T model based on Mn^{4+} and Mn^{3+} alone.

Table 4.6. *Comparison of B site-O bond distances between RMC and incommensurate models at RT.*

	Average structure (Incommensurate model) / Å	Local structure (RMC model) / Å	
		Mn - O	Ni – O
B site – O	1.99(2)	1.859(9) 1.946(11) 2.146(57) (6:3:3)*	2.075(1)

* Approximate ratio of separations obtained from the integrated areas of peaks in $g_{B\text{-}O}(r)$ for RMC model at RT.

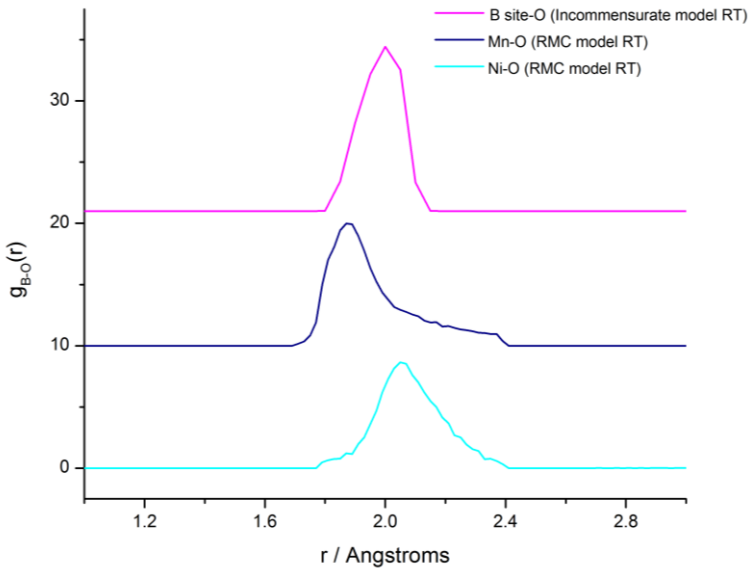

Figure 4.16. *Comparison of the partial pair correlation functions $g_{B\text{-}O}(r)$ between the RMC and incommensurate models at RT.*

The comparison of B-O-B angles (Table 4.7 and Figure 4.17) reveals comparable tilting of octahedra centred on Mn and Ni cations. However the O-B-O bond angle distributions, representing the internal angle of octahedra shows a difference between Mn and Ni atoms, with a narrower distribution of O-Ni-O demonstrating

less displaced Ni in comparison to Mn cations. This is expected as the Mn site contains contribution from both distorted Mn^{3+} and regular Mn^{4+}, in contrast to less displaced Ni^{2+} cations. Thus, the analysis of partial pair distribution function indicate the differences between Mn and Ni cations, whereas the average crystallographic structure provide the same bond distances and angles for both B site cations.

Table 4.7. *Comparison of B-O-B and O-B-O bond angle distributions between RMC and incommensurate models at RT.*

	Average structure (Incommensurate model) angle / °	Local structure (RMC model)	
		Angle / °	FWHM/ °
Mn-O-Mn Mn-O-Ni Ni-O-Ni	157.1	154.77(5)	24.19
		151.48(4)	26.49
		151.52(8)	25.28
O-Mn-O O-Ni-O	92.03 173.89	89.66(5), 165.57(14)	26.61, 20.31
		88.91(7), 168.38(34)	18.37, 19.51

(a) (b)

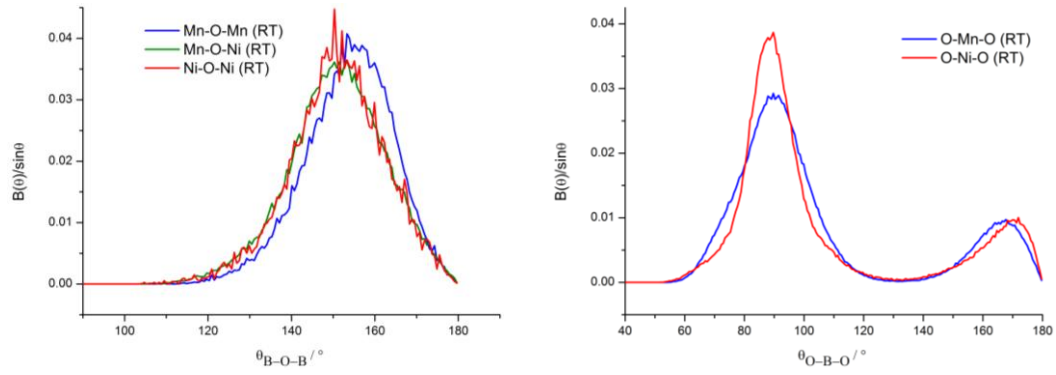

Figure 4.17. *Bond angle distributions of (a) B-O-B; (b) O-B-O for the local structure at RT.*

4.2.3 Analysis of A and B site cation displacements

The A and B site cation environments in the local and average structures are studied by calculations of Bi and B site cations displacements from the oxygen centroids in the same manner like for BTFM in chapter 3. The program calculate bond distances of Bi-O and Mn/Ni-O between the nearest twelve/six oxygen anions of Bi/B site cations respectively and then subtracts it from the already calculated average position. This provides the real displacements along polar $\langle 1\bar{1}0\rangle_p$ and two non-polar directions $\langle 110\rangle_p$ and $\langle 001\rangle_p$, as opposed to displacements from the average position. The calculation of the total A site cation displacements (Figure 4.18a) distribution along non-polar $\langle 110\rangle_p$ (Figure 4.18d) show bimodal displacements, characteristic for the antiferroelectric behavior of BMN, and a single Gaussian shape along polar $\langle 1\bar{1}0\rangle_p$ and non-polar $\langle 001\rangle_p$ (Figure 4.18b, c) in both the average incommensurate and the RMC models. The distribution along polar $\langle 1\bar{1}0\rangle_p$ is represented by a single broad Gaussian shape, indicating the presence of both positive and negative displacements of Bi^{3+} cations. Despite the presence symmetrical distribution, the commensurate subcell $P2_1mn$ produce polarity along $\langle 1\bar{1}0\rangle_p$, due to different magnitude of opposite displacements, however these polar regions cancel each other over long-range and demonstrate antiferroelectricity in the average incommensurate structure. The comparison of the distribution of atomic displacements show a broader feature in the RMC model than in the average incommensurate model. This is consistent with the difference observed for $g_{Bi\text{-}O}(r)$ distribution, and as a consequence is attributed to the instantaneous snapshot of thermal motion in the RMC model of local structure, as opposed to the averaging of this motion in the crystallographic structure.

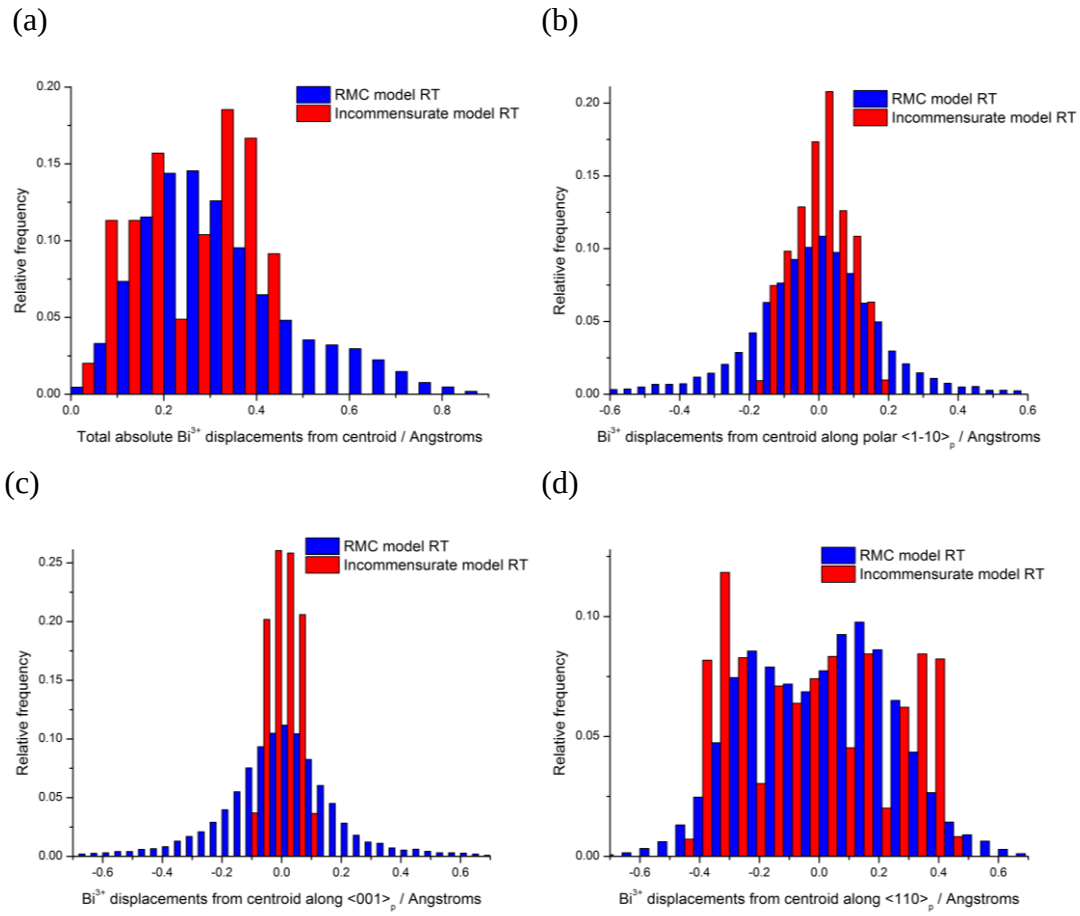

Figure 4.18. *Comparison between RMC and the incommensurate model of the (a) total absolute Bi^{3+} cations displacement calculated from the centroid of the twelve coordinating oxygens, and (b), (c) and (d) along polar $\langle 1\bar{1}0\rangle_p$, and two non-polar $\langle 001\rangle_p$ and $\langle 110\rangle_p$ directions respectively.*

The same calculations are performed for B site cations, where displacements of the octahedra are derived for every Mn and Ni atom in the RMC model. The distinct behavior of B site Ni cations present in the O-B-O bond angle distribution is also consistent with the measured displacements, where the observed distribution (Figure 4.19b, c) along the polar $\langle 1\bar{1}0\rangle_p$, and non-polar $\langle 001\rangle_p$ directions show less displaced Ni atoms in comparison to Mn.

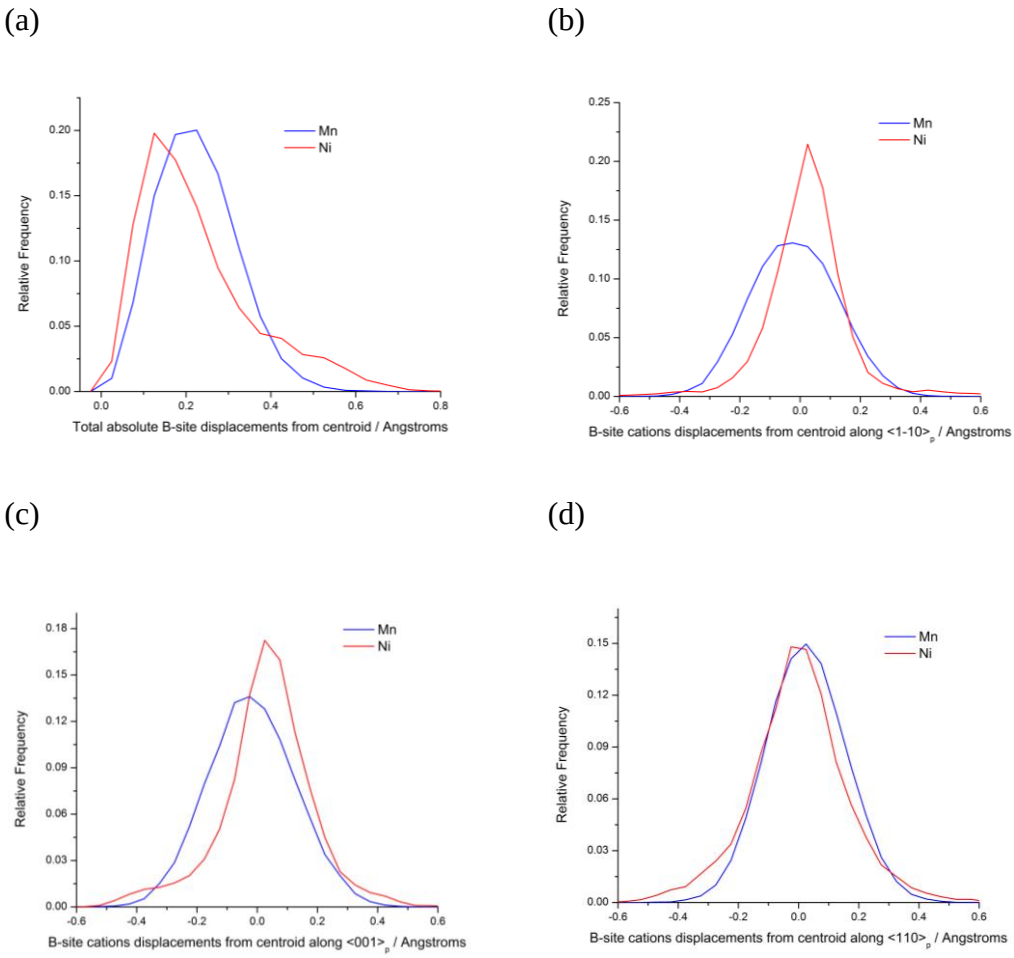

Figure 4.19. *(a) Total absolute displacements of the B site cations from the centroid of the coordinating oxygens for local structure at RT; (b), (c) and (d) Distribution of displacements of B site cations from oxygen centroid along polar* $\langle 1\bar{1}0\rangle_p$, *and two non-polar directions* $\langle 001\rangle_p$ *and* $\langle 110\rangle_p$ *respectively.*

Representations of the local structure are establish by deriving the most frequently occurring Bi and B site cation displacements (modal displacements), while oxygen atoms have crystallographically averaged positions (Figure 4.20a, b). The mode value of Bi^{3+} displacements in the RMC models have the most significant components of 0.283 Å along non-polar $\langle 110\rangle_p$ direction, while the modal displacement along polar $\langle 1\bar{1}0\rangle_p$ and non-polar direction $\langle 001\rangle_p$ have significantly reduced values 0.098 Å and 0.052 Å respectively. The distinct modal displacement along non-polar $\langle 110\rangle_p$ is attributed to strong antiparallel displacements of Bi^{3+} cations creating antiferroelectric pattern which dominate

over the ferroelectricity along polar $\langle 1\bar{1}0\rangle_p$ (demonstrated on the Figure 4.18b, d) On the other hand, the mode values of Mn (0.019 Å along $\langle 1\bar{1}0\rangle_p$ and -0.051 Å along $\langle 110\rangle_p$) and Ni (0.041 Å along $\langle 1\bar{1}0\rangle_p$ and -0.086 Å along $\langle 110\rangle_p$) indicate less displaced B site cations in comparison to Bi^{3+} cations (Figure 4.21a, b).

(a)

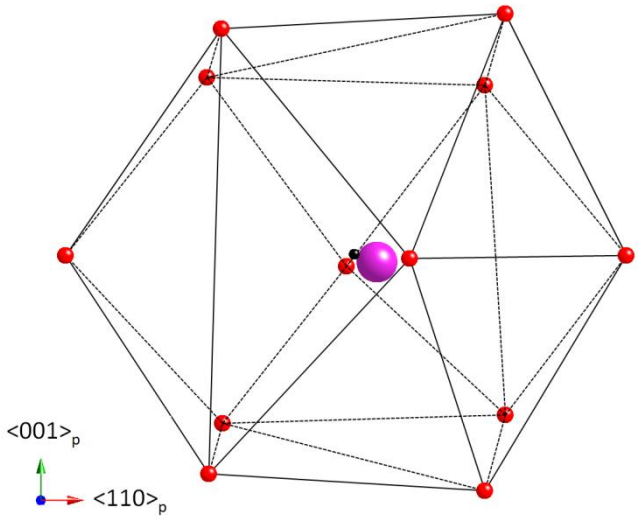

(b)

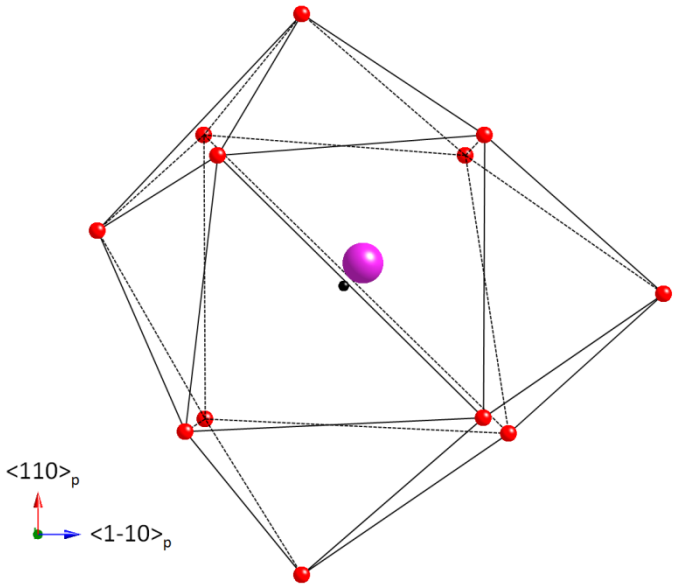

Figure 4.20. *Representation of the local structure of Bi cation (purple sphere, centroid indicated as a black sphere and O coloured as red spheres) with view down to (a)* $\langle 1\bar{1}0\rangle_p$ *and (b)* $\langle 001\rangle_p$*; The results are based on the mode value of the*

displacements in the RMC models with the most significant components of Bi^{3+} cations 0.283 Å along non-polar $\langle 110 \rangle_p$ and less significant 0.099 Å and 0.052 Å along polar $\langle 1\bar{1}0 \rangle_p$ and non-polar $\langle 001 \rangle_p$ directions respectively.

(a) (b)

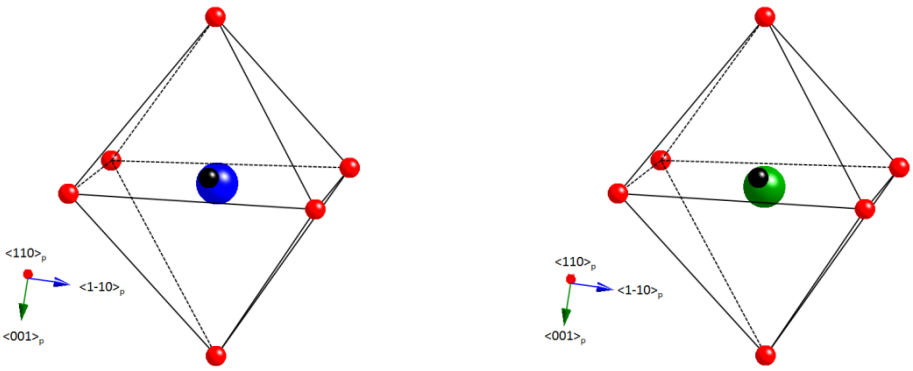

Figure 4.21. *Representation of the local structure of (a) Mn (blue sphere, centroid indicated as a black sphere and O coloured as red spheres) and (b) Ni cations (green sphere) based on modal displacement indicate less displaced B site cations than Bi^{3+} cations.*

4.2.4 Analysis of A and B site correlations

The displacement correlation functions (DCF) were first applied to $BiTi_{3/8}Fe_{1/4}Mg_{3/8}O_3$, to compute the ferroelectric correlations between A and B site cations (sections 3.2.4). The DCFs calculations between Bi^{3+} cations are resolved into distinct planes within the structure orthogonal to the polar $\langle 1\bar{1}0 \rangle_p$, and the two non-polar $\langle 001 \rangle_p$ and $\langle 110 \rangle_p$ directions, while the calculations of Bi-B site and B site- B site are resolved by DCF within a spherical volume, with correlations derived only along directions. To improve the statistical accuracy, the DCF results are calculated and averaged for all 20 RMC models. The differential DCFs of Bi-Bi in the RMC model are compared to the average incommensurate model and to antiferroelectric $PbZrO_3$ [28, 29] in order to determine the nature of correlated motion. The $\eta_{Bi\text{-}Bi}(r)$ for the RMC model (Figure 4.22a) and for the incommensurate model (Figure 4.22c) both demonstrate a pattern of small negative and positive peaks along $\langle 1\bar{1}0 \rangle_p$, indicating weak antiferroelectric correlations. We might expect polarity to arise from ferroelectric correlations,

which are not observed in the DCF between nearest neighbours. Instead, in this system polarity is produced by different magnitudes of positive and negative displacements along $\langle 1\bar{1}0\rangle_p$ in different directions, which add up to a net polarity; the different direction of displacement for the neighbouring atoms is the dominant affect in the DCF, and so correlations appear antiferroelectric. Thus, instead of observing polar nanoregions (with ferroelectric correlations in the DCF) we observe antiferroelectric correlations which are consistent with the long-range modulated average structure. We hypothesize that the polar correlations in the RMC model will become evident within a larger volume, rather than as correlations between single pairs of atoms as probed by DCF. In order to test this hypothesis we looked at the sum of Bi displacements within a volume in a further discussion in this section. On the other hand, the most intense peaks in the DCF of the RMC model are along the $\langle 110\rangle_p$ direction with both positive and negative peaks. This is an effect of the relatively large antiparallel displacement shifts between Bi^{3+} cations along this direction (Figure 4.22b) and is consistent with both Bi^{3+} cation displacement calculations and derived mode in previous section; larger displacements give rise to larger correlations. These antiferroelctric correlations are also observed in the average incommensurate model. The general picture of $\eta_{Bi\text{-}Bi}(r)$ performed for the average incommensurate model (Figure 4.22c) is similar to the RMC model results (Figure 4.22a), however broader peaks in the latter model indicate about bigger variations of displacements of Bi^{3+} cations in the local structure, which is consistent with $g_{Bi\text{-}O}(r)$ and earlier displacements results. Such significant antifferoelectric pattern observed in both RMC and average incommensurate models brought us to calculate DCF for the well-known antiferroelctric $PbZrO_3$ (PZ). PZ structure adopts the antiferroelctric space group *Pba*2 and demonstrates antiparallel displacement of Pb cations along $\langle 110\rangle_p$ [28]. The $\eta_{Bi\text{-}Bi}(r)$ of PZ (Figure 4.23a, b) shows dominant peaks along $\langle 110\rangle_p$ with the same pattern of positive and negative peaks as for the RMC model, confirming that previously calculated correlations of Bi^{3+} cations in the RMC and average incommensurate model of BMN have the same pattern as antiferroelectric PZ. This antifferoelectric pattern in the average structure of PZ still exists after randomization and subtraction, indicating that antiferroelctric

pattern coming from the average structure remain in the DCF. However, it is worth noting that the process of randomization, which is essential to the DCF analysis, is much more efficient at removing ferroelectric correlations than antiferroelectric correlations.

(a) (b)

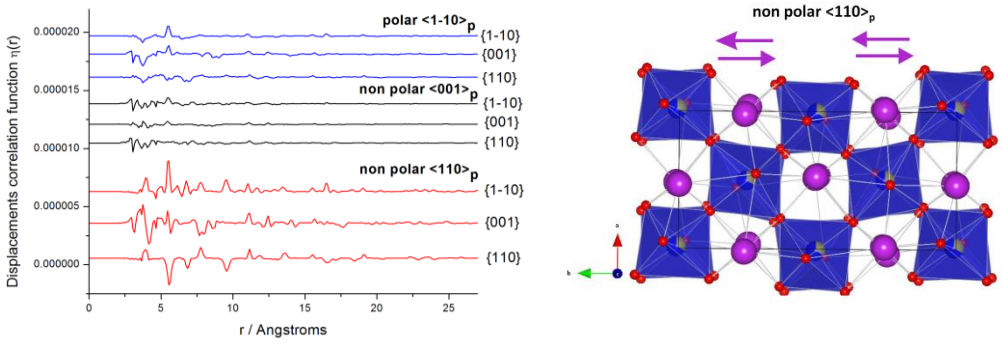

(c)

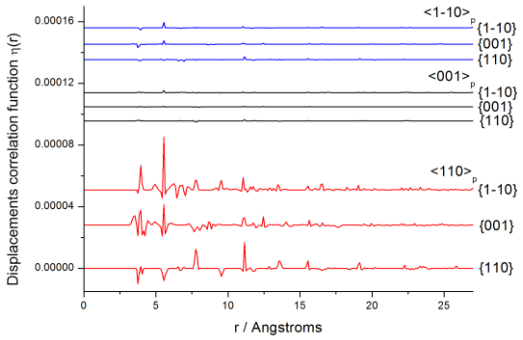

Figure 4.22. *(a) Differential DCF of Bi-Bi in the RMC model with (b) antiparallel displacement along* $\langle 110 \rangle_p$*; (c) Differential DCF of Bi-Bi for the average incommensurate model demonstrating general agreement between models.*

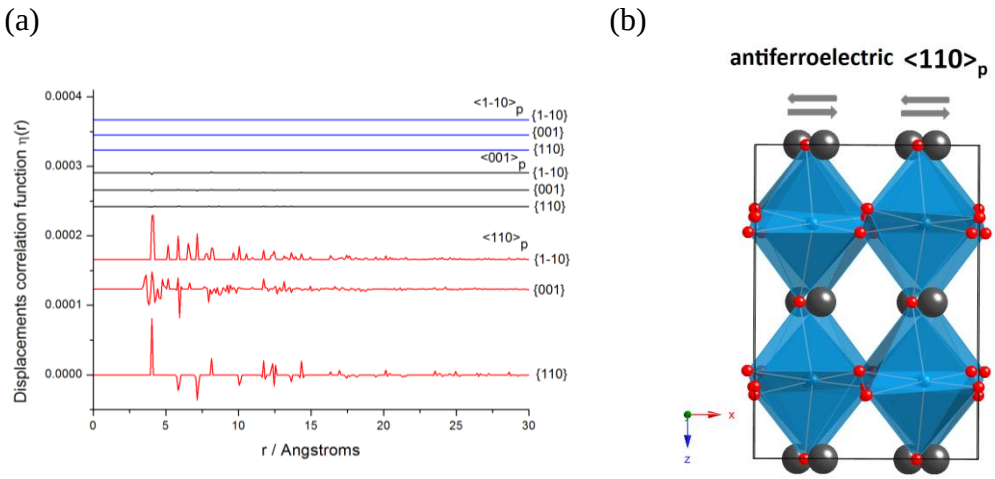

Figure 4.23. *(a) Differential DCF of of Pb-Pb in PZ with (b) antiparallel displacement along* $\langle 110 \rangle_p$.

The calculations of DCF within a spherical volume were first performed between the A site and B site cations. The results have shown that both Bi-Mn and Bi-Ni (Figure 4.24a and b) have only weak short-range correlations along the $\langle 110 \rangle_p$ direction. These non significant correlations are a possible effect of strong antiparallel displacement between Bi^{3+} cations, which are suppressed after the first nearest neighbour.

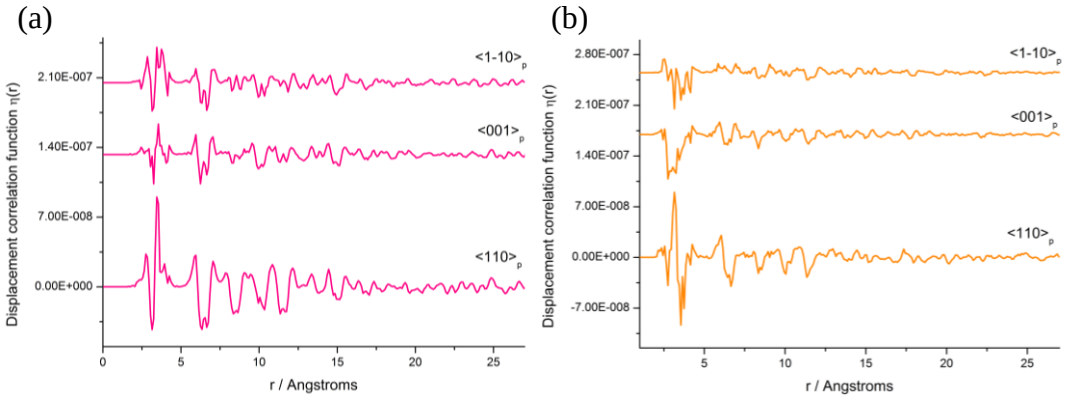

Figure 4.24. *Differential spherical DCF calculated for: (a) Bi-Mn and (b) Bi-Ni.*

The spherical DCF was also applied to the B site cations which did not reveal any correlation between B site cations, except for weak short-range ferroelectric correlations of first neighbours Mn-Mn homopairs along the $\langle 1\bar{1}0 \rangle_p$ direction (Figure 4.25).

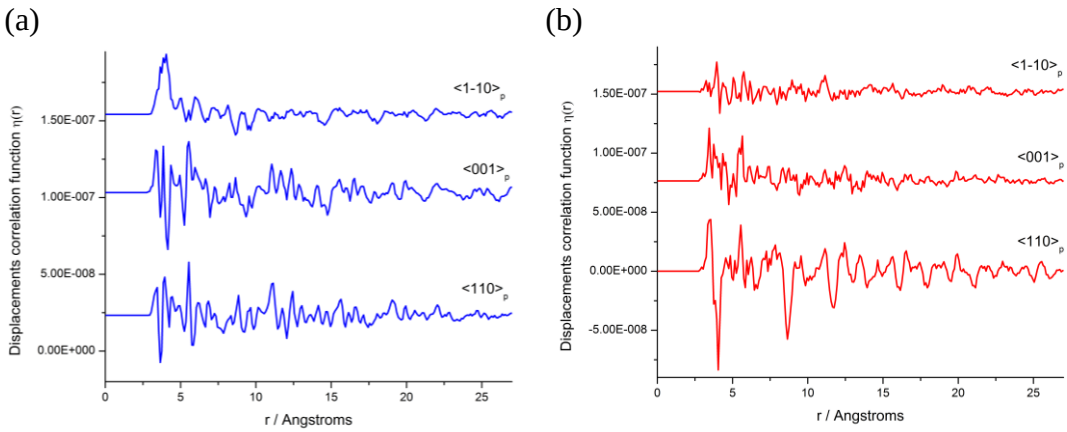

Figure 4.25. *Differential spherical DCF calculated for: (a) Mn-Mn and (b) Ni-Ni.*

To understand the complex nature of the A site displacements, the sum of Bi^{3+} displacements were calculated by taking the B site cations as the origin, and summing the displacement of every Bi^{3+} within a given *r*. An *r* value of 7.5 Å was selected in order to return an even number of Bi^{3+} cations and to cover a volume approximately equivalent to that of the polar commensurate subcell. The sum of the Bi^{3+} displacements along the polar $\langle 1\bar{1}0\rangle_p$ direction was calculated and the ratio of Bi^{3+} cations displaced in the same direction over all bismuth atoms were evaluated for each atomic shell (Figure 4.26a, b). Thus, the ratio expressed in equation 4.2 with values above 0.5 gives information about atomic correlations.

$$n(\sigma) = \left(\frac{\sum n(+)}{\sum(n(+)+n(-))}\right) \qquad \text{Equation 4.2}$$

where σ represents the atomic shell, $\sum n(+)$ correspond to sum of Bi^{3+} cations displaced in the same direction along $\langle 1\text{-}10\rangle_p$, and $\sum(n(+)+n(-))$ define overall sum of Bi^{3+} cations displaced in opposite direction along $<1\bar{1}0>_p$.

These calculations showed that local correlations of Bi^{3+} cation displacements exist within a distance of approximately 12 Å (Figure 4.26c) in comparison to randomly distributed Bi^{3+} cations (presented as an error bar around the value of 0.5 corresponding to zero total displacement). Figure 4.26d shows the supercell where the positive (red) and negative (blue) atoms represent sum of Bi displacements in opposite directions along $\langle 1\bar{1}0\rangle_p$; the figure shows groups of

atoms gathering in clusters clearly indicating the local ferroelectric correlations between Bi atoms. These clusters with oppositely displaced atoms, which are represented by positive (red) and negative (blue) sum of Bi atoms (Figure 4.26d), are similar to the polar regions in the long-range approximant supercell of incommensurate structure which cancel each other to produce long-range average antiferroelectricity. Polar domains are observed in both local and average structures, and their size (~12 Å) in RMC local structure are comparable to the size of polar commensurate subcell $P2_1mn$ in the long-range crystallographic structure.

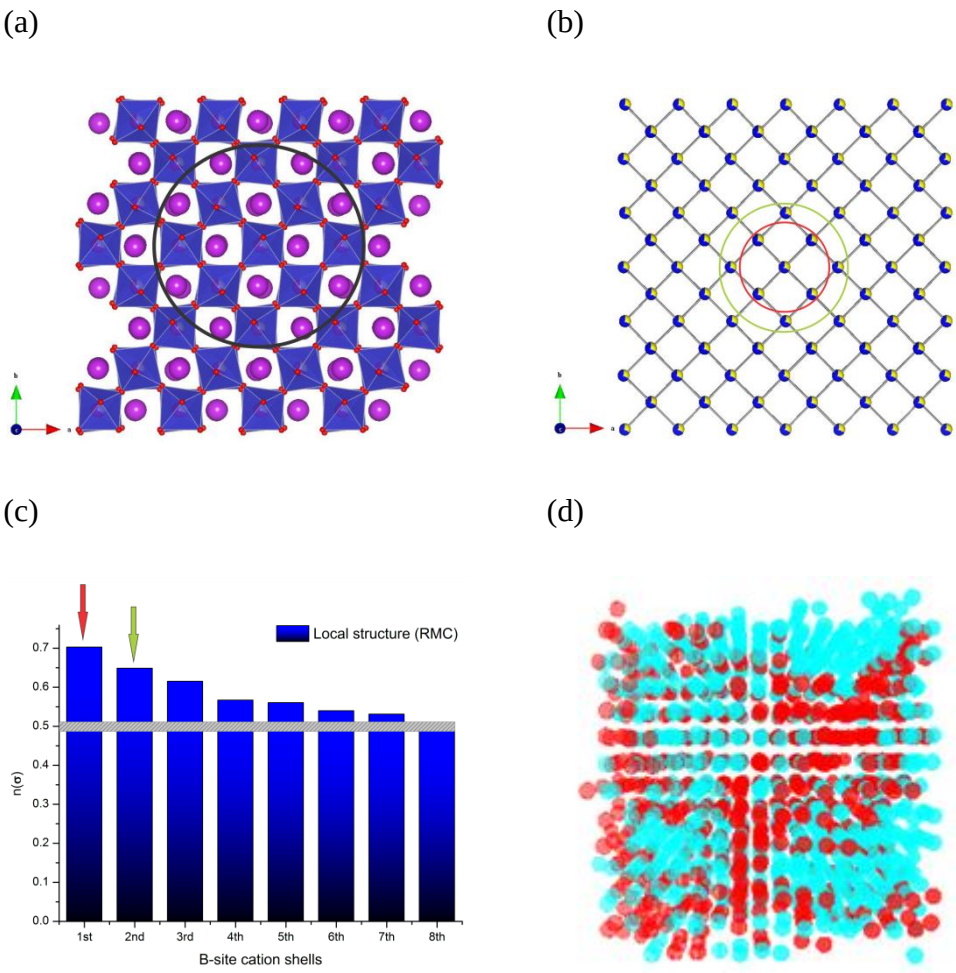

Figure 4.26. *Bi^{3+} cations sum of displacements within a 7.5 Å radius from a B site cation as an origin (b) B site atomic shells showing first (red) and second shell (green) as an example; (c) The ratio of Bi^{3+} cations displaced in the same direction along $\langle 1\bar{1}0\rangle_p$ over all bismuth atoms with random distribution of Bi^{3+}*

displacements presented as an error bar (grey) for local structure in the RMC model; (d) Supercell with atoms representing positive (red) and negative (blue) sum of Bi atoms with the B site cations as an origin along $\langle 1\bar{1}0\rangle_p$ *show clusters of opposite displaced group of atoms clearly indicating local ferroelectric correlations between the Bi atoms.*

The same calculations performed for the average incommensurate model indicated differences in correlations of Bi^{3+} cation displacements (Figure 4.27a, b) which can be attributed to the differences between the incommensurate structure and RMC structure descriptions. The incommensurate structure describes Bi^{3+} displacements by the sinusoidal modulation of the average displacements, evident in the large minima and maxima appearing at fixed distances (Figure 4.27a), which infinitely repeat within the lattice. The local structure generated from the RMC simulation of the total scattering data however shows how Bi^{3+} displacements are correlated in three dimensions on the local scale in real space.

(a) (b)

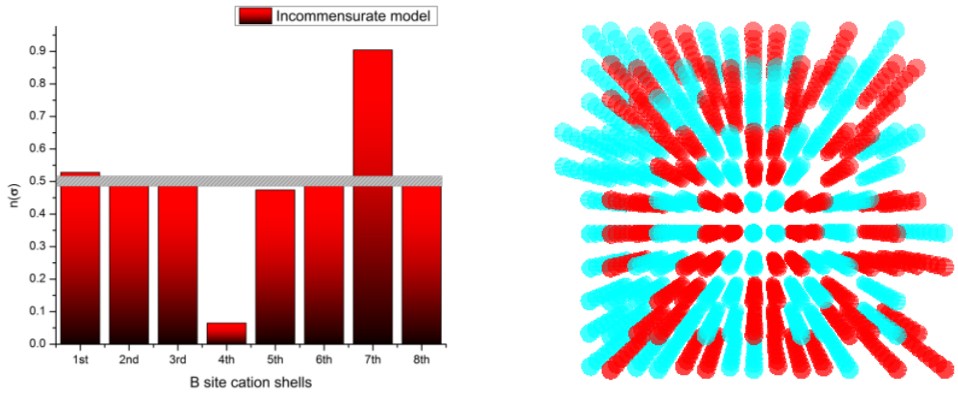

Figure 4.27. *(a) The ratio of* Bi^{3+} *cations displaced in the same direction along* $\langle 1\bar{1}0\rangle_p$ *over all bismuth atoms with random distribution of* Bi^{3+} *displacements presented as an error bar (grey) for average incommensurate model; (b) Supercell with atoms representing positive (red) and negative (blue) sum of Bi atoms with the B site cations as an origin along* $\langle 1\bar{1}0\rangle_p$ *show sinusoidal behaviour of displaced Bi atoms arising from the modulated character of this model.*

4.2.4 Nearest neighbours - B site cation ordering

The B site ordering was calculated directly from partial pair distribution function $g_{B\text{-}B}(r)$ (Figure 4.28), where the average numbers of neighbours for Mn and Ni atoms have been extracted, as described in the section 2.3.1.

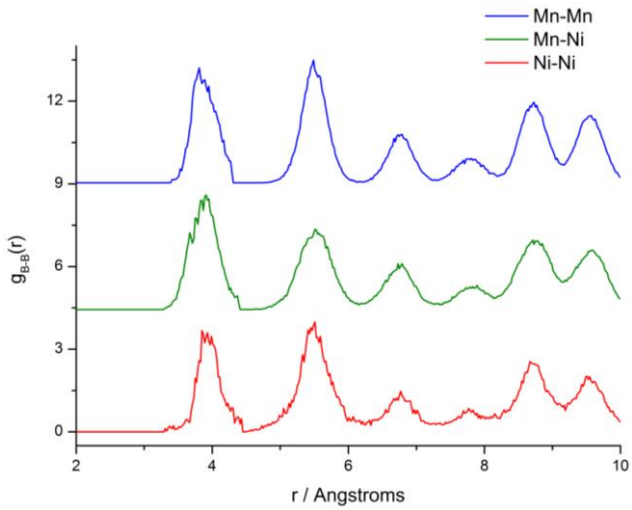

Figure 4.28. *The partial pair correlation functions $g_{B\text{-}B}(r)$ for the local structure at RT.*

RMC models resulting from the RMC refinement were compared with the completely random distribution. Random distributions were obtained by swapping B site cations during RMC modeling in absence of the data. There are differences in the average numbers of neighbours between the observed and random distribution (Table 4.7). The most pronounced differences in the RT structure are observed for the Ni cations where the average number 1.64(1) of Ni-Ni nearest neighbours pairs and 4.36(1) of Ni-Mn nearest neighbours pairs are significantly different from the values of 2 and 4 determined for the random distribution (Figure 4.29a, b). The *n(r)* calculations represent the average results of 20 simulated RMC models and the standard errors based on standard deviations of the 20 models were derived for all B site cations nearest neighbours. The values for the first and second neighbours calculated for 20 different RMC models were essentially the same for each model, and thus produce small standard deviation of 0.01, which confirms that this deviation from random cation ordering is a real

result of the experimental data used during RMC modeling. We therefore assign this observation of a reduction in Ni-Ni nearest neighbor pairs when compared to a random B site distribution to short-range Mn/Ni cation site ordering. Consistent with this, the Ni-Ni second nearest neighbor frequency is significantly higher than random. Thus, this decrease of the Ni-Ni nearest neighbor in the first shell coupled with an increase in the second shell show Mn/Ni ordering consistent with a bias towards rock-salt ordering within RMC models. This trend of B site cations behavior is observed in the RMC model (Figure 4.30), where B site cations are coloured relatively to the numbers of Ni/Mn in the six nearest neighbours, while grey atoms represent the average 4Mn:2Ni ratio. The regions of NaCl type ordering are visible in the configuration despite not equal ratio between Mn and Ni atoms (2:1), which is preferred for this type of ordering. In the consequence of this, there are regions of higher concentrations of Mn cations (blue), which is necessary in order to have the high concentrations of Ni cations (red), needed to form NaCl ordered regions. Thus, the visualization of B site cations in the RMC model confirmed the tendency of B site cations towards rock-salt ordering within RMC models. The search for possible further short-range ordering with the next nearest neighbours are prevented by overlap of atoms between shells which produces less accurate results than for the first two nearest neighbours.

Table 4.7. *B site nearest neighbours for the local structure of RT phase of* $Bi_2Mn_{4/3}Ni_{2/3}O_6$*. Comparison is given between the refined RMC model with standard errors and a fully disordered B site distribution.*

	n(r) of 1st shell - 6 neighbours		*n(r)* of 2nd shell - 12 neighbours		*n(r)* of 3rd shell - 8 neighbours	
B site – B site	Local structure (RMC model)	Disordered	Local structure (RMC model)	Disordered	Local structure (RMC model)	Disordered
Mn-Mn	3.82(1)	4.0	8.29(1)	8.0	5.21(2)	5.33
Mn-Ni	2.18(1)	2.0	3.71(1)	4.0	2.79(3)	2.66
Ni-Mn	4.36(1)	4.0	7.41(1)	8.0	5.54(6)	5.33
Ni-Ni	1.64(1)	2.0	4.59(1)	4.0	2.46(7)	2.66

(a) (b)

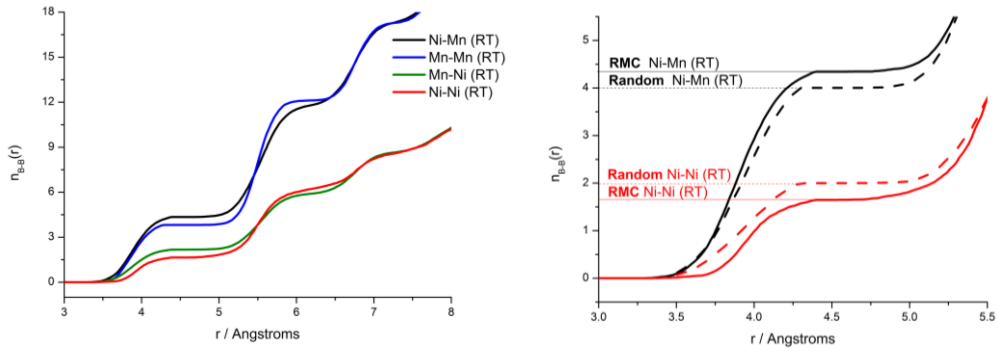

Figure 4.29. *Nearest neighbour functions $n_{B\text{-}B}(r)$ in the RMC configuration; (b) comparison of nearest neighbours of Ni atoms between RMC model and statistically-disordered distribution.*

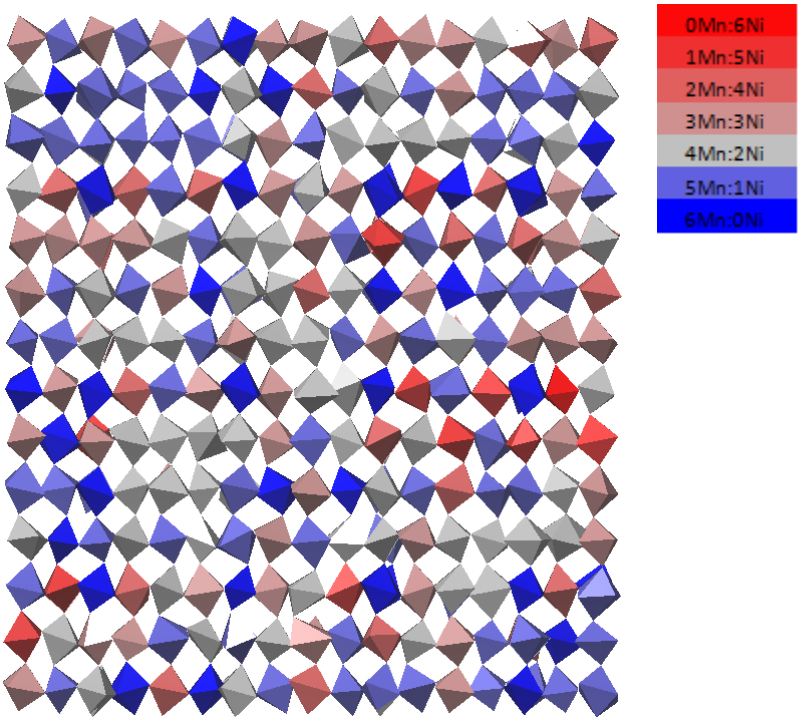

Figure 4.30. *Supercell of RMC model with Mn/Ni cations colour coded relative to number of Mn/Ni in the 6 nearest neighbours.*

The average incommensurate structure also shows nearest neighbor B site ordering which acts to reduce unfavorable Ni-Ni interactions, although the nature of the short-range ordering is different between the RMC and incommensurate models. The general pattern of B site ordering in the incommensurate structure is

presented in the long-range large approximant cell (395 × 147 × 5.5 Å) (section 4.1.2). In order to probe the local B site ordering present within the incommensurate model, the model was used to generate a supercell of the same size used in the RMC calculations, and Mn/Ni atoms were assigned to B sites using the fractional occupancies from the incommensurate structure. The generated average incommensurate model (55 × 62 × 55 Å) (Figure 4.31) shows the same behavior of B site cations like for the big approximant cell, where the rich regions of Mn and Ni cations are observed. These clusters of B site cations in the average incommensurate model differ with results observed in the local structure, and gives a random distribution when calculating *n(r)* (Table 4.8 and Figure 4.32a, b). The absence of similar ordering is presumably due to the modulation in the average incommensurate model, which create clustering of Mn/Ni cations instead of rock-salt type order as observed in the RMC model. Thus, the *n(r)* results and visualization of B site cations in the RMC model demonstrate Mn/Ni ordering with bias toward well-known NaCl type ordering, whereas average incommensurate model show clustering of Mn/Ni cations, where ordering is created by the presence of modulations at average structure.

Table 4.8. *Nearest neighbour results for the average incommensurate model with standard errors compared to fully disordered B site distribution.*

	n(r) of 1st shell - 6 neighbours		*n(r)* of 2nd shell - 12 neighbours		*n(r)* of 3rd shell - 8 neighbours	
B site – B site	Incom. model	Disordered	Incom. model	Disordered	Incom. model	Disordered
Mn-Mn	4.03(3)	4.0	8.05(6)	8.0	5.35(4)	5.33
Mn-Ni	2.02(3)	2.0	4.03(3)	4.0	2.70(2)	2.66
Ni-Mn	4.03(6)	4.0	8.08(8)	8.0	5.41(4)	5.33
Ni-Ni	2.02(4)	2.0	4.02(5)	4.0	2.66(4)	2.66

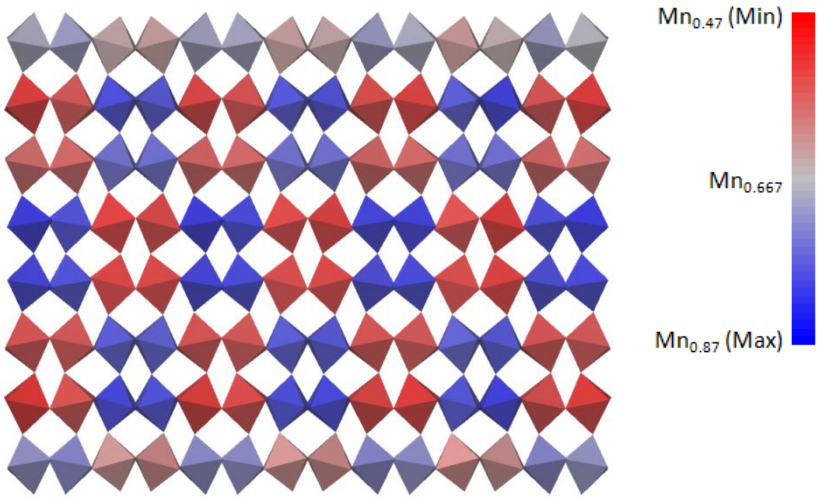

Figure 4.31. *Supercell of average incommensurate model with observed clustering of Mn/Ni cations.*

(a) (b)

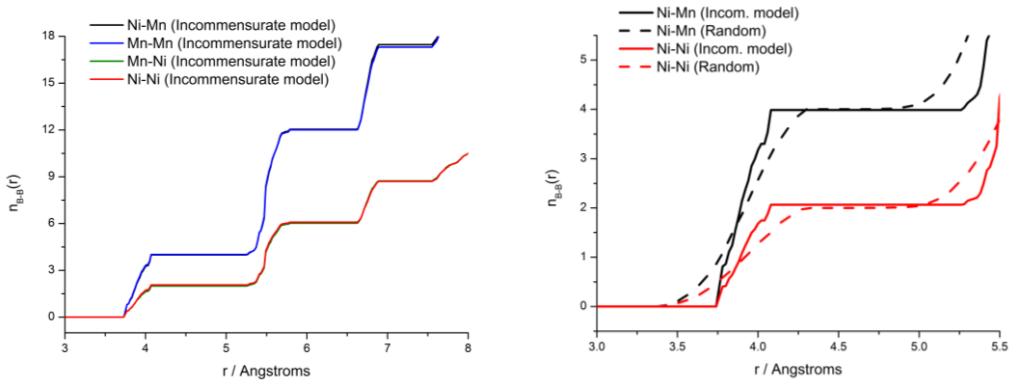

Figure 4.32. *Nearest neighbour functions $n_{B\text{-}B}(r)$ in the average incommensurate model; (b) comparison of nearest neighbours of Ni atoms between average incommensurate model and statistically-disordered distribution .*

4.3. Crystallographic average structure at high temperature

The superstructure peaks of the incommensurate structure at RT gradually decrease as the temperature is increased and the phase becomes commensurate at 200°C. The structure analysis with the reconstruction of reciprocal space and

Rietveld refinement provide the non-polar space group *Pnma* [12]. The phase transition from an incommensurate to a commensurate phase induce differences in the observed A and B site environment. In the room temperature phase the octahedra are distorted by the modulation whilst above the transition the average bond distances are very regular, varying by only 0.003Å. As with the B sites, below the phase transition A sites are distorted due to the long period antiferroelectric displacement modulation giving rise to a wide range of Bi environments, whereas above the transition this environment becomes more ordered with a simple antiferroelectric displacement (Figure 4.33).

(a) (b)

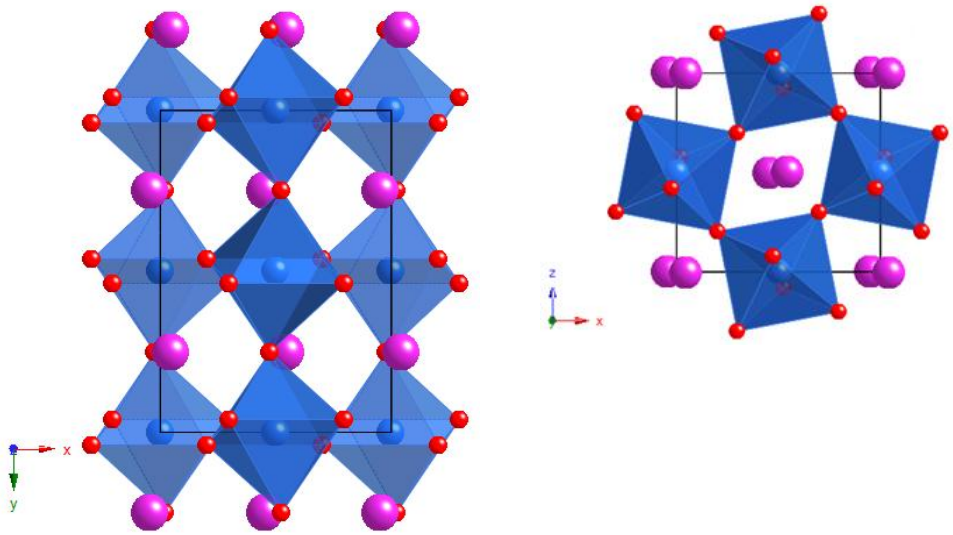

Figure 4.33. *Crystallographic structure of the commensurate phase at high temperature in the orthorhombic space group Pnma. The atom spheres are denoted by colours: Bi (purple), B site (blue) and oxygen (red).*

4.4 Local structure at high temperature

4.4.1 Generation of RMC model

Neutron total scattering data at high temperature (HT) were collected at the same time and under the same conditions as the RT data, at the GEM diffractometer at the ISIS pulsed spallation neutron source. The HT data were collected for 1135

μAh at 300°C, well above the transition temperature to be ensure that the phase transition was complete. Data was collected over the same scattering vector range, $0.3 \leq Q \leq 50$ Å, as used for the RT data. The same procedure of correction of total scattering data in GUDRUN and the *stog* utility in RMCProfile were applied in both RT and HT data in order to make the data comparable.

The starting configuration of the RMC model was generated from the average structure of commensurate orthorhombic subcell *Pnma* obtained in GSAS. This antiferroelectric orthorhombic space group was identified as the best approximation of average structure and gave a very good fit to the neutron experimental data (Figure 4.34). The *Pnma* structure was then converted to *Pcmn* settings *(abc->c̄ba)*, identical like at RT. This transformation allows comparing HT structure directly with the average incommensurate and local structure at RT.

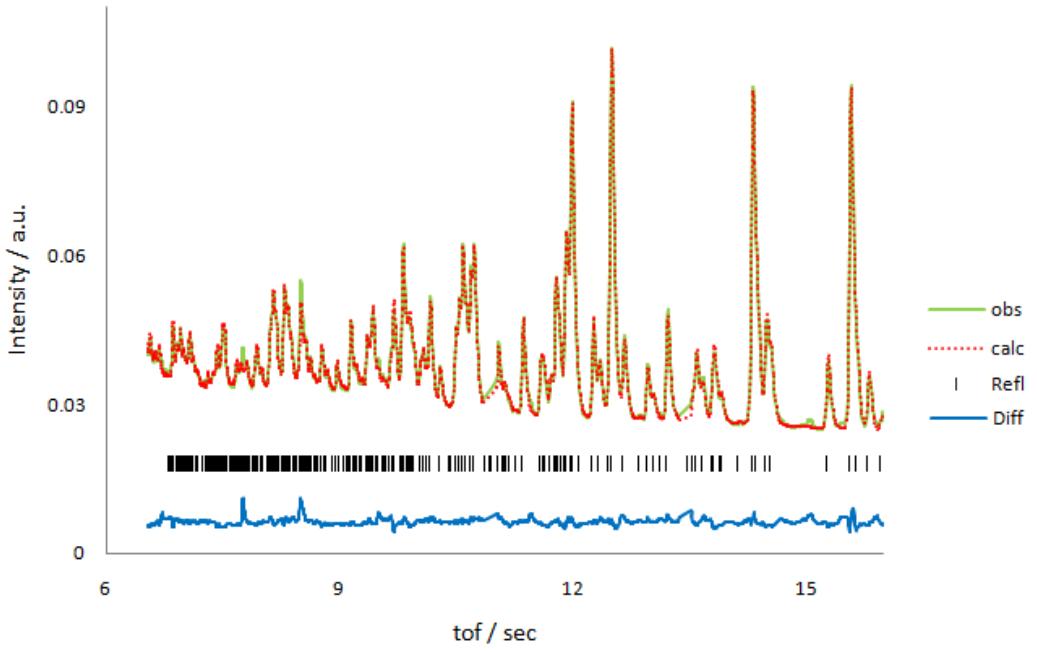

Figure 4.34. *Rietveld refinement of $Bi_2Mn_{4/3}Ni_{2/3}O_6$ (backscattering bank) at HT with space group Pnma, lattice parameters a = 5.5893 Å b = 7.8058 Å and c = 5.4513 Å and weighted agreement factor R_{wp}=2.43%. The red crosses are the calculated pattern, the solid green line is observed data, whereas the blue line represent the difference between observed and calculated patterns.*

A model built of 10*a* 7*b* 10*c* unit cells gave a HT supercell with dimension 55 × 55 × 55 Å^3 and 14,000 atoms (Figure 4.35). Due to setting conversion, the HT supercell has the same settings as RT phase and is aligned with ⟨100⟩ and ⟨010⟩ oriented along $\langle 1\bar{1}0\rangle_p$ and $\langle 001\rangle_p$ respectively in the primitive cubic perovskite cell and ⟨001⟩ oriented along $\langle 110\rangle_p$.

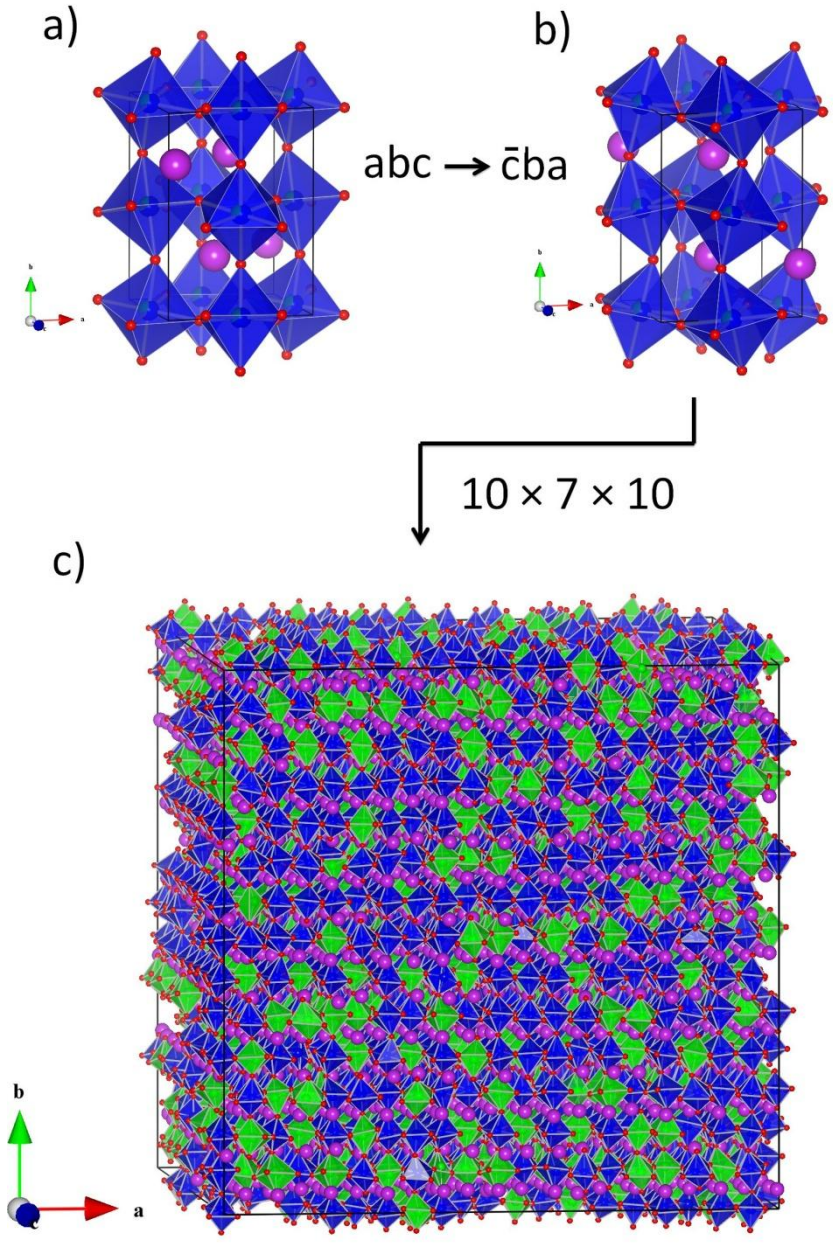

Figure 4.35. *(a) Subcell of commensurate average structure Pnma (abc settings) transformed to (b) Pcmn (c̄ba settings) identical like at RT; (c) RMC supercell*

obtained by multiplicity of 10 × 7 × 10 Pcmn subcells. The atom spheres are denoted by colours: Bi (purple), Mn (blue), Ni (green) and oxygen (red).

The RMC refinement of the HT structure only used the BVS constraints which helped to distinguish Mn and Ni cations occupied the same B site and protected the configuration from unphysical large distortions. Two stages of the RMC refinement were applied in order to obtain good fits to the observed Bragg profile, total scattering structure factor *F(Q)* and the pair distribution function *G(r)*. In the first stage the B site atoms in starting configurations were randomly swapped in absence to the data to obtain a completely random distribution of Mn and Ni cations. In the next step the RMC fit to the data was started with swapping and translating of atoms simultaneously. The refinement was continued until there was no further improvement in χ^2 and a very good fit to all experimental data was obtained (Figure 4.36).

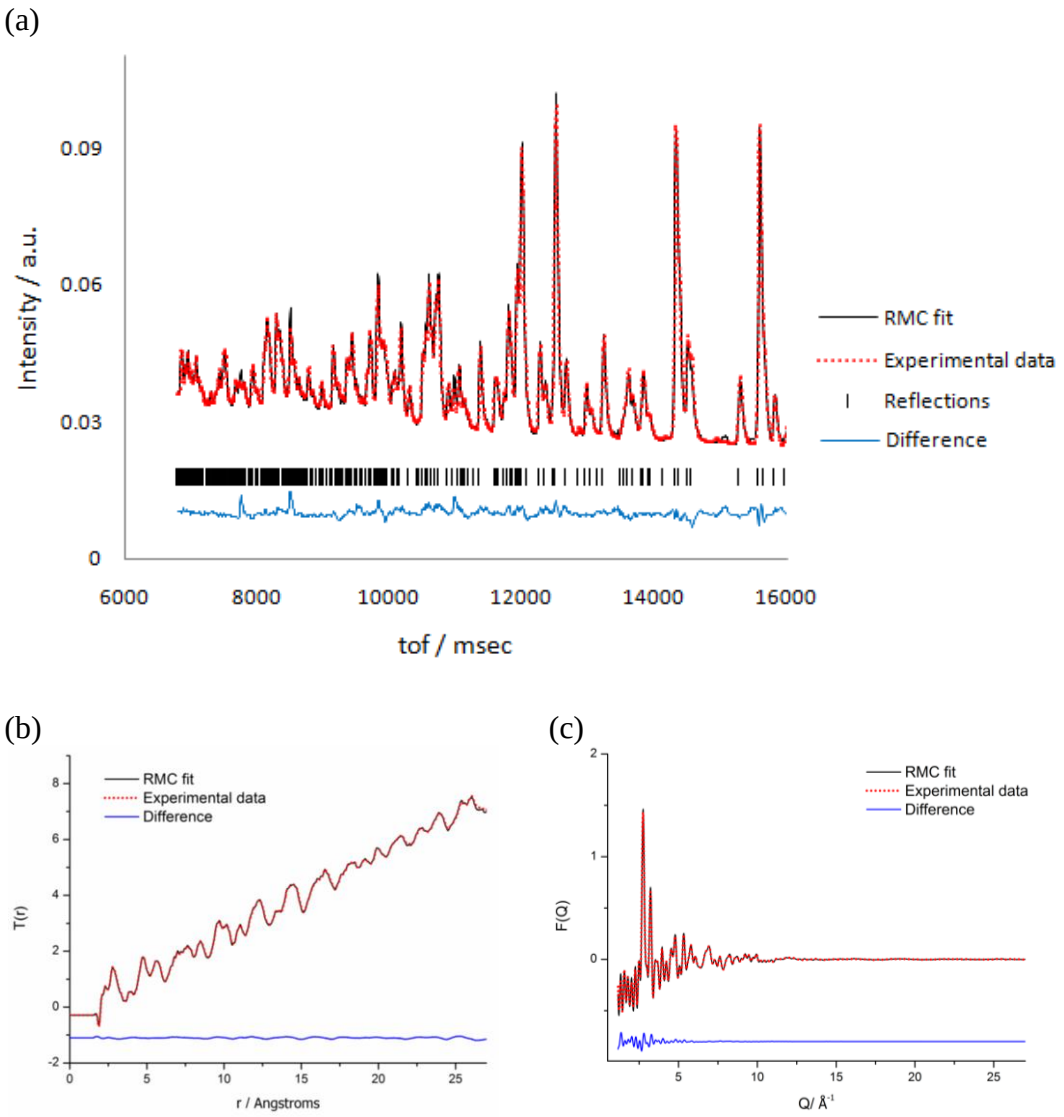

Figure 4.36. *Comparison between measured and calculated functions of one of the RMC model for the local structure of $Bi_2Mn_{4/3}Ni_{2/3}O_6$ commensurate HT phase: (a) Bragg profile data; (b) total correlation function T(r); (c) total scattering structure factor F(Q).*

The application of BVS constraints provided sensible oxidation state for every chemical elements (Bi/Mn/Ni and O). The oxidation states at HT are comparable to BVS results obtained at RT, except for the observed difference of B site cations. The lower value of Ni cations 1.88(2) at RT in comparison to 2.07(1) at HT, can be attributed to bigger thermal expansion at HT, which cause an increase of atomic vibrations and expansion of bond distances. The differences of BVS values between RT and HT can be also affected by interatomic potential restraints

applied to Ni cations at RT, which is likely to force the observed BVS to be closer to the expected value of 2 (Table 4.9 and Figure 4.37).

Table 4.9. *Oxidation states from bond valence distances fit to empirical values.*

	BVS (RT)	BVS (HT)
Bi	3.04(4)	3.07(1)
Mn	3.43(9)	3.32(1)
Ni	1.88(2)	2.07(1)
O	1.99(2)	1.99(1)

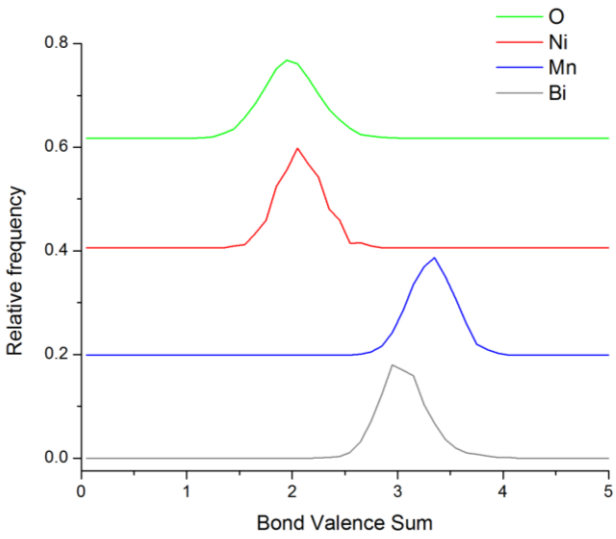

Figure 4.37. *The distribution of Bond Valence Sum for RMC models of BMN at HT.*

4.4.2 Analysis of the pair distribution functions of HT data

The mean bond distances were obtained by fitting Gaussian functions to the observed partial pair distributions functions *g(r)*, which were averaged from 20 RMC models to improve the statistical accuracy. The *g(r)* results were then compared to crystallographic average structure and local structure at RT.

Table 4.10. *Comparison of Bi-O bond distances from the partial pair distribution function $g_{Bi\text{-}O}(r)$ of the RMC models and crystallographic average structure at HT.*

	Average structure HT / Å	Local structure HT (RMC model) / Å	Local structure RT (RMC model) / Å
Bi-O	2.337 2.442 (x2) 2.448 2.659 (x2) 2.697 (x2) 3.171 3.217 3.383 (x2)	2.307(3) 2.611(2) 3.234(9) (3.84:2.89:5.26)*	2.252(5) 2.685(2) 3.151(9) (3.84:4.8:3.36)*

* Approximate ratio of bond distances (summed to 12 oxygen coordinate system) obtained from the integrated areas of peaks in $g_{Bi\text{-}O}(r)$ at HT.

The local structure of Bi-O at HT is consistent with the crystallographic structure. There are three group of Bi-O bond distances (2.307(3) Å, 2.611(2) Å and 3.234(9) Å), very comparable to the average structure and within the same range of bonds (2.337 Å - 3.383Å) (Table 4.10). Despite the same number of bond distances between the local structures at RT and HT, the differences in $g_{Bi\text{-}O}(r)$ are observed (Figure 4.38), where the peaks are more clearly separated at RT as the atomic thermal motion is reduced at lower temperature. The increased atomic motion at HT also affect the range of Bi-O bond distances between RT and HT, where bigger variation of bond distances are observed at higher temperature. Despite the various bond distances calculated from $g_{Bi\text{-}O}(r)$, the integrated are under these peaks provide identical ratios for first group of bond distances between RT (3.84: 4.8:3.36) and HT (3.84: 2.89:5.26) indicating that Bi^{3+} cations create short bond distances by displacement towards four nearest oxygen neighbours. On the other hand, the comparison of second and third group of bond distances ratios between RT and HT demonstrate increase of longer bond distance at HT which are attributed to bigger thermal motion at 300°C.

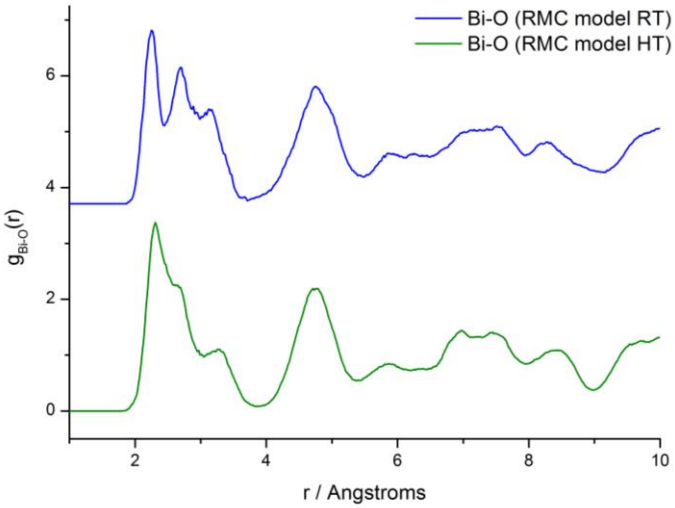

Figure 4.38. *Comparison of the partial pair correlation functions of $g_{Bi\text{-}O}(r)$ between the local structure at RT and HT.*

Inspection of the distribution of bond distances between Bi and B site cations (Figure 4.39) shows the same trend like at RT between Bi and B site cations. Bi^{3+} cations prefer to move toward Ni atoms and away from manganese cations which is in agreement with expectations based on electrostatics. These differences are shown by the respective distances: Bi-Mn 3.358(14) Å and Bi-Ni 3.224(12) Å in the HT structure (Table 4.11). The observed difference between Bi and Mn/Ni cations is also visible for the crystallographic average structure where two bond distances with values 3.1972(9) 3.3624(13) are noticed.

Table 4.11. *Comparison of Bi-B site bond distances between the average commensurate structure and local structure from RMC model.*

	Average structure / Å	Local structure (RMC model) / Å	
		Bi - Mn	Bi – Ni
Bi – B site	3.1972(9) 3.3624(13)	3.358(14)	3.224(12)

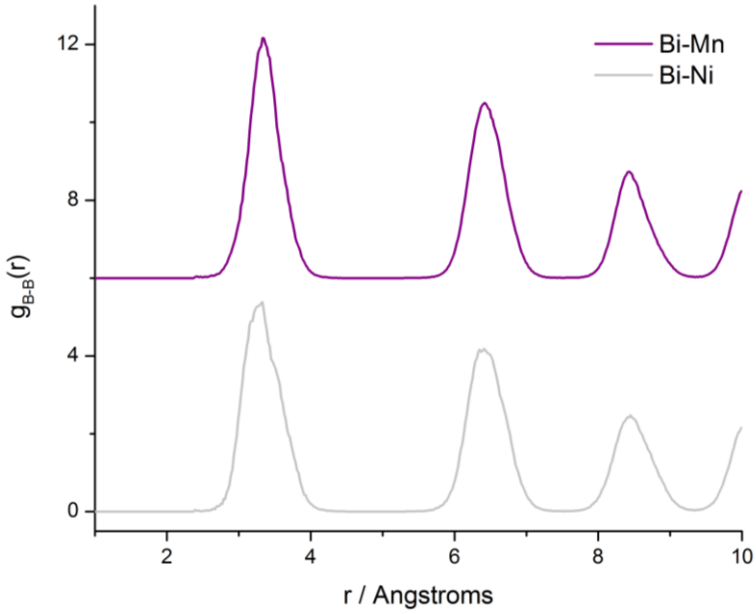

Figure 4.39. *The partial pair correlation functions of $g_{Bi\text{-}B}(r)$ derived from the local structure at HT.*

The local bonding on the B site is revealed by the partial pair distribution $g_{B\text{-}O}(r)$ and the instantaneous bond angle distributions $g_{O\text{-}B\text{-}O}(\theta)$, $g_{B\text{-}O\text{-}B}(\theta)$. The partial $g_{Ni\text{-}O}(r)$ in the RMC model gives a very regular distribution with bond distances of 2.069(6) Å, very similar to 2.075(1) at RT. Furthermore, the three Gaussians functions used to derive the mean bond distances of $g_{Mn\text{-}O}(r)$ at RT is also applied at HT and provide a very good fit to the Mn-O distribution, indicating about the presence of 2:2:2 J-T distortion types. The general shape of the distribution $g_{Mn\text{-}O}(r)$ remain the same like at RT, with a broader feature at a higher r value (Table 4.12 and Figure 4.40). Despite these similarities, the mean bond distances derived at HT (1.888(6), 1.975(7) and 2.114(29)) have smaller range of bonds in contrast to RT results (1.859(9), 1.946(11), 2.145(57)), suggesting more distorted Mn cations in the latter model and different type distortions than ideal JT. The previous results and different ratio of $g_{Mn\text{-}O}(r)$ between HT (9:9:6) and RT (6:3:3), indicate that on the local scale Mn cations at HT adopt a different intermediate oxygen coordination environment between that expected Mn^{4+} and Mn^{3}, than at RT. Furthermore, the less distorted Mn cations at HT in comparison to RT results is consistent with the trend of average crystallographic results where B site cations at HT are more regular than at incommensurate structure at RT.

Table 4.12. *Comparison of B site-O bond distances between commensurate model and local structure at HT phase.*

	Bond length		
	Average structure / Å	Local structure (RMC model) / Å	
		Mn - O	Ni – O
B site – O	2.01	1.888(6) 1.975(7) 2.114(29) (9:9:6)*	2.069(6)

* Approximate ratio of separations obtained from the integrated areas of peaks in $g_{B\text{-}O}(r)$ for RMC model at HT.

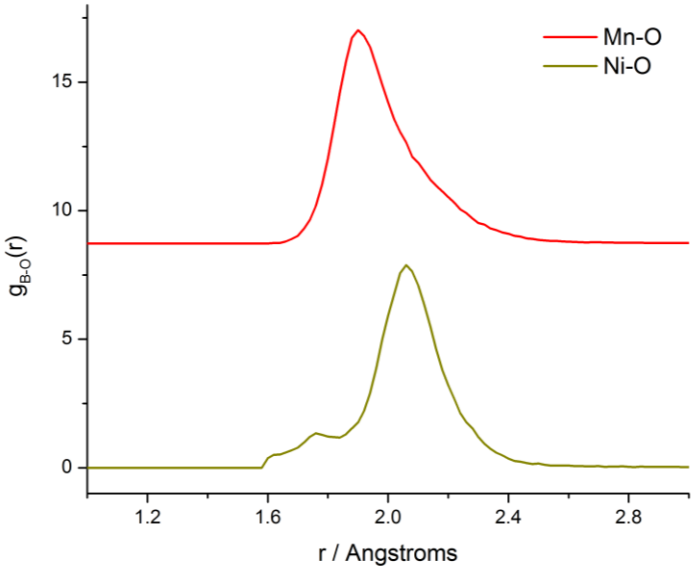

Figure 4.40. *The partial pair correlation functions of $g_{B\text{-}O}(r)$ derived from the local structure at HT.*

The comparison of B-O-B bond angle distribution linking the octahedra, and O-B-O showing the internal angle of octahderas demonstrate the comparable tilting for both Mn and Ni cations (Table 4.13 and Figure 4.41), except the equatorial angle within the octahedra. These results suggest that, octahedras in the average structure are less distorted 179.96(1) in comparison to local structure of Mn and Ni atoms 169.94(6), 169.76(13) respectively.

Table 4.13. *Comparison of B-O-B and O-B-O bond angle distributions between RMC model and average structure at HT.*

	Average structure angle / ° (HT)	Local structure (RMC model) (HT)	
		Angle / °	FWHM/ °
Mn-O-Mn Mn-O-Ni Ni-O-Ni	153.14(8)	152.82(2)	19.10
		150.18(2)	19.07
		147.64(5)	19.92
O-Mn-O O-Ni-O	89.84(6) 179.96(1)	89.97(2), 169.94(6)	17.50, 14.37
		89.55 (4), 169.76(13)	17.38, 16.34

(a) (b)

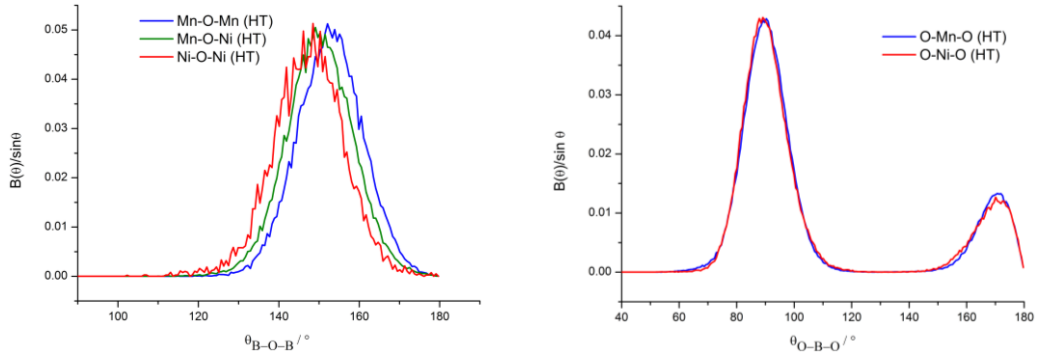

Figure 4.41. *Bond angle distributions of (a) B-O-B; (b) O-B-O for the local structure at HT.*

4.4.3 Analysis of A and B site cation displacements

The collapsed RMC models onto the original orthorhombic cell, is performed for the RMC model at HT (Figure 4.42a), where two clouds of bismuth atoms are displaced in opposite direction. This confirming the simple antiferroelectric character of the A site cations in this commensurate structure in comparison to complex distribution at RT (Figure 4.42b). The direct comparison of A and B site cations in the local scale, also show more diffused clouds of the atoms at RT, which is in agreement with difference observed between partial *g(r)*, where more

ordered A site environment in the $g_{Bi\text{-}O}(r)$ and lower range of displacements of $g_{Mn\text{-}O}(r)$ is observed at HT local structure.

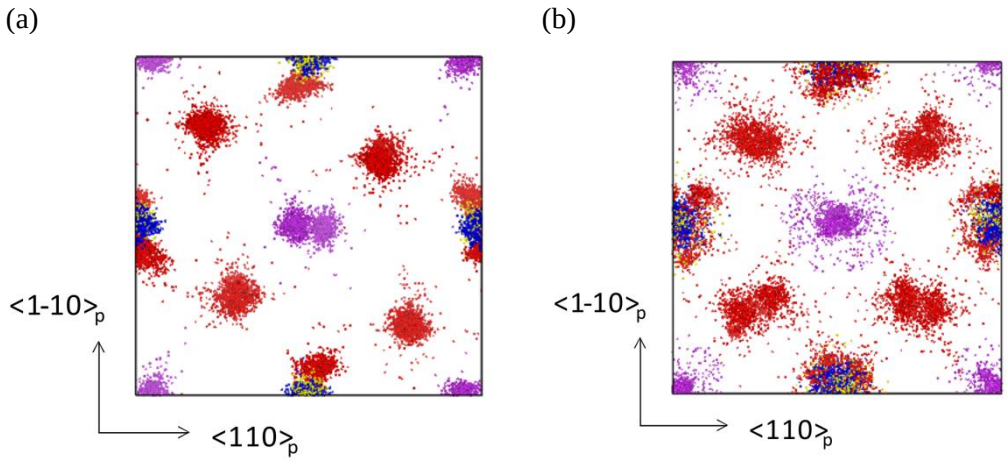

Figure 4.42. *The projection of the collapsed RMC models onto the original orthorhombic cell of BMN viewed down along* $<001>_p$ *and shown for the local structure at: (a) HT and (b) RT . Atoms are colored as follows: (Bi purple, Mn blue, Ni yellow and O red).*

The B site environments are also investigated by displacement calculations, where displacements from the oxygen centroids of the octahedra are derived for every Mn and Ni atom in the RMC model. The same behaviour of less displaced Ni cations indicated by slightly narrower distribution is observed as at RT (Figure 4.43a, c). This is in agreement with the presence of distorted Mn^{3+} cations within Mn site, than regular Ni cations. These differences are however less significant than observed at RT, which is consistent with the smaller range of mean bond distances obtained in the $g_{Mn\text{-}O}(r)$ at HT.

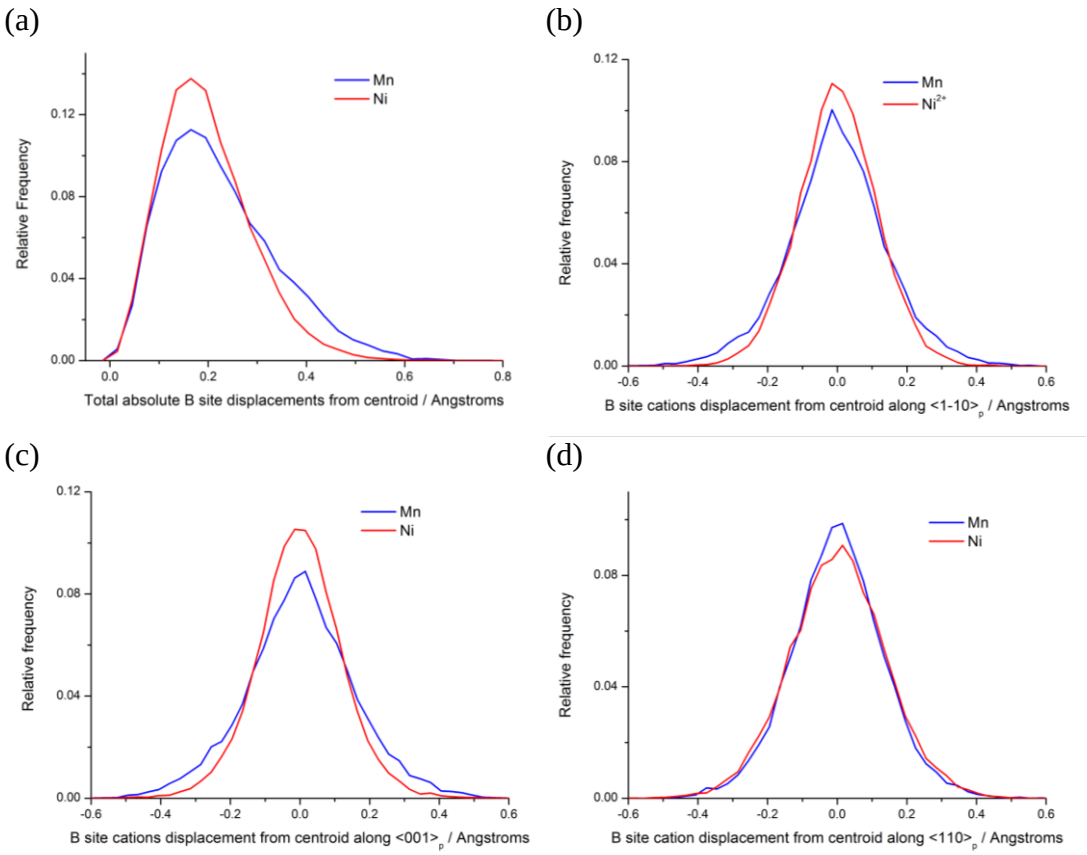

Figure 4.43. *(a) Total absolute displacements of the B site cations from the centroid of the coordinating oxygens for local structure at HT; (b), (c) and (d) Distribution of displacements of B site cations from oxygen octahedra along* $\langle 1\bar{1}0\rangle_p$, $\langle 001\rangle_p$ *and* $\langle 110\rangle_p$ *respectively.*

4.4.4 Analysis of A and B site correlations

The analysis of correlations between the A and B site cation displacements and comparison to RT results, are identified through evaluation of the DCF described earlier in section 3.2.3. The $\eta_{Bi\text{-}Bi}(r)$ in the local structure at HT reveals the expected intense peaks along $\langle 110\rangle_p$, where Bi cations are strongly antiparallel shifted to each other (Figure 4.44a). Thus, the $\eta_{Bi\text{-}Bi}(r)$ show similar antiferroelectric displacements between Bi-Bi at RT and HT along $\langle 110\rangle_p$, but broader peaks at HT indicate that Bi^{3+} cations are antiparallel displaced by longer distances from each other. On the other hand, the most significant differences are observed along the $\langle 1\bar{1}0\rangle_p$ and $\langle 001\rangle_p$ directions, where correlations almost disappear in comparison to DCF peaks at RT (Figure 4.44b). This difference in

comparison to DCF peaks at RT can be attributed to the non modulated character HT structure. Furthermore, the suppression of correlations between single pairs of atoms in the HT structure can also enhance decreased variation of displacements in this non modulated structure. In order to probe whether correlations are observed when considered on a larger scale, we also looked at the sum of displacements within a larger volume within our RMC supercell.

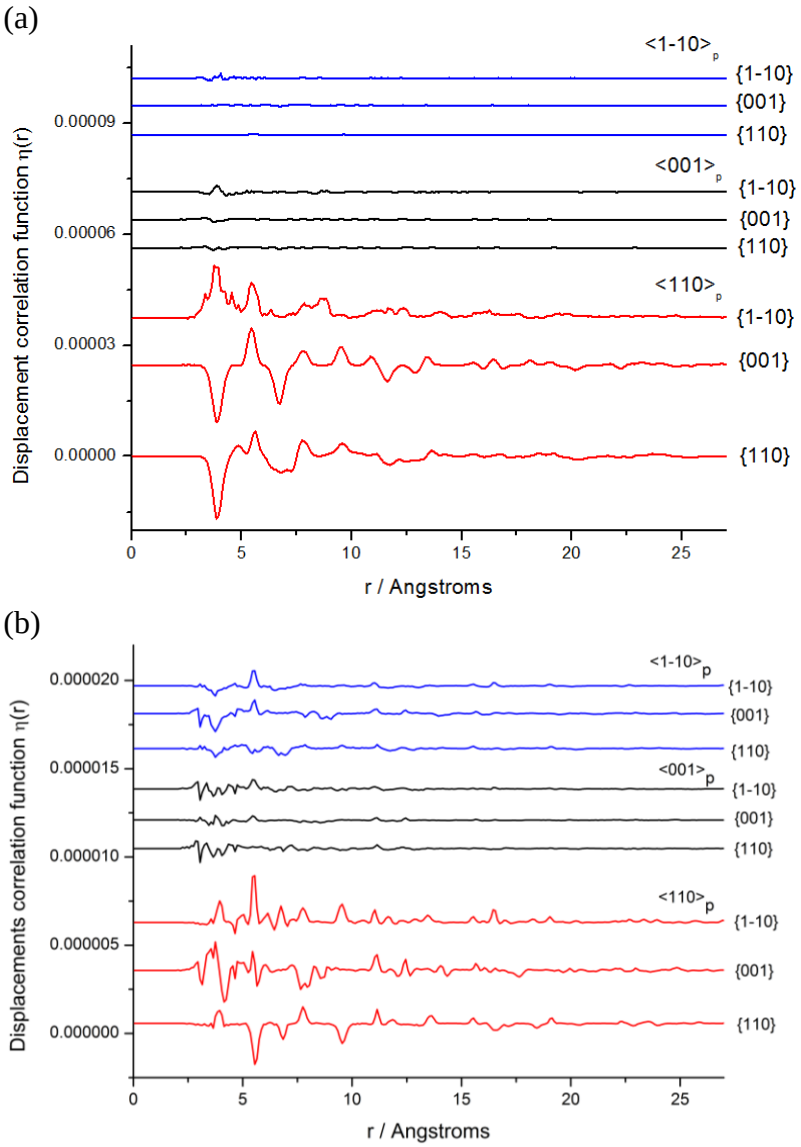

Figure 4.44. *Differential displacement correlation functions calculated for Bi-Bi cations for local structure of* $Bi_2Mn_{4/3}Ni_{2/3}O_6$ *along* $\langle 1\bar{1}0\rangle_p$, $\langle 001\rangle_p$ *and* $\langle 110\rangle_p$ *directions at (a) HT and (b) RT.*

The calculations of Bi^{3+} sum displacement were also applied at HT along the same $\langle 1\bar{1}0\rangle_p$ direction. The results revealed the local ferroelectric correlations

with dimensions of up to 12 Å, with clusters of sum of Bi atoms displaced in the same direction (Figure 4.45a, b). This is unexpected as the average structure demonstrate antiferroelectricity. The displacements of Bi^{3+} cations at average HT commensurate structure completely cancel out (red columns in Figure 4.44a) which is in agreement with this antiferroelectric pattern. Thus, this transformation from the average antiferroelectric to local ferroelectric correlations existing at HT can be assigned to the effect of dynamic local fluctuations of Bi^{3+} cations, not captured by the average crystallographic structure.

(a) (b)

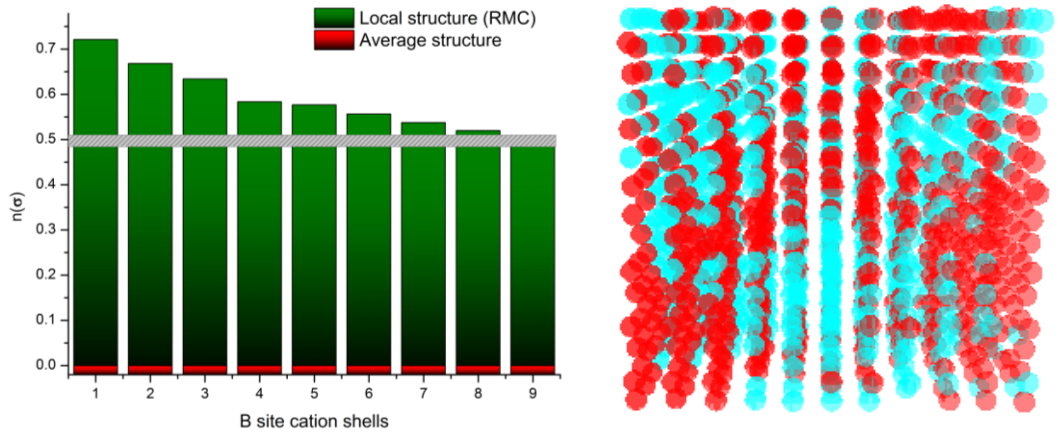

Figure 4.45. *(a) Comparison of the ratio of Bi^{3+} cations displaced in the same direction along $\langle 1\bar{1}0\rangle_p$ over all bismuth atoms between the local structure (green) and average commensurate structure (red) with random distribution presented as an error bar (grey); (b) Supercell with atoms representing positive (red) and negative (blue) sum of Bi atoms with the B site cations as an origin along $\langle 1\bar{1}0\rangle_p$ show clusters of opposite displaced group of atoms.*

4.4.5 Nearest neighbours - B site cation ordering

The average numbers of neighbours for Mn and Ni cations have been calculated directly from partial pair distribution function $g_{B\text{-}B}(r)$ (Figure 4.46), as described in the section 2.3.1.

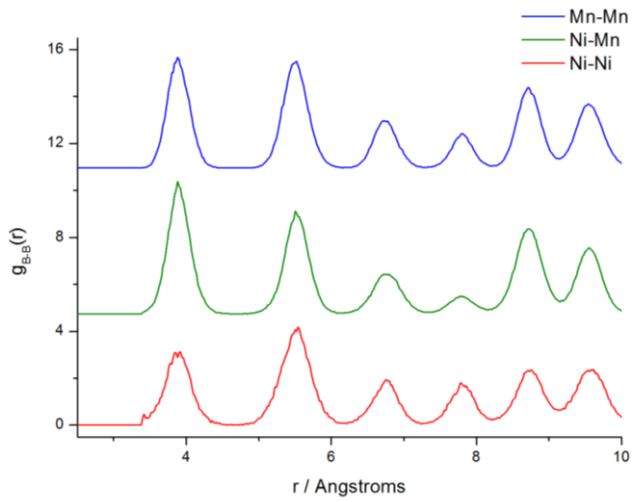

Figure 4.46. *The partial pair correlation functions $g_{B\text{-}B}(r)$ for local structure at RT*

The distribution of B site cations in the RMC models are compared with the completely random distribution, obtained by swapping B site cations during RMC modeling in absence of the data. The average nearest neighbour results of 20 RMC models indicate that the short range Mn/Ni cation order effect persists at high temperature. The first nearest neighbours *n(r)* values 1.51(3) and 4.48(3), of Ni-Ni and Ni-Mn respectively, are significantly different from values 2 and 4 representing random distribution. Furthermore the values of second neighbours 4.49(4) and 7.52(4), have lower values than expected 4 and 8 for random distribution. (Table 4.14 and Figure 4.47a, b). Thus, the same trend of B site ordering is also observed at HT, where the decrease of the Ni-Ni nearest neighbor in the first shell and increase in the second show Mn/Ni ordering is consistent with a bias towards rock-salt ordering within RMC models. The further calculations of the third *n(r)* are prevented by overlap of atoms between shells which then produces less accurate results than for the first two *n(r)*. Thus, the *n(r)* results at HT are comparable to RT, which is consistent with the absence of B site cation diffusion over this restricted temperature range and also reveals the inappropriate nature of the single site in the average structure for the HT phase.

Table 4.14. *B site nearest neighbours for the local structure of HT phase of $Bi_2Mn_{4/3}Ni_{2/3}O_6$. Comparison is given between the refined RMC model with standard errors and a fully disordered B site distribution.*

	n(r) of 1st shell - 6 neighbours		*n(r)* of 2nd shell - 12 neighbours		*n(r)* of 3rd shell - 8 neighbours	
	Local structure (RMC model)	Disordered	Local structure (RMC model)	Disordered	Local structure (RMC model)	Disordered
Mn-Mn	3.76(2)	4.0	8.25(3)	8.0	5.28(5)	5.33
Mn-Ni	2.24(2)	2.0	3.75(3)	4.0	2.71(7)	2.66
Ni-Mn	4.49(3)	4.0	7.52(4)	8.0	5.41(6)	5.33
Ni-Ni	1.51(3)	2.0	4.48(4)	4.0	2.60(8)	2.66

(a) (b)

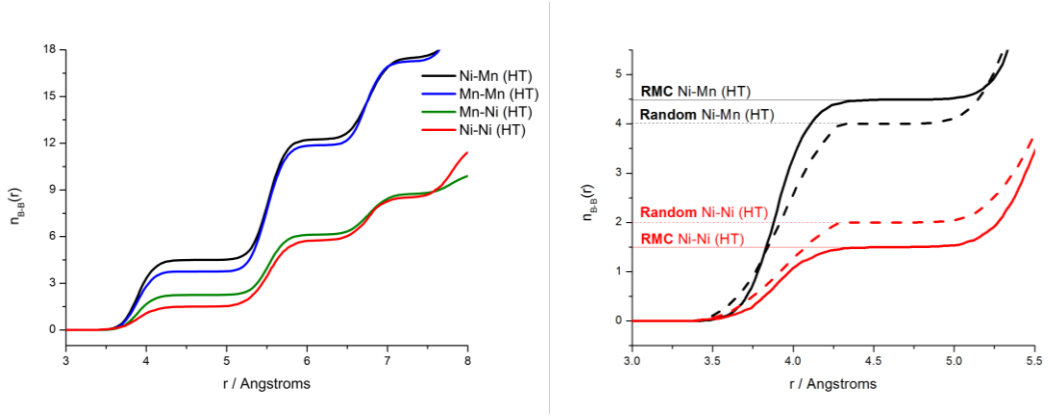

Figure 4.47. *Nearest neighbour functions $n_{B\text{-}B}(r)$ in the RMC configuration; (b) comparison of nearest neighbours of Ni atoms between RMC model and statistically-disordered distribution .*

4.5 Conclusions

We have applied Reverse Monte Carlo modeling to neutron total scattering data for the incommensurate and commensurate structures of $Bi_2Mn_{4/3}Ni_{2/3}O_6$ at room temperature and 300°C, respectively. The local structure results at RT derived from RMC models of dimensions 55 × 62 × 55 Å were compared to the average incommensurate model of a comparable supercell size.

Both models show nearest neighbor B site ordering which acts to reduce unfavorable Ni-Ni interactions, although the nature of the short-range ordering is different for RMC and incommensurate models. *n(r)* calculations in the RMC models show Mn/Ni ordering consistent with a bias towards rock-salt ordering. The regions of NaCl type ordering are also visible in the RMC configuration, where Mn and Ni cations are coloured based on the first shell neighbour results. The average occupancies in the incommensurate structure instead shows a clustering of Mn/Ni cations, which results in an apparently random distribution when calculating *n(r)*. The absence of similar ordering is presumably due to the modulation in the average incommensurate model, where Mn/Ni cations create clustering instead rock-salt type order which is observed in the RMC model. Thus, the modulated description used in the incommensurate model means that the true short-range B site ordering, as revealed through RMC modeling, is not apparent in the incommensurate description.

Initial inspection of partial pair distribution functions for both the RMC and average incommensurate models showed similar Bi-O bond distances, however closer inspection of $g_{Bi\text{-}O}(r)$ for incommensurate models shows two different shapes of discontinuous distribution which differ in shape and number of bond distances with continuous Bi-O distribution obtained from RMC models. Calculation of Bi^{3+} displacements showed a bimodal distribution along the non-polar $\langle 110 \rangle_p$, accounting for the antiferroelectric behavior of BMN, and a single Gaussian shape along polar $\langle 1\bar{1}0 \rangle_p$ and non-polar $\langle 001 \rangle_p$ in both the average incommensurate model and the RMC model, but with broader feature for latter model. These relatively broad atomic distributions in the RMC model are attributed to thermal motion; the RMC model represents a snapshot in time of the structure undergoing thermal motion, whereas the average incommensurate model includes thermal motion as time averaged thermal ellipsoids around an average atomic position. The Bi-Bi DCF analysis also demonstrate the similar shape of peaks at most distance range between both RMC and incommensurate models, with strongest peaks along non-polar $\langle 110 \rangle_p$ demonstrating much stronger antiparallel displacement consistent with antiferroelectric behavior. We also observe weak antiferroelectric correlations instead ferroelectric along $\langle 1\bar{1}0 \rangle_p$

which are consistent with the long-range modulated average structure. The polar behavior of BMN was revealed by calculations within a larger volume, rather than looking at correlations between single pairs of atoms as probed by DCF. We looked at the sum of Bi displacements within a volume, where ferroelectric correlations within the RMC model at RT are visible along $\langle 1\bar{1}0\rangle_p$ with a polar clusters size of up to 12 Å. The visibly dense areas of oppositely displaced atoms, which represent sum of Bi^{3+} cations at RT are similar to the polar regions in the long-range approximant supercell of incommensurate structure which cancel each other to produce long-range average antiferroelectricity. Furthermore, this calculation performed on the average incommensurate model confirmed the sinusoidal modulated behaviour of displaced Bi atoms, resulting from the *sine* terms used to describe the average displacement. On the other hand, the same calculation performed at HT along $\langle 1\bar{1}0\rangle_p$ also revealed the local ferroelectric correlations of the size 12 Å, in contrast to antiferroelectric correlations of the average crystallographic structure, where atomic displacements of Bi cations completely canceled out. The transformation of an antiferroelectric into local ferroelectric correlations at HT indicating that they may be dynamic in nature.

The significant difference between the RMC and the average incommensurate model are observed for B site environment at RT structure. The complex multiple B site cations are distinguished after applying BVS and interatomic potential constraints in the RMC model, where complex Mn site with regular Mn^{4+} and 2:2:2 JT distortions type of Mn^{3+} cations has different mean bond lengths than Ni-O distribution, in contrast to single B site in the average incommensurate model.

Thus, the analysis of the RMC and average incommensurate models of the comparable supercell size indicate the importance of recognizing the length-scale of the probe used for structural characterization, which can have a huge bearing on the details of the structure observed.

4.6. References

1. Hughes, H., Allix, M. M. B., Bridges, C. A., Claridge, J. B., Kuang, X. J., Niu, H. J., Taylor, S., Song, W. H., Rosseinsky, M. J., *A polar oxide with*

a large magnetization synthesized at ambient pressure. Journal of the American Chemical Society, 2005. **127**(40): p. 13790-13791.

2. Hughes, H., *Synthesis and characterization of a potential multiferroic materials*, in *Chemistry*2008, University of Liverpool: Liverpool.
3. Ishiwata, S., Azuma, M., Takano, M., Nishibori, E., Takata, M., Sakata, M., Kato, K., *High pressure synthesis, crystal structure and physical properties of a new Ni(II) perovskite $BiNiO_3$.* Journal of Materials Chemistry, 2002. **12**(12): p. 3733-3737.
4. Inaguma, Y., and Katsumata, T., *High pressure synthesis, lattice distortion, and dielectric properties of a perovskite $BiNi_{1/2}Ti_{1/2}O_3$.* Ferroelectrics, 2003. **286**: p. 833-839.
5. Inaguma, Y., Miyaguchi, A., and Katsumata, T., *Synthesis and lattice distortion of ferroelectric/antiferroelectric Bi(III)-containing perovskites*, in *Solid-State Chemistry of Inorganic Materials Iv*, M.A. AlarioFranco, et al., Editors. 2003, Materials Research Society: Warrendale. p. 471-476.
6. Suchomel, M.R., Thomas, C. I., Allix, M., Rosseinsky, M. J., Fogg, A. M., Thomas, M. F., *High pressure bulk synthesis and characterization of the predicted multiferroic $BiFe_{1/2}Cr_{1/2}O_3$* Applied Physics Letters, 2007. **90**(20).
7. Kimura, T., Kawamoto, S., Yamada, I., Azuma, M., Takano, M., Tokura, Y., *Magnetocapacitance effect in multiferroic $BiMnO_3$.* Physical Review B, 2003. **67**(18).
8. Azuma, M., Takata, K., Saito, T., Ishiwata, S., Shimakawa, Y, Takano, M., *Designed ferromagnetic, ferroelectric Bi_2NiMnO_6.* Journal of the American Chemical Society, 2005. **127**(24): p. 8889-8892.
9. Carlsson, S.J.E., Azuma, M., Shimakawa, Y., Takano, M., Hewat, A., Attfield, J. P., *Neutron powder diffraction study of the crystal and magnetic structures of $BiNiO_3$ at low temperature.* Journal of Solid State Chemistry, 2008. **181**(3): p. 611-615.
10. Kanamori, J., *Superexchange interaction and symmetry properties of electron orbitals.* Journal of Physics and Chemistry of Solids, 1959. **10**(2-3): p. 87-98.

11. Goodenough, J.B., *Theory of the role of covalence in the perovskite-type manganites La,M(II)MnO_3.* Physical Review, 1955. **100**(2): p. 564-573.
12. Claridge, J.B., Hughes, H., Bridges, C. A., Allix, M., Suchomel, M. R., Niu, H., Kuang, X., Rosseinsky, M. J., Bellido, N., Grebille, D., Perez, O., Simon, C., Pelloquin, D., Blundell, S. J.,Lancaster, T., Baker, P. J., Pratt, F. L., Halasyamani, P. S., *Frustration of Magnetic and Ferroelectric Long-Range Order in $Bi_2Mn_{4/3}Ni_{2/3}O_6$.* Journal of the American Chemical Society, 2009. **131**(39): p. 14000-14017.
13. Hervieu, M., Malo, S., Perez, O., Beran, P., Martin, C., Baldinozzi, G., Raveau, B., *New type of charge/orbital ordering above room temperature in the perovskite $Bi_{2/3}Sr_{1/3}MnO_3$.* Chemistry of Materials, 2003. **15**(2): p. 523-527.
14. Frontera, C., Garcia-Munoz, J. L., Aranda, M. A. G., Hervieu, M., Ritter, C., Manosa, L., Capdevila, X. G., Calleja, A., *Charge and zener polaron order in $Bi_{0.75}Sr_{0.25}MnO_3$.* Physical Review B, 2003. **68**(13).
15. Giot, M., Beran, P., Perez, O., Malo, S., Hervieu, M., Raveau, B., Nevriva, M.,Knizek, K., Roussel, P., *$Bi_{1-x}Ca_xMnO_3$ (x=0.4 and 0.45): X-ray single crystal and electron microscopy study.* Chemistry of Materials, 2006. **18**(14): p. 3225-3236.
16. Petrícek, V., Dusek, M., and Palatinus, L., *Jana2006 - the crystallographic computing system.* 2006; Available from: www-xray.fzu.cz/jana.
17. Hannon, A.C., *Results on disordered materials from the GEneral Materials diffractometer, GEM, at ISIS.* Nuclear Instruments & Methods in Physics Research Section a-Accelerators Spectrometers Detectors and Associated Equipment, 2005. **551**(1): p. 88-107.
18. McLain, S.E., Bowron, D. T., Hannon, A. C., Soper, A. K., *Gudrun. A computer program developed fro analysis of neutron diffraction data.*, 2006: ISIS Facility, Rutherford Appleton Laboratory, Chilton, Didcot, OXON, UK, OX11 0QX.
19. Tucker, M.G., Goodwin, A.L., and Dove, M.T., *RMCProfile User Manual: Code version 6.4.7*2010.

20. Tucker, M.G., Keen, D. A., Dove, M. T., Goodwin, A. L., Hui, Q., *RMCProfile: reverse Monte Carlo for polycrystalline materials.* Journal of Physics-Condensed Matter, 2007. **19**(33).

21. Chong, S.Y., Szczecinski, R. J., Bridges, C. A., Tucker, M. G., Claridge, J. B., Rosseinsky, M. J., *Local structure of a pure Bi A site polar perovskite revealed by Pair Distribution Function analysis and reverse Monte Carlo modeling: Correlated off-axis displacements in a rhombohedral material.* Journal of the American Chemical Society, 2012. **134**(13): p. 5836-5849.

22. Salamon, M.B. and Jaime, M., *The physics of manganites: Structure and transport.* Reviews of Modern Physics, 2001. **73**(3): p. 583-628.

23. Ashcroft, N. and Mermin, N., *Solid State Physics*1976, Philadelphia: Saunders College Publishing.

24. Rodriguez-Carvajal, J., Hennion, M., Moussa, F., Moudden, A. H., Pinsard, L., Revcolevschi, A., *Neutron-diffraction study of the Jahn-Teller transition in stoichiometric $LaMnO_3$.* Physical Review B, 1998. **57**(6): p. R3189-R3192.

25. Billinge, S.J.L., Proffen, T., Petkov, V., Sarrao, J. L., Kycia, S., *Evidence for charge localization in the ferromagnetic phase of $La_{1-x}Ca_xMnO_3$ from high real-space-resolution x-ray diffraction.* Physical Review B, 2000. **62**(2): p. 1203-1211.

26. Louca, D., Egami, T., Brosha, E. L., Roder, H., Bishop, A. R., *Local Jahn-Teller distortion in $La_{1-x}Sr_xMnO_3$ observed by pulsed neutron diffraction.* Physical Review B, 1997. **56**(14): p. R8475-R8478.

27. Brown, I.D. and Altermatt, D., *Bond valence parameters obtained from a systematic analysis of the inorganic crystal structure database.* Acta Crystallographica Section B-Structural Science, 1985. **41**(AUG): p. 244-247.

28. Jona, F., Shirane, G., Mazzi, F., Pepinsky, R., *X-ray and neutron diffraction study of antiferroelectric Lead Zirconate, $PbZrO_3$.* Physical Review, 1957. **105**(3): p. 849-856.

29. Fujishita, H., Shiozaki, Y., Achiwa, N., Sawaguchi, E., *Crystal structure determination of antiferroelectric $PbZrO_3$ - Application of profile analysis*

method to powder method of x-ray and neutron diffraction. Journal of the Physical Society of Japan, 1982. **51**(11): p. 3583-3591.

Chapter 5. Synthesis and characterization of crystallographic average structure of $BiFe_{0.6}Mn_{0.4}O_3$

5.1 Introduction

This chapter reports on the synthesis and characterization of $BiFe_{0.6}Mn_{0.4}O_3$ (BFM), which is one of the few bismuth based perovskite materials synthesized under ambient pressure conditions. Up to now, the single phase of $BiFe_{1-x}Mn_xO_3$ has been obtained only within the composition range x=0-0.3, whereas this study describes the synthesis and structural characterization of $BiFe_{1-x}Mn_xO_3$ with an extended composition range of x=0.4.

Structural investigations using Powder X-ray Diffraction and Time of Flight Neutron Powder Diffraction are reported, where characterization were carried out with the aid of Dr. John B. Claridge, Dr. Philip Chater and Prof. Matthew J. Rosseinsky. The electron microscopy study was carried out by Dr. Z. Xu.

5.2 Previous work on $BiFe_{1-x}Mn_xO_3$

There are several reports of the synthesis of the ferroelectric $BiFeO_3$ doped with a limited amount of Mn cations at ambient pressure; $BiFe_{1-x}Mn_xO_3$ where x=0, 0.1, 0.2 and 0.3 can be successfully synthesized using conventional methods. The further substitution of Mn cations into the B site cause the generation of secondary phases sillenite $Bi_{25}FeO_{39}$, and mullite $Bi_2Fe_4O_9$. These impurities also occur during synthesis of the well known $BiFeO_3$. Thus, extra precautions must be taken to obtain a single phase of $BiFe_{1-x}Mn_xO_3$ or pure bismuth ferrite. The origin of these secondary phases was explained by Alford and coauthors, based on the X-ray diffraction results and microstructural analyses [1]. Their synthesis of $BiFeO_3$ was performed with oxides with different concentrations of impurities, and showed that implementation of oxides Bi_2O_3 and Fe_2O_3 with 99.9% purity influenced the phase composition. It was shown that these starting oxides generated small amounts of sillenite $Bi_{25}FeO_{39}$ ‘S’ and mullite $Bi_2Fe_4O_9$ ‘F’ secondary phases, as visible in the diffraction pattern and backscattering electron image where dark ($Bi_2Fe_3O_9$) and white spots ($Bi_{25}FeO_{39}$) are also present with

grey spots of $BiFeO_3$ (Figure 5.1). On the other hand, the application of ultra pure (99.9995%) starting oxides Bi_2O_3 and Fe_2O_3 helped to obtain a single phase of pollycrystaline $BiFeO_3$. The pure bismuth ferrite during sintered at 880°C for 2-5 hours remained solid with small grains of sub-micrometer size, in contrast to the sample sintered at 800°C containing sillenite $Bi_{25}FeO_{39}$ and mullite $Bi_2Fe_4O_9$ secondary phases. Thus, the purity of the starting oxides play important role in a successful synthesis of single phase of $BiFeO_3$.

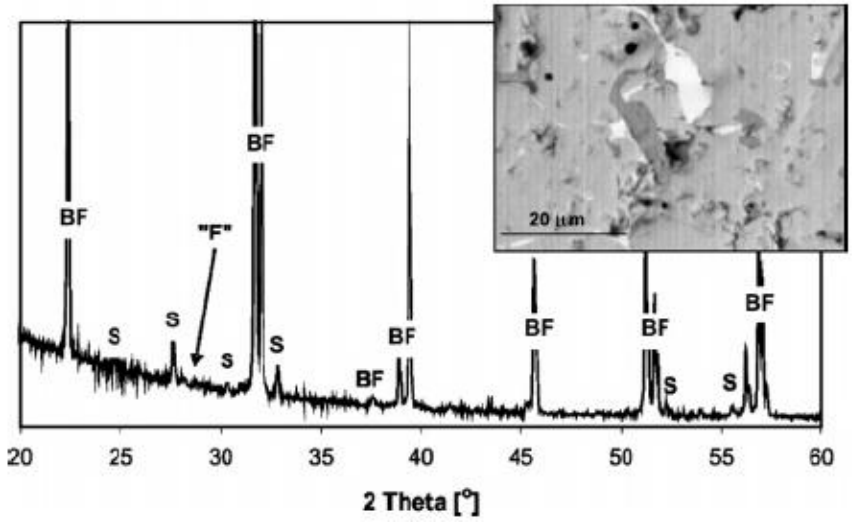

Figure 5.1. *X-Ray diffraction pattern of $BiFeO_3$ (BF) and backscattering electron image containing secondary phases of sillenite $Bi_{25}FeO_{39}$ ('S' - white spots), and mullite $Bi_2Fe_4O_9$ ('F' - dark spots) [1].*

The substitution of different cations into the $BiFeO_3$ structure provide even more difficulties when attempting to control the synthesis to produce a pure phase. The structural analysis of BFM (x=0, 0.1, 0.2 and 0.3) described by Sosnowska [2-4] and others [5-10] are based on the X-ray and neutron powder diffraction data, and showed no phase transitions within the composition range studied. The structure is described by the space group *R*3*c* of the parent ferroelectric phase, $BiFeO_3$. The substitution of Mn cations on the B site provide an amount of disorder and generates microstructural changes, which cause the peak broadening in the diffraction pattern and also cause the generation of small impurity peaks belonging to $Bi_{12}MnO_{24}$ [11]. The doping of Mn cations also affect the magnetic properties, where a transformation is observed from the long-range G-type spiral spin modulation (SMSS) of $BiFeO_3$ with a periodicity of 62 nm to a G-type

collinear antiferromagnetic structure with spin along the $\langle 110 \rangle_p$ direction ($\langle \rangle_p$ refers to the parent cubic perovskite unit cell) [3, 12, 13]. As the Mn doping is increased, the propagation vector changes, and the average magnetic moment gradually decreases. These changes to the magnetic structure observed upon doping $BiFeO_3$ are also reflected in the analysis of the full width at half maximum (FWHM) of the magnetic peaks. The profile parameters of pure $BiFeO_3$ and the sample with x=0.1 demonstrate much broader magnetic peaks in contrast to less broadened $BiFe_{0.8}Mn_{0.2}O_3$ (x=0.2). Thus, the FWHM of magnetic peaks decrease with increase doping, which indicate that the substitution of Mn cations on the B site and replacement of Fe cations stabilizes the collinear magnetic structure instead of incommensurate spiral magnetic structure (SMSS) as observed in the pure bismuth ferrite. The structural and properties analysis of $BiFe_{1-x}Mn_xO_{3+d}$ (x=0, 0.1, 0.2 and 0.3) in the Selbach report [14] also demonstrate that Mn substitution with oxygen hyperstoichiometry affect the crystallographic properties and increase the B site disorder, which is most likely the origin of the increasing broadening of structural Bragg peaks. The gradually decrease of T_c and the polar displacements of Bi^{3+} cations during doping of Mn in the $BiFe_{1-x}Mn_xO_{3+d}$ (x=0, 0.1, 0.2 and 0.3) suggest, that the B site cations may play a bigger role in ferroelectricity than previously thought. The replacement of Fe^{3+} cations by Mn^{3+} with higher energy of e_g orbitals show that partial covalent bonding between Fe 3*d* and O 2*p* orbitals can be equally important to bonding between Ti 3*d* and O 2*p* in $BaTiO_3$ or $PbTiO_3$ [15]. The reduced Neel temperature with increasing x and excess oxygen δ is most likely caused by the number of e_g electrons between Fe (2 electrons) and Mn (1 electron) responsible for antiferromagnetic superexchange interactions. The solubility limit investigated by Selbach [14] was determined to be $x \leq 0.3$, which suggested that high pressure was needed to form single phase perovskites at higher x. The high pressure (3GPa) synthesis of $BiFe_{1-x}Mn_xO_3$ within an entire range composition (*x*=0-1) were reported by Azuma [16, 17]. A phase transition was observed from rhombohedral structure of $BiFeO_3$ for x=0-0.1, to orthorhombic with $x \geq 0.2$ and lattice parameters $\sqrt{2}a_p \times 4a_p \times 2\sqrt{2}a_p$ similar to that observed for $Bi_2Mn_{4/3}Ni_{2/3}O_6$ [18]. Furthermore, another phase transition was observed at x=0.8 where structure becomes monoclinic with the

$BiMnO_3$-type structure [19]. Thus, it was found that the $BiFeO_3$ and $BiMnO_3$ form a solid solution in the entire composition range under high pressure, however our aim was to form single-phase perovskite at ambient pressure at a higher doping level than previously reported.

5.3 Ceramic Synthesis

The sample was synthesized using standard ceramic methods, where stoichiometric quantities of high purity Bi_2O_3 (Alfa Aesar 99.9995%), MnO_2 (Alfa Aesar 99.999%) and Fe_2O_3 (Alfa Aesar 99.999%) were accurately weighed, ground in a ball mill with Mg-stabilised zirconia milling media for 12 hours and then pelletized. During the synthesis the pellets were always placed on platinum foil in an alumina boat to avoid reaction with alumina. Initially an attempt was made to prepare $BiFe_{0.6}Mn_{0.4}O_3$ (BFM) by a standard ceramic method with several heating stages. The sample was heated at 800°C for 12 hours, 850°C for 12 hours, 875°C for 12 hours, 890°C for 12 hours and finally twice at 900°C for 12 hours. After each firing stage the pellet was ground by hand with an agate mortar and pestle, and XRD data were collected in order to monitor progress of the synthesis. All steps used a heating and a cooling rate of 5°C or 10°C per minute. During this long synthesis process the BFM material formed the desired perovskite structure, but this was alongside secondary phase impurities of sillenite $Bi_{25}FeO_{39}$ and mullite $Bi_2Fe_4O_9$ (Figure 5.2).

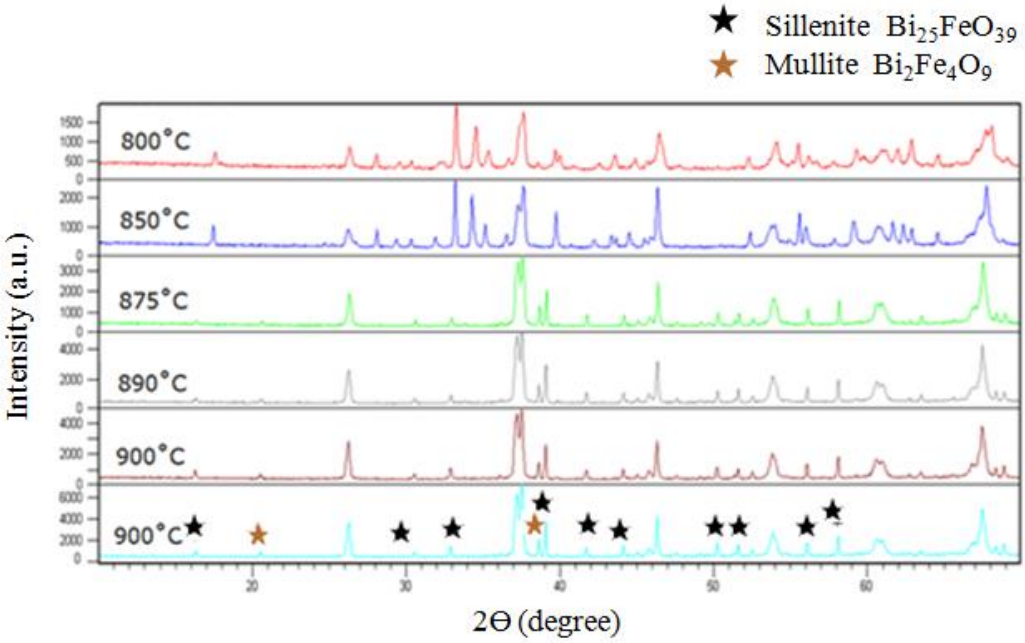

Figure 5.2. *X-Ray diffraction pattern of $BiFe_{0.6}Mn_{0.4}O_3$ at various temperatures containing secondary phases of sillenite $Bi_{25}FeO_{39}$ and mullite $Bi_2Fe_4O_9$.*

Several attempts was made to obtain the single phase of perovskite structure at ambient pressure where the temperature and heating time as well as heating and cooling rates were changed many times (Table 5.1). Despite the many varied synthesis conditions tested, the secondary phases of sillenite $Bi_{25}FeO_{39}$ and mullite $Bi_2Fe_4O_9$ were always present in the final material and it was not possible to determine trend in the conditions used which led to a decreasing the impurities observed in the diffraction pattern.

Table 5.1. *Different conditions of synthesis of $BiFe_{0.6}Mn_{0.4}O_3$ containing secondary phases.*

	800°C	850°C	875°C	900°C	925°C
Heating rate 5/min; Cooling rate 5/min	Major presence of $Bi_{25}FeO_{39}$ and $Bi_2Fe_4O_9$	Major presence of $Bi_{25}FeO_{39}$ and $Bi_2Fe_4O_9$	Minor presence of $Bi_{25}FeO_{39}$ and $Bi_2Fe_4O_9$	Minor presence of $Bi_{25}FeO_{39}$ and $Bi_2Fe_4O_9$	melted
Heating rate 5/min; Cooling rate 10/min	Major presence of $Bi_{25}FeO_{39}$ and $Bi_2Fe_4O_9$	Major presence of $Bi_{25}FeO_{39}$ and $Bi_2Fe_4O_9$	Minor presence of $Bi_{25}FeO_{39}$ and $Bi_2Fe_4O_9$	Minor presence of $Bi_{25}FeO_{39}$ and $Bi_2Fe_4O_9$	melted
Heating rate 10/min; Cooling rate 10/min	Major presence of $Bi_{25}FeO_{39}$ and $Bi_2Fe_4O_9$	Major presence of $Bi_{25}FeO_{39}$ and $Bi_2Fe_4O_9$	Minor presence of $Bi_{25}FeO_{39}$ and $Bi_2Fe_4O_9$	Minor presence of $Bi_{25}FeO_{39}$ and $Bi_2Fe_4O_9$	melted

A new synthesis method of rapid liquid phase sintering was implemented in an attempt to obtain a single phase of the BFM material. This technique has been applied to $BiFeO_3$ by Wang [20], where the sample was sintered for 450 s in air, within a temperature range of 750-880°C. Reaction at temperatures between 750-820°C gave rise to the presence of a $Bi_{36}Fe_2O_{57}$ impurity phase, whereas rapid liquid phase sintering the sample at 880°C provided the pure phase of rhombohedral $BiFeO_3$. The application of a higher sintering temperature than the melting point of Bi_2O_3 (817°C) is important, as this creates the liquid phase which will then accelerate the synthesis reaction with Fe_2O_3, MnO_2 and prevent the formation of the impurity phases. Recent successful rapid liquid phase sintering synthesis of pure $BiFeO_3$ caused a boost for further investigation of this technique by doping other cations on the B site. An example of doping Co or Ti on the B site in $BiFeO_3$ showed the phase transition from rhombohedral *R*3*c* to cubic or orthorhombic respectively [21, 22]. There have also been attempts to study the influence of Mn substitution in $BiFeO_3$, however within the doping limit x=0-0.3 crystal structure of the BFM material was unaffected [23].

In this study the Mn substitution into the B site at a higher doping value of x=0.4 was synthesized by rapid liquid phase sintering technique within the temperature range 845-900°C. The sample was rapidly heated to 845-900°C by insertion the pellet into a preheated furnace, dwelled for 5 minutes and quenching to room temperature by removing it from the furnace and placing it onto an alumina plate. X-ray diffraction pattern results after synthesis in the range 845-880°C still contained the secondary phases of sillenite and mullite (Figure 5.3), whereas the attempt at 890°C provided a single phase. PXRD data for the single phase BFM (x=0.4) material were collected for an extended data collection time at an improved signal-to-noise ratio and impurities were still not visible (Figure 5.4).

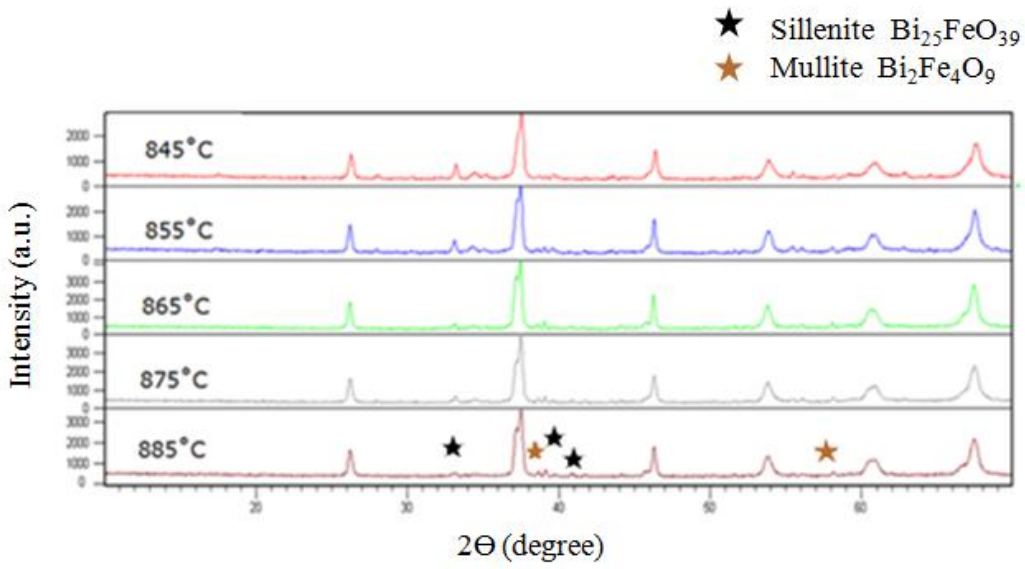

Figure 5.3. *X-Ray diffraction pattern of $BiFe_{0.6}Mn_{0.4}O_3$ at various temperatures synthesized by rapid liquid phase sintering, containing secondary phases of sillenite $Bi_{25}FeO_{39}$ and mullite $Bi_2Fe_4O_9$.*

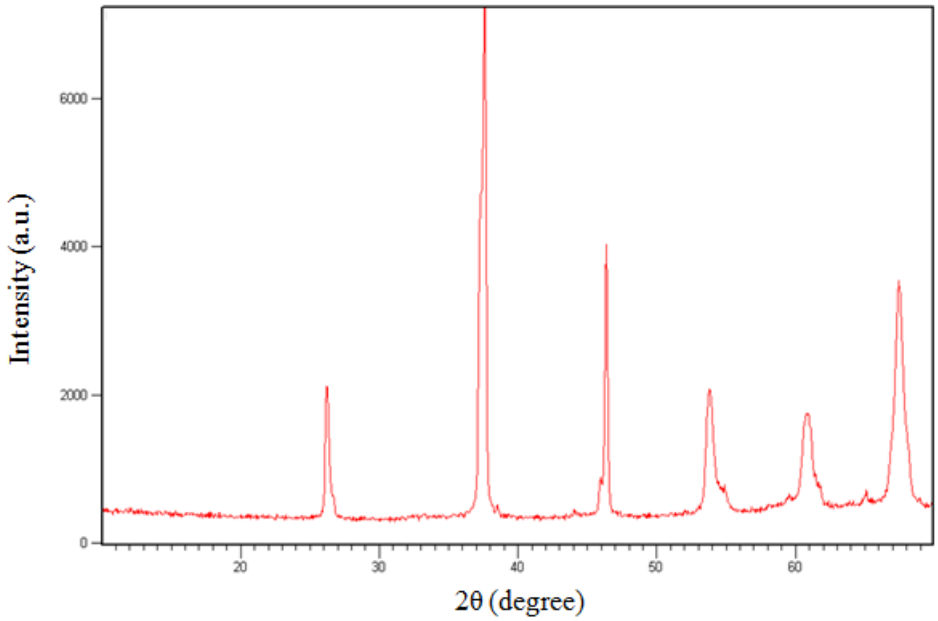

Figure 5.4. *X-Ray diffraction pattern of $BiFe_{0.6}Mn_{0.4}O_3$ at 890˚C containing single phase synthesized by rapid liquid phase sintering.*

To check the composition, energy dispersive spectroscopy (EDS) was applied and the results were in agreement with the target composition $BiMn_{0.4}Fe_{0.6}O_3$ (Table 5.2. and Figure 5.5).

Table 5.2. *The comparison of the calculated experimental average composition with expected composition and standard deviation values.*

Elements	Average EDS Composition (%)	Standard deviation in EDS value	Expected Composition (%)
Bi	49.8	0.92	50
Fe	30.5	1.42	30
Mn	19.7	1.06	20

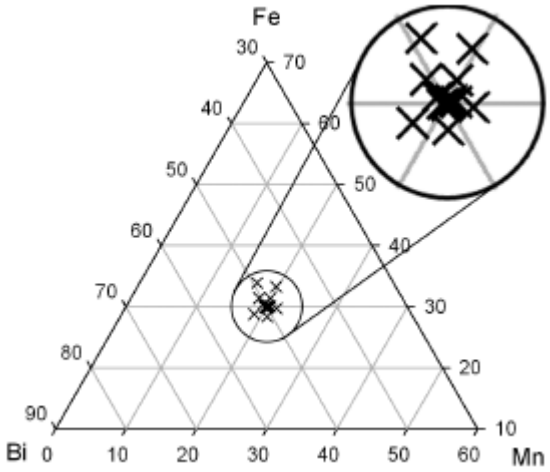

Figure 5.5. *Energy dispersive spectroscopy of perovskite of $BiFe_{0.6}Mn_{0.4}O_3$.*

The collected X-ray diffraction pattern (Figure 5.4) shows broad peaks demonstrating the less than optimal crystallinity of the BFM material. To increase the sharpness of the peaks, the BMF material was annealed at lower temperatures than the synthesis temperature. Several attempts at 800, 700, 600, 500, and 400°C for 24, 48 and 72 hours for each sample were performed. After every attempt annealing at lower temperature generated extra peaks, which were identified as sillenite $Bi_{25}FeO_{39}$ and mullite $Bi_2Fe_4O_9$ impurities, indicating that BFM structure is very prone to decomposition at elevated temperatures, and that its crystallinity cannot be improved (Figure 5.6).

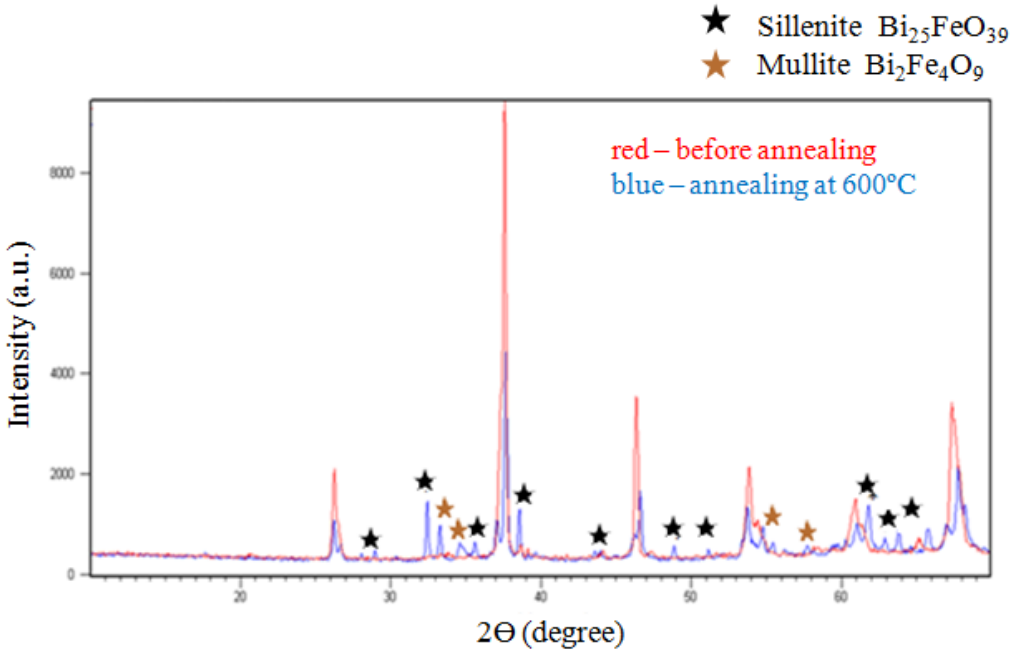

Figure 5.6. *Comparison of X-Ray diffraction pattern of $BiFe_{0.6}Mn_{0.4}O_3$ before and after annealing, containing impurities.*

Further synthesis of the BFM (x=0.4) material was performed at ULVEC Mini Lamp Annealer MILA P-N furnace with the aim of improving the crystallinity and providing more accurate synthesis conditions than are possible by quenching by hand with a standard furnace. The initial synthesis in this furnace at 890°C (the same temperature as used in the furnace quenching method) resulted in the pellet sample completely melting; further syntheses were tried at lower temperatures. Samples were synthesized within a range of 660-780°C, with different reaction times between 3-10 minutes, in air and vacuum (Table 5.2). All of the syntheses attempted within these conditions produced secondary phases as observed in the X-ray diffraction pattern (Figure 5.7a). The dominant factor affecting the quantity of secondary phases was the slow cooling rate of the lamp annealer. The cooling rate is obtained in natural way of changing the air pressure in the lamp annealer. The measured cooling rate is presented with one of the synthesis example of 0.75 bar of air (Figure 5.7b), where very slow temperatures decrease were used (in contrast to the rapid cooling used to produce pure samples using a standard furnace).

Table 5.2 *Rapid liquid phase sintering different condition in synthesis of* $BiFe_{0.6}Mn_{0.4}O_3$ *still contains secondary phases.*

	Time / mins	Temperature condition / °C	
		660-780	≥800
Air environment (gas pressure 0.75 bar)	3-7	Presence of $Bi_{25}FeO_{39}$ and $Bi_2Fe_4O_9$	Melted
Vacuum	3-7	660-740	≥760
		Presence of $Bi_{25}FeO_{39}$ and $Bi_2Fe_4O_9$	Melted

(a)

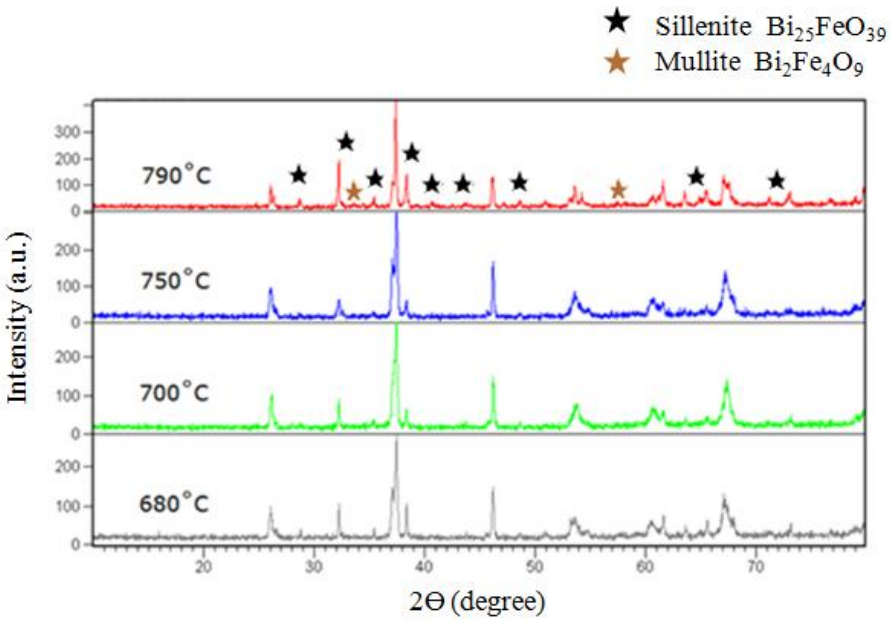

(b)

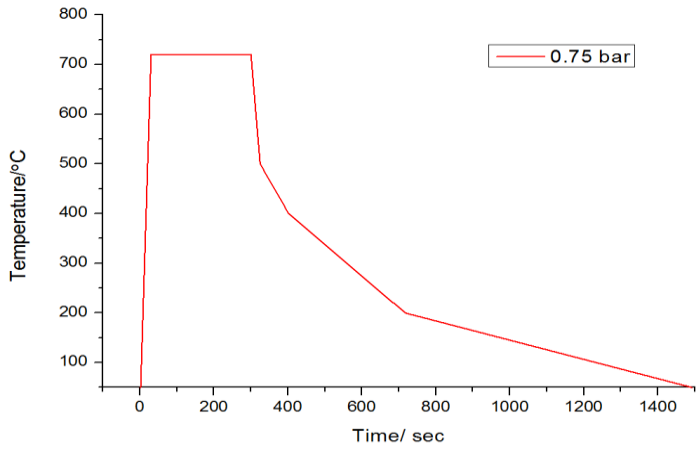

Figure 5.7. *(a) Comparison of X-Ray diffraction pattern of $BiFe_{0.6}Mn_{0.4}O_3$ containing impurities, synthesized in MILA lamp annealer; (b) The example of synthesis with temperature stages versus time at a pressure of 0.75 bar of air showing slow cooling rate.*

To increase the cooling rate the different pressures have been applied to lamp annealer, and the range between 0.75-3 bars of air have been examined in terms of cooling rate. Increased pressure gradually increased the cooling rate as expected,

and the application of 2.5 bar instead of previously used 0.75 bar helped to significantly reduce the cooling time (Table 5.3.).

Table 5.3. *The cooling rate in the mini lamp annealer at various pressures.*

	0.75 bar (5 mins) / Pa	1 bar (5 mins) / Pa	1.25 bar (5 mins) / Pa	1.5 bar (5 mins) / Pa	1.75 bar (5 mins) / Pa	2.5 bar (5 mins) / Pa	2.5 bar (7 mins) / Pa	2.5 bar (3 mins) / Pa
720°C	0	0	0	0	0	0	0	0
500°C	25"	20"	18"	16"	15"	12"	15"	11"
400°C	1'37"	1'25"	1'10"	59"	54"	39"	44"	35"
200°C	6'52"	6'05"	5'17"	4'31"	4'08"	3'05"	5'24"	2'52"
50°C	19'47"	17'57"	15'55"	13'58"	12'50"	10'09"	14'49"	9'20"

The application of the higher pressure (and therefore higher cooling rate) helped to minimize the secondary phases, however the BFM (x=0.4) material still contained an amount of sillenite $Bi_{25}FeO_{39}$ and mullite $Bi_2Fe_4O_9$ (Figure 5.8). Increasing the pressure further destabilized the temperature sensor inside the mini lamp annealer so that the synthesis could not be performed. Thus, the single phase of BFM (x=0.4) material can be only obtained in the standard furnace, where synthesis temperature is higher than the melting point of Bi_2O_3, and cooling rate is sufficient short to avoid forming of secondary phases $Bi_{25}FeO_{39}$. Therefore, the further structural analysis was performed on the BFM (x=0.4) material synthesized in the standard furnace.

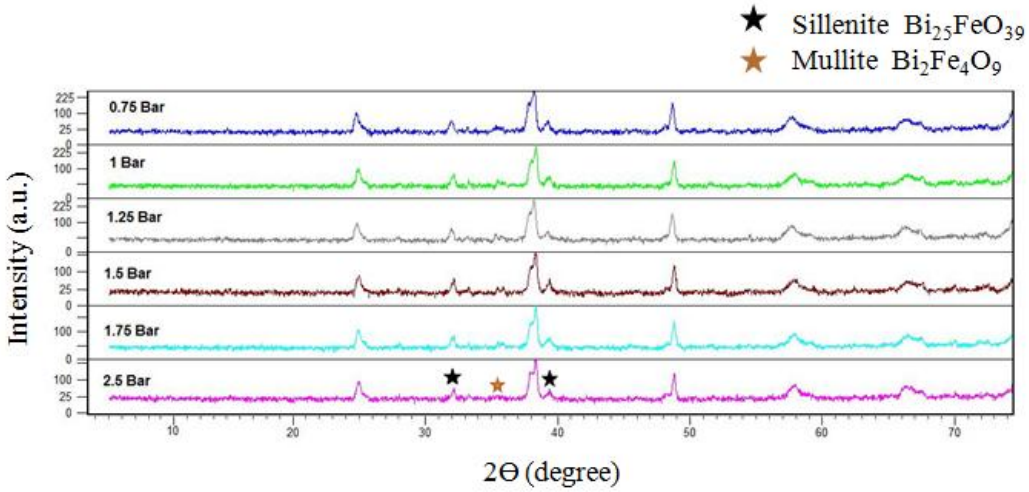

Figure 5.8. *Comparison of X-Ray diffraction pattern of $BiFe_{0.6}Mn_{0.4}O_3$ at various pressures containing impurities.*

5.4 TEM analysis

The BFM (x=0.4) material synthesized by the rapid liquid phase sintering technique was analyzed by Transmission Electron Microscopy (TEM). The Selected Area Electron Diffraction (SAED) patterns show that it has a double perovskite structure ($a=2a_p$, where a_p denotes the single perovskite cubic lattice parameter) with modulations along $\langle 110\rangle_p$ and an average incommensurate modulation vector $q=0.247^* \langle 110\rangle_p$ (Figure 5.9). The HRTEM also demonstrate that the sample has a modified double perovskite structure along $\langle 110\rangle_p$, however the modulations are a mixture of 4-fold and 5-fold modulations along basic lattice $\langle 110\rangle_p$ as indicated in the inset on the Figure 5.10. The HRTEM provides the average incommensurate vector with value $0.207^*\langle 110\rangle_p$ in contrast to approximate 4-fold modulations observed by SAED. Furthermore, a local 4-fold ($4a_p$) commensurate modulation along $\langle 001\rangle_p$ was found in the HRTEM (absent in SAED), as observed in the inset of the framed area in Figure 5.11. As an effect of this modulation, supercell diffraction peaks can be indexed as $0.25^*\langle 001\rangle_p$. The presence of $0.25^*\langle 001\rangle_p$ reflections in HRTEM are similar to 4-fold superstructure reflections along $\langle 001\rangle_p$ in $Bi_{0.75}La_{0.25}FeO_3$ [24], which have been found on electron diffraction and X-ray diffraction pattern, as an effect of coupling antipolar displacement and tilting distortions of octahedra. However, superstructure reflections along $\langle 001\rangle_p$ in BFM (x=0.4) are limited in nanoscale

and only present in HRTEM. Furthermore these reflections could not be simultaneously observed with others superstructure reflections $0.207*\langle 110\rangle_p$ in the same electron diffraction pattern like in $Bi_{1-x}Nd_xFeO_3$ [25], and thus it is likely to be origin of different phase. Twin boundaries were also observed, resulting from modulations directed along different equivalent $\langle 110\rangle_p$ directions on both sides (Figure 5.12). Thus, the analysis of HRTEM and SAED demonstrate the modulated character of BFM material, which is unexpected as only BFM (x=0.25) at high pressure adopt an incommensurate structure [7] similar to $Bi_{(1-x)}La_xFeO_3$ [24]. Furthermore there are also relatively few reports where the other Bi-based perovskites (such as $Bi_{1-x}Sr_xMnO_3$ [26, 27] or $Bi_2Mn_{4/3}Ni_{2/3}O_6$ [28]) demonstrating incommensurate superstructures. The incommensurate structure of BFM (x=0.4), as observed by SAED and HRTEM, was investigated by powder diffraction methods.

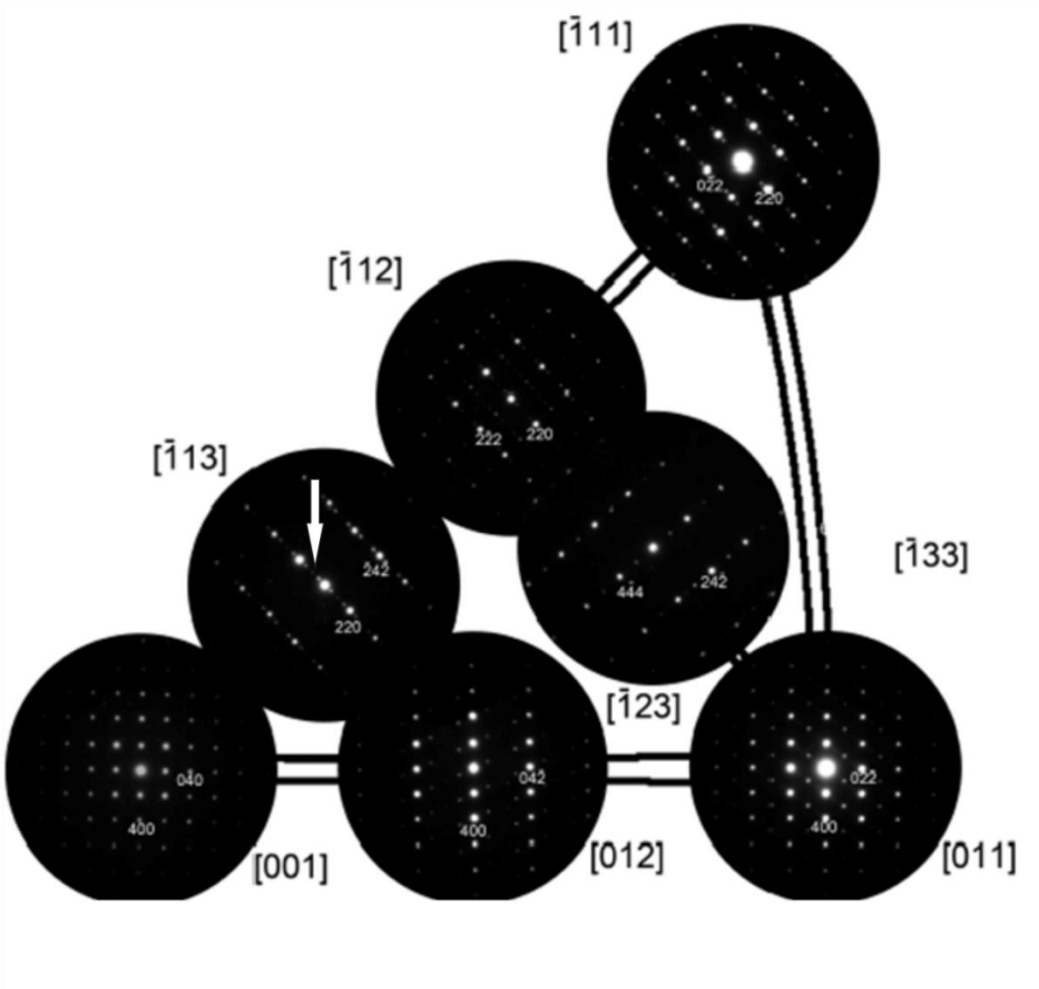

Figure 5.9. *SAED patterns with the average incommensurate modulations along* $\langle 110 \rangle_p$.

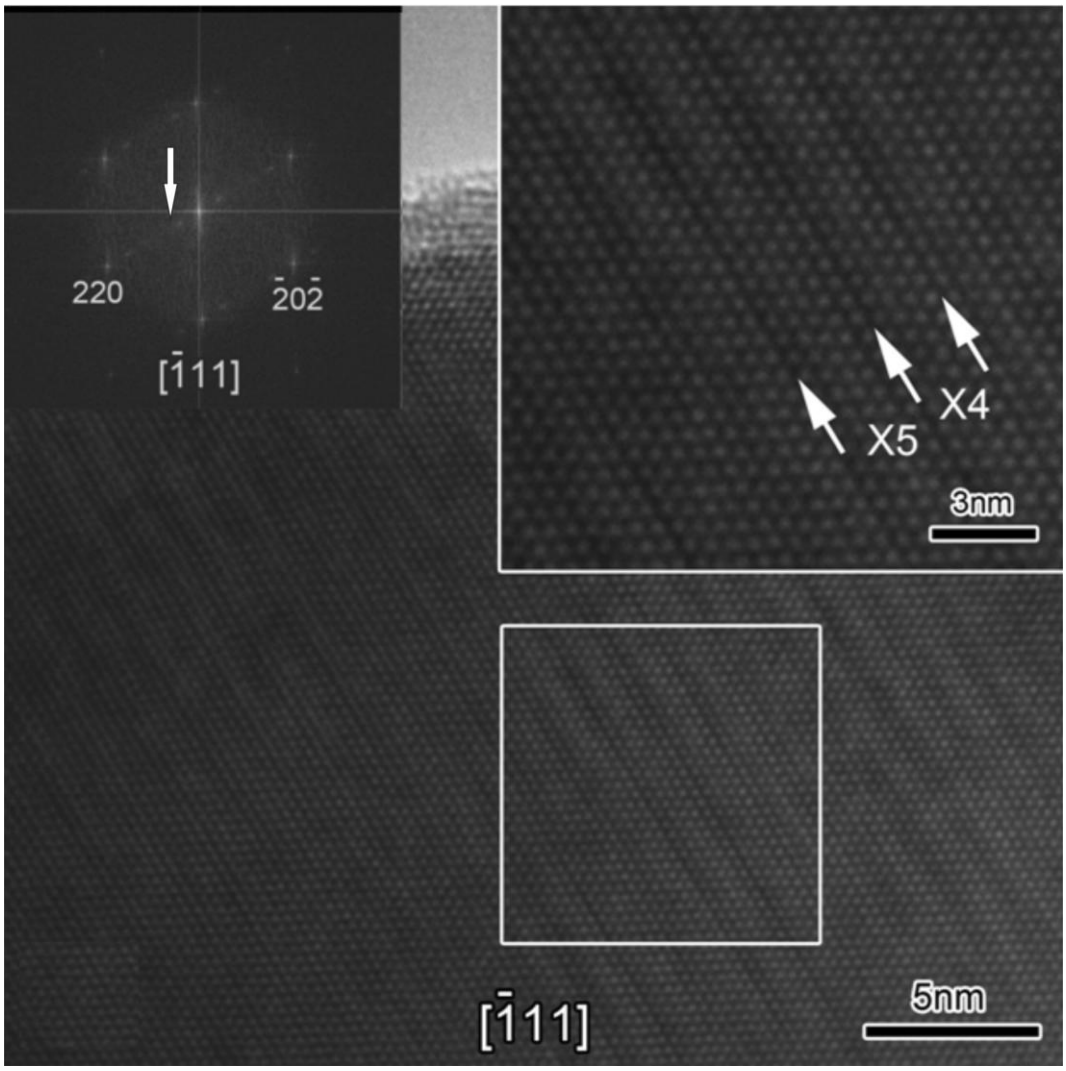

Figure 5.10. [$\bar{1}$11] *HRTEM image with incommensurate modulation vector q= 0.207* ⟨110⟩$_p$.*

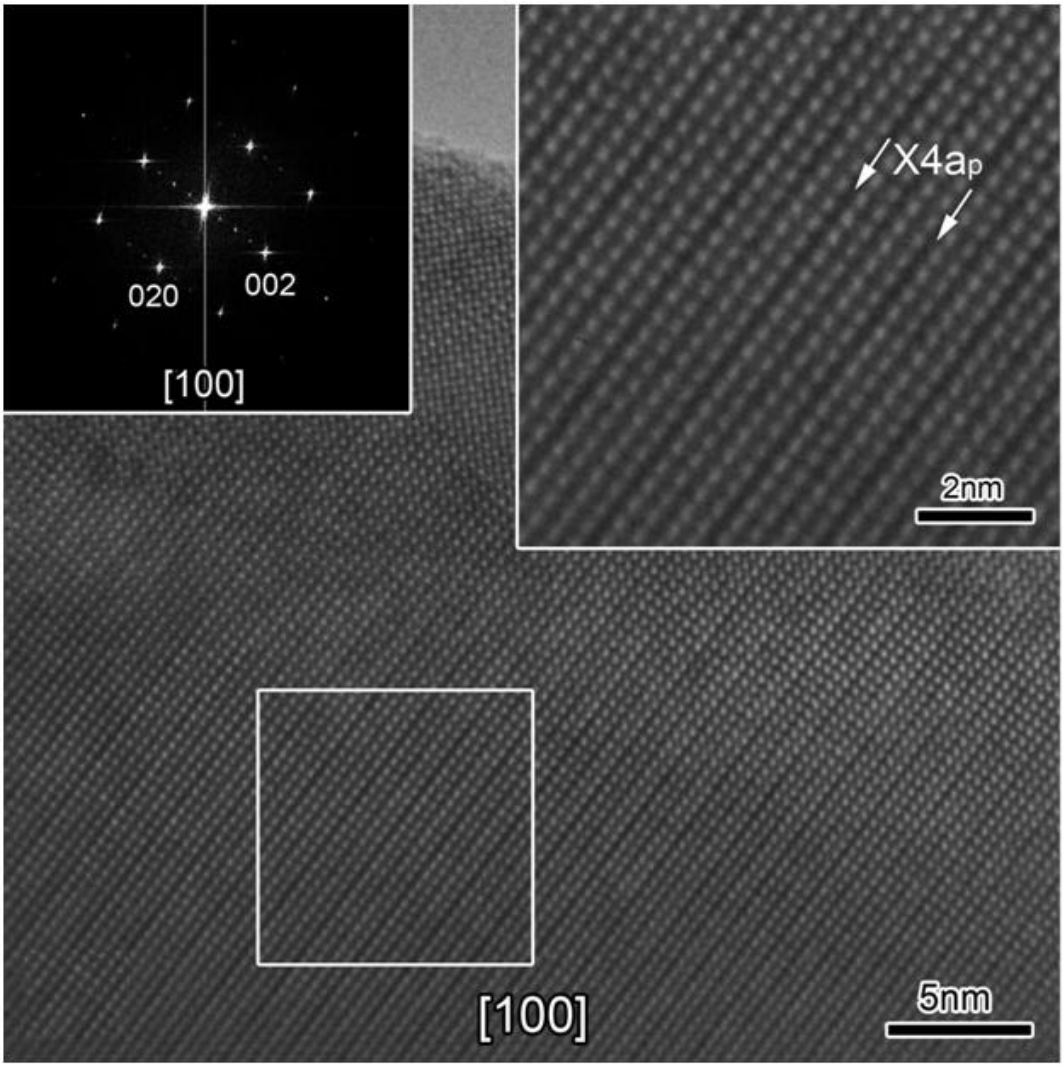

Figure 5.11. *[100] HRTEM image with commensurate modulation vector q= 0.25* ⟨001⟩$_p$.*

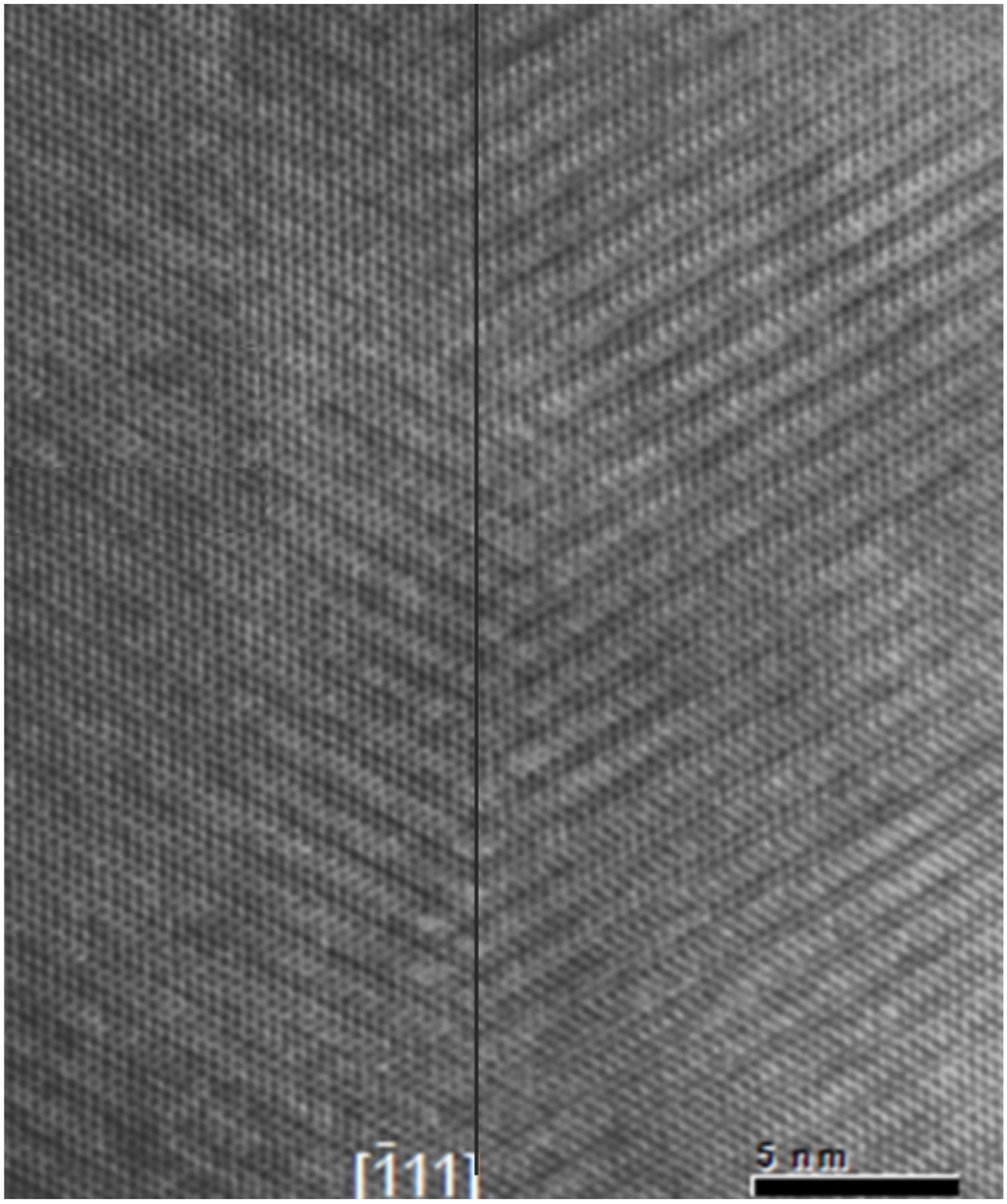

Figure 5.12. [$\bar{1}$11] *HRTEM image with observed twin boundaries when modulations directed along different equivalent* $\langle 110 \rangle_p$ *on both sides.*

5.5 X-ray and neutron powder diffraction analysis

Room temperature X-ray powder diffraction pattern data were collected on a Panalytical X-pert pro diffractometer with a Co $K\alpha_1$ X-ray source. At first the powder pattern appeared to index a unit cell based on the original rhombohedral *R*3*c*, which describe the $BiFe_{1-x}Mn_xO_3$ within the composition range x=0-0.3.

Rietveld refinement was performed with the computer program Jana [29]. The refinement showed that the *R*3*c* model did not give a satisfactory fit as observed in Figure 5.13a, where strong misfits of the peaks $(11\bar{4})$ and (006) are revealed.

Table 5.4. *Comparison of agreement factors of space groups with their lattice parameters.*

Space groups	*R3c*	*Cc*	*Imma*	*Pnma*
R_{wp} / %	9.56	6.21	9.78	7.24
a / Å	5.5721(1)	9.7024(3)	5.5869(4)	5.6236(1)
b / Å	5.5721(1)	5.5857(2)	7.8633(3)	7.8728(2)
c / Å	13.7694(3)	5.6121(2)	5.6087(2)	5.5976(2)
Alfa /°	90	90	90	90
Beta / °	90	125.75(1)	90	90
Gamma /°	120	90	90	90

Further Rietveld analysis showed that a better fit would be obtained with a lower symmetry monoclinic space group *Cc* with R_{wp}=6.21% (Figure 5.13b) in contrast to agreement factor for *R*3*c* of R_{wp}=9.56%. On the other hand the application of orthorhombic space group *Imma*, which were successfully applied to describe the incommensurate structure other Bi-based perovskites, gave significantly worst fit in comparison to monoclinic *Cc* (Table 5.4). Furthermore, the antiferroelectric *Pnma* like-$PbZrO_3$ structure used to define BFM at high pressure gave the worst results when compared to the monoclinic *Cc* model.

(a)

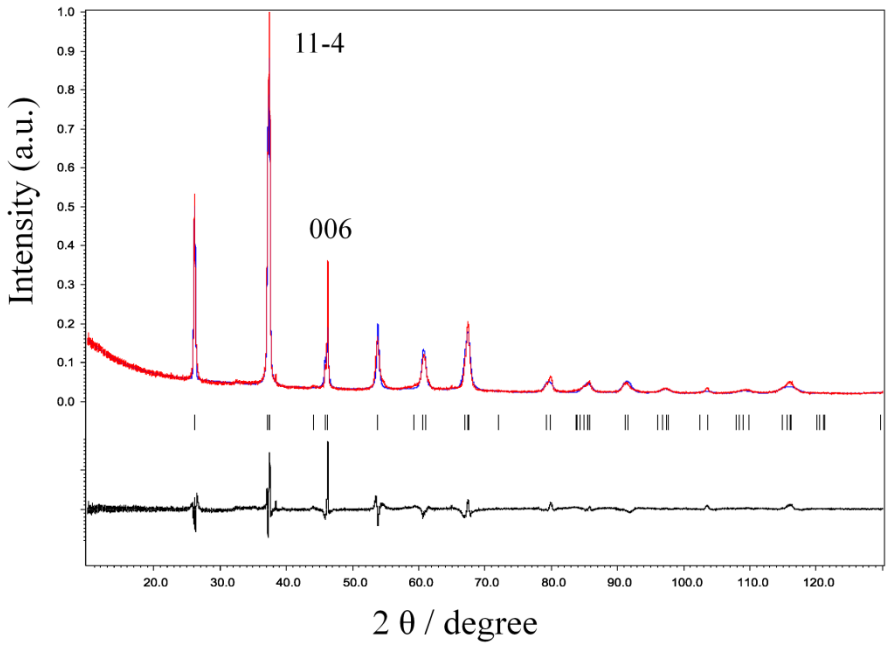

(b)

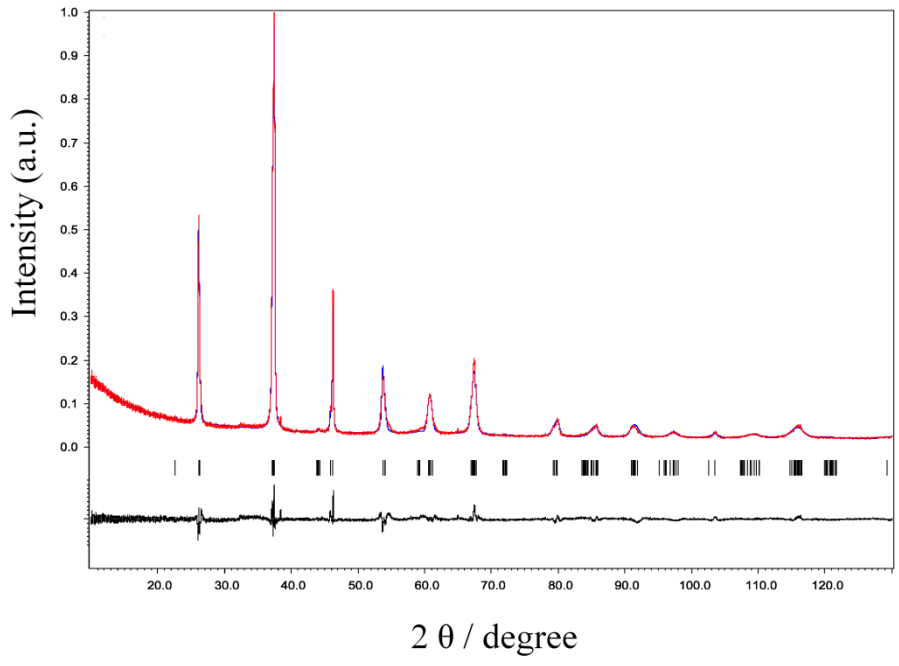

Figure 5.13. *Rietveld refinement of powder X-ray diffraction pattern for the sample* $BiFe_{0.6}Mn_{0.4}O_3$ *with (a) rhombohedral R3c space group which describe* $BiFe_{1-x}Mn_xO_3$ *within the composition range x=0, 0.1, 0.2 and 0.3, and (b) low*

symmetry monoclinic Cc space group. The red points are observed data, the solid blue line is the calculated pattern, whereas the black line represent the difference between observed and calculated patterns.

The TEM analysis based on the HRTEM and SAED results demonstrated modulations along $\langle 110 \rangle_p$ where satellite spots are very close to main spots as demonstrated by arrow on the Figure 5.9. This can be indexed by a modulation vector $q=\alpha\mathbf{a}^*+\gamma\mathbf{c}^*$ ($\alpha\sim1$ and $\gamma\sim1/4$) in the monoclinic *Cc* space group, where **a*** and **c*** represent vectors of reciprocal lattice of the basic structure. A similar modulated structure was observed for Pb_2CoWO_6, with planar monoclinic superspace group *I2/m(=α0γ)0s*, with $\alpha\sim9/10$ and $\gamma\sim3/17$ [30, 31]. Pb_2CoWO_6 displays a complex ferroelastic domain state in the incommensurate structure and was investigated by single crystal, X-ray and neutron diffractions pattern analysis. Thanks to neutron diffraction analysis, the modulated displacements of light atoms were determined, allowing an accurate description of the modulation of both the cations and the O-atom framework. The Rietveld refinement demonstrated a displacive model for the phase transition, involving significant atomic shifts for Pb atoms and a quite complex mixing of tilt and deformation of the oxygen octahedra.

The modulation vector of BFM (x=0.4) suggested by our TEM analysis was used to index the X-ray diffraction pattern. Rietveld refinement was performed with an applied modulation vector q to account for the incommensurate character of BFM, and the periodicity was described by a fraction of lattice translations of the basic unit cell $q=0.9762\ \mathbf{a}^*+0.2164\ \mathbf{c}^*$. The refined irregular value of modulation vector 0.2164 along $\langle 110 \rangle_p$ is more close to the obtained mixture of 4-fold and 5-fold modulations along basic lattice $0.207^*\langle 110 \rangle_p$ observed in the HRTEM than approximate 4-fold modulations $0.247^*\langle 110 \rangle_p$ in SAED. On the other hand, the refined modulation $\alpha=0.9762$ is in agreement with SAED analysis, where satellite and main spots are close to each other. However, the determination of the modulation vector is very challenging, as both satellite and main reflections are represented by broad Bragg peaks in diffraction pattern, as an effect of a relatively low degree of crystallinity of the material. Probably as a consequence of the

relatively broad observed peaks, the results of Rietveld refinement with applied modulation vector q=0.9762 **a***+ 0.2164 **c***, did not significantly improve the fit, as the agreement factor R_{wp}=6.01% is only slightly smaller than for the commensurate case R_{wp}=6.21% (Figure 5.14). The non significant difference between incommensurate and commensurate case is most likely caused by broad Bragg peaks in X-ray powder diffraction pattern, as mentioned earlier, and thus with the satellite reflections very close to the main Bragg reflections cannot be sufficiently resolved.

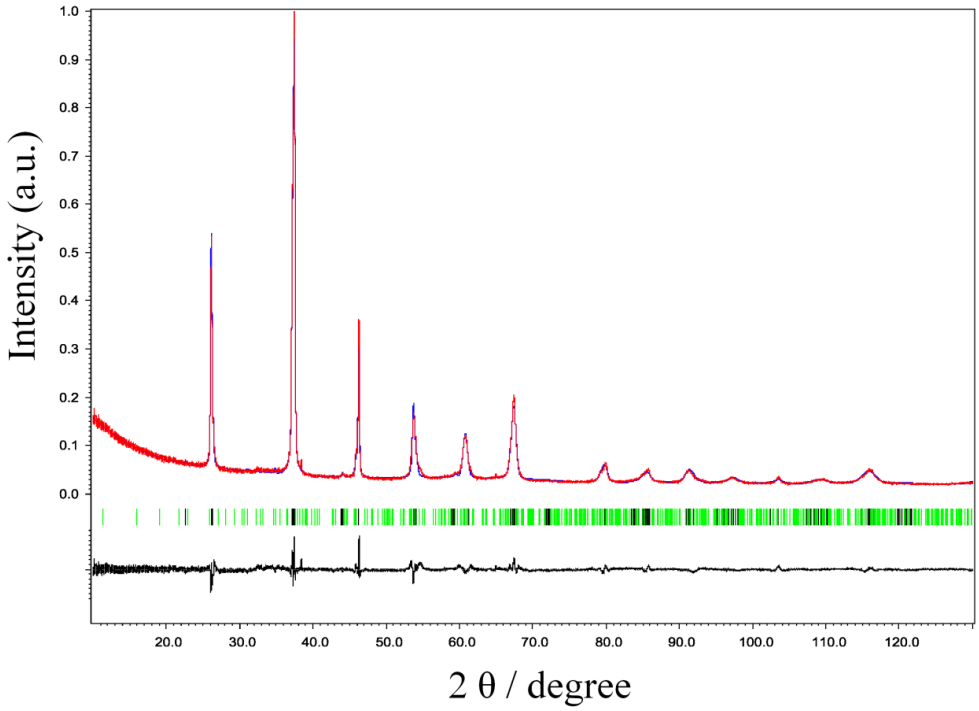

Figure 5.14. *Rietveld refinement of powder X-ray diffraction pattern for the sample* $BiFe_{0.6}Mn_{0.4}O_3$ *with monoclinic Cc(α0γ) superspace group and applied incommensurate modulation vector q=0.9762* ***a*****+ 0.2164* ***c*****. The red points are observed data, the solid blue line is the calculated pattern, whereas the black line represent the difference between observed and calculated patterns. The black and green reflections correspond to main and satellite reflections in the incommensurate structure respectively.*

In order to derive more accurate modulated displacements, the BFM material was analyzed by neutron diffraction. The neutron powder diffraction data were

collected at the Polaris instrument [32] at the ISIS pulsed spallation neutron source as described in section 2.3.2. The sample of approximate weight 0.5 g, was collected for 1000 *μAh*. The neutron powder diffraction analysis was performed simultaneously on data from two banks: backscattering bank (C), which gives the best resolution within the range d-spacing 0.2-3.2 Å, and 90 degrees bank (E) providing the medium resolution but within extended range of d-spacing 0.2-4 Å.

The Rietveld refinements were performed for both commensurate and incommensurate structures, as for the X-ray data. The previously identified modulation vector q=0.9762 **a***+ 0.2164 **c*** was applied in both 90 degrees bank and high resolution backscattering bank. Upon refinement the value of the applied modulation refined to q=0.968 **a***+ 0.235 **c***, and the obtained mixture of 4-fold and 5-fold modulations along basic lattice $\langle 110 \rangle_p$ are close to SAED average incommensurate modulation (q=0.247* $\langle 110 \rangle_p$), with the α component remaining very close to unity. Thanks to application of modulation vectors, the agreement factors for the incommensurate model for the 90 degrees bank R_{wp}=3.88% and backscattering bank R_{wp}=3.26%, were significantly improved in comparison to commensurate subcell model for these banks (R_{wp}=4.95% and R_{wp}=4.40% respectively) (Table 5.5). This is achieved by relatively comparable scattering power of heavy Bi and light O in a neutron diffraction pattern, which help to define atomic position of lighter elements with better accuracy, in contrast to the X-ray where diffraction pattern is dominated by heavy elements. The Rietveld refinement of the medium resolution bank (E) (Figure 5.15a) shows an acceptable fit for incommensurate case for monoclinic *Cc* space group, whereas the high resolution backscattering bank (C) (Figure 5.15b) despite the improved fit, revealed misfits of two peaks $(22\bar{2})$ and (220) at 2.0 and 2.3 Å respectively. These observed misfits at 2.0 and 2.3 Å are an effect of less accurate fit of broad peaks by satellite reflections, indicating that modulations in this material are more complex than the model adopted. Analysis of the Fourier map helps to visualize the modulation functions, where atoms are described as a undulating strings of high density [33]. The two dimensional section of the (3+1)-dimensional Fourier map (parallel to x_3, x_4, where x_3 and x_4 correspond to $\langle 110 \rangle_p$ direction and modulation vector respectively) show atomic strings corresponding to Bi and O

cations respectively (Figure 5.16a, b and c). Maximum density traces in terms of the physical space section t, which define the component of the modulation function of Bi and O atoms, is in a good agreement with position of Bi and O cations in refined structural model. The Fourier map shows a more complex modulation function than simple *sine* term, due to presence of two components α and γ, standing with reciprocal lattice **a*** and **c*** (q=0.968 **a***+ 0.235 **c***). The superposition of two components in the modulated vector, where one is parallel and the second lies perpendicular to the plane, provide the complex shape of modulation especially for oxygen atoms (Figure 5.16b, c), which is possible to determine thanks to improved detection of oxygen in neutron diffraction technique. These complex shape modulations observed in the Fourier maps are most likely responsible for misfits observed in the high resolution backscattering bank (Figure 5.15b). Furthermore, the presence of modulation components values close to 1 provide evidence for the true modulation function being a discountinous, and correct description the structure in the future may require the application of a crenel function, as observed for $BiCo_{1/2}Ti_{1/2}O_3$ [34]. Despite the observable misfit for these two peaks, the applied low symmetry monoclinic *Cc* space group provides the best possible fit to the experimental neutron diffraction pattern, and thus is different than applied rhombohedral *R*3*c* used to describe low doped $BiFe_{1-x}Mn_xO_3$ (x=0, 0.1, 0.2 and 0.3).

Table 5.5. *Comparison of commensurate and incommensurate agreement factors and lattice parameters.*

Space group	*Cc*	*Cc* ($\alpha 0 \gamma$)
R_{wp} / % (90° bank)	4.95	3.88
R_{wp} / % (backscattering bank)	4.40	3.26
a / Å	9.7172(9)	9.6927 (10)
b / Å	5.5928 (6)	5.5866(6)
c / Å	5.6368 (7)	5.6206(7)
α / °	90	90
ß / °	125.877 (7)	125.75(6)
γ / °	90	90
(α, *0*, γ)	-	(0.968, 0, 0.235)

(a)

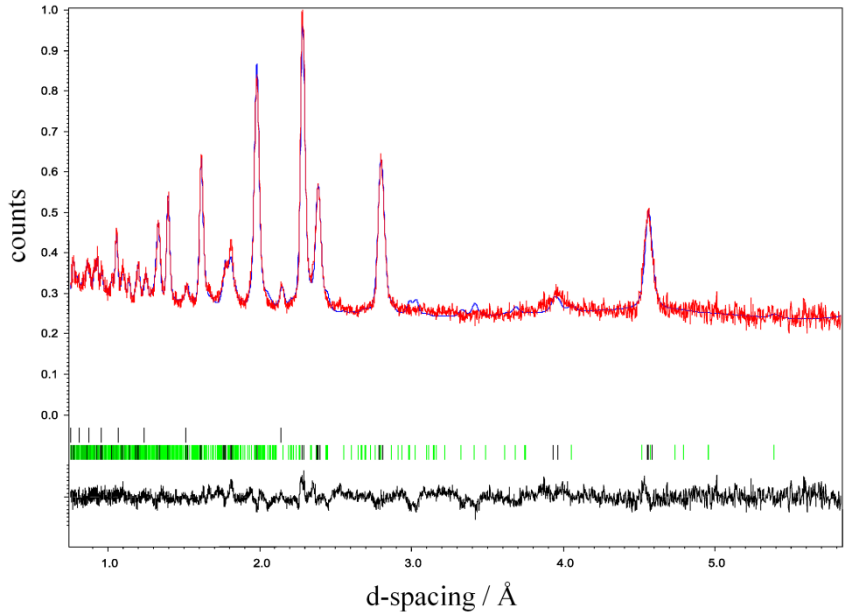

(b)

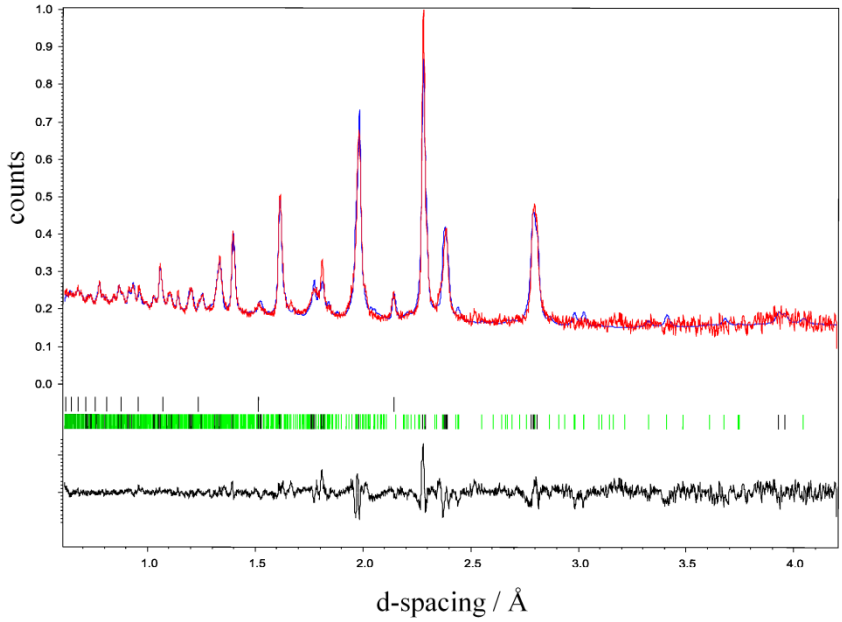

Figure 5.15. *Rietveld refinement of (a) 90 degrees bank and (b) backscattering bank of neutron powder diffraction pattern for the sample* $BiFe_{0.6}Mn_{0.4}O_3$ *with*

*monoclinic superspace group Cc(α0γ) and applied incommensurate modulation vectors q=0.968**a***+0.235**c***. The red points are observed data, the solid blue line is the calculated pattern, whereas the black line represent the difference between observed and calculated patterns. The upper reflections correspond to the vanadium from the sample container, whereas the lower black and green reflections correspond to main and satellite reflections in the incommensurate structure respectively.*

(a)

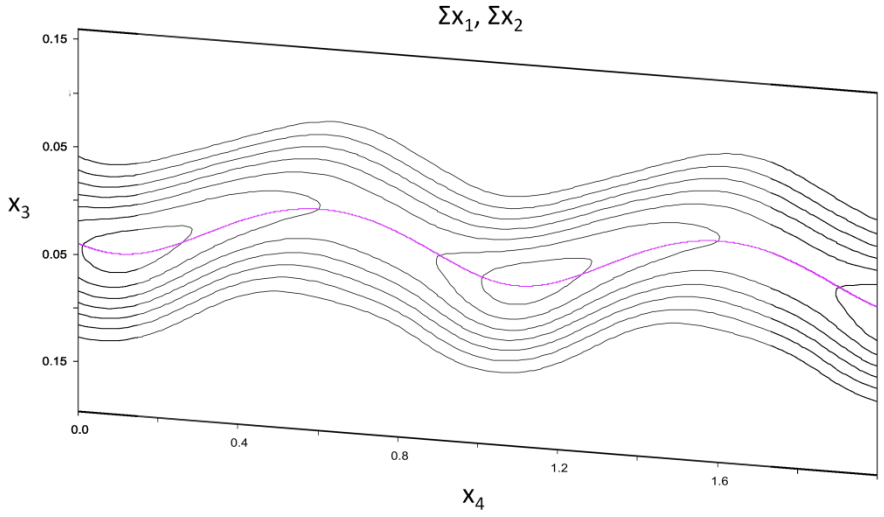

(b)

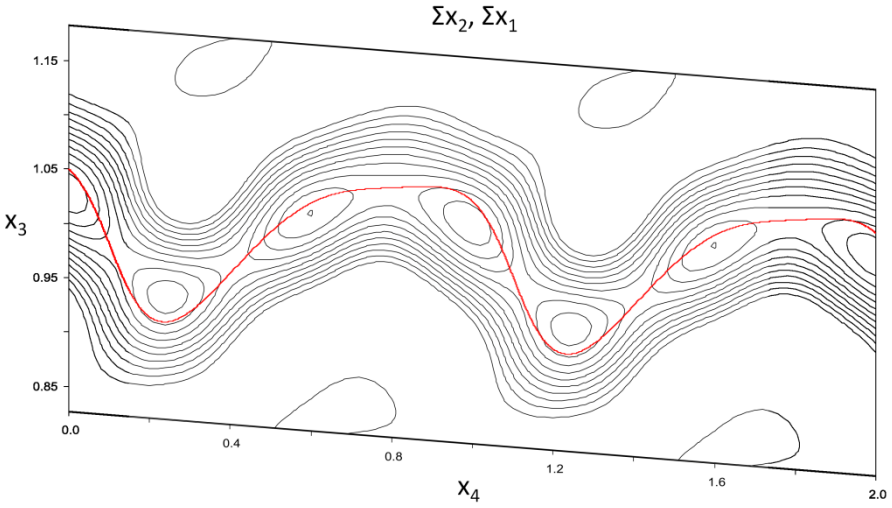

(c)

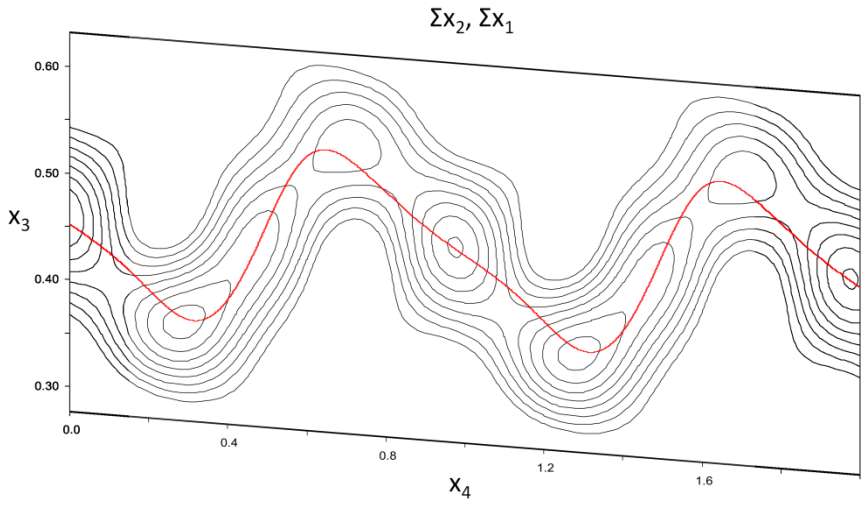

Figure 5.16. *Sections of difference Fourier maps in superspace of BFM (x=0.4) corresponding to: (a) Bi; (b) and (c) O cations. Contours and strings (black) are related to the density of electrons, while the violet and red colours correspond to the atomic positions of Bi and O atoms within modulated crystallographic model.*

Due to the complex modulations in BFM (x=0.4) structure the analysis of bond distances were performed for commensurate subcell, and average bond distances were compared to examples $BiTi_{3/8}Fe_{1/4}Mg_{3/8}O_3$, $Bi_2Mn_{4/3}Mn_{2/3}O_6$ and other reports of BFM (x=0, 0.1 and 0.2). The A site environment of commensurate subcell demonstrate three short (2.268(2) Å, 2.374(6) Å, 2.430(12) Å), three long (3.254(2) Å, 3.328(6) Å, 3.369(12) Å) and 6 intermediate bond distances within range 2.7-3.0 Å (Table 5.6 and Figure 5.17). These twelve bond distances calculated from the twelve oxygen coordinate system are very comparable to results obtained for $BiTi_{3/8}Fe_{1/4}Mg_{3/8}O_3$ (chapter 3), where Bi^{3+} cations also create with O anions three short (~ 2.3 Å), three long (~ 3.4 Å), and six intermediate bond distances with comparable range (2.6-3.15 Å). Such significant bond distance range observed in both examples is due to the Bi^{3+} lone pair of electrons on the outermost subshell $6s^2$, which stabilize the off-center displacement of Bi^{3+} cations from oxygen cage. The bond distances of BFM (x=0.4), on the other hand, are lower than observed for the incommensurate structure of $Bi_2Mn_{4/3}Mn_{2/3}O_6$

(BMN), where three group of bond distances are present (2.241(13) Å, 2.428(32) Å, 2.989(34) Å), as demonstrated in the chapter 4. While the shortest bonds of 2.241(13) Å in BMN are close to observed three short bond distances in BFM (x=0.4), the other two groups at 2.428(32) Å and 2.989(34) Å have much lower range of Bi-O bond lengths, than intermediate (2.7-3.0 Å) and long bonds (3.254(2) Å, 3.328(6) Å, 3.369(12) Å) in BFM (x=0.4) material. Thus, the observed range of Bi-O bonds in BFM (x=0.4) are closer to those observed for the ferroelectric $BiTi_{3/8}Fe_{1/4}Mg_{3/8}O_3$ than those observed for the less displaced antiferroelectric $Bi_2Mn_{4/3}Mn_{2/3}O_6$.

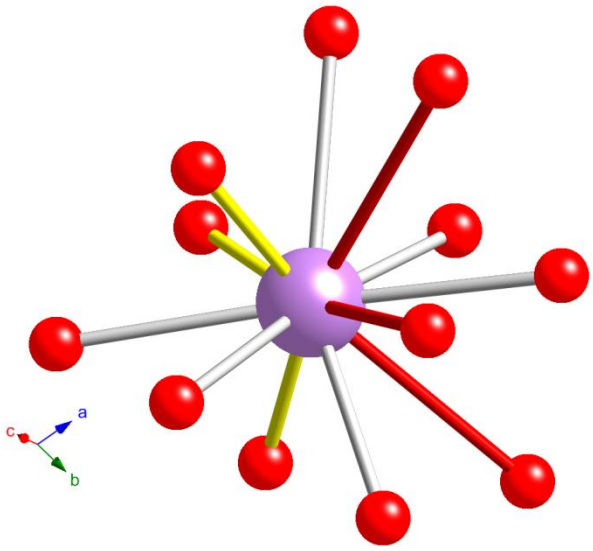

Figure 5.17. *The A site environment within 12 oxygen coordinate system with 3 long (red), 3 short (yellow) and 6 intermediate bond distances (grey). Bi atoms shown in purple color, O atoms as red spheres.*

The A site environment in BFM (x=0.4) is also consistent with a trend observed in BFM (x=0, 0.1 and 0.2). The pure $BiFeO_3$ form four groups of bond distances (2.273(1) Å, 2.526(4) Å, 3.216(7) Å and 3.446(1) Å), which are an effect of off-center displacement of Bi^{3+} cations within twelve oxygen coordinate system, and create the well-known ferroelectric displacement along the $\langle 111 \rangle_p$ direction as explained in chapter 1. The substitution of Fe^{3+} by Mn^{3+} cations causes significant changes to the A site bond distances. The pure bismuth ferrite has range of Bi-O bonds 2.273(1) Å - 3.446(1) Å, whereas in the BFM (x=0.2) the range of Bi-O

bond distances gradually decrease to values 2.293(2) Å - 3.390(2) Å (Table 5.6). The consequence of smaller separations between Bi^{3+} and O upon doping of Mn is a decrease in the polar displacement of Bi^{3+} cations, giving rise to less distorted structures [11]. This is in agreement with Selbach report [14], where Mn substitution and O excess reduces the *c* lattice parameter (parallel to the polar displacement) more than the *a* lattice parameter in *R*3*c* (in the hexagonal setting), indicating that unit cell becomes less distorted. Higher doping of Mn^{3+} cations (x=0.4) in our BFM study gives rise to a structure with the low symmetry monoclinic *Cc* space group, which provides twelve different bond distances for the A site environment, instead of four groups of identical bond distances as observed in rhombohedral BFM (x=0.1, 0.2). Despite the adopting monoclinic lower symmetry of BFM (x=0.4), the Bi-O bond distances sustain a trend of gradually decrease upon Mn doping in rhombohedral BFM (x=0.1, 0.2) [11] and demonstrate a narrower range of bonds 2.268(2) Å – 3.369(12) Å. On the other hand, the calculated displacement of Bi^{3+} cations from the oxygen coordinate system of BFM (x=0.4) 0.383 Å rapidly decrease with increased Mn doping (Table 5.6). The displacement of Bi^{3+} cations in rhombohedral *R*3*c* is purely along polar $\langle 111 \rangle_p$ (Figure 5.18b), whereas displacement in the monoclinic *Cc* structure is more deviated with preference going toward $\langle 110 \rangle_p$ direction (Figure 5.18a). Thus, the replacement of Fe^{3+} by Mn^{3+} cations on the B site, affects the A site–O bond distances resulting in reduced Bi^{3+} displacements with increased Mn doping levels.

Table 5.6. *Comparison of the A site interatomic distances (top) and Bi displacements from O centroid (bottom) of non-modulated $BiFe_{0.6}Mn_{0.4}O_3$ and other compositions of $BiFe_{1-x}Mn_xO_3$ with different doping level (x=0, 0.1 and 0.2). Bond distances for $BiFe_{1-x}Mn_xO_3$ (x=0, 0.1 and 0.2) are from the literature [11].*

	Non modulated average structure $BiFe_{0.6}Mn_{0.4}O_3$ (x=0.4) / Å	$BiFe_{0.8}Mn_{0.2}O_3$ (x=0.2) / Å	$BiFe_{0.9}Mn_{0.1}O_3$ (x=0.1) / Å	$BiFeO_3$ (x=0) / Å
Bi-O	2.268(2) 2.374(6) 2.430(12) 2.67(2) 2.699(12) 2.80(2) 2.82(2) 2.92(2) 3.008(8) 3.254(2) 3.328(6) 3.369(12)	2.293(2) × 3 2.534(2) × 3 3.176(2) × 3 3.390(2) × 3	2.277(1) × 3 2.530(2) × 3 3.202(1) × 3 3.429(1) × 3	2.273(1) × 3 2.526(4) × 3 3.216(7) × 3 3.446(1) × 3
Bi displacement from O centroid	0.383	0.611	0.650	0.671

(a) (b)

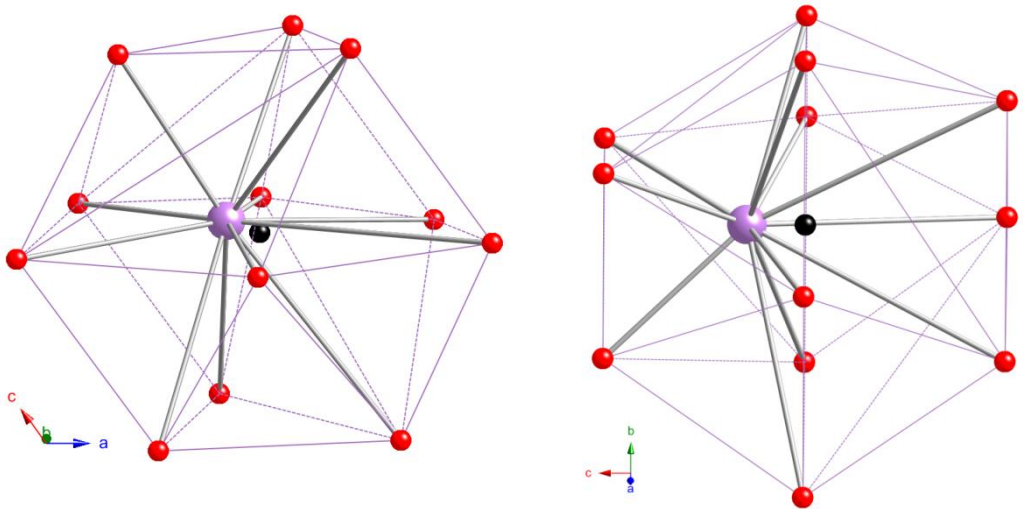

Figure 5.18. *Comparison of Bi^{3+} cation displacement (purple sphere, centroid indicated as a black sphere) within 12 oxygen coordinate system (red spheres) of (a) $BiFe_{1-x}Mn_xO_3$ (x=0.4) and (b) $BiFeO_3$. $BiFe_{1-x}Mn_xO_3$ (x=0.4) demonstrate*

off-center deviated displacement with preference going toward $\langle 110 \rangle_p$ *(c direction in monoclinic Cc) whereas* $BiFeO_3$ *show* Bi^{3+} *cation displacement purely along* $\langle 111 \rangle_p$ *(c direction in rhombohedral R3c).*

The B site environment analysis of BFM at lower Mn doping levels (x=0.1, 0.2) does not show any significant differences within the B site octahedra, indicating that substitution of Mn cations has a more significant effect on the A site environment than on the B site. On the other hand, higher doping of Mn in BFM (x=0.4) demonstrate broader range of B site-O bond distances than in lower doping levels (x=0, 0.1, 0.2) (Table 5.7). The octahedra, representing B site cations within six coordinate oxygen atoms, has six different bond distances, as a result of adopting a low symmetry monoclinic space group. These six unique bond lengths in BFM (x=0.4) create the pattern of one short and long bonds (1.902 Å and 2.191 Å) and four intermediate bond distances (1.94 Å - 2.04 Å) (Figure 5.19), while the less doped BFM (x=0.1, 0.2) adopting higher symmetry rhombohedral space group R3c, have a two regular bond distances (3 × 1.951(1) Å, 3 × 2.113(1) Å) (Table 5.7).

Table 5.7. *Comparison of the B site interatomic distances (top) and displacements from O centroid (bottom) of non-modulated* $BiFe_{0.6}Mn_{0.4}O_3$ *and other compositions of* $BiFe_{1-x}Mn_xO_3$ *with different doping level (x=0, 0.1 and 0.2) derived from Sosnowska report [11].*

	Non modulated average structure $BiFe_{0.6}Mn_{0.4}O_3$ / Å	$BiFe_{0.8}Mn_{0.2}O_3$ (x=0.2) / Å	$BiFe_{0.9}Mn_{0.1}O_3$ (x=0.1) / Å	$BiFeO_3$ (x=0) / Å
Fe/Mn-O	1.902(1) 1.938(1) 2.024(11) 2.028(2) 2.045(7) 2.191(2)	1.946(2) × 3 2.102(3) × 3	1.951(2) × 3 2.106(2) × 3	1.951(1) × 3 2.113(1) × 3
Fe/Mn displacement from O centroid	0.193	0.271	0.262	0.263

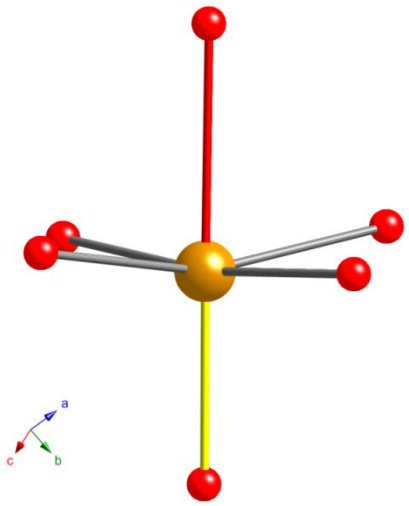

Figure 5.19. *The B site environment within 6 oxygen coordinate system with one short (1.902 Å, yellow) and long bonds (2.191 Å, blue) and four intermediate bond distances (1.94 Å - 2.04 Å, grey). B site atom shown in orange color, O atoms as red spheres.*

The apical short and long bond distances in BFM (x=0.4) cause the displacement of Fe/Mg cations from oxygen octahedra along the ⟨011⟩ direction of the monoclinic unit cell (Figure 5.20a). Despite the broader range of B site-O bond distances, the analysis of B site environment demonstrate smaller displacement from centroid of octahedra (0.193 Å) than in rhombohedral BFM (x=0, 0.1, 0.2) where magnitude of displacements ~0.26 Å is only along $\langle 111 \rangle_p$ (Table 5.7 and Figure 5.20b). Thus, the B site environment in monoclinic BFM (x=0.4) is different in both magnitude and direction of displacement in comparison to rhombohedral *R*3*c*.

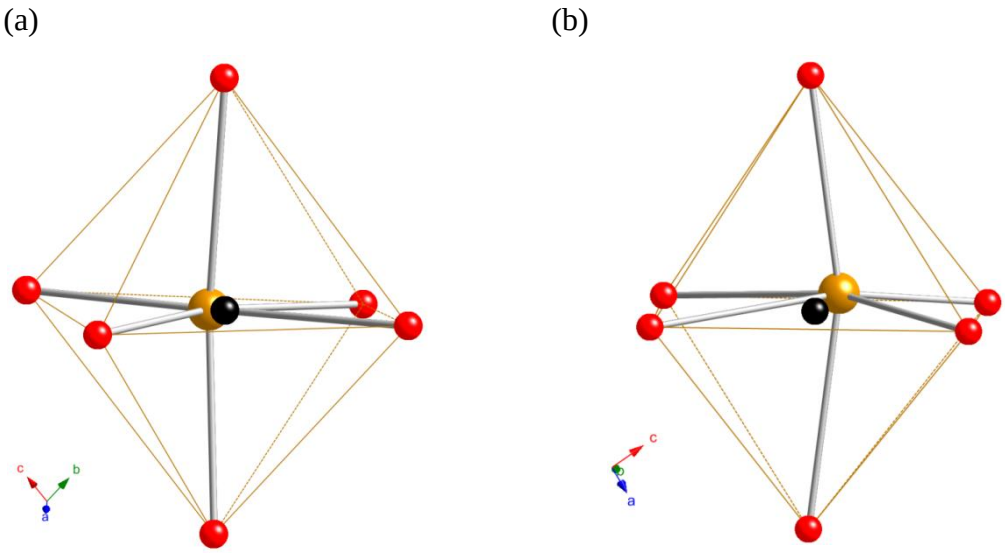

Figure 5.20. *Comparison of B site cation displacement (orange sphere, centroid indicated as a black sphere) within oxygen octahedral (red spheres) of (a) $BiFe_{1-x}Mn_xO_3$ (x=0.4) and (b) $BiFeO_3$. $BiFe_{1-x}Mn_xO_3$ (x=0.4) demonstrate off-center deviated displacement along the ⟨011⟩ direction of the monoclinic unit cell (b and c direction correspond to $⟨1\text{-}10⟩_p$ and $⟨110⟩_p$ directions respectively in monoclinic Cc) whereas $BiFeO_3$ show B site cation displacement purely along $⟨111⟩_p$ (c direction in rhombohedral R3c).*

The magnetic structure was also investigated, where commensurate G-type magnetic model was applied in Jana refinement. A purely magnetic peak was observed in the neutron diffraction pattern at a *d* spacing 4.55 Å. The same magnetic peak was observed for the well-known $BiFeO_3$, as well as $BiFeO_3$ doped with manganese (despite these structures adopting a higher symmetry rhombohedral structure, *R*3*c*) [3, 4]. The pure $BiFeO_3$ investigated first by Kiselev in the 1960s [35] showed first approximation with G-type antiferromagnetic structure, however later in 1980s was found by Sosnowska [12], that G-type antiferromagnetic structure is modulated. The splitting of pure magnetic peaks at 4.55 Å was revealed, due to the advanced high resolution diffractometer OSIRIS, and the satellite splitting was assigned to the long-period range (λ=620 Å) modulations with spiral direction along $⟨110⟩_p$ and spin rotation plane $(110)_p$,

called spiral modulated spin structure (SMSS) [4]. When Fe was partially replaced by Mn, the splitting gradually disappeared and the modulated G-type magnetic order was transformed to a G-type collinear antiferromagnetic structure (Figure 5.21a). The magnetic moments of pure bismuth ferrite (3.75(2) μ_B) was also decreased upon Mn doping; the propagation vector changes and the average magnetic moment gradually decrease with increased Mn content to a value of 2.98(4) μ_B for $BiFe_{0.8}Mn_{0.2}O_3$ [3].

This trend was also observed in our studying of BFM (x=0.4), as the magnetic peak (1-10) has a regular shape with no sign of splitting (Figure 5.21b). The G-type antiferromagnetic structure is observed, where each Fe magnetic ion is surrounded by six Fe^{3+} nearest neighbours with antiparallel magnetic moments (Figure 5.21c). The refined magnetic moments of BFM (x=0.4) has a value of 2.576 μ_B, which is smaller than pure bismuth ferrite (3.75(2) μ_B) and doped $BiFe_{0.8}Mn_{0.2}O_3$ (2.98(4) μ_B). The trend of decreasing magnetic moment with increased Mn substitution indicates that Mn doping into Fe site generates magnetic disorder (spread of orientations of the magnetic moments) on the B site, reducing the observed average magnetic moment and changing spin direction. Thus, further replacing Fe by Mn cations in BFM (x=0.4) is consistent with observed transformation from the spiral modulated structure to collinear antiferromagnetic structure in perovskite $BiFe_{1-x}Mn_xO_3$.

(a)

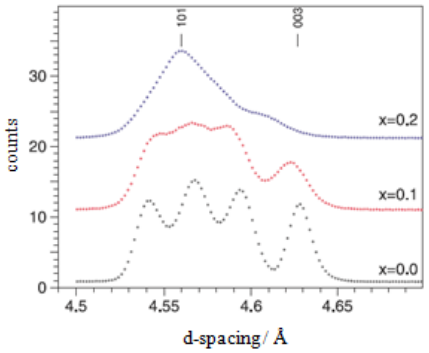

(b)

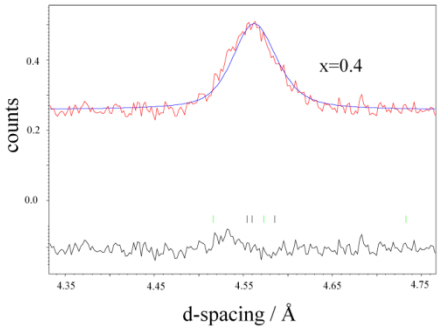

(c)

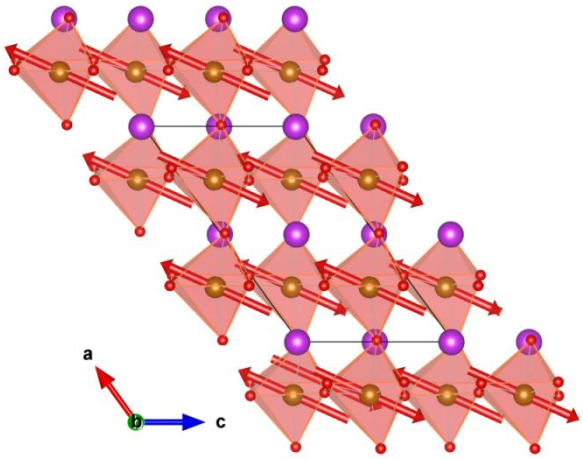

Figure 5.21. *(a) Pure magnetic reflections of BFM (x=0, 0.1 and 0.2) at different Mn doping levels, as reported by Sosnowska [3]; (b) Pure magnetic reflection observed for BFM (x=0.4), demonstrating no signs of splitting. The observed data is shown in red, the calculated fit is shown in blue and the difference is shown in grey; (c) The G-type antiferromagnetic structure of BFM (x=0.4), with Fe magnetic ion surrounded by six Fe^{3+} nearest neighbours with antiparallel magnetic moments (red arrows). Fe is shown in brown, Bi in purple and O in red.*

5.6 Conclusions

$BiFe_{0.6}Mn_{0.4}O_3$ (BFM) has been successfully synthesized at ambient pressure, in contrast with reports suggesting that high pressure is required to obtain pure $BiFe_{1-x}Mn_xO_3$ above x=0.3 [6, 9, 14]. The rapid liquid phase sintering technique prevents the formation of the impurity phases of sillenite $Bi_{25}FeO_{39}$ and mullite $Bi_2Fe_4O_9$. The application of a higher sintering temperature than the melting point of Bi_2O_3 (817°C) creates a liquid phase which accelerates the synthesis reaction with other oxides Fe_2O_3 and MnO_2. The TEM analysis indicated that the $BiFe_{0.6}Mn_{0.4}O_3$ revealed a modulated character observed along the $\langle 110 \rangle_p$ direction. Structural analysis of X-ray and neutron diffraction patterns showed a better agreement between the observed and calculated data for the incommensurate structure than for the commensurate subcell, but did not produce significant differences between crystallographic models. The Rietveld refinement of neutron diffraction data was best able to distinguish between the incommensurate and commensurate cases and showed a more significant improvement for the incommensurate model compared to the X-ray data; we attribute this to the better sensitivity of oxygen atoms which are involved in the modulated behavior with neutron diffraction when compared to X-ray diffraction. The obtained modulation vectors from the Rietveld refinement of neutron diffraction patterns (q=0.968 **a***+ 0.235 **c***) are very close to obtained the average incommensurate modulation vector 0.247* $\langle 110 \rangle_p$ in the SAED; this is in contrast to the X-ray results where the modulation vector was more significantly different (q=0.9762 **a***+ 0.2164 **c***). Despite the application of an incommensurate structural model, the Rietveld refinement still revealed misfits, indicating that atomic modulated displacements are more complex than can be modeled by modulation vector q=0.968 **a***+ 0.235 **c***. The Fourier map confirmed the complex modulation function, especially for oxygen atoms, which were attributed to the presence of two imposed components α and γ in the modulation vector q= α**a*** + γ**c***, and suggest that a more accurate description of structure may require further investigation with the use of a crenel function. The magnetic structure investigation demonstrated G-type antiferromagnetic of Fe^{3+} cations with the smaller average magnetic moments than less doped $BiFe_{1-x}Mn_xO_3$ (x=0-0.3), and

thus the x=0.4 follows the same trend observed for lower doping levels where Mn substitution into B site causes a transformation from the spiral modulated structure (SMSS) to a collinear antiferromagnetic structure.

5.7. References

1. Valant, M., Axelsson, A.K., and Alford, N., *Peculiarities of a solid-state synthesis of multiferroic polycrystalline $BiFeO_3$.* Chemistry of Materials, 2007. **19**(22): p. 5431-5436.
2. Sosnowska, I., Schafer, W., and Troyanchuk, I.O., *Investigations of crystal and magnetic structure of $BiMn_{0.2}Fe_{0.8}O_3$.* Physica B, 2000. **276**: p. 576-577.
3. Sosnowska, I., Schaffer, W., Kockelmann, W., Andersen, K. H., , *Crystal structure and spiral magnetic ordering of $BiFeO_3$ doped with manganese.* Applied Physics a-Materials Science & Processing, 2002. **74**: p. S1040-S1042.
4. Sosnowska, I.M., *Neutron scattering studies of $BiFeO_3$ multiferroics: a review for microscopists.* Journal of Microscopy, 2009. **236**(2): p. 109-114.
5. Kothari, D., Reddy, V. R., Gupta, A., Phase, D. M., Lakshmi, N., Deshpande, S. K., Awasthi, A. M., *Study of the effect of Mn doping on the $BiFeO_3$ system.* Journal of Physics-Condensed Matter, 2007. **19**(13).
6. Yang, C.H., Koo, T.Y., and Jeong, Y.H., *How to obtain magnetocapacitance effects at room temperature: The case of Mn doped $BiFeO_3$.* Solid State Communications, 2005. **134**(4): p. 299-301.
7. Belik, A.A., Abakumov, A. M., Tsirlin, A. A., Hadermann, J., Kim, J., Van Tendeloo, G., Takayama-Muromachi, E., *Structure and magnetic properties of $BiFe_{0.75}Mn_{0.25}O_3$ perovskite prepared at ambient and high pressure.* Chemistry of Materials, 2011. **23**(20): p. 4505-4514.
8. Troyanchuk, I.O., Chobot, A. N., Mantytskaya, O. S., Tereshko, N. V., *Magnetic properties of $BiFe_{1-x}M_xO_3$ (M = Mn, Ti).* Inorganic Materials, 2010. **46**(4): p. 424-428.

9. Ianculescu, A., Gheorghiu, F. P., Postolache, P., Oprea, O., Mitoseriu, L., *The role of doping on the structural and functional properties of $BiFe_{1-x}Mn_xO3$ magnetoelectric ceramics.* Journal of Alloys and Compounds, 2010. **504**(2): p. 420-426.

10. Sahu, J.R., *Beneficial modification of the properties of multiferroic $BiFeO_3$ by cation substitution.* Solid State Sciences, 2007. **9**(10): p. 950-954.

11. Sosnowska, I., Schafer, W., Kockelmann, W., Troyanchuk, I. O., *Neutron diffraction studies of the crystal and magnetic structures of $BiMn_xFe_{1-x}O_3$ solid solutions*, in *Epdic 7: European Powder Diffraction, Pts 1 and 2*, R. Delhez and E.J. Mittemeijer, Editors. 2001, Trans Tech Publications Ltd: Zurich-Uetikon. p. 616-620.

12. Sosnowska, I., Peterlinneumaier, T., and Steichele, E., *Spiral magnetic ordering in Bismuth Ferrite.* Journal of Physics C-Solid State Physics, 1982. **15**(23): p. 4835-4846.

13. Sosnowska, I. and Zvezdin, A.K., *Origin of the long-period magnetic ordering in $BiFeO_3$.* Journal of Magnetism and Magnetic Materials, 1995. **140**: p. 167-168.

14. Selbach, S.M., Tybell, T., Einarsrud, M. A., Grande, T., *Structure and properties of multiferroic oxygen hyperstoichiometric $BiFe_{1-x}Mn_xO_{3+delta}$.* Chemistry of Materials, 2009. **21**(21): p. 5176-5186.

15. Cohen, R.E., *Origin of ferroelectricity in perovskite oxides.* Nature, 1992. **358**(6382): p. 136-138.

16. Azuma, M., Takata, K., Saito, T., Ishiwata, S., Shimakawa, Y., Takano, M., *Designed ferromagnetic, ferroelectric Bi_2NiMnO_6.* Journal of the American Chemical Society, 2005. **127**(24): p. 8889-8892.

17. Azuma, M., Kanda, H., Belik, A. A., Shimakawa, Y., Takano, M., *Magnetic and structural properties of $BiFe_{1-x}Mn_xO_3$.* Journal of Magnetism and Magnetic Materials, 2007. **310**(2): p. 1177-1179.

18. Hughes, H., Allix, M. M. B., Bridges, C. A., Claridge, J. B., Kuang, X. J., Niu, H. J., Taylor, S., Song, W. H., Rosseinsky, M. J., *A polar oxide with*

a large magnetization synthesized at ambient pressure. Journal of the American Chemical Society, 2005. **127**(40): p. 13790-13791.

19. Kimura, T., Kawamoto, S., Yamada, I., Azuma, M., Takano, M., Tokura, Y., *Magnetocapacitance effect in multiferroic $BiMnO_3$.* Physical Review B, 2003. **67**(18).
20. Wang, Y.P., Zhou, L., Zhang, M. F., Chen, X. Y., Liu, J. M., Liu, Z. G., *Room-temperature saturated ferroelectric polarization in $BiFeO_3$ ceramics synthesized by rapid liquid phase sintering.* Applied Physics Letters, 2004. **84**(10): p. 1731-1733.
21. Zhu, J.C., Hu, X., Mao, X. Y., Wang, W., Chen, X. B., *Properties of Co substituted Bismuth Ferrite system by rapid liquid phase sintering*, in *Advanced Materials Forum V, Pt 1 and 2*, L.G. Rosa and F. Margarido, Editors. 2010, Trans Tech Publications Ltd: Stafa-Zurich. p. 356-360.
22. Kumar, M., and Yadav, K.L., *Magnetic field induced phase transition in multiferroic $BiFe_{1-x}Ti_xO_3$ ceramics prepared by rapid liquid phase sintering.* Applied Physics Letters, 2007. **91**(11).
23. Kumar, M., and Yadav, K.L., *Rapid liquid phase sintered Mn doped $BiFeO_3$ ceramics with enhanced polarization and weak magnetization.* Applied Physics Letters, 2007. **91**(24).
24. Rusakov, D.A., Abakumov, A. M., Yamaura, K., Belik, A. A., Van Tendeloo, G., Takayama-Muromachi, E., *Structural evolution of the $BiFeO_3$-$LaFeO_3$ system.* Chemistry of Materials, 2011. **23**(2): p. 285-292.
25. Karimi, S., Reaney, I. M., Levin, I., Sterianou, I., *Nd-doped BiFeO3 ceramics with antipolar order.* Applied Physics Letters, 2009. **94**(11).
26. Frontera, C., Garcia-Munoz, J. L., Aranda, M. A. G., Hervieu, M., Ritter, C., Manosa, L., Capdevila, X. G., Calleja, A., *Charge and zener polaron order in $Bi_{0.75}Sr_{0.25}MnO_3$.* Physical Review B, 2003. **68**(13).
27. Hervieu, M., Malo, S., Perez, O., Beran, P., Martin, C., Baldinozzi, G., Raveau, B., *New type of charge/orbital ordering above room temperature in the perovskite $Bi_{2/3}Sr_{1/3}MnO_3$.* Chemistry of Materials, 2003. **15**(2): p. 523-527.

28. Claridge, J.B., Hughes, H., Bridges, C. A., Allix, M., Suchomel, M. R., Niu, H., Kuang, X., Rosseinsky, M. J., Bellido, N., Grebille, D., Perez, O., Simon, C., Pelloquin, D., Blundell, S. J., Lancaster, T., Baker, P. J., Pratt, F. L., Halasyamani, P. S., *Frustration of magnetic and ferroelectric long-range order in $Bi_2Mn_{4/3}Ni_{2/3}O_6$.* Journal of the American Chemical Society, 2009. **131**(39): p. 14000-14017.

29. Petrícek, V., Dusek, M., and Palatinus, L., *Jana2006 - the crystallographic computing system.* 2006; Available from: www-xray.fzu.cz/jana.

30. Bonin, M., Paciorek, W., Schenk, K. J., Chapuis, G., *X-ray study and structural approach to the incommensurate perovskite Pb_2CoWO_6.* Acta Crystallographica Section B-Structural Science, 1995. **51**: p. 48-54.

31. Baldinozzi, G., Calvarin, G., Sciau, P., Grebille, D., Suard, E., *Neutron Rietveld refinement of the incommensurate phase of the ordered perovskite Pb_2CoWO_6.* Acta Crystallographica Section B-Structural Science, 2000. **56**: p. 570-576.

32. Hull, S., Smith, R. I., David, W. I. F., Hannon, A. C., Mayers, J., Cywinski, R., *The Polaris powder diffractometer at ISIS.* Physica B, 1992. **180**: p. 1000-1002.

33. Van Smaalen, S., *Incommensurate Crystallography*. International Union of Crystallography Book Series2007: Oxford University Press.

34. Claridge, J.B., *Personal communications.*

35. Kiselev, S.V., Ozerov, R., and Zhanov, G.S., *Detection of magnetic order in ferroelectric $BiFeO_3$ by neutron diffraction.* Sov. Phys. Dokl. , 1963. **7**: p. 742-744.

Chapter 6. Conclusions

The local structures of Bi-based perovskite materials were investigated by Reverse Monte Carlo modeling in this thesis. This novel technique using neutron total scattering was applied for the first time to search for possible short-range ordering and displacement correlations between atoms to understand complex perovskite structure of materials.

The local structure of perovskite $BiTi_{3/8}Fe_{1/4}Mg_{3/8}O_3$ at various temperatures were described in chapter 3, where the main goal was to investigate displacements correlations of Bi^{3+} and B site cations, which helped to differentiate between rhombohedral and monoclinic symmetry at room temperature (RT) structures. Another investigation effort was to focus on clarifying the role of the three distinct B site cations (Ti^{4+}, Fe^{3+} and Mg^{2+}) in stabilizing this material at ambient pressure.

The local structure investigation based on atomic pair distribution function and calculated displacements of Bi cations from oxygen centroid showed comparable bond distances of A site environment between local and average structures at RT. The analysis of the A site cation displacements at this temperature confirmed the presence of ferroelectricity and rhombohedral symmetry as the major component was along polar direction. The local fluctuations of Bi cations were also revealed in the direction orthogonal to it, where it was observed that two dominant density peaks (domains) were consistent with the lower monoclinic symmetry rather than the threefold pattern associated with a purely rhombohedral symmetry. The same set of calculations and comparison between low temperature (LT) and RT data, showed similar behavior of Bi cations, as expected due to the lack of phase transition. The differences were only observed in peaks shape, which were more separated and sharper at LT data, as a consequence of decreased atomic thermal motion. On the other hand, the analysis of the A site cations environment in the high temperature (HT) cubic phase, revealed the presence of locally off-centered displaced Bi^{3+}cations which were not previously captured by the average crystallographic cubic structure $Pm\bar{3}m$. The distorted behavior of Bi cations was attributed to the lone pair of electrons $6s^2$, which stabilize the off-center

displacements of these A site cations in the same way like in the well-known Pb-based perovskites. Further calculations of displacement correlation function (DCF) at RT and their analysis showed the local ferroelectric correlations of Bi^{3+}cations within 10-15 Å along polar direction and also revealed that local displacements along off-polar axes are also correlated. These ferrolectric correlations producing the local domains were consistent with monoclinic symmetry and existence displacements other than rhombohedral$<111>_p$. The comparison of DCF between LT and RT shows stronger ferroelectric correlations of Bi atoms in the LT data, indicating that ferroelectric correlations between Bi atoms are static and increased atomic thermal motion at RT reduce the magnitude of ferroelectric correlations. Furthermore, the same calculations performed at HT cubic phase also revealed locally weak ferroelectric correlations of the off-center displaced Bi^{3+}cations previously observed in atomic pair distribution function and displacement results, however they were significantly smaller in comparison to correlations observed in ferroelectric material at LT and RT data.

The local B site environment also investigated in chapter 3 showed comparable results within the same phase at LT and RT data, where Ti^{4+}cations demonstrate the more extensive flexibility in its coordination geometry than Fe^{3+} and Mg^{2+}cations. The different behavior of Ti cations was attributed to the hybridization of the lowest unoccupied d^0 energy levels with 2p orbital of O ions which allowed 2^{nd} order of Jahn-Teller distortions, and thus permitted a broad range of distorted octahedral environments which were consistently observed in broader pair distribution functions and octahedral displacements results. Moreover, the DCF calculated between A site and B site cations demonstrated independence of Ti cations, and so their own local displacements, whereas those of Fe^{3+} and Mg^{2+} were driven by Bi^{3+}cations. The ability of Ti being strongly locally displaced along different directions within the octahedra played important role in stabilizing small Bi^{3+}cations within the pure A site of this perovskite structure.

The local structure of $Bi_2Mn_{4/3}Ni_{2/3}O_6$ described in chapter 4 was generated from RMC modeling and compared to average incommensurate and commensurate structures at room temperature (RT) and high temperature (HT) respectively. The main focus during this study was put at RT data, where the average structure defined by incommensurate superstructure descriptions might not faithfully represent the local structure of a complex A site and multiple B site cations as it was still derived from the long-range phenomena of diffraction.

The initial inspection of partial pair distribution functions between RMC models representing local structure and incommensurate models representing average structure showed similar Bi-O bond distances, however closer inspection of incommensurate models revealed two discontinuous distributions as an effect of choosing different initial phases of this modulated structure. Theyalso showed difference in shape and number of bond distances with continuous distribution obtained from RMC models. Furthermore, the analysis of atomic pair distribution function of B site environment also provided the significant difference between the local and average structures at RT. The multiple B site cations were distinguished in the RMC model, where a complex Mn site with regular bond distances of Mn^{4+} and 2:2:2 JT distortions of Mn^{3+}cations had different average bond lengths and distribution shape than Ni cations, in contrast to single B site cations environment observed in the average incommensurate structure. On the other hand, the determination of A site cations displacement correlations at RT, as one of the goals, was revealed by calculations of sum of Bi displacements within a volume. It demonstrated ferroelectric correlations with clusters size up to 12Å, very similar to the polar regions observed in commensurate polar cell, which was previously identified as the best commensurate approximation in 3-dimensional crystallographic structure. Moreover, these ferroelectric correlations creating clusters with opposite displacement direction were also consistent with incommensurate structure, where polar regions canceled each other and produced long-range average antiferroelectricity. The initial similarities between local and average structures were also observed on B site where Mn and Ni order was also investigated. Both local and average incommensurate structure show nearest neighbor B site ordering, which acts to reduce unfavorable Ni-Ni interactions,

however the nature of the B site ordering was different for both structures. The calculations of *n(r)* in the RMC models showed Mn/Ni ordering consistent with a bias towards rock-salt pattern, whereas the incommensurate structure demonstrated clustering of cations based on their average modulated occupancies. Thus, the true short-range B site ordering, as revealed through RMC modeling, was not apparent in the incommensurate structure.

The synthesis and structural characterization of perovskite $BiFe_{0.6}Mn_{0.4}O_3$ (BFM) was described in chapter 5, where traditional crystallography was used to determine the modulated behavior and distorted structure of this material. The highly doped BFM has been successfully synthesized at ambient pressure, in contrast with the reports suggesting that high pressure is required to obtain single phase of this material. The applied rapid liquid phase sintering technique with temperature higher than the melting point of Bi_2O_3 prevented the formation of the impurity phases of sillenite $Bi_{25}FeO_{39}$ and mullite $Bi_2Fe_4O_9$ and formed single phase of perovskite structure. The transmission electron microscopy and electron diffraction analysis indicated that material possessed a modulated character, and thus structural analysis both of X-ray and neutron diffraction patterns were investigated as both commensurate and incommensurate structures. The Rietveld refinement of X-ray data showed a better agreement between observed and calculated diffraction pattern for the lower monoclinic symmetry *Cc* than higher rhombohedral space group R3c, previously identified as the best for low doped BFM ($BiFe_{1-x}Mn_xO_3$, x=0, 0.1, 0.2). However, the X-ray analysis in highly doped BFM did not provide significant differences between incommensurate and commensurate crystallographic models as expected. On the other hand, the Rietveld refinement of neutron diffraction data, due to relatively comparable scattering power of heavy and light elements (e.g. Bi and O), helped to better distinguish crystallographic models, and the calculated and observed diffraction pattern were more consistent for the incommensurate structure. Furthermore, the obtained modulation vectors from the Rietveld refinement of neutron diffraction patterns were in good agreement with modulation vector calculated from the electron diffraction. Beside nuclear structure, the magnetic structure was also investigated and demonstrated G-type antiferromagnetism of Fe^{3+}cations on the B

site with smaller average magnetic moments and changed spin direction in comparison to previously reported less doped BFM.

Therefore, the further Mn doping into BFM besides generating magnetic disorder also showed phase transition from rhombohedral*R3c* to lower monoclinic symmetry *Cc* with modulated character as revealed by electron microscopy and Rietveld refinements.

The average structure derived from Bragg scattering is an invaluable tool for structure characterization on the long length scale, as showed in chapter 5, but total scattering with important structural characteristics such as short-range order or cooperative displacements provided new insights into the structures of $BiTi_{3/8}Fe_{1/4}Mg_{3/8}O_3$ and $Bi_2Mn_{4/3}Ni_{2/3}O_6$.The comparison and analysis of the local and average structures in chapters 3 and 4 showed different results between crystallographic and Reverse Monte Carlo models and thus, recognizing the length-scale of the probe used for structural characterization was very important for the interpretation of the results. Therefore, further investigation of local structure of complex materials (e.g. Bi-based perovskite) is necessary to better understand local atomic environments of materials and their property relations, so new materials with improved ferroelectric properties can be synthesized in the future.